Icahn School of Medicine at Mount Sinai

Translational & Molecular Imaging Institute

7th Annual Symposium

April 7, 2017

New York, NY

Table of Contents

Davis Auditorium – Leon and Norma Hess Center for Science and Medicine
Icahn School of Medicine at Mount Sinai – April 7, 2017

SYMPOSIUM SCHEDULE

7:00am – 8:00am — Check-in / Walk-up Registration / Poster Set-up (2nd floor)
Refreshments and Light Breakfast

OPENING REMARKS

8:00am – 8:15am — **Zahi Fayad, PhD** (Director, Translational & Molecular Imaging Institute)

8:15am – 8:30am — **Dennis Charney, MD** (Dean, Icahn School of Medicine at Mount Sinai)

KEYNOTE ADDRESS – Moderator: Joel Dudley, PhD

8:30am – 9:30am — **Michael McConnell, MD** (Verily Life Sciences/Alphabet, Stanford, CA)
"Leveraging Technology to Re-engineer Healthcare"

9:30am – 10:00am — **Break**

SESSION I – NEUROIMAGING – Moderator: Rafael O'Halloran, PhD

10:00am – 10:45am — **Kendal Lee, MD, PhD** (Mayo Clinic; Rochester, MN)
"Neuromodulation: Challenges and Opportunities"

10:45am – 11:00am — ***Yu Huang, MS*** *(City College of the City University of New York; New York, NY)*
"Measurements and models of electric fields in the in vivo human brain during transcranial electric stimulation"

SESSION II – Cardiovascular Imaging – Moderator: Claudia Calcagno, MD, PhD

11:00am – 11:45am — **Marc Kachelrieß, PhD** (German Cancer Research Center, Heidelberg, Germany)
"Cardiac Imaging: CT, and How Other Modalities may Benefit "

11:45am – 12:00pm — ***Audrey Kaufman, MD*** *(Icahn School of Medicine at Mount Sinai; New York, NY)*
"Effect of acquisition and reconstruction parameters on quantification of thrombus volume in pulmonary embolism using computed tomography pulmonary angiography: Implications for multicenter studies"

12:00pm – 1:00pm **Lunch**

POSTER SESSION – Moderators: Sara Lewis MD, Phil Robson, PhD, Carlos Perez-Medina, PhD, Cheuk Tang, PhD

1:00pm – 2:00pm **Poster Viewing**

SESSION III – CANCER & BODY IMAGING – Moderator: Sara Lewis, MD

2:00pm – 2:45pm **Robert Gillies, PhD** (H. Lee Moffitt Cancer Center & Research Institute, Tampa, FL)
"MR Imaging of Tumor Habitats"

2:45pm – 3:00pm ***Paul Kennedy, PhD*** *(Icahn School of Medicine at Mount Sinai; New York, NY)*
"Simultaneous liver and spleen 2D and 3D MRE acquisitions: preliminary results"

3:00pm – 3:30pm **Break**

SESSION IV – NANOMEDICE – Moderator: Carlos Pérez-Medina, PhD

3:30pm – 4:15pm **Michael McMahon, PhD** (Johns Hopkins School of Medicine, Baltimore, MD)
"Developing High Sensitivity Organic MRI Contrast Agents for Molecular Imaging"

4:15pm – 4:30pm ***Mandy van Leent, MD*** *(Icahn School of Medicine at Mount Sinai; New York, NY);*
"Targeted CD40-TRAF6 inhibition resolves macrophage accumulation in atherosclerosis"

CLOSING REMARKS & AWARDS

4:30pm – 5:00 pm **Burton Drayer, MD** (Chair of Radiology, Icahn School of Medicine at Mount Sinai)

Message from the Translational and Molecular Imaging Institute Director

I can't be more pleased to welcome you to the 7th Annual TMII Symposium. We have again assembled a group of world-renowned scientists who share our vision of giving researchers and medical professionals an opportunity to gain insight into the current translational imaging research.

In the ever-changing landscape integrating big data and medicine, we have Dr. Michael McConnell of Verily Life Science who will expand on his exciting work on "Leveraging Technology to Re-engineer Healthcare". We continue exploring new technology with Dr. Kendall Lee's talk on novel methods of neuromodulation being developed at the Mayo Clinic. Dr. Mark Kachelrieß then explores the cutting edge of cardiac CT pushing the envelope of spatial and temporal resolution and how it the technics could be applied to other organs and modalities.

After lunch we will hear Dr. Robert Gillies will explain how his group at H. Lee Moffitt Cancer Center & Research Institute is using multiparametric imaging to classify the micro-environment of malignant cancers to aid with diagnosis and treatment. Our day concludes with the last session where Dr. Michael McMahon delves into his work at Johns Hopkins School of Medicine using CEST imaging to improve the sensitivity of molecular imaging.

Beyond these luminaires, we have some of the brightest young scientists giving oral presentations in each session and a stellar poster session with groups from throughout the Mount Sinai Health System in addition to the New York Metro area. They are not to be missed.

We truly hope you enjoy this program we have put together.

Zahi A. Fayad, PhD

TMII Director
Mount Sinai Endowed Chair in Medical Imaging and Bioengineering
Professor of Radiology and Medicine (Cardiology)

Translational and Molecular Imaging Institute

Our mission is centered around development, validation, translation and education of innovative technology in biomedical imaging to address both basic and clinical research problems and therefore improve human health.

The Translational and Molecular Imaging Institute (TMII) is a state of the art research facility housed in ~ 20,000 square feet in the Center of Science and Medicine (CSM). TMII (Director, Zahi A. Fayad, PhD) is comprised of faculty, staff and trainees responsible for coordinating and executing all research projects performed in these facilities. Currently TMII has over 50 members with expertise in all aspects of translational imaging research. The faculty consists of Biomedical and Electrical Engineers and Radiologists who are leading experts in neuroimaging, cardiovascular imaging, body/cancer imaging, and nanomedicine. Highly skilled staff provides a full suite of support services for image acquisition, image analysis, scheduling and performance of the proposed experiments.

Access to the TMII facility is based on a fee for service schedule (https://tmii.mssm.edu/imaging-core/resource-fees/). These user fees are calculated to cover the operating and maintenance costs of the instruments and related Core expenses. These rates are determined and periodically reviewed by the Dean's Office and adjusted to reflect the actual costs. User fees include technical support for operation of imaging equipment.

For internal Mount Sinai users, resource usage time is compiled from the web-based scheduling system and charged directly to your account on a monthly basis. Any questions on the charges should be addressed to the TMII Director.

The user fee listed in https://tmii.mssm.edu/imaging-core/resource-fees includes support for:

Study Start-up	Study design/ IRB review & consultations
	Maintenance self-scheduling system
Scan Protocol	Scan parameter Implementation/ Optimization (HiRes Structural, DTI, EPI ...)
	Adaptation of C2P sequences to our scanners
Task Protocol	fMRI Software administration (Eprime, PsychToolBox, PschoPy(thon), Matlab, Cogent)
	Basic task modifications (Triggering, Physio monitoring control, etc)
Stimulus Equipment	Visual (LCD, 3D goggles)
	Audio (Headphones, ear buds)
	Eye-tracking equipment (not software control support
Physiological Monitoring	Set up (SpO2, Heart rate, Respiration, ECG, GSR, EMG, Skin Temperature)
Data Handling	Long-term online image archive (XNAT)

	Burn anonymized data to CD for external sites
Data Analysis	Computer Lab with preloaded analysis software (BV, SPM, FSL, Osirix, Custom In House tools, Matlab)
PET isotopes	Standard tracers: FDG, NaF
Report	Radiological read and report of incidental findings

A. HUMAN & LARGE ANIMAL FACILITES - CSM – SC2

1 . MR/PET (3T) Siemens mMR.

The 3T MR/PET is a fully integrated and capable of simultaneous whole body PET and MRI scanning. This allows more precisely coregistered functional and structural acquisition while r educing the radiation dose in PET imaging by replacing the CT scans with an MRI scan. True simultaneous acquisition of MR and PET data by the hybrid system merges the highly sensitive PET metabolic information with the highly specific MR anatomical and functional information. The 3T MRI system is a whole body imaging system, capable of routine as well as advanced imaging of all body regions. The PET scanner will be fully integrated into the MR, utilizing state of the art solid-state technology for simultaneous PET imaging during MR image or spectrum acquisition. The 3T MR-PET is designed for the purposes of oncological and neurological diagnostic imaging. The highly integrated nature of these systems provides the capability for full spatial and temporal correlation between both modalities. The maximum gradient amplitude will be approximately 40 mT/m per axis, with a maximum gradient slew rate of about 200 T/m/s per axis. The system's magnet has an integrated cooling system and active shielding. The shimming capabilities include: Active (with 3 electric and 5 electric nonlinear linear shim channels) and Passive shims for maintaining very high homogeneity and excellent image quality over a wide range of applications. Online shimming is performed in less to then 20 seconds in order to optimize homogeneity. The RF transmit and receive system include: compact, air cooled tube RF amplifier providing 35 kW peak power; integrated electronics with cabinet water cooling; integrated circularly polarized whole body RF coil; up to 32 receive channels. The PET system include: adaptation to a work environment within high magnetic fields including APD and LSO based detector technology; adaptation and optimization of numerous MR components to an integrated PET imaging unit; high-resolution, high-count rate, positron emission tomography (PET) imaging of metabolic and physiologic processes; high quality metabolic and anatomic image registration and fusion for optimal lesion detection and identification within the body; state-of-the-art 3D PET data acquisition and analysis tools; state-of-the-art 3D PET reconstruction, attenuation and scatter correction software. Expected PET performance specifications: spatial resolution: <6.5mm; timing resolution: < 4.5 ns; sensitivity: > 0.5%; axial FOV: > 19 cm ; transaxial FOV: up to 45 cm. The system also supports MR and PET gated scan acquisition;

support for list mode acquisition, offline histogramming and reconstruction; special calibration. Alignment and quality control sources including shielding; multimodality workplace; 3D iterative reconstruction.

2. 7T Siemens MR whole body scanner.

This is an ultrahigh field 7.0 Tesla actively shielded whole body MRI scanner. The super-conducting magnet is self-shielded, reducing its overall footprint and making it compact and lightweight by 7T standards, weighing 24-tons. The (warm) inner bore of the magnet is 82 cm, which houses the 60 CM inner patient bore. The dimensions of the magnet without covers is approximately 2.5 m in length, 2.6 m in width, and 2.65 m in height. The 5-Gauss line extends slightly further than for a 3T scanner with 5.6 m radial and 7.8 m axial dimension. A whole-body gradient system provides gradient amplitude of up to 70 mT/m per axis, and a maximum slew rate of up to 200 T/m/s. The RF transmit system comes with 8 parallel transmit channels; 8 individually shaped RF pulses can be prescribed simultaneously and independently in amplitude and phase. The multi-nuclei package allows for imaging and spectroscopy at non-proton frequencies, i.e. detection of e.g. 19F, 31P, 7Li, 23Na, 13C, 17O. Our 7T/820AS is configured to accommodate an 8-channel Tx-array and 48-channel Rx receivers. Several coils are currently available such as the 1-channel Tx and 32-channel Rx head coil and the 8-channel Tx and 8-channel Rx head coil.

3. 3T Siemens MAGNETOM Skyra.

This is an FDA approved 3 Tesla human MRI scanner. Its wide bore design (173 cm system length with 70 cm) can accommodate subjects with larger body compositions compared to the 60 cm bore of a typical clinical 1.5T & 3T. A newly deigned RF system and coil architecture integrates (Tim 4G) with all digital-in/digital-out technology. The scanner has an actively shielded water-cooled gradient system and zero helium boil-off. Specialized RF distribution increases uniformity in all body regions. Onboard software is available for: neuro, angio, cardiac, body, onco applications. A variety of coils for all body parts and configuration is available.

4 PET/CT Siemens Biograph mCT. The PET/CT is equipped with a 40 slices multidetector CT and LSO PET crystals. Utilizing timing information (time-of-flight) between the two PET coincidence events, coupled with high definition resolution recovery, the system provides improved image signal-to-noise which can be used to either enhance image quality and/or reduce acquisition time. With a system timing resolution of 555 ps, image quality is clearer with more defined images and provides distortion-free image quality for the entire of the field of view. Specialized image processing techniques utilizing more accurate point spread functions produces higher quality 3D iterative reconstruction with enhanced contrast and higher resolution. Supported image matrices include 128x128, 200x200, 256x256, 400x400, and 512x512.

5 Multidetector CT (MDCT) Siemens Somatom Definition Flash. This Dual Source CT, uses two X-ray sources and two detectors simultaneously, to cover the entire thorax in less than a second. A 2 meter scan requires only 5 seconds, enhancing the efficiency of perfusion or dynamic vascular imaging and reduction the dose for all scans, resulting, e.g. in dose down to sub-mSv for cardiac imaging. Dual Energy automatically provides a second contrast for without any extra dose. Advance software efficiently manages the reduction in dose allowing for: limited exposure to radiation-sensitive organs and increases tissue contrast with no sacrifice to image quality.

6 (2) 1.5T Siemens MR MAGNETOM Aera. Short and open appearance (145 cm system length with 70 cm Open Bore Design) can accommodate subjects with larger body compositions compared to the 60 cm bore of a typical clinical 1.5T & 3T. Newly deigned RF system and coil architecture integrates with all digital-in/digital-out technology, one system use standard gradients (33 mT/m @125 T/m/s) and the second system has advanced gradients (45 mT/m @ 200 T/m/s). Actively shielded water-cooled gradient system with zero helium boil-off. Inline software is specially designed for: neuro, angio, cardiac, body, onco, breast, ortho, pediatric and scientific specialties such as Magnetic Resonance Elastography; a technique that measures the stiffness of tissues by introducing shear waves and imaging their propagation.

7 Siemens ACUSAN S3000 ARFI Ultrasound - The ultrasound system automatically produces an acoustic 'push' pulse that generates shear-waves, which propagate into the tissue. Using image-based localization and a proprietary implementation of acoustic radiation force impulse (ARFI) technology, shear wave speed may be quantified, in a precise anatomical region, focused on a region of interest, with a predefined size, provided by the system. Measurement value and depth are also reported, and the results of the elasticity are expressed in m/s. This system provides new method for the evaluation of the elastic properties of tissues is now available in the Cancer/Body Core. Clinical applications of ARFI imaging include: liver fibrosis quantification, breast, colorectal and prostate tumor imaging.

8 Siemens Force CT. The Force is the third iteration of Siemens' dual-source CT design which features two sets of x-ray tubes and detectors for enhanced imaging of all patients, including young

children, patients with renal insufficiency, and those who cannot hold their breath. Due to its low-kV imaging technique, Force broadens CT's application for patients with renal insufficiency and offers an acquisition speed of 737 mm/sec, so an entire adult chest, abdomen, and pelvis study can be done in one second with no breath-holds. In cardiac imaging, Force can obtain an entire study within one-quarter of a heart beat at a temporal resolution of 66 msec, which is the speed required to freeze the fastest-moving anatomy, such as the right coronary artery.

9 "Mock" MR PSTNet.

The MRI simulator will allow researchers to acclimatize the subjects to the 'enclosed' and loud MRI environment before they actually go into a real scanner. This is especially important for studies involving children.

10 fMRI peripherals All the MRI scanners will be fully equipped with the latest state of the art peripherals for functional imaging including LCD goggles, integrated eye-tracking, fiber optic subject response gloves, pneumatic computerized headphones with microphones as well as a full spectrum of physiological recording probes for ECG, GSR, pulse-Ox etc. There is also a specialized MRI compatible computerized olfacto-meter.

11 Neuro Testing room

A sound proofed and independent temperature controlled neuro testing room is located near the 3T MRI for physiological testing such as EEG, ERP and other modalities. This room is also equipped with large monitors for paradigm training and testing.

B. SMALL ANIMAL FACILITES - CSM-SC1

1 9.4T MR Bruker.

This is a high-resolution rodent only MRI scanner allowing for high-resolution *in-vivo* imaging of mice and smaller specimens. It is 9.4 Tesla 89-mm bore MRI system operating at a proton frequency of 400 MHz (Bruker, Billerica, MA). The 9.4T is equipped with a mouse respiratory and cardiac sensor connected to a monitoring and gating system (SA Instruments, Inc., Stony Brook, NY). Sedation is administered by an Isoflurane/O_2 gas mixture delivered through a nose cone and placed in a 30 mm birdcage coil with an animal handling system. Additionally, a temperature controller is available in the bore of the magnet, to maintain the animal in the RF coil at a selected temperature. Recent upgrades (Bruker Paravision 4) have enabled the use of navigator pulses to allow for cardiac and/or respiratory gating without the use of electrodes.

2 7.0T MR Bruker Biospec 70/30.

This is a high-resolution MR scanner for small animals. The maximum bore diameter for imaging is 15.4cm. This system is equipped with two gradient choices, a large built-in gradient system with up to 200 mt/m and a slew rate of 640 T/m/s. This gradient in combination with a large circular polarized coil will allow imaging of animals up to 15.4cm in diameter. The system is also equipped with a high performance gradient insert with 440mT/m and slew rate of 3,440 T/m/s for high-resolution imaging. The system has 2 transmit and 4 receive channels. There is a 35mm ID circular polarized coil for in-vivo mouse imaging as well as a 4-channel phased array for mouse brain and a 4 channel phased array for mouse cardiac imaging. There are also 3 other dual tuned 20mm surface coils for 31P, 13C and 19F. The 7T Bruker is equipped with the Autopac system, a fully integrated animal handling, laser guided positioning system. Animal warming holders are available for rats and mice as well as a full spectrum of monitoring peripherals for ECG, triggering and respiratory monitoring etc.

3 Biophotonic IVIS-Spectrum.

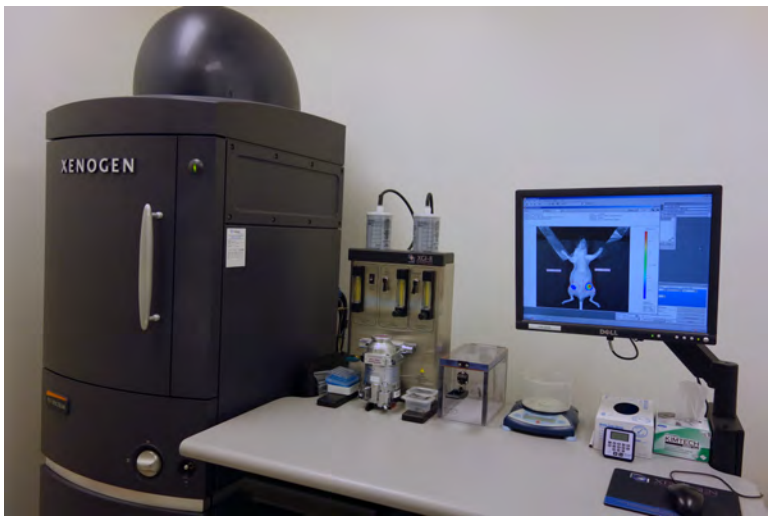

The **IVIS Spectrum** in vivo imaging system uses a novel patented optical imaging technology to facilitate non-invasive longitudinal monitoring of disease progression, cell trafficking and gene expression patterns in living animals. The IVIS Spectrum is a versatile and advanced in vivo imaging system. An optimized set of high efficiency filters and spectral un-mixing algorithms lets you take full advantage of bioluminescent and fluorescent reporters across the blue to near infrared wavelength region. It also offers single-view 3D tomography for both fluorescent and bioluminescent reporters that can be analyzed in an anatomical context using our Digital Mouse Atlasor. For advanced fluorescence pre-clinical imaging, the IVIS Spectrum has the capability to use either trans-illumination (from the bottom) or epi-illumination (from the top) to illuminate in vivo fluorescent sources. 3D diffuse fluorescence tomography can be performed to determine source localization and concentration using the combination of structured light and trans illumination fluorescent images. The instrument is equipped with 10 narrow band excitation filters (30nm bandwidth) and 18 narrow band emission filters (20nm bandwidth) that assist in significantly reducing autofluorescence by the spectral scanning of filters and the use of spectral unmixing algorithms. In addition, the spectral unmixing tools allow the researcher to separate signals from multiple fluorescent reporters within the same animal. http://www.perkinelmer.com/Catalog/Product/ID/IVISSPE

4 Micro Ultrasound Vevo 2100 VisualSonics.

This is dedicated Ultrasound system for small animal models (mice to rabbits) of disease. This scanner is capable of all imaging modes found in clinical US scanners such as color Doppler, M-mode, 3D imaging and volume analysis but at much higher spatial resolution. It allows for rapid animal screening of tumor and other models. The higher resolution of this system will also allow for image-guided injection. **B-Mode (2D)** imaging for anatomical visualization and quantification, with enhanced temporal resolution with frame rates up to 740 fps (in 2D for a 4x4 mm FOV) , and enhanced image uniformity with multiple focal zones. **M-Mode** is for visualization and

quantification of wall motion in cardiovascular research, single line acquisition allows for the very high-temporal (1000 fps) resolution necessary for analysis of LV function. **Anatomical M-Mode** is for adjustable anatomical orientation in reconstructed M-Mode imaging; software automatically optimizes field of view for maximum frame rate. **Pulsed-Wave Doppler Mode (PW) is** for quantification of blood flow. **Color Doppler Mode** is used for detection of blood vessels including flow directional information and mean velocities; as well as for identification of small vessels not visible in B-Mode. **Power Doppler Mode** is for detection and quantification of blood flow in small vessels not visible in B-Mode; increased frame rates allow for significantly faster data acquisition. **Tissue Doppler Mode** for quantification of myocardial tissue movement; for example in assessing diastolic dysfunction. **Vevo MicroMarker® Nonlinear Contrast Agent Imaging** can be used for quantification of relative perfusion & molecular expression of endothelial cell surface markers; enhanced sensitivity to Vevo MicroMarker contrast agents as linear tissue signal is suppressed. **3D-Mode** Imaging is for anatomical and vascular visualization, when combined with either B-Mode, Power Doppler Mode or Nonlinear Contrast Imaging; allows for quantification of volume and vascularity within a defined anatomical structure. **Digital RF-Mode** is for the acquisition and exportation of radio frequency (RF) data in digital format for further analysis; full screen acquisition provides a complete data set for more comprehensive analysis and tissue characterization. **ECG and Respiration Gating** is used to suppress imaging artifacts due to respiration and cardiac movements. Both are important in cardiac and abdominal imaging for both 2D and 3D data sets. **Transducers:** * MS-200 12.5 or 21 MHz, Depth from 2mm to 36mm *MS-250 16 or 21 MHz, Depth from 2mm to 30mm *MS-400 24 or 30 MHz, Depth from 2mm to 20mm *MS-550D 32 or 40 MHz, Depth from 1mm to 15mm
http://www.visualsonics.com/vevo2100

5 Near IR Frangioni imager. This rodent scanner is designed to visualize cellular probes that fluoresce in the Near IR region which provides much better tissue penetration than traditional Green Fluorescent Proteins.

6 Radiochemistry. This laboratory is equipped radiochemical preparations and calibration.

C. Nanomedicine Laboratory - CSM-7th Floor.

This laboratory has 2 modules: the synthetic lab and the analytical/biochemistry/biology lab. We are able to synthesize established imaging reagents for supply and distribution. In the synthetic lab, there are 2 large synthetic chemistry hoods that can accommodate 4 synthetic chemists working simultaneously. Each scientist has individual bench space for work-up and for storing samples, reagents, buffers and the like. The analytical/biochemistry/biology lab has 2 smaller hoods for doing wet chemistry work. Both facilities have been equipped with state-of-the-art instruments to support the work. The synthetic lab is well equipped for investigators to perform small-scale syntheses of organic, inorganic and organometallic compounds for use in a multitude of imaging modalities as well as drug delivery nanoparticles. In addition, we are also capable of labeling peptides and antibodies with commercially available optical dyes, CT, or MR contrast agents.

D. Image Analysis and Data Center - CSM- 1st Floor.

One of the main functions of TMII is to provide the infrastructure for access to research imaging. A comprehensive set of Image modalities are supported for both human as well as animal work. Scheduling support for access to the different scanners consist of web-based online calendars as well as live telephone scheduling support. TMII also provides a central hub for image distribution and archival. There are 32TB of online storage where all imaging data is pushed to and distributed from. The capacity will be expanded annually as needed.

1. Image Analysis Core. TMII provides image analysis for cardiovascular, body/oncological and neuro imaging support through the Image Analysis Core. The image analysis for specific projects needs to be discussed directly with the TMII core (contact TMII Director Dr. Zahi Fayad.) This core consists of IT personnel, software engineers, imaging physicists, research assistants and other support personnel. Expert consultation for research projects including protocol design, specialized pulse sequences, special image acquisition hardware (coils), custom made functional MRI stimulus hardware are all supported. Comprehensive project based image analysis support is also provided. Modalities supported include PET, MRI, fMRI, DTI and its variants, resting state fMRI. Image analysis training is also supported for those researchers who want to learn more about image analysis in general. Training range from regular classroom based graduate course taught by TMII faculty to hands on training on the use of specific software packages such as FSL, SPM, Brainvoyager and TMII's own in house developed software packages in all areas (neuro, body, oncology and cardiovascular). The data center has a dedicated server room which houses a larger Mac Server Cluster with 2 x 16TB of initial online storage with direct connectivity to all the imaging modalities in CSM. In addition, there is also an image analysis room equipped with large viewing display and more than 15 high performance workstations open for the researcher to learn or perform image analysis.

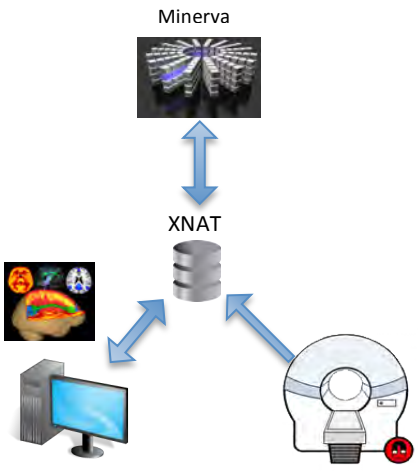

2. TMII XNAT. TMII XNAT serves as the central point for research data transfer, archive, and sharing. TMII XNAT is built upon a secure database, supports automated pipelines for processing managed data, and provides tools for exploring the data. Only users authorized by the study investigators can access their data. TMII XNAT is fully HIPAA compliant. The TMII XNAT team provides support for data migration between various DICOM repositories, HIPAA de-identification, image preprocessing, image quality control, and other customized services. Currently TMII XNAT runs on two mirrored Linux servers with 60TB storage space on each. It can host more than 15,000 image sessions with backups. TMII XNAT user training, documentation, and imaging data management consultations are available by request

(https://tmii.mssm.edu/xnat). A yearly service support contract has been established with the XNAT developer group from Radiologics Inc.

3. Image reconstruction tools for PET and fast MR imaging. TMII is equipped with a dedicated workstation for PET images reconstructions, such as the Siemens e7-tools and the open-source package STIR (http://stir.sourceforge.net/). The e7-tools are a collection of Microsoft Windows command line programs that allow the processing and reconstruction of Siemens PET emission data both using iterative and analytical algorithms. The software is capable of generating of other correction factors including attenuation, scatter and normalization. The software also allows for listmode histogramming and rebinning. The software is installed on an external computer to reconstruct PET images away from the scanners. STIR software on the other hand is an open source toolbox that offers the same functionalities as the e7tools, but is not limited to the analysis of Siemens PET emission data. Also available is a dedicated workstation housing PET-SORTEO (Simulation Of Realistic Tridimensional Emitting Objects), a simulation tool that uses Monte Carlo techniques to generate realistic PET data from voxelized descriptions of tracer distributions, in accordance with the scanner geometry and physical characteristics.

4. Soma Server. TMII also hosts a dedicated quad 2.2GHz, 8-core processors server for reconstruction of fast MR images techniques, such as compressed sensing, with 1xK20 GPU (expandable to a second GPU). The specifications of the server are : CPUs, 4 Intel Xeon E5-4620, 2.2 GHz (8-Core, HT, 16 MB Cache); RAM: 256GB (16x16GB DDR3-1600 ECC Registered 2R DIMMs) operating at 1600 MT/s Max; Management: Integrated IPMI 2.0 & KVM with Dedicated LAN; Controller: Dual-Port Intel X540 10GbE plus 8 Ports 6Gb/s SAS LSI 2208 HW RAID, and 6 Ports SATA; Hot-Swap Drive - 1: 3TB Seagate Constellation ES.3 (6Gb/s, 7.2K RPM, 128MB Cache) 3.5-inch SATA; Power supply: Redundant 1400W Power Supply with DSC and PMBus - 80 PLUS Platinum Certified; Rail Kit: Quick-Release Rail Kit for Square Holes, 26.5 - 36.4 inches; OS: Linux Ubuntu 13.10; PCIe 3.0 x16 - 1: NVIDIA Tesla Kepler K20 GPU Compute Board PCIe 2.0 x16. Matlab R2013b (www.mathworks.com) is installed on this server and can be used for heavy duty image reconstruction tasks, by exploiting the servers parallel computing capabilities. The server is available to all TMII researchers through remote login.

More information is also available online@ http://tmii.mssm.edu &

Contact:

Zahi A. Fayad, PhD – Director, TMII
Zahi.fayad@mssm.edu
(212) 824-8452

Christopher J. Cannistraci, MS – Program Manager
Christopeher.cannistraci@mssm.edu
(212) 824-8466

Biographies of Host & Invited Speakers

Zahi A. Fayad, PhD, FAHA, FACC, FISMRM
Mount Sinai Endowed Chair in Medical Imaging and Bioengineering
Professor of Radiology and Medicine (Cardiology)
Director, Translational and Molecular Institute
Vice chair for Research, Department of Radiology
Icahn School of Medicine at Mount Sinai
New York, NY

Biography

Dr. Fayad serves as professor of Radiology and Medicine (Cardiology) at the Mount Sinai School of Medicine. He is the founding Director of the Translational and Molecular Imaging Institute; Vice chair for Research, Department of Radiology at the Icahn School of Medicine at Mount Sinai. Dr. Fayad's interdisciplinary and discipline bridging research - from engineering to biology and from pre-clinical to clinical investigations - has been dedicated to the detection and prevention of cardiovascular disease with many seminal contributions in the field of multimodality biomedical imaging (MR, CT, PET and PET/MR) and nanomedicine. His work has recently expanded in understanding the effect of stress on the immune system and cardiovascular disease. He has authored more than 300 peer-reviewed publications (h-index of 71 accessed 01/02/2017 on Thomson Reuters Web of Science), 50 book chapters, and over 500 meeting presentations. He is currently the Principal Investigator (PI) of 5 federal grants (4 R01s and 1 P01) funded by the National Institutes of Health's National Heart, Lung and Blood Institute and National institute of Biomedical Imaging and Bioengineering. He is also PI on three NIH sub-contracts with UCSD, Columbia and the Brigham and Women's Hospital. In addition, he serves as Principal Investigator of the Imaging Core of the Mount Sinai National Institute of Health (NIH)/Clinical and Translational Science Awards (CTSA). He is a PI of one of the 3 projects in the Strategically Focused Prevention Research Network Center grant funded by the American Heart Association (AHA) to promote cardiovascular health among high-risk New York City children, and their parents, living in Harlem and the Bronx. Moreover, he currently leads four pharmaceutically funded multicenter clinical trials for the evaluation of novel cardiovascular drugs.

He is Associate Editor for the Journal of the American College of Cardiology Imaging (JACC Imaging), Section Editor for Journal of the American College of Cardiology (JACC) and Consulting Editor for Arteriosclerosis Thrombosis and Vascular Biology (ATVB) and past associate Editor of Magnetic Resonance in Medicine (MRM). In 2013, he became a Charter Member, NIH Center of Scientific Review, Clinical Molecular Imaging and Probe Development Study Section. In 2015, he chaired the Scientific

Advisory Board of the Institut National de la Santé et de la Recherche Médicale (INSERM) PARCC program at the HEGP in Paris.

Dr. Fayad had his engineering trainings at Bradley University (BS, Electrical Engineering '89), the Johns Hopkins University (MS, Biomedical Engineering '91) and at the University of Pennsylvania (PhD. Bioengineering '96). From 1996 to 1997 he was junior faculty in the Department of Radiology at the University of Pennsylvania. In 1997 he joined the faculty at Mount Sinai School of Medicine.

Dr. Fayad is the recipient of multiple prestigious awards. In 2007 he was given the John Paul II Medal from Krakow, Poland in recognition for the potential of his work on humankind. As a teacher and mentor, Dr. Fayad has been also extremely successful. He has trained over 100 postdoctoral fellows, clinical fellows and students. His trainees have received major awards, fellowships, and positions in academia and industry. In 2008, he received the Outstanding Teacher Award from the International Society of Magnetic Resonance in Medicine (ISMRM) for his teaching on cardiovascular imaging and molecular imaging. In 2009 he was awarded the title of Honorary Professor in Nanomedicine at Aarhus University in Denmark. Recently, he was one of opening speakers at the 2011 97th Scientific Assembly and Scientific meeting of the Radiological Society of North America (RSNA). In 2012, he was invited to give the Henry I Russek Lecture at the 45th Anniversary of the ACCF New York Cardiovascular Symposium. In 2013, he was elected Fellow of the International Society of Magnetic Resonance In Medicine, Magnetic Resonance Imaging, received a Distinguished Reviewer from Magnetic Resonance in Medicine and was selected as an Academy of Radiology Research, Distinguished Investigator In 2014 he received the Centurion Society award from his alma matter (highest award) Bradley University for his bringing national and international credit to his alma matter. In 2014, he received the Editor's Recognition Award, from the Journal Radiology. In 2015, he was the Dr. Joseph Dvorkin Memorial Lecturer at the Cardiac Research Day of the Mazankowski Alberta Heart Institute, University of Alberta, Edmonton, Canada. In 2015, he became the Mount Sinai Endowed Professor in Medical Imaging and Bioengineering. The Mount Sinai Professorships were established in 2007 by the Mount Sinai Boards of Trustees to honor the achievements and contributions of some of Icahn School of Medicine's most outstanding faculty. A total of eight Mount Sinai Professorships have been awarded to date in Alzheimer's Research, Diabetes and Aging, Gene Medicine, Medical Imaging and Bioengineering, Orthopaedics, Orthopaedic Research, Psychiatric Genomics, and Structural Biology. In 2016, he was the Heart & Stroke/Richard Lewar lecturer at the Center of Excellence in Cardiovascular Research in Toronto.

He is married to Monique P. Fayad, MBA and is the proud father of Chloé (15 year old) and Christophe (10 year old) and after spending seven years in Manhattan now lives in Larchmont, runs in Central Park and participates regularly in New York Road Runners races. He also enjoys regular sailing and stand-up board paddling in Larchmont, New York, Connecticut, Rhode Island, Cape Cod, Martha's Vineyard, Nantucket, the Caribbean Islands and beyond. He also practices all type of daily fitness regimens that include strength, cardiovascular, core, flexibility and high intensity interval trainings for fun.

Dennis S. Charney, MD
Anne and Joel Ehrenkranz Dean
Icahn School of Medicine at Mount Sinai
Executive Vice President for Academic Affairs
The Mount Sinai Medical Center
New York, NY

Biography

Dennis S. Charney, MD, is Anne and Joel Ehrenkranz Dean of the Icahn School of Medicine at Mount Sinai and President for Academic Affairs for the Mount Sinai Health System. An internationally acclaimed expert in the neurobiology and treatment of mood and anxiety disorders, Dr. Charney has made fundamental contributions to the understanding of the causes of human anxiety, fear, and depression, and to the discovery of new treatments for mood and anxiety disorders.
Under Dean Charney's leadership, the Icahn School of Medicine at Mount Sinai has risen to, and maintained, its strength among the top 15 U.S. medical schools in National Institutes of Health (NIH) funding, and currently ranks second in funding per faculty member from all sponsored projects. With an emphasis on innovation and discovery and a track record of strategic recruitments across the biomedical sciences and in genomics, computational biology, and information technology, the School has cultivated a supercharged, Silicon Valley-like atmosphere in the academic setting. As the sole medical school partnering with the seven hospitals of the Mount Sinai Health System, the Icahn School of Medicine at Mount Sinai has one of the most expansive educational, research and clinical footprints in the nation.

Early in his tenure as Dean, Dr. Charney unveiled Mount Sinai's $2.25 billion strategic plan, which laid the foundation for establishing multidisciplinary research institutes as hubs for scientific and clinical collaboration. Within and across the institutes, faculty investigators and physicians work together to push the boundaries of science and medicine in order to address the most pressing biomedical challenges of our time. Dr. Charney is now overseeing the creation of complementary clinical institutes for the entire Mount Sinai Health System. These new institutes are Centers of Excellence for disease-specific areas such as cancer, heart disease, diabetes, HIV, and pulmonary diseases. Together the research and clinical institutes are generating game-changing models in translational research, clinical excellence and standards of care.

Recent affiliations with Rensselaer Polytechnic Institute, Google, IBM and Apple further enhance the landscape for discovery at Icahn School of Medicine at Mount Sinai. These unique relationships have expanded opportunities for cross-fertilization of ideas and programs, and present exciting educational, scientific and clinical possibilities for our students and faculty alike.

Dean Charney's career began in 1981 at Yale University School of Medicine, where, within nine years, he rose from Assistant Professor to tenured Professor of Psychiatry. While at Yale, he chaired the National Institute of Mental Health (NIMH) Board of Scientific Counselors, which advises the institute's director on intramural research programs. In 2000, the NIMH recruited Dr. Charney to lead their Mood and Anxiety Disorder Research Program — one of the largest programs of its kind in the world — and the Experimental Therapeutics and Pathophysiology Branch. That year, Dr. Charney was elected to the National Academies of Medicine.

In 2004, Dr. Charney was recruited to Icahn School of Medicine at Mount Sinai as Dean of Research. In 2007, he was appointed Dean of the School and Executive Vice President for Academic Affairs of the Medical Center. In 2013, Dr. Charney was named President for Academic Affairs for the Health System. He is currently one of the longest-serving Deans of any American medical school.

Dr. Charney's own robust research program has garnered recognition through virtually every major award in his field. His investigations of the causes and treatment of depression have generated new hypotheses regarding the mechanisms of antidepressant drugs and have resulted in novel therapies, including Lithium and Ketamine for treatment-resistant depression. The work of his research team demonstrating that Ketamine as a rapidly acting antidepressant has been hailed as one of the most exciting developments in antidepressant therapy in more than half a century.

Dr. Charney is a committed educator and role model who lectures within Mount Sinai, nationally and internationally. He has mentored and taught scores of junior faculty, postdoctoral fellows, medical students and graduate students throughout his career.

Recently, Dr. Charney's pioneering research has expanded to include the psychobiological mechanisms of human resilience to stress, and has led to the identification of ten key resilience factors for building the strength to weather and recover from stress and trauma. This work is in the basis for his inspiring book for lay audiences, Resilience: The Science of Mastering Life's Greatest Challenges, co-authored by Steven Southwick and published by Cambridge University Press in 2012.

A prolific author, Dr. Charney has written more than 600 publications, including groundbreaking scientific papers, chapters, and books. His many books include: Neurobiology of Mental Illness (Oxford University Press, USA, Fourth Edition, 2013); The Peace of Mind Prescription: An Authoritative Guide to Finding the Most Effective Treatment for Anxiety and Depression (Houghton Mifflin Harcourt, 2004); The Physician's Guide to Depression and Bipolar Disorders(McGraw-Hill Professional, 2006), Resilience and Mental Health: Challenges Across the Lifespan (Cambridge University Press, 2011).

Burton Drayer, MD, FACR
Professor of Radiology
Chair of the Department of Radiology
Icahn School of Medicine at Mount Sinai
New York, NY

Biography

Burton Paul Drayer, MD is currently the Dr. Charles M. and Marilyn Newman Professor and Chairman of the Department of Radiology (1995-present) at the Icahn School of Medicine at Mount Sinai and the Executive Vice President for Risk at The Mount Sinai Medical Center. Additionally, from 2003 to 2008, Dr. Drayer served as President of The Mount Sinai Hospital. He also serves as CEO of the Mount Sinai Doctors Faculty Practice and Dean for Clinical Affairs at the Icahn School of Medicine at Mount Sinai. He completed his internship and Neurology residency at the University of Vermont and then a Radiology residency and Neuroradiology fellowship at the University of Pittsburgh Health Center. He is Board certified in both Neurology and Radiology and a fellow of both the American College of Radiology and the American Academy of Neurology.

Dr. Drayer served as Associate Professor and Professor of Radiology at Duke University from 1979 to 1986 where he was also Director of Neuroradiology. In 1986, he joined the Barrow Neurological Institute as Director of Magnetic Resonance Imaging and Research. Internationally known for his CT and MRI research on the aging brain and neurodegenerative disorders, brain infarction, multiple sclerosis, and physiological and functional brain imaging, Dr. Drayer has written over 200 publications as well as multiple book chapters. He was the first to describe metrizamide encephalopathy, nonradioactive xenon enhanced CT for measuring rCBF (ASNR Cornelius G. Dyke Award 1977) and the normal and abnormal distribution of brain iron using MRI. He also popularized carotid and intracranial MRA and educated a generation of physicians in the efficient clinical use of brain and spine MRI. He has been on numerous editorial boards and was the editor of Neuroimaging Clinics of North America from 1990 to 2005.

Dr. Drayer was elected President of the ASNR in 1996, was the inaugural Chairman of its Research Foundation, and was awarded the ASNR Gold Medal in 2011 and RSNA Gold Medal in 2016. In 2003, Dr. Drayer was elected to the Board of Directors of the RSNA and in 2009 ascended to Chairman of the Board, 2010 President elect, and 2011 RSNA President. He was Chairman of the Board of Trustees of the RSNA Research and Education Foundation (2015-2016), is a past-President of the New York Roentgen Ray Society, and has served on numerous national advisory boards for multiple sclerosis, stroke, and Alzheimer's disease.

Michael McConnell, MD, MSEE
Head, Cardiovascular Health Innovations
Verily Life Sciences/ Alphabet Inc.
Professor of Medicine at Stanford University
Stanford, CA

Biography

Dr. McConnell is a cardiologist and bioengineer with research and clinical expertise in imaging, prevention, and mobile health. He leads cardiovascular and connected health efforts at Verily (formerly Google) Life Sciences. He is also a Professor of Cardiovascular Medicine and, by courtesy, Electrical Engineering at Stanford University. His career has focused on the development and clinical translation of novel technologies to detect and prevent cardiovascular disease.

Keynote

"Leveraging Technology to Re-engineer Healthcare"

Technological advances in imaging, sensors, and data sciences are providing myriad opportunities to re-engineer how we deliver healthcare and promote health. We also need approaches that can scale to address the increases in data, costs, and worldwide burden of disease. Multiple efforts are going on across academia, industry, and non-profit organizations to move the "point-of-care" out of the hospital and to the patient (or consumer). Mobile/wearable devices, for example, provide powerful ways to "image" people on a real-time basis and in their real-world environment, while also allowing interactive feedback and support. Bringing together relevant data with predictive analytics and user-centered design can move us toward the proactive, preventive healthcare we deserve.

Kendall Lee, MD, PhD
Director, Mayo Clinic Neural Engineering Laboratories
Professor, Neurosurgery
Professor, Physiology and Biomedical Engineering,
Professor, Physical Medicine and Rehabilitation
Chair, Enterprise Neurosurgery Research
Mayo Clinic
Rochester, MN

Biography

Dr. Lee received a B.A. degree in biology with a minor in philosophy from the University of Colorado at Denver. He attended Yale University Graduate School where he received a Master of Philosophy degree, as well as an M.D. and a Ph.D. in neurobiology. He completed an internship in internal medicine at the Hospital of St. Raphael, Yale University School of Medicine, and a residency year in neurology at Harvard Medical School. He trained further at Dartmouth Hitchcock Medical Center, completing an internship in general surgery, a residency in neurosurgery and a chief residency in neurosurgery.

In his clinical practice, Dr. Lee is an expert on neurological disorders, seeing patients with Parkinson's disease, Tourette's syndrome, dystonia and other neurodegenerative and psychiatric diseases. He is leading research efforts at Mayo Clinic to develop the Wireless Instantaneous Neurotransmitter Concentration System (WINCS), a series of devices to monitor and record electrical/chemical reactions in the brain during deep brain stimulation (DBS). WINCS will allow physicians to establish a precise relationship between stimulation and the resulting amount and type of chemicals the brain releases during DBS. This technology will provide a powerful new tool for intraoperative neurochemical monitoring for use during functional neurosurgery.

Dr. Lee's research is funded by National Institutes of Health, National Institute of Neurological Disorders and Stroke and multiple private donor foundations. His findings have been published in peer-reviewed journals such as Proceedings of the National Academy of Sciences, Neuron, Journal of Neural Engineering, Epilepsia, Movement Disorders, Journal of Neurosurgery and Archives of Neurology. He is an internationally recognized speaker and serves as an editorial board member on the following journals: Journal of Neural Engineering; Biomedical Engineering Letters; Stereotactic and Functional Neurosurgery; and Neuromodulation. Dr. Lee is also a commander in the United States Navy Reserve

Neuroimaging Session

"Neuromodulation: Challenges and Opportunities"

Recent studies to understand the mechanisms of action of neuromodulation of the brain, spinal cord, and peripheral nerve have emerged as exciting novel therapies for a variety of neurologic and psychiatric disorders. These investigations have suggested the possibility of continuous monitoring of *in vivo* changes in neurochemical activity across multiple anatomical targets in pathologic brain so as to provide real-time feedback control of neurochemical levels in an effort to optimize therapeutic efficacy. The Mayo Clinic Neural Engineering Laboratories have demonstrated the conceptualization, engineering design, fabrication, and implementation of a device called WINCS Harmoni that employs fast-scan cyclic voltammetry (FSCV) to measure stimulation-driven neurochemical release as a novel form of neurochemical feedback controlled neuromodulation. FSCV is a well-established electroanalytical technique that can detect and measure neurochemicals *in vitro* and *in vivo* by imposing a voltage waveform that ramps through the oxidation and reduction potentials of the species of interest at a carbon fiber electrode while monitoring the nanoampere scale electrical current that is generated by redox reactions at specific voltages. Using WINCS Harmoni, we demonstrate the measurement and characterization of neurochemical signals (including dopamine, adenosine, and serotonin), real-time synchronization with therapeutic interventions such as deep brain stimulation (DBS), adaptive control of therapeutic delivery, and closed-loop control of neuromodulation. In addition, we have used neuromodulation technologies in animals and in humans for restoration of function after paralysis from spinal cord injury. Systems and tools like those described here raise the exciting possibility to improve our understanding of the dynamics of brain physiology in the context of neurologic disease and therapeutic interventions, which may lead to the development of precision medicine and personalized therapies for optimal therapeutic efficacy.

Marc Kachelrieß, PhD, Dipl-Phys
Professor of X-Ray Imaging and CT
German Cancer Research Center (DKFZ)
Heidelberg, Germany

Biography

Prof Kachelrieß focuses on manifold areas regarding computed tomography. His research covers image reconstruction of cone-beam CT data, iterative image reconstruction, compressive sensing, image reconstruction algorithms in general, and sophisticated calibration techniques. Marc Kachelrieß is further active in the field of cardiac CT, including cardiac perfusion measurements, and in the field of respiratory-correlated imaging. He is involved in developing algorithms for automatic expo-sure control for CT, algorithms for dual and multi-energy CT imaging, methods to reduce CT artifacts, and patient dose reduction techniques. Marc Kachelrieß develops non-rigid registration techniques to be used for motion-compensated imaging; work which he does not only apply to CT or cone-beam CT imaging but also to MR and PET/MR imaging. His work also includes the design and development of micro-CT scanner hard- and software, micro-CT pre- and post processing software and image quality optimization techniques. Since 2010 Marc Kachelrieß is also active in the field of interventional projective and tomographic imaging where he was able to demonstrate that tomographic fluoroscopy can be achieved at the same dose levels as conventional projective fluoroscopy. An additional focus is high performance medical imaging, using standard PC hardware, graphics processing units (GPUs), Xeon Phi processors and field programmable gate array (FPGA) hardware, which enables real-time imaging even for highly complex algorithms in clinical routine. Marc Kachelrieß is not only active in the medical imaging field, where clinical CT scanners, cone-beam CT systems for radiation therapy guidance and C-arm CT scanners are dominating, but also in the field of non-destructive testing, luggage screening, electron beam CT, industrial CT, CT metrology, and dimensional CT.

Marc Kachelrieß is author or coauthor of more than 550 publications, among these 80 original scientific papers, more than 10 review articles, and more than 100 proceedings articles, and he is organizer of several conferences and workshops in the field of tomographic and high performance computational imaging.

Cardiovascular Imaging Session

"Cardiac Imaging: CT, and How Other Modalities may Benefit"

Volumetric heart imaging with high isotropic spatial resolution (0.3 mm) and high temporal resolution (63 ms), with subsecond scan times (0.2 s) for the whole heart, seeing the coronaries, quantifying their lumen, characterizing calcified and vulnerable plaques, detecting coronary stenoses with highest sensitivity and specificity, computing functional values such as ejection fraction, myocardial perfusion or fractional flow reserve while requiring only a small amount of contrast agent? This is routinely possible with cardiac CT.

This lecture highlights the technology of high end diagnostic CT systems with their application in cardiac imaging. Hardware technology, such as x-ray sources and detectors, such as spectral shaping and protocol design is discussed, as well as state-of-the art reconstruction software technology. Thereby, it is shown, why the x-ray dose values are so low (1 to 2 mSv), today.

The presentation then discusses future developments such as iterative image reconstruction combined with motion compensation techniques to push the temporal resolution beyond the theoretical limit, and to reduce dose. Such approaches are being tested in preclinical systems, such as micro-CT imaging of small rodents. Finally, it is shown how new developments in CT imaging of moving organs can be translated to other modalities, such as MR, PET, and PET/MR imaging.

Robert J. Gillies, PhD

Martin Silbiger Chair of the Department of Cancer Imaging and Metabolism
Director of the Center of Excellence in Cancer Complexity
Vice-chair for Research in the Department of Radiology
Scientific Director of the Small Animal Imaging Lab (SAIL)
H. Lee Moffitt Cancer Center and Research Institute
Tampa, FL

Biography

Dr. Robert J. Gillies is the Martin Silbiger Chair of the Department of Cancer Imaging and Metabolism; Director of the Center of Excellence in Cancer Complexity; Vice-chair for Research in the Department of Radiology; and Scientific Director of the Small Animal Imaging Lab (SAIL) at the H. Lee Moffitt Cancer Center and Research Institute in Tampa, FL.

In addition to authoring over 240 peer-reviewed manuscripts, Dr. Gillies has received numerous local, national, and international awards for his teaching and research, including; Researcher of the Year-2012 (Moffitt Cancer Center), the Furrow Award for Innovative Teaching (U. Arizona), the Yuhas Award for Radiation Oncology Research (U. Penn), the TEFAF professorship (U. Maastricht), and the award for Distinguished Basic Scientist of 2009 from the Academy of Molecular Imaging.

Dr. Gillies' vision for the Moffitt imaging initiative includes development of new applications to diagnose, predict and monitor therapy response using noninvasive imaging. This work spans from molecular and chemical, from animal studies to human clinical trials and patient care. Dr. Gillies also leads a post-doctoral/resident training program in cancer imaging. His research is focused on functional and molecular imaging of cancer, specifically with an emphasis on the use of imaging to inform evolutionary models of carcinogenesis and response to therapy.

Cancer & Body Imaging Session

"MR Imaging of Tumor Habitats"

Malignant cancers are characterized by microenvironmental heterogeneity that leads to genomic heterogeneity through evolutionary selection, which is a major factor in therapy resistance. In our

current studies, microenvironmental heterogeneity is observed radiographically by combining multiparametric mpMR images to form data cubes for each voxel. Clustering algorithms (e.g. fuzzy C-means, Gaussian mixture models, Otsu thresholding) are then applied to create groups of hyper-voxels that contain similar data combinations. We call these groups "habitats" as they reflect specific physiologies. The quantity and quality of the habitats can be prognostic, and change with therapy in clinical disease (GBM, prostate cancer, sarcoma). To better identify the underlying pathophysiology within these habitats, mpMR images of pre-clinical models of breast cancer (4T1 murine mammary tumor, MDA-mb-231 human breast cancer xenografts and pediatric sarcoma PDX tumors were co-registered to histology using an image-informed 3D printed cradle to orient cutting planes of resected samples. Distinct habitats are identifiable from deep analysis of the histological and immunohistochemical images, and can be related to the MRI-defined intratumroal habitats.

Michael T. McMahon, PhD
Associate Professor, F.M. Kirby Research Center for Functional Brain Imaging
Associate Professor, Department of Radiology
Johns Hopkins School of Medicine,
Baltimore, MD

Biography

Dr. Michael T. McMahon obtained his bachelor's degree in Physics at the University of Richmond and his doctoral degree in Physical Chemistry at the University of Illinois at Urbana-Champaign specializing in NMR spectroscopy. He was awarded an NIH NRSA postdoctoral fellowship to further develop methods for determining the structures of peptides under Robert Griffin, Director of the Francis Bitter Magnet Laboratory at Massachusetts Institute of Technology. During this time he became interested in medical imaging, and moved to the F.M Kirby Research Center for Functional Brain Imaging, Kennedy Krieger Institute and the Department of Radiology, Johns Hopkins School of Medicine where he is an Associate Professor.erests include Chemical Exchange Saturation Transfer MRI, Fluorine MRI, Molecular Imaging and Hyperpolarization. He has been elected Secretary and Program Director at the International Society for Magnetic Resonance in Medicine (ISMRM), recognized as a distinguished reviewer for the journal: Magnetic Resonance in Medicine and most recently awarded a President's International Fellowship by the Chinese Academy of Sciences.

Nanomedicine Session

"Developing High Sensitivity Organic MRI Contrast Agents for Molecular Imaging"

Due to its exquisite soft tissue contrast and high spatial resolution, magnetic resonance imaging (MRI) is a pre-eminent clinical diagnostic tool. Relaxation-based agents, including gadolinium complexes, manganese and iron oxides, were the status quo for exogenous MRI contrast until Ward and Balaban suggested an alternative contrast mechanism, Chemical Exchange Saturation Transfer (CEST). We are developing high sensitivity organic MRI contrast agents using CEST with a focus on agents for clinical 3 T scanners. In order to optimize CEST imaging at this field strength, we have introduced the concept of

including intra-molecular hydrogen bonds in the structures to increase the chemical shift of labile protons and tune their exchange rate. I will describe a number of examples and show how these can be applied to molecular imaging.

Biographies of Moderators

Keynote Moderator

Joel Dudley, PhD
Associate Professor of Genetics and Genomic Sciences
Associate Professor of Population Health Science and Policy Associate Professor of Medicine
Director of Institute for Next Generation Healthcare
Director of Biomedical Informatics
Icahn School of Medicine at Mount Sinai
New York, NY

Biography

Dr. Dudley is a recognized leader in applying biomedical Big Data to healthcare and drug discovery. He currently holds positions as Associate Professor of Genetics and Genomic Sciences and Director of Biomedical Informatics at the Icahn School of Medicine at Mount Sinai. He also directs the newly formed Institute for Next Generation Healthcare at Mount Sinai. Prior to Mount Sinai, he held positions as Co-founder and Director of Informatics at NuMedii, Inc., one of the first companies to apply Big Data to drug discovery, and Consulting Professor of Systems Medicine in the Department of Pediatrics at Stanford University School of Medicine. His work is focused on developing and applying advanced computational methods to integrate the digital universe of information to build better predictive models of disease, drug response. He and his team are also developing pioneering methods to bring about a next generation of medicine that leverages advances in diagnostics, wearables, digital health to enable new approaches to precision medicine and scientific wellness. He has authored and co-authored more than 80 publications and his research has been featured in the *Wall Street Journal*, *Scientific American*, *Forbes*, and other popular media outlets. His recent work using a Big Data approach to identify sub-types of Type 2 diabetes was recently highlighted by NIH director Francis Collins on the NIH Director's Blog as a significant advance in precision medicine. He was named in 2014 as one of the 100 most creative people in business by *Fast Company* magazine. He is co-author of the book Exploring Personal Genomics from Oxford University Press, which is used as a text in personalized and precision medicine courses at universities worldwide. He holds an MS and PhD in Biomedical Informatics from Stanford University School of Medicine. Dr. Dudley serves on the Scientific Advisory boards of numerous startups and companies in biotech and healthtech.

Neuroimaging Session Moderator

Raphael O'Halloran, PhD
Assistant Professor of Radiology
Assistant Professor of Psychiatry
Icahn School of Medicine at Mount Sinai
New York, NY

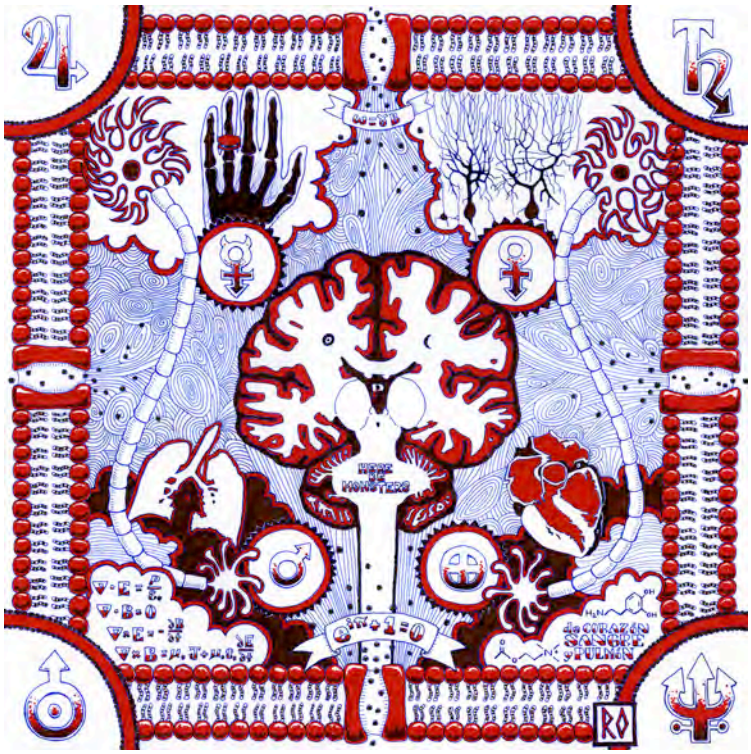

Biography

Dr. O'Halloran is a medical physicist working to develop and apply imaging technology to help patients with neuropsychiatric disease. Using MRI, primarily diffusion-weighted MRI, Dr. O'Halloran studies changes in the brain associated with diseases such as schizophrenia, depression, drug addiction, and epilepsy. Dr. O'Halloran is studying similar approaches to improve planning of surgical interventions for patients with a range of conditions including Parkinson's disease and brain tumors.

(Left) "Here Be Monsters" is an original drawing by Dr. O'Halloran and is on display at the "Windows to Our Body" art exhibit – Grady Alexis Gallery at El Taller. April 7-13, 2017

Cardiovascular Imaging Session Moderator

Claudia Calcagno, MD, PhD
Instructor of Radiology
Icahn School of Medicine at Mount Sinai
New York, NY

Biography

Dr. Calcagno, MD, PhD, is an Instructor of Radiology at the Icahn School of Medicine at Mount Sinai. She was trained in Medicine and Surgery at the University of Genoa, Italy and holds a PhD in Computational Biology from the Mount Sinai Graduate School of Biological Sciences/New York University. Her research focuses on the development and application of non-invasive quantitative imaging to cardiovascular disease, with specific focus on the measurement of atherosclerotic plaque permeability and inflammation with MRI (Calcagno et al, Arterioscl Thromb Vasc Biol, 2008) and PET (Calcagno C et al Eur J Nucl Med Mol Imaging 2013). She has been extensively involved in applying these techniques in pre-clinical drug trials in atherosclerotic rabbits (Lobatto M et al, Mol Pharm, 2010; Vucic E et al, JACC Cardiovasc Imaging 2011 and 2012), and clinical trials in humans (der Valk FM et al, Nanomedicine, 2015). As a post-doctoral fellow, Dr. Calcagno was supported by a prestigious fellowship from the American Heart Association (2013-2015), which focused on optimizing and validating 3 dimensional, fast MR image acquisition for atherosclerosis using compressed sensing reconstruction (Kim Y et al, Proc Nati Acad Sci U S A, 2014; Lobatto ME, Calcagno C et al, ACS Nano, 2015). During this time, together with other collaborators at Mount Sinai, she also worked on validating novel PET/MRI to quantify plaque inflammation (Bini J et al, Int J Cardiovasc Imaging, 2015). Dr. Calcagno was awarded a highly competitive Scientist Development Grant from the American Heart Association in 2016. By taking advantage of an optmimized self-gated acquisition and compressed sensing reconstruction, this application aims to develop high temporal and spatilal resolution DCE-MRI to quantify endothelial permeability in the aortic root of atherosclerotic mice. By investigating the relationship between imaging, and genetics, cellular and molecular assays in the arterial wall, the application also aims to take the first step in integrating quantitative, non-invasive imaging with -omics in this important animal model of cardiovascular disease.

Cancer & Body Session Moderator

Sara C. Lewis, MD
Assistant Professor of Radiology
Icahn School of Medicine at Mount Sinai
New York, NY

Biography

Dr. Lewis is an Assistant Professor of Radiology in the Body Imaging/Body MRI Section at Icahn School of Medicine at Mount Sinai (ISMMS). After finishing residency in Diagnostic Radiology at ISMMS where she also served as Chief Resident, Dr. Lewis then went on to complete an additional year of sub-specialization in abdominal MRI and CT. She subsequently joined the Body Imaging Section in 2011 and the Quantitative Imaging Research Lab (PI: Taouli) in TMII in 2016. Dr. Lewis is actively involved in multiple areas of clinical research in abdominal imaging. Her work is focused on conducting clinical translational imaging research centered on the use of advanced MRI methods in characterizing hepatobiliary neoplasms, renal transplant dysfunction and prostate cancer. Dr. Lewis has received grant support from SAR (2015) and RSNA (2016) for imaging research.

Dr. Lewis has authored and co-authored numerous peer-reviewed publications and actively lectures around the country. She is a peer reviewer for multiple peer-reviewed imaging journals and NIH/NCI. Dr. Lewis is also actively involved in radiology resident education, serving as a member of the Core Clinical Competency Committee and chair of the Program Evaluation Committee. She is a member of the Alpha Omega Alpha Medical Honor Society, Radiologic Society of North America, American Roentgen Ray Society and Society of Abdominal Radiology. She is board-certified by the American Board of Radiology in Diagnostic Radiology.

Nanomedicine Session Moderator

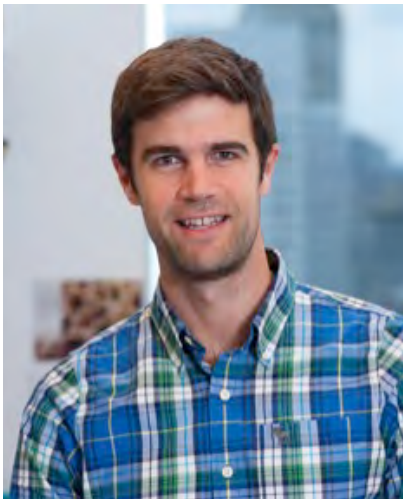

Carlos Pérez-Medina, PhD
Instructor of Radiology
Icahn School of Medicine at Mount Sinai
New York, NY

Biography

Carlos Pérez Medina, PhD, is Instructor of Radiology at the Translational and Molecular Imaging Institute (TMII) at the Icahn School of Medicine at Mount Sinai. He holds a Bachelor's degree in Chemistry, graduating with honors, and a PhD *cum laude* in Organic Chemistry, both obtained in Madrid (Spain). After postdoctoral stays at Trinity College in Dublin (Ireland) and University College in London (UK), he joined the Nanomedicine lab at TMII in 2013. His research work has been carried out on the interface between chemistry and the biomedical sciences, revolving around radiotracer design and development and the implementation of radiolabeling strategies for nanoparticles for their imaging with positron emission tomography (PET) or single-photon emission computed tomography (SPECT). In 2015 and 2016 he was awarded the Society of Nuclear Medicine and Molecular Imaging Alavi-Mandell prize

Selected Abstracts
Oral Presentations

Measurements and models of electric fields in the *in vivo* human brain during transcranial electric stimulation

Yu Huang[1], Anli A. Liu[2], Belen Lafon[1], Daniel Friedman[2], Michael Dayan[3], Xiuyuan Wang[2], Marom Bikson[1], Werner K. Doyle[2], Orrin Devinsky[2], Lucas C. Parra[1]
[1]Department of Biomedical Engineering, City College of the City University of New York, New York, NY 10031
[2]Comprehensive Epilepsy Center, New York University School of Medicine, New York, NY 10016
[3]Department of Neurology, Mayo Clinic, Rochester, MN 55902

Introduction

Transcranial electric stimulation (TES) aims to stimulate the brain by applying weak electrical currents at the scalp. However, the magnitude and spatial distribution of electric fields in the human brain are unknown. Despite increasing sophistication in the computational models for TES, none of them have been directly validated to-date. Here we aim to address this with in vivo intracranial recordings in humans by directly measuring field intensities produced by TES at the cortical surface and deeper brain areas.

Methods & Results

Electric potentials were recorded intracranially from ten patients undergoing invasive monitoring for epilepsy surgery, with subdural grids, strips, and depth electrodes. These recordings were then compared to various detailed computational models, including differential conductivity between skull spongiosa and compacta, and white matter anisotropy. Models were also calibrated using the recordings to minimize the difference between measurements and model predictions. In doing so, we obtain calibrated models that conclusively answer outstanding questions about stimulation magnitudes, spatial distribution, and modeling choices.

A summary of the model validations is shown in Fig. 1. The distribution accuracy is indicated by the correlation r between recorded and model-predicted values, and magnitude accuracy by the slope s of the best linear fit with predicted value as "independent" and measurement as "dependent" variables. Conductivities reported in the literature used in existing models tend to overestimate the voltages and electric field magnitudes (Fig. 1CD under "literature"). The measured voltages are tightly correlated with the predicted electric potentials (Fig. 1A). The correlation of predicted and measured electric fields is lower than for the raw potentials (Fig. 1B), as the calculated field is the difference of two close-by measurements, each with some inherent noise. The best fitted conductivity values vary across individuals (Fig. 1EFG). The median of these optimal conductivities differ from the literature values, but are largely in the same proportions. Compared to models using literature conductivities, the models with median values across subjects give significantly better accuracy in terms of predicting the electric field distribution and the magnitude (Fig. 1BD). Fig. 2A--E shows the recorded data and the predictions from the calibrated head model for one subject. When collapsing all recordings across subjects (Fig. 2FG) we find correlation between measured and predicted field projections of r=0.89 and r=0.84 for cortical and depth electrodes respectively.

Conclusion

After calibrating the models using recorded data, we found that the electric field intensities in the brain reach 0.4 V/m when using 2 mA transcranially, approximately half as strong as previous predictions using computational models. Individualized models provide predictions that are highly correlated with actual recordings (r>0.8). Including variables such as anisotropic white matter and inhomogeneous bone compartments does not improve prediction performance.

Clinical Relevance

This is the first study to validate and calibrate current-flow models with *in vivo* intracranial recordings in humans, providing a solid foundation to target transcranial stimulation and interpret clinical trials.

Figures and tables

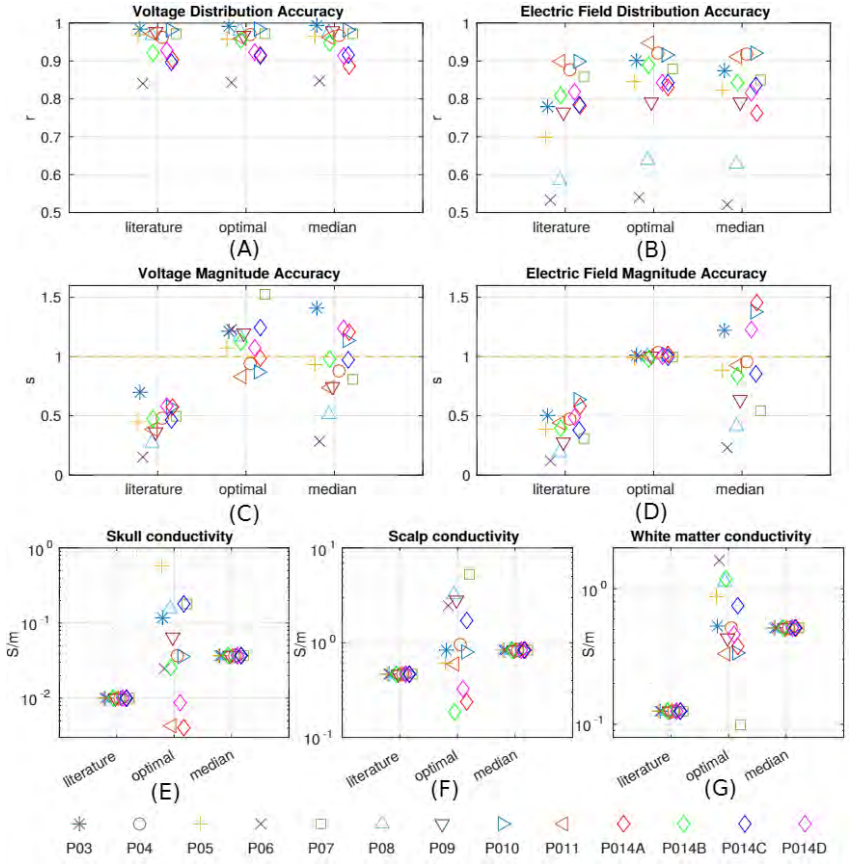

Fig. 1

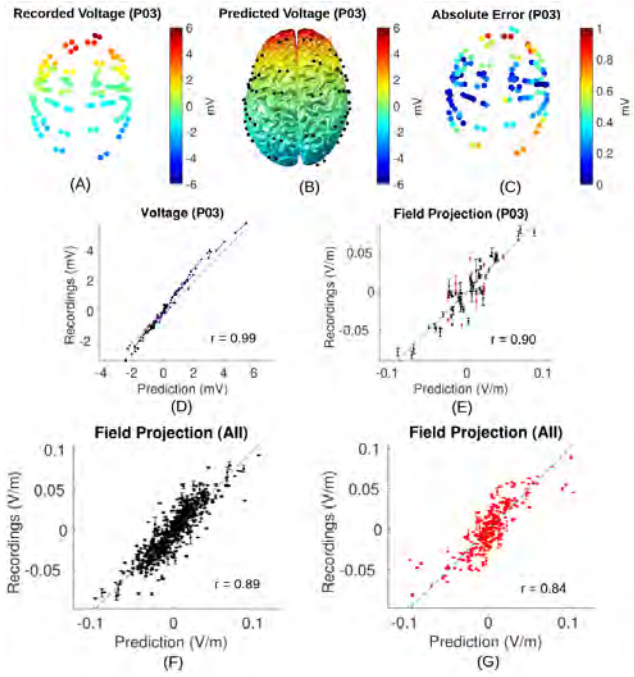

Fig. 2

Effect of acquisition and reconstruction parameters on quantification of thrombus volume in pulmonary embolism using computed tomography pulmonary angiography: Implications for multicenter studies

Audrey E Kaufman MD[1,2], Alison N Pruzan ScB[1,2], Ching Hsu,PhD[3], Sarayu Ramachandran MS[1,2], Adam Jacobi MD[1], Valentin Curt MD[3], Lee Schwocho, PhD[3], Michele Mercuri, MD[3], Zahi A. Fayad PhD[1,2], Venkatesh Mani PhD[1,2].
[1]Department of Radiology, Icahn School of Medicine at Mount Sinai, New York, NY, United States, [2]Translational and Molecular Imaging Institute, Icahn School of Medicine at Mount Sinai, New York, NY, United States, [3]Daiichi Sankyo, Inc., Edison, NJ, United States

Introduction
This study was performed to establish the effects of CT image acquisition and reconstruction parameters on pulmonary embolism (PE) clot volume quantification and to assess reproducibility of clot volume analysis using computed tomography pulmonary angiography (CTPA) to affect its potential use in multicenter clinical trials.

Methods & Results
This study was performed using anonymized data in conformance with HIPAA and IRB Regulations (3/2015-11/2016).

Methods: This is a two-part study. For the in vitro portion of the study we designed and scanned a ten blood clot phantom on a Siemens Force dual energy CT scanner (SOMATOM Force, Siemens Healthcare GmBH, Erlangen, Germany) using various image acquisition and reconstruction parameters including the following factors: pitch (0.6, 0.9, 1.2); the Siemens Advanced Modeled Iterative Reconstruction known as ADMIRE (Yes/No); energy level in kVp (80, 90, 100, 110, 120) and slice thickness in millimeters (0.6, 1, 1.5, 2). We used a range of clot and tube sizes in an attempt to replicate in vivo emboli found within central and segmental branches of the pulmonary arteries. Clot volume was the measured parameter and was analyzed by a single image analyst using a semi-automated region growing algorithm implemented in the FDA-approved Siemens syngo.via image analysis platform. Mixed model analysis was performed on the in vitro data. For the in vivo portion of the study, anonymized CTPA data was acquired from 23 scanners (18 centers) using each site's standard PE protocol. Volume measurements of the in vivo pulmonary emboli were performed on Siemens syngo.via image analysis platform by two independent image analysts to determine inter-observer reproducibility. One analyst repeated the analysis a second time to establish intra-reader reproducibility. Total thrombus volume was calculated for each patient. Intra-class correlation coefficient (ICC) was assessed for total thrombus volume in the in vivo study.

Results: In vitro results indicated that none of the various CT image acquisition and reconstruction parameters examined had a significant effect on absolute clot volume quantification. The in vivo study's inter- and intra-observer variability measurements indicated excellent reproducibility of the semi-automated method for quantifying PE volume burden. ICC for the endpoint of total thrombus volume was greater than 0.95 for inter- and intra-observer analysis. Bland-Altman analysis indicated no significant biases.

Conclusion
The in vitro study showed that varying the CTPA image acquisition parameters and using iterative reconstructions had no significant impact on clot volume quantification. The in vivo study showed that our image analysis methodology is reproducible and therefore suitable for future use in a multicenter setting.

Clinical Relevance
Objectively measuring thrombus volume from CTPA data can be particularly useful to evaluate the efficacy of treatments for PE.[1] Clinical pharmaceutical trials of drugs such as thrombolytics rely upon objective measures including total thrombus volume to assess drug effectiveness and potency and to help determine the optimal duration of therapy.[2] This study furthers the body of knowledge regarding assessment of PE by quantifiable metrics and the ability to evaluate these metrics when acquired in a multicenter setting.

References
1. Furlan A, Patil A, Park B, Chang CC, Roberts MS, Bae KT. Accuracy and reproducibility of blood clot burden quantification with pulmonary CT angiography. AJR Am J Roentgenol. 2011 Mar;196(3):516-23. doi: 10.2214/AJR.10.4603.
2. Aghayev A1, Furlan A, Patil A, Gumus S, Jeon KN, Park B, Bae KT. The rate of resolution of clot burden measured by pulmonary CT angiography in patients with acute pulmonary embolism. Am J Roentgenol. 2013 Apr;200(4):791-7. doi: 10.2214/AJR.12.8624.

Figures:

Figure 1: (a) Clot Phantom (b-e) CT acquired images of clots.

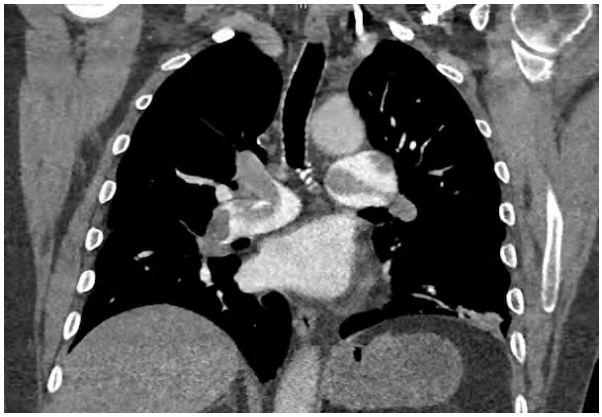

Figure 2: Coronal Image CTPA, bilateral emboli present (syngo.via).

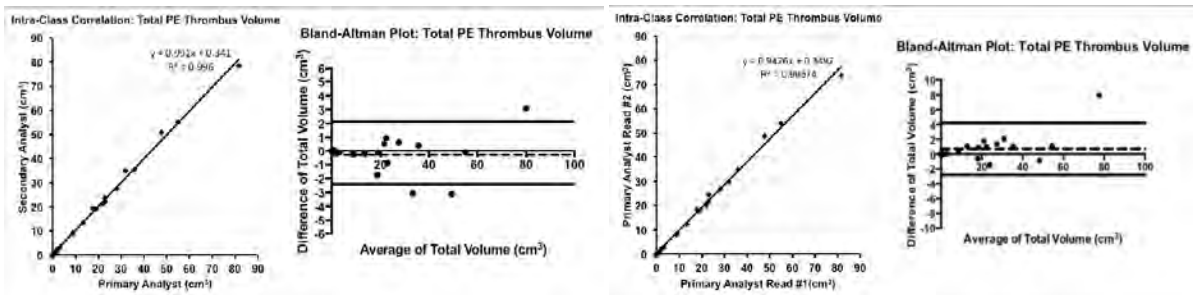

Figure 3: ICC plots and Bland-Altman plots comparing the results of the primary and secondary image analysts for inter-observer reproducibility of the total thrombus volume are shown on the left and the intra-observer reproducibility for the primary analyst first and second read is shown on the right.

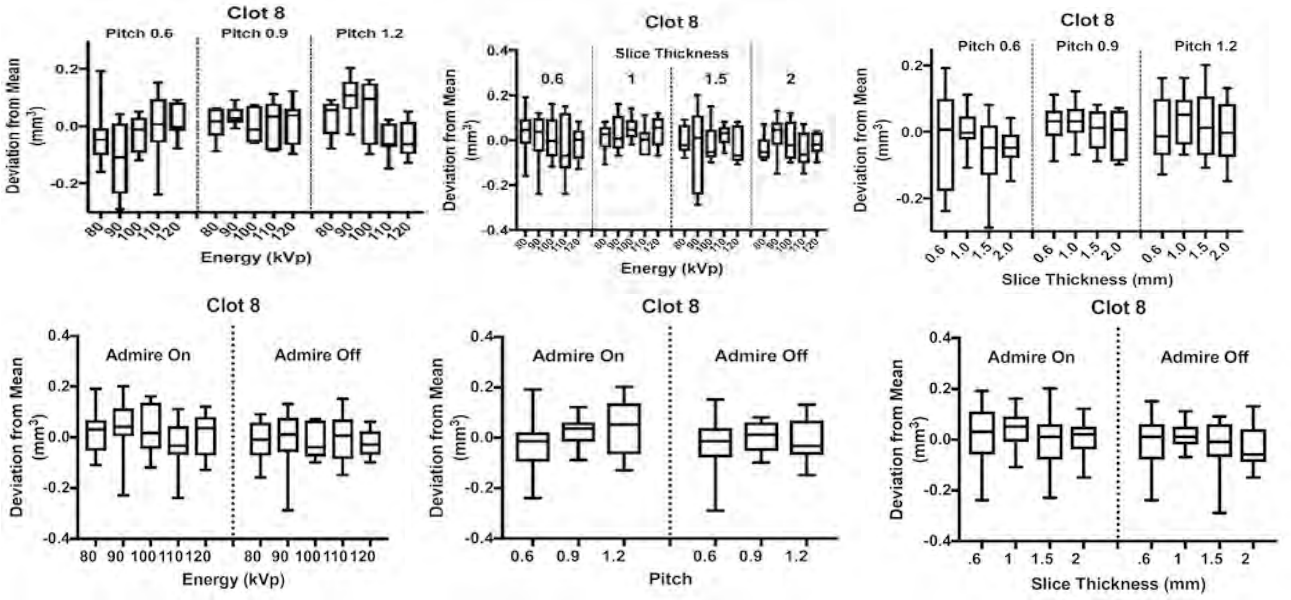

Figure 4: Box plots for Clot 8 read from left to right showing the difference from the mean measured volume for energy and pitch, energy and slice thickness, slice thickness and pitch, energy and ADMIRE, pitch and ADMIRE, and lastly slice thickness and ADMIRE.

Simultaneous liver and spleen 2D and 3D MRE acquisitions: preliminary results

Paul Kennedy PhD[1], Kevin Glaser PhD[2], Curtis L. Johnson[3], Jalpan Jani RT[1], Kashif Khokar RT[1], Richard L. Ehman MD[2], Bachir Taouli MD[1,4]

[1]Translational and Molecular Imaging Institute, Icahn School of Medicine at Mount Sinai, NY. [2]Department of Radiology, Mayo Clinic, Rochester, MN. [3]Department of Biomedical Engineering, University of Delaware; Newark, DE. [4]Department of Radiology, Icahn School of Medicine at Mount Sinai, NY.

Introduction

2D scalar MR elastography (MRE) has excellent accuracy for the assessment of liver fibrosis, while splenic MRE may have potential utility in assessing portal hypertension (1). 3D vector MRE encodes and analyzes all 3 components of the vector motion to addresses the issues of through-plane wave propagation which may cause increased stiffness in 2D. We report initial results of liver and spleen stiffness from 2D and 3D MRE processing of 3D MRE data acquired using a dual-driver configuration. The primary objective is to compare the ability of 2D and 3D MRE to detect liver cirrhosis. The secondary objective is to investigate whether stiffness determined using 2 drivers is the same as with 1 driver.

Methods & Results

13 subjects were included in this preliminary, prospective IRB-approved study [5 healthy volunteers and 8 liver disease patients (6 cirrhotic), 8M/5F, mean age 53y]. 60-Hz SE-EPI vector MRE was performed at 3T (GE 750) using 2 drivers for simultaneous liver and spleen acquisition. In healthy volunteers, MRE was acquired using each driver individually and then both drivers simultaneously to assess the effect of possible wave interference on the reported stiffness **(Fig. 1)**. To enable an accurate comparison, the 3D MRE data were processed using both 2D scalar (2) and 3D vector (3) MRE inversions, ensuring the slice locations, applied vibrations, and image characteristics were identical **(Fig. 2)**. ROIs of the liver and spleen, based on magnitude images and the 2D inversion confidence maps were drawn using ImageJ (NIH, Maryland, USA) with care taken to avoid morphological structures and areas of poor wave propagation. Mann-Whitney U tests were used to test the significance of the difference between 2D and 3D MRE stiffnesses and stiffnesses obtained using single and dual drivers.

In non-cirrhotic subjects, 2D MRE measured higher mean stiffness than 3D MRE in the liver (2D MRE stiffer by 0.450.21 kPa, p=0.07) and spleen (2D MRE stiffer by 0.92±0.58 kPa, p=0.06) without reaching significance (**Table 1**). In cirrhotic subjects, 2D MRE stiffness was not significantly higher than 3D MRE stiffness in the liver and spleen. The mean trend was to a higher 3D MRE stiffness in liver (3D MRE stiffer by 0.24±0.62 kPa, p=0.6) and higher 2D MRE stiffness in spleen (2D MRE stiffer by 0.53±0.57 kPa, p=0.5). Bland-Altman plots of the difference in stiffness between 2D and 3D MRE are shown in **Fig. 3**. 3D MRE showed a significantly increased stiffness in cirrhotic subjects compared to non-cirrhotic subjects in liver (p <0.01), however spleen stiffness difference did not reach significance (p=0.08). Stiffness measurements obtained using single and dual drivers were not significantly different regardless of organ or inversion method (p >0.4), with mean coefficient of variation (CV) ≤5% for liver and spleen using both 2D and 3D MRE.

Conclusion

These initial findings suggest 3D MRE is an effective tool for the detection of liver cirrhosis. The 3D and vector aspects of the 3D MRE processing provide a more accurate assessment of wave propagation and hence stiffness, however larger numbers of patients are required to validate this. Future work includes accelerated patient recruitment, multifrequency acquisitions, and analysis of additional parameters available from 3D MRE processing (e.g., volumetric strain). This will enable additional improvements in the characterization of liver and spleen changes due to fibrosis, cirrhosis, and portal hypertension.

Clinical Relevance

These initial findings suggest 3D MRE is an effective tool for the detection of liver cirrhosis. The 3D and vector aspects of the 3D MRE processing provide a more accurate assessment of wave propagation and hence stiffness and may improve the diagnostic accuracy of MRE.

References

1. Nedredal GI, Yin M, McKenzie T, et al. Portal hypertension correlates with splenic stiffness as measured with MR elastography. J Magn Reson Imaging JMRI. 2011;34(1):79–87. 2. Dzyubak B, Glaser K, Yin M, et al. Automated Liver Stiffness Measurements with Magnetic Resonance Elastography. J

Magn Reson Imaging JMRI. 2013;38(2):371–379. 3. Shi Y, Glaser KJ, Sudhakar VK, Ben-Abraham EI, Ehman RL. Feasibility of Using 3D MR Elastography to Determine Pancreatic Stiffness in Healthy Volunteers. J Magn Reson Imaging JMRI. 2015;41(2):369–375.

Figures and tables

	Non-cirrhotic			Cirrhotic		
	3D MRE	**2D MRE**	***p (2D vs 3D)***	**3D MRE**	**2D MRE**	***p (2D vs 3D)***
Liver (kPa)	1.91±0.27	2.39±0.43	0.07	3.97±1.20	3.73±1.71	0.69
Spleen (kPa)	4.50±0.53	5.42±1.01	0.06	6.70±2.58	7.33±2.47	0.55

Table 1: Mean±SD of liver and spleen stiffness using 2D and 3D MRE. Resulting p-values from Mann-Whitney U tests of significance are shown.

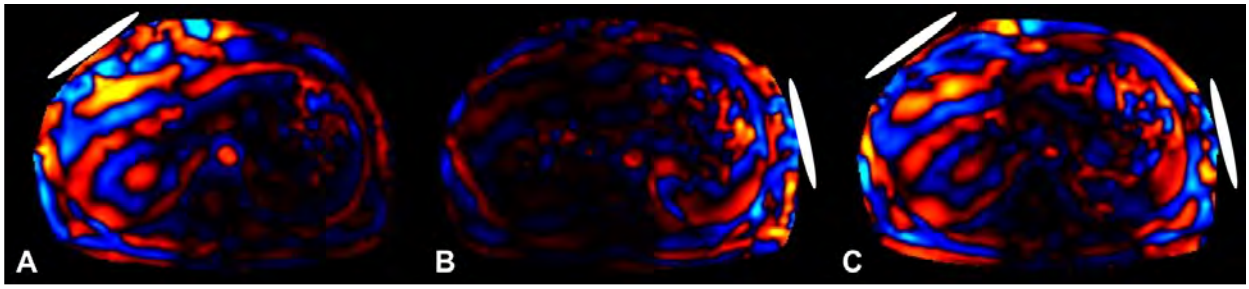

Figure 1: Wave images from the A) liver-side driver, B) spleen-side driver, and C) both drivers. Driver placement is illustrated in each case.

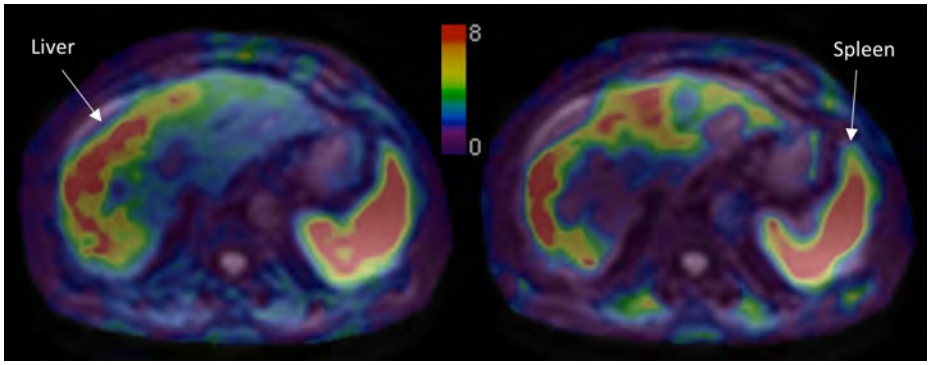

Figure 2: Example 3D (left) and 2D (right) elastograms from a 75-year-old female patient with liver cirrhosis and portal hypertension. Stiffness values for 3D MRE were: liver = 6.27±2.45 kPa, spleen = 9.00±2.64 kPa. 2D MRE stiffnesses were: liver = 6.86±1.10 kPa, spleen = 9.14±1.49 kPa.

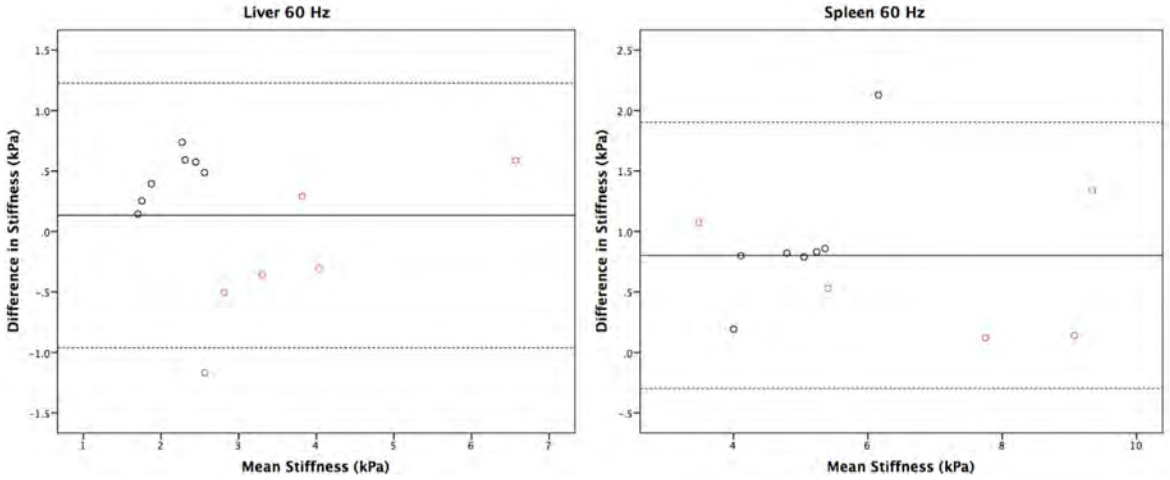

Figure 3: Bland-Altman plots displaying the difference between 2D and 3D MRE liver and spleen stiffness. Cirrhotic patients are highlighted in red. Negative values indicate 3D MRE stiffness is higher than 2D MRE stiffness. Variation is seen in cirrhotic subjects, with higher 3D MRE stiffness more prevalent in liver. In spleen, 2D MRE is stiffer than 3D MRE. Bold line depicts mean difference, dashed lines represent upper and lower confidence intervals.

Targeted CD40-TRAF6 inhibition resolves macrophage accumulation in atherosclerosis.

Marnix Lameijer[1,2], Tina Binderup[3], Mandy M.T. van Leent[1,2], Max L. Senders[1,2], Francois Fay[1], Joost Malkus[1], Brenda L. Sanchez-Gaytan[1], Nicolas Karakatsanis[1], Phillip Robson[1], Xianxiao Zhou[1], Yuxiang Ye[4], Gregory Wojtkiewicz[4], Jun Tang[5], Tom T.P. Seijkens[2], Erik S.G. Stroes[2], Andreas Kjaer[3], Jordi Ochando[1], Thomas Reiner[5], Carlos Pérez-Medina[1], Claudia Calcagno[1], Edward A. Fischer[6], Bin Zhang[1], Ryan E. Temel[7], Filip K. Swirski[4], Matthias Nahrendorf[4], Zahi A. Fayad[1], Esther Lutgens[2,8], Willem J.M. Mulder[1,2], Raphaël Duivenvoorden[1,2].

[1]Icahn School of Medicine at Mount Sinai, New York, USA. [2]Academic Medical Center, Amsterdam, The Netherlands. [3]Rigshospitalet and University of Copenhagen, Copenhagen, Denmark. [4]Harvard Medical School, Boston, USA. [5]Memorial Sloan Kettering Cancer Center, New York, USA. [6]NYU School of Medicine, New York, USA. [7]University of Kentucky, Lexington, USA. [8]Ludwig Maximilian's University, Munich, Germany

Introduction

Macrophages play a pivotal role in destabilization and rupture of atherosclerotic plaques, causing atherothrombotic events. CD4+ T-lymphocytes activate macrophages via CD40-CD40 ligand (CD40-CD40L) interaction. Therefore, interrupting CD40 signaling in macrophages is a promising target to modulate plaque inflammation. We developed a high-density lipoprotein nanoparticle containing a small molecule inhibiting the CD40 signaling pathway (TRAF6i-HDL), specifically targeting myeloid cells. We investigated the efficacy and mechanism of action in an atherosclerotic mouse model (Apoe-/-) and the safety and biodistribution in non-human primates.

Methods & Results

Twenty week old Apoe-/- mice fed a high cholesterol diet for 12 weeks were used as an atherosclerotic mouse model to assess targeting properties and efficacy of TRAF6i-HDL. Flow cytometry analysis of whole aortas showed that 86% of macrophages and 81% of Ly6C^{hi} monocytes had taken up DiO-labeled TRAF6i-HDL, indicating myeloid cell specificity. Subsequently, Apoe-/- mice were treated during one week with four intravenous injections of either placebo, HDL, or TRAF6i-HDL to evaluate in vivo efficacy. In vivo FMT/CT was performed to visualize protease activity in the aortic sinus area, reflecting macrophage activity. TRAF6i-HDL therapy decreased protease activity by 60% as compared to placebo ($p=0.002$). Histologic cross-sections of plaques in the aortic sinus area showed a 36% ($p=0.001$) decrease in the TRAF6i-HDL treated mice as compared to placebo. Flow cytometry analysis of whole aortas corroborated the histology results and showed that macrophage and Ly6C^{hi} monocyte content decreased by 66% ($p<0.001$) and 49% ($p<0.001$) respectively in the TRAF6i-HDL treated group. Plaque macrophages were isolated by laser capture microdissection for whole transcriptome analysis. This analysis revealed that TRAF6i-HDL treatment specifically downregulates genes involved in cell migration, indicating that the mechanism of action of this nanoimmunotherapy is impairment of monocyte recruitment. In order to assess the safety of TRAF6i-HDL therapy, non-human primates were injected with placebo or a single dose of TRAF6i-HDL (1,25 mg/kg). Complete blood count and blood chemistry analysis were similar in both groups. Biodistribution of Zirconium-89 (^{89}Zr) labeled TRAF6i-HDL was evaluated by PET/MR. Highest uptake was found in liver, spleen and kidneys. Post mortem histological analysis showed no signs of tissue damage in these organs.

Conclusion

We developed a myeloid cell specific particle inhibiting the CD40 signaling pathway. A single week of treatment resolved inflammation in a murine model of advanced atherosclerosis, mainly caused by reduced monocyte recruitment. The fact that TRAF6i-HDL proved to be safe in non-human primates supports the translational potential of this study.

Clinical Relevance

Currently, there are no specific therapies available that target atherosclerotic plaque inflammation. We envision that a short term induction nanotherapy with immune modulating properties can be used to rapidly suppress plaque inflammation in patients at high risk of cardiovascular events. While targeted delivery enhances the local efficacy of the drug, its short term application minimizes the risks associated with prolonged immunosuppression.

Figures and tables

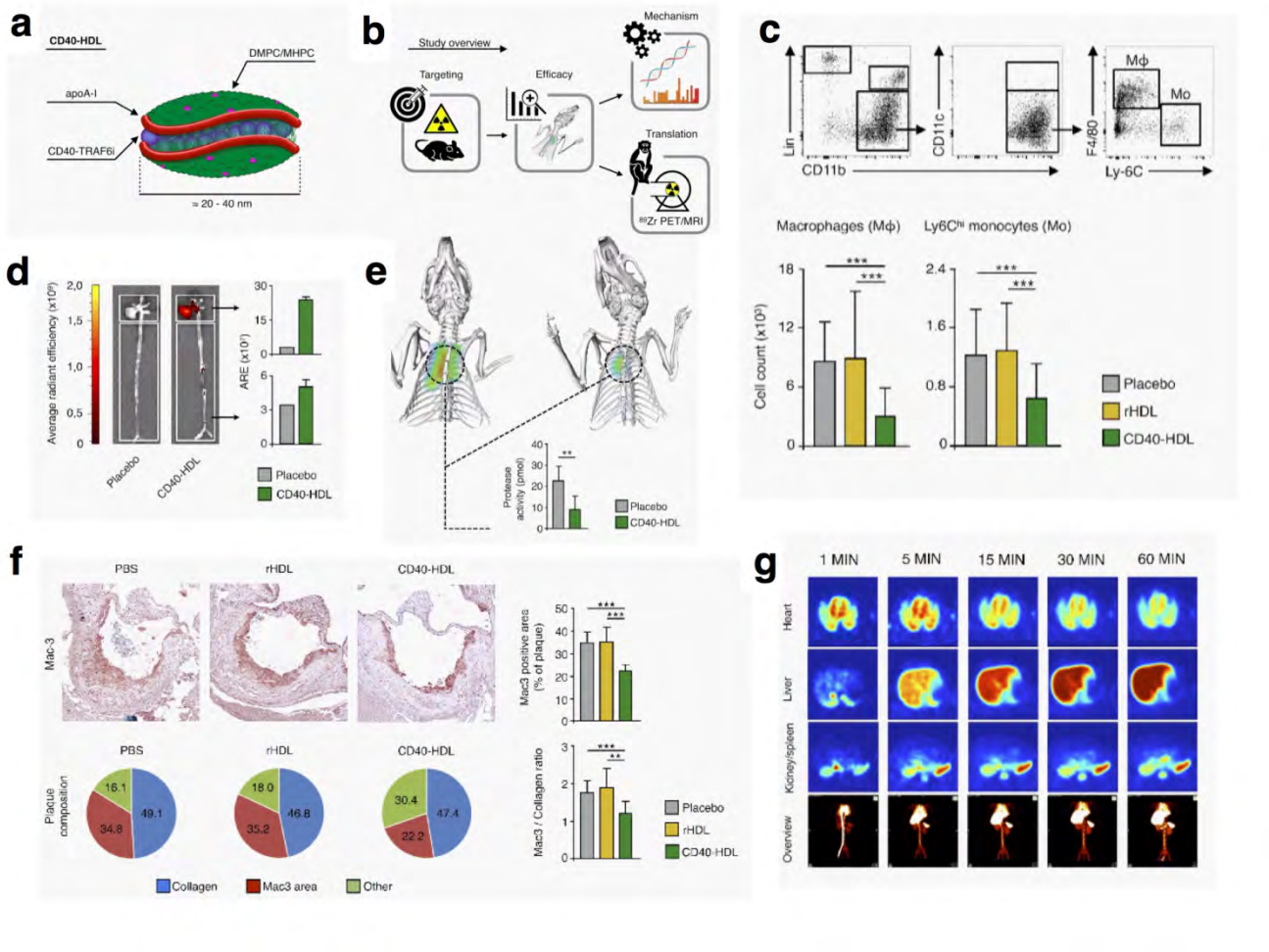

Figure 1 Biodistribution and efficacy of CD40-HDL nanoimmunotherapy
(a) A schematic representation of CD40-HDL, which was created by combining human apoA-I, lipids (DMPC and MHPC) and a small molecule inhibitor of CD40-TRAF6 interaction. (b) Study overview, showing the subsequent steps that were taken to investigate CD40-HDL. (c) Gating and quantification of aortic plaque macrophages and Ly6C^{hi} monocytes after treatment with placebo, rHDL or CD40-HDL (N=27 per group). (d) NIRF imaging of DiR-labeled CD40-HDL distribution in mouse aorta (n=2), showing accumulation of CD40-HDL in the aortic root area. (e) Representative FMT/CT images and quantification of protease activity in the aortic root in the CD40-HDL (n=7) and placebo (n=8) treated group. (f) Histological evaluation of Mac3 positive area in the aortic root after treatment with placebo, rHDL or CD40-HDL (N=10 per group). (g) Dynamic PET images of non-human primates at 1, 5, 15, 30 and 60 minutes after injection of CD40-HDL. Images are split up to visualize liver and other organs separately.

Abstract Selected Poster Presentations

Cancer & Body Imaging

Multiparametric MRI of renal transplant: preliminary results and repeatability study in patients with stable renal function

Octavia Bane[1,2], Stefanie Hectors [1,2], Sonja Gordic[1,2], Paul Kennedy[1,2], Mathilde Wagner [1,2], Philip Robson[2], Jeff Zhang [3], Madav Menon[4], Fadi Salem[5], Sara Lewis [1,2], Bachir Taouli[1, 2]
[1]Radiology, Icahn School of Medicine at Mount Sinai, [2]TMII, Icahn School of Medicine at Mount Sinai, [3]Radiology, University of Utah, [4]RMTI, Icahn School of Medicine at Mount Sinai, [5]Pathology, Icahn School of Medicine at Mount Sinai

Introduction

MRI provides an accurate assessment of the morphology of the transplanted kidney, as well as of vascular or obstructive renal disorders. The long-term goal of our study is to validate functional MRI as a "virtual biopsy" by developing a multiparametric MRI protocol using advanced quantitative MRI sequences in renal transplant (Tx) patients. We report initial results and test-retest repeatability of quantitative mpMRI parameters of diffusion, perfusion and hypoxia in renal allografts.

Methods & Results

Eleven initial patients (M/F 5/6, mean age 57y), 10 with functional renal allografts (estimated MDRD serum eGFR 48-84 ml/min/1.73m^2) and 1 with chronic renal dysfunction (GFR 24.6) were enrolled in this prospective study. All patients underwent mpMRI (Table 1) at 1.5T (Aera, Siemens) including intravoxel-incoherent motion DWI (IVIM-DWI), DTI, BOLD and DCE-MRI renography with injection of 4 ml of macrocyclic non-ionic gadolinium agent (Dotarem). IVIM-DWI, and BOLD signal curves, as well as DTI FA values, were measured from circular ROIs placed at the upper, middle and lower renal allograft poles, using OsiriX. All fitting of ROI-averaged signal curves was performed in MATLAB. IVIM-DWI parameters (true diffusion D, pseudodiffusion D*, perfusion fraction PF and ADC) were obtained by Bayesian fitting. R_2* transverse relaxation rate was obtained by monoexponential fit of BOLD signal curves. Cx, Med, the collecting system and the iliac artery at the level of the allograft were semi-automatically segmented from DCE-MRI data using previously validated software (Fig.1). Volume-averaged concentration-time curves were analyzed according to a previously validated three-compartment model to extract GFR, Cx and Med renal plasma flow (RPF) and mean transit time (MTT) (Fig. 1). Test-retest repeatability for all MRI metrics was assessed by measuring the coefficients of variation (CV) in 5 patients (average delay of 24 days between MRIs).

IVIM-DWI parameters were highly repeatable (CV <5%; Table 2), except for PF (CV Cx/Med 7.8%/14.6%; Table 2) and D* (CV Cx/Med 32.7%/20.3%, Table 2). R_2* and FA had acceptable repeatability (CV<15%, Table 2). DCE-MRI had acceptable repeatability for GFR (CV 12.18%), and poorer repeatability for RPF and MTT (CV 14-30%). Med FA and PF were significantly higher compared to Cx (Table 3; p=0.002/p=0.037). Cx D and RPF were significantly higher compared to Med (p=0.039/p=0.008). There was no significant correlation between serum eGFR and MRI parameters, between IVIM-DWI or BOLD and DCE-MRI parameters.

Conclusion

Quantitative mpMRI is moderately-to-highly repeatable in renal Tx, depending on the parameter. All parameter values agreed with literature values for patients with functional renal Tx, except for D* and Cx R_2*, which were higher than published values.

Clinical Relevance

Knowledge of test-retest repeatability would allow investigators to identify differences in mpMRI-derived parameters that reflect intrinsic renal dysfunction rather than normal physiological variation and measurement noise. The value of mpMRI-derived metrics for characterizing renal allograft dysfunction will be investigated in a larger study.

Table 1. mpMRI acquisition parameters.

	IVIM-DWI	DTI	BOLD	T_1	DCE-MRI
Orientation	Coronal	Coronal	Coronal	Coronal	Coronal
Sequence type	2D EPI	2D EPI	2D GRE	3D SPGR	3D SPGR
TR (ms)	4700	4100	311	4.3	4.5
TE (ms)	75	74	2,8,14,20, 26,32,38, 44,50, 56,68,79	1.28	1.23
FA (deg)	90	90	35	2,10	12
b-values (s/mm^2)	0,10,30,50, 80,120,200 400,800	50,500	-	-	-
Diffusion directions	3	6	-	-	-
FOV (mm^2)	315 x 360	360 x 360	348 x 360	380 x 380	288 x 384
Slices	20	40	3	20	24
Slice thickness (mm)	6	4	10	3	2.5
Matrix	268 x 384	256 x 256	300 x 384	308 x 384	356 x 379
Acceleration	GRAPPA R=2	GRAPPA R=2	GRAPPA R=2	GRAPPA R=2	CAIPIRINHA R=4
Acquisition time	5 min	2:10 min	23 s	11 s	5 min

Figure 1. DCE-MRI acquisition in a 46 year-old female with renal transplant (serum eGFR= 51.41 ml/min/1.73 m^2 and DCE-MRI GFR= 50.4 ml/min/1.73 m^2). DCE-MRI slices through the hilum of functional allograft show enhancement of cortex (upper left) and collecting system (upper right), with fitted concentration-time curves in the iliac artery, cortex and medulla (bottom).

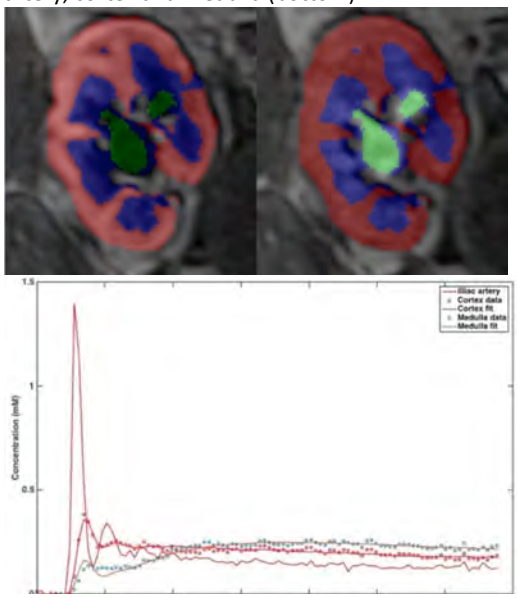

Table 2. Test-retest coefficients of variation (mean CV, %) in 5 patients for IVIM-DWI, DTI, BOLD and DCE-MRI parameters for cortex and medulla.

IVIM-DWI CV (%)							
Cortex				Medulla			
D	PF	D*	ADC	D	PF	D*	ADC
4.8	7.8	32.7	3	4.2	14.6	20.3	3.1

DTI (FA) CV (%)	
Cortex	Medulla
12.2	9.3

BOLD (R_2*) CV (%)	
Cortex	Medulla
13.6	8.2

DCE-MRI CV (%)							
Kidney			Cortex		Medulla		
GFR	RPF	MTT_K	RPF	MTT_A	MTT_P	RPF	MTT_L
12.2	23.9	16.3	22.2	30.3	14.3	30.7	18.9

Table 3. Parameter values (mean ± standard deviation) derived from IVIM-DWI, DTI, BOLD and DCE-MRI acquisitions in n=10 patients with functional Tx. PF: perfusion fraction (%), D: diffusion coefficient (10^{-3} mm^2/s), D*: pseudo-diffusion coefficient (10^{-3} mm^2/s), ADC: apparent diffusion coefficient (10^{-3} mm^2/s), FA: fractional anisotropy, transverse relaxation rate R_2* (s-1), GFR: glomerular filtration rate (ml/min/1.73 m2), RPF: renal plasma flow (ml/min), MTT_K: whole kidney mean transit time (s), MTT_A: vascular compartment mean transit time (s), MTT_P: proximal tubule mean transit time (s), MTT_L: Loop of Henle mean transit time (s).

IVIM-DWI							
Cortex				Medulla			
D	PF	D*	ADC	D	PF	D*	ADC
1.8±0.1*	20.7±3.6	18.4±7.3	2.1±0.1	1.7±0.1	24±4.6**	21.7±14.2	2.1±0.1

DTI (FA)	
Cortex	Medulla
0.2 ± 0.1	0.4 ± 0.1***

BOLD (R_2*)	
Cortex	Medulla
18 ± 5.2	18.1 ± 4.2

DCE-MRI							
Kidney			Cortex			Medulla	
GFR	RPF	MTT_K	RPF	MTT_A	MTT_P	RPF	MTT_L
68.8±11.9	482.5±130.7	177.7±39.3	405.3±114.2§	11.9±3.1	93.3±15.4	77.2±23.2	71.1±24.3

*D significantly higher in Cx than Med (Wilcoxon p=0.039);
**PF significantly higher in Med than in Cx (p=0.037);
***FA significantly higher in Cx than Med (p=0.002);

Sequential PET/CT and PET-MRI in the assessment of patients with advanced head and neck cancer after primary therapy.

Jad Bou-Ayache MD[1], Somali Gavane MD[1], Peter Som MD [2], Brett Miles DDS MD[3], Lale Kostakoglu[1] MD, MPH
1- Department of Nuclear Medicine, Icahn School of Medicine at Mount Sinai; New York; New York; USA
2- Department of Neuroradiology, Icahn School of Medicine at Mount Sinai; New York; New York; USA
3- Department of Otolaryngology, Icahn School of Medicine at Mount Sinai; New York; New York; USA

Introduction

Post-treatment anatomical distortion and artifacts pose major challenges in the surveillance of head and neck cancer (HNC) patients. PET-MRI has shown similar diagnostic accuracy to PET-CT in prior studies. Our objective was to assess the feasibility and the diagnostic performance of PET-MRI versus contrast enhanced MRI (CE-MRI) and PET-CT in the assessment of recurrence in patients with advanced HNC after primary therapy.

Methods & Results

This was a single center prospective study (GC13-1994) performed in patients with locally advanced HNC after primary therapy. Patients with ferromagnetic implants, pacemakers, or severe claustrophobia were excluded. A total of 26 patients underwent PET-CT and PET-MRI sequentially on the same day after administration of a single dose of F18-FDG. A separate dedicated PET with or without contrast enhanced CT of the neck was then performed as part of the routine HNC PET-CT protocol. MR sequences included T1&T2, T2 fat-saturated, T1 post gadolinium administration. Contrast was not given when contraindicated. The presence of local recurrence (LR) and pathologic lymphadenopathy and SUV max was recorded during a blinded readout session. All patients had either histologic correlation (17) or imaging follow up to ascertain recurrence (9).

All 26 patients underwent PET-CT and PET-MRI without any complications. The results are shown in Table 1. Disease recurrence was present in 14 patients with a total of 22 disease sites: 13 LR; 9 lymph nodes (LNs). 20/22(90.9%) sites were detected on diagnostic CE-MRI, 21/22 on PET-CT (95.4 %), 22/22(100%) on PET-MRI. 2 (2 LR), 6 (2 LR+4 LN's), and 2 (2 LR) were incorrectly categorized as disease sites on CE-MRI, PET-CT and PET-MRI, respectively (Table 1). False positive cases on PET-MRI were attributed to focal uptake adjacent to the surgical bed, which was found to be inflammatory changes rather than recurrence (Figure 1).

Conclusion

PET-MRI correctly detected more cases of local recurrence compared to CE-MRI alone and PET-CT while having fewer false positive LNs than PET-CT in post-treatment patients with advanced HNC. This may be attributed to superior soft tissue contrast provided by PET-MRI and the limitations associated with metallic artifacts on PET-CT in post-treatment patients. Larger studies are underway to further assess the clinical utility of PET-MRI in follow up of HNC patients as the preferred single modality over a combination of anatomical and functional imaging.

Clinical Relevance

We aimed to assess the performance of novel PET/MR modality in comparison to PET/CT in the early detection of recurrence in patients with advanced HNC after primary therapy.

Figures and tables

Table 1 / Figure 1

	MRI	PET-CT	PET-MRI
True positive (22)	20	21	22
False positive	2	6	2

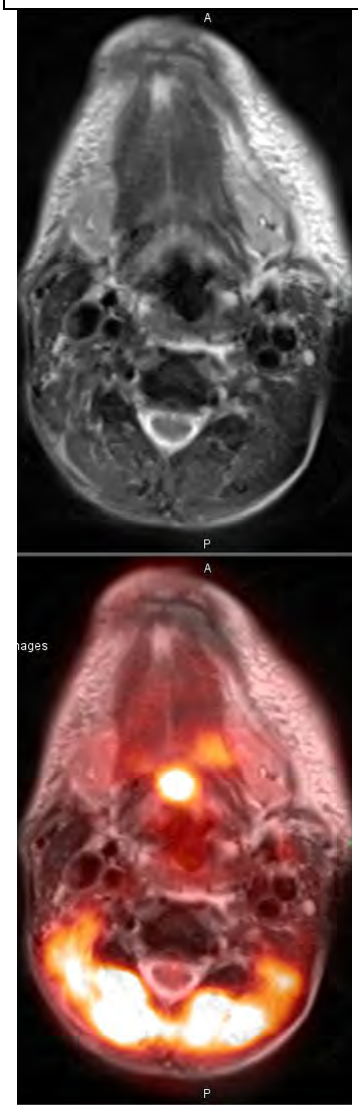

Intravital imaging of tumor cell dissemination during metastasis

Jose Javier Bravo-Cordero, PhD
Department of Medicine, Division of Hematology and Medical Oncology, Icahn School of Medicine, Tisch Cancer Institute at Mount Sinai, New York, New York 10029, USA.

Introduction

Metastasis accounts for more than 90% of cancer related deaths. Histological techniques provide valuable information about metastasis but it only give static images and lack dynamic and spatial information. To visualize the dynamic process of metastatic dissemination in real time *in vivo* at subcellular resolution we use high-resolution two-photon intravital microscopy.

Methods & Results

By using intravital microscopy we have identified the different motility behaviors that govern tumor cell motility *in vivo* in patient-derived breast tumor xenografts reveling macrophage-assisted migration as a key step in tumor dissemination. A crucial step in metastatic spread is blood vessel intravasation, involving transendothelial migration, a process that is not completely understood. In particular, tumor-associated macrophages facilitate tumor cell invasion and intravasation *in vitro* and *in vivo*. We have shown that heterotypic cell contact between tumor cells and macrophages induces the formation of invadopodia in tumor cells, invasive structures necessary for matrix degradation and tumor cell intravasation. However, what remained to be determined was the signaling pathway that regulates this heterotypic cell contact-mediated phenomenon and its role in tumor dissemination. We found that in the absence of Notch1 signaling, macrophage-induced invadopodium formation and tumor cell intravasation *in vivo* are abolished (revealed by high-resolution intravital microscopy in combination with mammary imaging windows, to image primary tumors over time).

Conclusion

These results show that Notch1 signaling regulates heterotypic cell contact mediated invadopodium formation and metastatic dissemination.

Clinical Relevance

Prevention of tumor cell dissemination from the primary tumor is an essential step to block in order to prevent metastasis formation. Our results reveals a novel mechanism for both invadopodium formation and the Notch pathway providing mechanistic information essential to the use of therapeutic inhibitors of metastasis.

Evaluation of HCC Response to Locoregional Therapy: Validation of MRI-Based Response Criteria Against Explant Pathology

Sonja Gordic MD[1,2], Idoia Corcuera-Solano MD[3], Ashley Stueck MD[5], Cecilia Besa MD[1], Pamela Argiriadi MD[3], Preethi Guniganti MD[3], Michael King MD[3], Shingo Kihira MD[1], James S. Babb[4], Swan Thung MD[5], Bachir Taouli MD[1,3]

[1]TMII, [3]Radiology, [5]Pathology, Icahn School of Medicine at Mount Sinai, [2]Institute of Diagnostic and Interventional Radiology, University Hospital Zurich, [4]Bernard and Irene Schwartz Center for Biomedical Imaging, New York University School of Medicine

Introduction

Locoregional therapies (LRT) play an important role in the management of patients with hepatocellular carcinoma (HCC). The evaluation of HCC response post LRT is essential in directing management of HCC, for indication of repeat treatment and prognostication. A limited number of MRI-pathological correlation studies with relatively small number of patients have shown conflicting results regarding the potential of the Response Evaluation Criteria in Solid Tumors (RECIST), European Association for the Study of the Liver (EASL) criteria, modified RECIST (mRECIST) and diffusion-weighted imaging (DWI) to predict complete pathological necrosis (CPN). Image subtraction, furthermore, has been shown to enable accurate assessment of necrosis of HCC after LRT, however it has never been compared to other imaging response criteria. This study evaluates the performance of various magnetic resonance imaging (MRI) response criteria in a large series, including RECIST, EASL, mRECIST, image subtraction and DWI, for the prediction of complete pathologic necrosis (CPN) of hepatocellular carcinoma (HCC) post LRT using explant pathology as reference.

Methods & Results

We included 61 patients (M/F 46/15, mean age 60y) who underwent liver transplantation after LRT with transarterial chemoembolization plus radiofrequency or microwave ablation (n=56), or ^{90}Yttrium radioembolization (n=5). MRI was performed within 90 days of liver transplantation. Three independent readers assessed the following criteria: RECIST, EASL, mRECIST, percentage of necrosis on subtraction images, and diffusion-weighted imaging (DWI) [qualitative (signal intensity) and quantitative (apparent diffusion coefficient, ADC)]. Degree of necrosis was retrospectively assessed at histopathology. Intraclass correlation coefficient (ICC) and Cohen's kappa were used to assess inter-reader agreement. Logistic regression and ROC analyses were used to determine imaging predictors of CPN. Pearson correlation was performed between imaging criteria and pathologic degree of tumor necrosis. 97 HCCs (mean size 2.3±1.3 cm) including 28 with CPN were evaluated (**Table 1**). There was excellent inter-reader agreement (ICC 0.77-0.86, all methods). EASL, mRECIST, percentage of necrosis and qualitative DWI were all significant (p<0.001) predictors of CPN, while RECIST and ADC were not. EASL, mRECIST and percentage of necrosis performed similarly (AUCs 0.810-0.815) while the performance of qualitative DWI was lower (AUC 0.622) (**Table 1**, **Figure 1** and **2**). Image subtraction demonstrated the strongest correlation (r=0.71-0.72, p<0.0001) with pathologic degree of tumor necrosis.

Conclusion

EASL/mRECIST criteria and image subtraction have excellent diagnostic performance for predicting CPN in HCC treated with LRT, with image subtraction correlating best with pathologic degree of tumor necrosis. Thus, MR image subtraction is recommended for assessing HCC response to LRT.

Clinical Relevance

Evaluation of tumor response post LRT is essential in directing management in HCC, for indication of repeat treatment and prognostication. Our study showed that MR image subtraction performed best and therefore is recommended to be used when assessing HCC response to LRT.

Table 1. Characteristics of 97 treated HCC lesions.

	No/partial necrosis (n=69)				CPN (n=28)				p
Measure	Mean	SD	Median	IQR	Mean	SD	Median	IQR	Value
RECIST (cm)	2.1	1.1	1.8	1.7	2.5	1.3	2.4	2.07	0.28
EASL (cm^2)	2.5	3.7	1.2	2.8	0.2	0.8	0	0	**<0.001**
mRECIST (cm)	1.4	1.2	1.3	1.6	0.2	0.5	0	0	**<0.001**
Necrosis (AP, %)	38.7	44.3	16.7	93.3	90.9	28	100	0	**<0.001**
Necrosis (PVP, %)	38.2	44.1	10	93.3	90.9	28	100	0	**<0.001**
ADC* ($x10^{-3}$ mm^2/s)	1.77	0.69	1.72	0.95	1.54	0.75	1.5	1.35	0.357

Abbreviations: SD, standard deviation; IQR, interquartile range; ADC, apparent diffusion coefficient, AP: arterial phase, PVP: portal venous phase

Table 1. Diagnostic performance expressed as areas under the ROC curve [AUROC, estimates and 95% confidence intervals (CI)], and threshold observed to maximize the sensitivity and specificity determined by ROC analysis to assess the utility of each measure as predictor of tumor complete pathologic necrosis.

			AUROC		Sensitivity (%)		Specificity (%)	
Measure	p	Threshold	Estimate	CI	Estimate	CI	Estimate	CI
RECIST (cm)	0.093	> 2.6	0.565	0.48-0.64	48.1	37.7-60.0	68.1	61.3-74.4
EASL (cm^2)	**<0.001**	0	0.815	0.77-0.86	86.9	77.8-93.3	74.4	67.9-80.2
mRECIST (cm)	**<0.001**	0	0.813	0.76-0.85	86.9	77.8-93.3	74.4	67.9-80.2
Necrosis (AP, %)	**<0.001**	> 90	0.81	0.76-0.86	86.9	77.8-93.3	73.9	67.4-79.8
Necrosis (PVP, %)	**<0.001**	> 90	0.813	0.77-0.86	86.9	77.8-93.3	74.4	67.9-80.2
DWI (SI)	**<0.001**	NA	0.622	0.56-0.68	81	70.9-88.7	43.3	36.6-50.5
ADC ($x10^{-3}$ mm^2/s)	0.238	≤ 1.29	0.592	0.41-0.77	50	24.7-75.3	73.5	55.6-87.1

Abbreviations: DWI, diffusion-weighted imaging; ADC, apparent diffusion coefficient, AP: arterial phase, PVP: portal venous phase

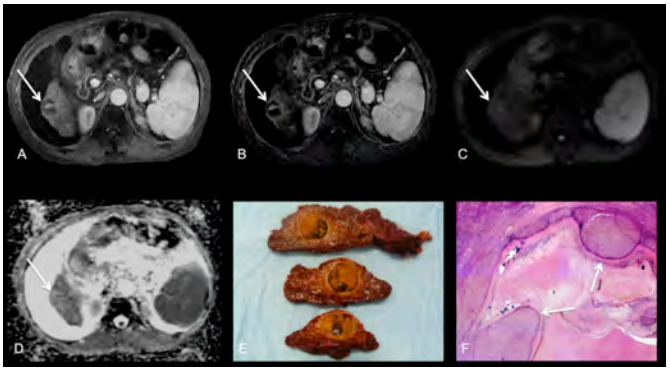

Figure 1: 72-year-old woman with HCV cirrhosis and treated HCC post TACE/RFA in right hepatic lobe. Treated HCC (arrows) shows nodular enhancement on post-contrast T1 weighted image obtained during arterial phase (A). The measurements of the three readers for RECIST were 2.7 cm, 3.1 cm and 3.1 cm, for EASL: 0.78 cm^2, 1.05 cm^2 and 0.57 cm^2, and for mRECIST 1.3 cm, 2.1 cm and 1.9 cm. On subtraction image (B) two readers rated the necrosis at 90% and one reader as 70%. On DWI (b 500) (C) and ADC map (D) two readers rated the signal intensity of the lesion as high and one as isointense to the liver. Corresponding explant images show a cirrhotic liver and a 2.5 cm HCC with 70% necrosis (E). Section of the tumor shows 30% viable HCC at the periphery (arrows, x20 H&E stain) (F).

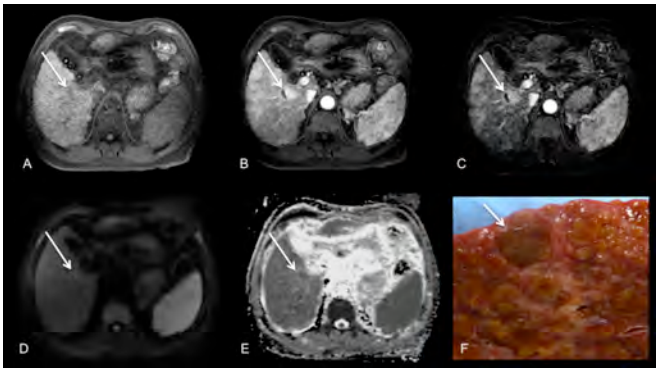

Figure 3: 60-year-old man with HCV cirrhosis and HCC post TACE/RFA in right hepatic lobe (segment 5, arrows). Treated HCC demonstrates a isointense/partially hypointense signal on pre-contrast T1-weighted image (A) with arterial phase hyperenhancement (B). The measurements of the three readers for RECIST were 2.8 cm, 2.5 cm and 2.1 cm, for EASL: 4.6 cm^2, 2.6 cm^2 and 2.94 cm^2, and for mRECIST: 2.3 cm, 2 cm and 2.1 cm. On subtraction image (C) two readers rated the necrosis at 20% and one reader at 10%. On DWI (b 500) (D) and ADC map (E) two readers rated the signal intensity of the lesion as high and one as isointense to the liver. Corresponding histopathological images shows cirrhotic liver with 2.1 cm 100% viable HCC (arrow) (F).

Intravoxel Incoherent Motion Imaging of Human Achilles Tendon by Stimulated Echo RESOLVE (ste-RESOLVE)

Authors & Affiliations
Xiang He, Kenneth Wengler, Dharmesh Tank, Mingqian Huang, Elaine Gould and Mark Schweitzer
Department of Radiology, Stony Brook University School of Medicine, Stony Brook, NY, United States

Introduction
Clinically, Achilles tendon (AT) rupture accounts for 40% to 60% of all operative tendon repairs, with 75% due to sports-related activities[1]. Conventional MR images exhibit poor contrast and specificity in delineating low-grade tendon injuries[2]. AT vasculature plays an integral role in the devolpment of injury and the repair proccess[3]. Intravoxel incoherent motion imaging is sensitive to blood flow and blood volume but application of the method to AT is hindered by short T2/T2* relaxation time constant (~1 ms in healthy subjects)[4]. In this study, a novel approach of combining stimulated-echo based IVIM[5] with readout segmented multi-shot EPI[6] (ste-RESOLVE) has been developed and evaluated. This enables, for the first time, a robust investigation of the changes on Achilles tendon blood flow and blood volume in tendinopathy patients.

Methods & Results
Three healthy volunteers and three AT tendinopathy patients were recruited for this IRB approved study. All experiments were performed on 3T Siemens Prisma scanners using a flexible 4-channel coil. To boost AT MR signal from magic angle effect, subjects were instructed to lay on their side with the tendon positioned ~55 degrees with respect to magnet B_0 field. The stimulated echo RESOLVE (ste-RESOLVE) sequence (**Fig. 1**) was modified from Siemens RESOLVE sequence by replacing the bipolar diffusion preparation block with a stimulated echo diffusion prep block. The sequence parameters for ste-RESOLVE IVIM were: FOV of 160×100 mm^2 ; matrix of 80×50; 8, 6mm thick axial slices with 100% separation; TR/TE of 2200/20 ms; b-values of 0, 20, 40, 60, 80, 120, 200, 400, and 600 s/mm^2; 3 diffusion directions; total acquisition time was ~8 min. The AT was segmented into proximal, medial, and distal (calcaneous insertion) sections. Within each section, the average signal at each b-value was fit according to $S(b) = S_0(1 - f_p) \cdot e^{-bD} + f_p \cdot e^{-bD^*}$, where f_p reflects tendon blood volume and $D^* \times f_p$ reflects tendon blood flow[7].

Figure 2 displays ste-RESOLVE IVIM images at different diffusion weightings from a representative subject. **Table 1** lists the AT IVIM results from three healthy controls and three patients. In healthy subjects, both D* and f_p values are lowest in the medial section, consistent with the notion of lowest blood volume and blood perfusion in mid tendon[2]. Patient P1 has gone through rehab for a partial tendon tear and showed regions of inflammation/edema. Patient P2 developed moderate tendinopathy discomfort one year after surgery in the contralateral tendon. Both subjects experienced no pain, and reduced tendon blood volume and perfusion were observed in the affected areas. Patient P3 has mild tendon pain in the medial section and showed increased perfusion in this region, consistent with pain-associated tendon perfusion increases[8].

Conclusion
The developed ste-RESOLVE IVIM protocol is capable of measuring blood flow and blood volume within Achilles tendon in both healthy subjects and tendinopathy patients.

Clinical Relevance
Achilles tendon ste-RESOLVE IVIM can be used to investigate the role of revascularization and microcirculation in tendon healing/remodeling.

Presentation category, please mark your preference [X]Cancer/Body [ ]Cardiac [ ]Nano [ ]Neuro
The Abstract must outline original research and the text is limited to one page. Figures and/or tables are also limited to one page and should be inserted on the second page

Figures and tables

Figure 1. Ste-RESOLVE pulse sequence.

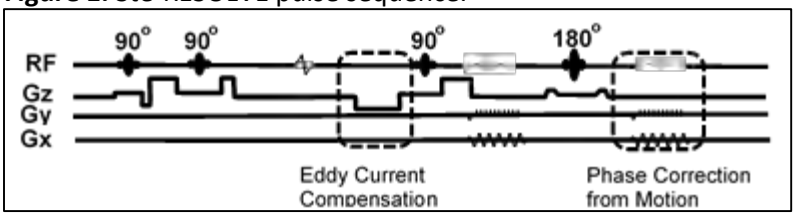

Figure 2. Typical Achilles tendon IVIM images using the proposed ste-RESOLVE sequence.

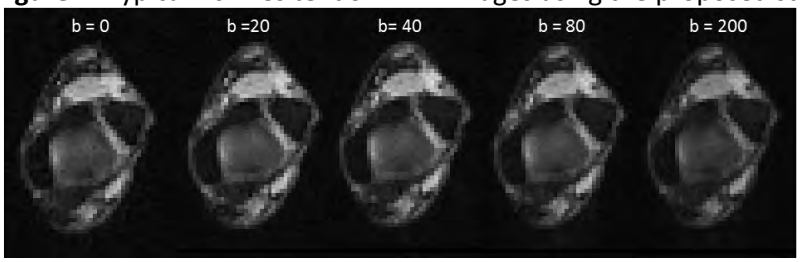

Table 1. Achilles tendon IVIM parameters for 3 healthy controls and 3 patients (affected regions are highlighted).

Subject		Proximal Section				Medial Section				Distal Section			
		D (mm^2/s $x10^{-3}$)	D* (mm^2/s $x10^{-3}$)	f_p	D* ● f_p	D (mm^2/s $x10^{-3}$)	D* (mm^2/s $x10^{-3}$)	f_p	D* ● f_p	D (mm^2/s $x10^{-3}$)	D* (mm^2/s $x10^{-3}$)	f_p	D* ● f_p
Healthy Controls	C1	0.97	11.14	0.057	0.63	0.90	5.25	0.041	0.22	0.68	5.35	0.068	0.36
	C2	1.32	7.99	0.081	0.65	0.97	5.42	0.043	0.23	0.78	5.04	0.077	0.39
	C3	1.22	11.87	0.056	0.66	1.12	9.67	0.024	0.23	1.04	5.38	0.073	0.39
	Mean	1.17±0.18	10.33±2.06	0.065±0.01	0.65±0.01	1.00±0.11	6.78±2.5	0.036±0.01	0.23±0.01	0.83±0.19	5.26±0.19	0.073±0.00	0.38±0.02
Patients	P1	1.38	7.26	0.048	0.35	1.50	4.04	0.010	0.04	1.26	4.19	0.020	0.08
	P2	0.94	3.71	0.068	0.25	1.05	8.89	0.014	0.12	0.99	5.21	0.043	0.22
	P3	0.80	6.71	0.114	0.76	0.88	6.23	0.090	0.56	0.82	4.48	0.087	0.39
	Mean	1.04±0.30	5.89±1.91	0.08±0.03	0.46±0.27	114±0.32	6.39±2.43	0.04±0.05	0.24±0.28	1.02±0.22	4.63±0.53	0.05±0.03	0.23±0.15

References

1. Järvinen TAH, Kannus P, Maffulli N, Khan KM. Achilles Tendon Disorders: Etiology and Epidemiology. *Foot and Ankle Clinics.* 2005;10(2):255-266.
2. Schweitzer ME, Karasick D. MR imaging of disorders of the Achilles tendon. *American Journal of Roentgenology.* 2000;175(3):613-625.
3. Fenwick SA, Hazleman BL, Riley GP. The vasculature and its role in the damaged and healing tendon. *Arthritis Research & Therapy.* 2002;4(4):252.
4. Filho GH, Du J, Pak BC, et al. Quantitative characterization of the Achilles tendon in cadaveric specimens: T1 and T2* measurements using ultrashort-TE MRI at 3 T. *AJR Am J Roentgenol.* 2009;192(3):W117-124.
5. Merboldt KD, Hänicke W, Bruhn H, Gyngell ML, Frahm J. Diffusion imaging of the human brain in vivo using high-speed STEAM MRI. *Magnetic resonance in medicine.* 1992;23(1):179-192.
6. Porter DA, Heidemann RM. High resolution diffusion-weighted imaging using readout-segmented echo-planar imaging, parallel imaging and a two-dimensional navigator-based reacquisition. *Magn Reson Med.* 2009;62(2):468-475.
7. Le Bihan D, Turner R. The capillary network: a link between ivim and classical perfusion. *Magnetic Resonance in Medicine.* 1992;27(1):171-178.
8. Astrom M, Rausing A. Chronic Achilles tendinopathy. A survey of surgical and histopathologic findings. *Clin Orthop Relat Res.* 1995(316):151-164.

Advanced diffusion-weighted imaging modeling for prostate cancer characterization: correlation with quantitative histopathologic tumor tissue composition.

Authors & Affiliations
Stefanie Hectors, Sahar Semaan, Christopher Song, Sara Lewis, George K Haines, Ashutosh Tewari, Ardeshir Rastinehad, Bachir Taouli; Icahn School of Medicine at Mount Sinai

Introduction
Advanced diffusion-weighted imaging (DWI) methods can potentially improve noninvasive characterization of prostate cancer (PCa) using MRI. There is recent interest in the use of diffusion tensor imaging (DTI) and high b-value DWI for PCa imaging. The fractional anisotropy (FA) parameter from DTI has shown to correlate with the histopathological Gleason score, a marker for PCa aggressiveness. At high b-values non-Gaussian diffusion behavior occurs, which is thought to reflect tissue heterogeneity and irregularity. This non-Gaussian diffusion component can be quantified using diffusion kurtosis imaging (DKI) and stretched-exponential (SE-DWI) models. The goal of this study was to correlate advanced DWI (DTI, DKI and SE-DWI) parameters in PCa with histopathological tissue composition measurements.

Methods & Results
24 PCa patients (mean age 63 y, range 53 – 76 y) that underwent prostate MRI including high b-value DWI and DTI at 3.0T (Siemens Skyra) before (2 – 102 days) undergoing prostatectomy were included in this prospective IRB-approved study. Trace-weighted DWI was performed using axial SS-EPI DWI with b-values 50, 1000, 1600 and 2000 s/mm^2. DTI was performed using SS-EPI with 6 diffusion directions and b-values 100 and 600 s/mm^2. DKI [ADC_{DKI} and kurtosis parameter K] and SE-DWI [ADC_{SE} and anomalous exponent α] parameter maps were constructed from the high b-value DWI data. A mono-exponential fit was performed to determine ADC_{ME} (conventional ADC). DTI (ADC_{DTI} and FA) parameter maps were generated by the scanner. Regions of interest were drawn in healthy peripheral zone (PZ) tissue and in the index PCa lesion. For each PCa lesion, an H&E-stained section was available. Using semi-automated segmentation (Positive Pixel Count in ImageScope; Aperio Technologies)[4], nuclear, cytoplasmic, cellular (nucleus + cytoplasm), stromal and luminal tumor tissue fractions and nuclear-cytoplasmic ratios (N/C=nuclear/cytoplasmic fraction) were derived (**Figure 1**). Differences in diffusion parameters between PZ and PCa lesions were tested using Wilcoxon signed rank tests. Spearman correlation coefficients between PCa diffusion parameters and histological measurements were calculated. In addition, correlation between histology and combinations of parameters was assessed using multiple linear regression.
24 lesions were analyzed (1/patient, average size 15 ± 6 mm). Representative diffusion parameter maps are shown in **Figure 2**. All DWI parameters were significant different between PZ and PCa (**Table 1**). Significant correlations between the histology and diffusion parameters are displayed in **Table 2**. ADC_{ME}, ADC_{DKI} and ADC_{SE} all significantly negatively correlated with the cytoplasmic and cellular tumor fractions and positively with stromal fractions. K also correlated with the same tissue fractions, but in opposite sign. ADC_{DTI} positively correlated with the stromal fractions, while FA correlated negatively with these fractions. Based on these correlations, it was hypothesized that combined parameters ADC_{DKI}+K and/or ADC_{DTI}+FA may show a stronger correlation with histology compared to individual diffusion parameters. ADC_{DKI}+K indeed showed stronger correlations compared to individual parameters (**Table 2**) although the correlations were not stronger compared to ADC_{ME}. ADC_{DTI}+FA did not show stronger correlation compared to individual parameters (**Table 2**).

Conclusion
Based on our results, DKI seems the most promising advanced DWI method for noninvasive assessment of PCa tissue composition, given the multiple additional correlations with tissue fractions for K compared to ADC values. The exact role value of DKI for PCa tissue characterization needs to be established in future research.

Clinical Relevance
Diffusion kurtosis parameters may serve as novel markers for histopathologic properties of prostate cancer and could potentially be used for improved characterization of prostate cancer.

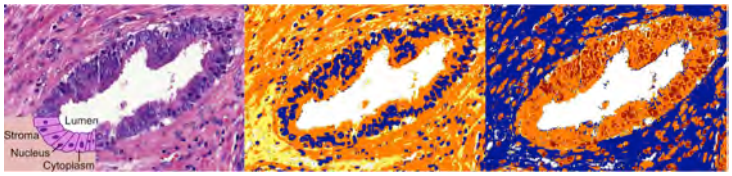

Figure 1: Histological processing of an H&E-stained prostate tumor section of a 60 year-old patient with Gleason 7 and pathology stage T2 prostate cancer. Left: zoomed image of H&E-stained section. Location of nuclei, cytoplasm, lumen and stroma is schematically depicted in the inset drawing bottom left. Middle: segmentation of nuclei (blue). Right: segmentation of cells (orange/red) and stroma (blue). The lumen is shown in white on both segmentation images.

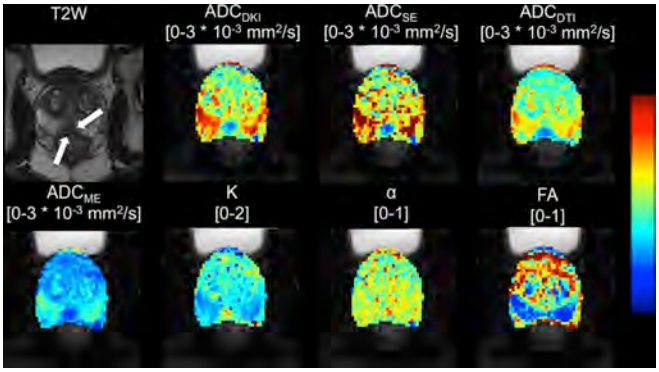

Figure 2: Representative T_2-weighted imaging and DWI parameter maps of a 66 year-old PCa patient with a 12 mm lesion in the right PZ (white arrow on T2W). ADC_{ME} = ADC from monoexponential fit, ADC_{DKI} = ADC from diffusion kurtosis modeling, K = kurtosis parameter from diffusion kurtosis modeling, ADC_{SE} = ADC from stretched-exponential modeling, α = anomalous exponent from stretched-exponential modeling, ADC_{DTI} = ADC from diffusion tensor imaging, FA = fractional anisotropy from diffusion tensor imaging.

Parameter	PZ	PCa	p
ADC_{ME} (10^{-3} mm²/s)	1.31±0.17	0.72±0.19	<0.001
ADC_{DKI} (10^{-3} mm²/s)	2.35±0.38	1.06±0.33	<0.001
K	0.56±0.08	0.83±0.46	0.007
ADC_{SE} (10^{-3} mm²/s)	3.17±0.99	1.08±0.46	<0.001
α	0.60±0.06	0.67±0.13	0.019
ADC_{DTI} (10^{-3} mm²/s)	1.98±0.24	1.05±0.36	<0.001
FA	0.14±0.07	0.25±0.08	<0.001

Table 1: Average parameter values in PZ and PCa. P-values result from Wilcoxon signed-rank tests. All parameters showed a significant difference between PZ and PCa. ADC_{ME} = ADC from mono-exponential fit, ADC_{DKI} = ADC from diffusion kurtosis modeling, K = kurtosis parameter from diffusion kurtosis modeling, ADC_{SE} = ADC from stretched-exponential modeling, α = anomalous exponent from stretched-exponential modeling, ADC_{DTI} = ADC from diffusion tensor imaging, FA = fractional anisotropy from diffusion tensor imaging.

Diffusion method	Parameter	Cytoplasmic fraction	Cellular fraction	Stromal fraction
ME-DWI	ADC_{ME}	-0.629 (**0.000**)	-0.604 (**0.002**)	0.690 (**0.000**)
SE-DWI	ADC_{SE}	-0.516 (**0.010**)	-0.498 (**0.013**)	0.640 (**0.000**)
	α	-0.233 (0.273)	-0.098 (0.650)	0.138 (0.519)
	ADC_{SE} + α	0.639 (**0.001**)	0.549 (**0.005**)	0.712 (**0.000**)
DKI	ADC_{DKI}	-0.525 (**0.008**)	-0.546 (**0.006**)	0.669 (**0.000**)
	K	0.487 (**0.016**)	0.485 (**0.016**)	-0.422 (**0.040**)
	ADC_{DKI} + K	0.632 (**0.000**)	0.645 (**0.000**)	0.711 (**0.000**)
DTI	ADC_{DTI}	-0.333 (0.112)	-0.380 (0.067)	0.512 (**0.010**)
	FA	0.308 (0.143)	0.274 (0.195)	-0.413 (**0.045**)
	ADC_{DTI} + FA	0.377 (0.069)	0.398 (0.054)	0.551 (**0.005**)

Table 2: Correlations of individual ME-DWI, SE-DWI, DKI and DTI parameters and combinations of parameters with histological measurements. ADC_{ME} = ADC from monoexponential fit, ADC_{DKI} = ADC from diffusion kurtosis modeling, K = kurtosis parameter from diffusion kurtosis modeling, ADC_{SE} = ADC from stretched-exponential modeling, α = anomalous exponent from stretched-exponential modeling, ADC_{DTI} = ADC from diffusion tensor imaging, FA = fractional anisotropy from diffusion tensor imaging.

Evaluating risk factors associated with CT guided biopsy related pneumothorax

Charles Hua, MD, Cherisse Wada, MD, Luis Perez, MD, Anik Patel, DO, Sumeet Bahl, MD, Nii Koney, MD, Brandon Olivieri, MD, Mustafa Syed, DO, Ronald Dreifuss, MD, Adie Friedman, MD, FSIR
Mount Sinai St. Luke's-West Hospitals New York, NY

Introduction

Pneumothorax is the most common complication of CT guided percutaneous needle lung biopsies. Clinically significant pneumothoraces require chest tube placement and hospitalization at the hospital's expense. The purpose of this study was to evaluate the risk factors associated with CT guided percutaneous needle lung biopsy.

Methods & Results

A retrospective review of 127 CT guided lung biopsies which occurred between October 2013 and March 2015 were evaluated. Statistical analysis was performed with Chi-squared or the Fischer's exact test. 103 patients underwent CT guided percutaneous lung biopsy using a 19/20-gauge coaxial biopsy system, 16 patients using a 17/18-gauge coaxial biopsy system, and 8 patients with a 21-gauge fine needle aspiration.

The overall mean age was 64.4 years, female/male ratio of 70/57. Emphysema was demonstrated in 27 patients (21%). The mean nodule size was 2.2 cm (range 0.4 to 11 cm). 37 lung nodules were in the right upper lobe, 10 lung nodules were in the right middle lobe, 26 lung nodules were in the right lower lobe, 31 lung nodules were in the left upper lobe, 16 lung nodules were in the left lower lobe, 4 lung nodules were in the lingual, and 3 lung nodules were in the left pleura. The procedure was performed supine on 53 patients (42%), prone on 72 patients (57%), and in the left lateral decubitus in 2 patients (2%). The mean distance from the pleura to nodule was 2.3 cm (range 0 to 6.7cm).

Pneumothorax occurred in 43 patients (33%). 14 of 27 patients (33%) with emphysema developed a pneumothorax ($p = 0.026$). Pneumothorax was observed in 14 of 53 patients (26%) in the supine position, 28 of 72 patients (39%) in the prone position, and 1 of 2 patients (50%) in the left lateral decubitus position ($p = NS$). There was no statistical significance to the location of the lung tumor. Pneumothorax was observed in 3 of 16 patients with the 17/18-gauge coaxial biopsy system (19%), 37 of 103 patients with the 19/20-gauge coaxial biopsy system (36%), and 3 of 8 patients with the 21-gauge fine needle aspiration (38%) ($p = NS$). The odds ratio for pneumothorax for nodules greater 2 cm was 0.43 (95% CI OR: 0.16-1.1, $p = 0.08$). The odds ratio for pneumothorax for pleura to nodule distance greater 2 cm was 5.31 (95% CI OR: 1.96-15.34, $p = 0.001$).

Conclusion

Emphysema and distance from pleura are important risk factor to the development of CT guided lung biopsy related pneumothorax. The following factors did not significantly affect the rate of pneumothorax development: patient positioning, tumor location within the lung, and tumor size.

Clinical Relevance

Pneumothorax is the most common complication of CT guided percutaneous needle lung biopsies. Clinically significant pneumothoraces require chest tube placement and hospitalization at the hospital's expense. Therefore, it is important to identify risk factors that may assist in the reduction of clinically significant pneumothoraces and chest tube placements.

Quantitative Assessment of Primary Liver Cancers using Advanced DWI Histogram Analysis with Histopathologic Correlation

Steven Peti MD[2], Sara Lewis MD[1,2], Stefanie J Hectors PhD[1,2], Michael King MD[1], Juan Putra MD[3], Swan Thung MD[3], Bachir Taouli MD[1,2]

Affiliations:

[1]Translational and Molecular Imaging Institute, Icahn School of Medicine at Mount Sinai, New York, NY, United States

[2]Department of Radiology, Icahn School of Medicine at Mount Sinai, New York, NY, United States

[3]Department of Pathology, Icahn School of Medicine at Mount Sinai, New York, NY, United States

Introduction

Primary liver cancers, including hepatocellular carcinoma (HCC), intrahepatic cholangiocarcinoma (ICC) and "combined" hepatocellular-cholangiocarcinoma (HCC-ICC) share common risk factors, are rising in incidence and differ in terms of treatment strategy. Diffusion weighted imaging (DWI) and apparent diffusion coefficient (ADC) quantification have shown promise for characterizing focal liver lesions. The goal of this study was to evaluate the ability of quantitative ADC histogram parameters to determine the histological diagnosis and grade of primary malignant liver cancers.

Methods & Results

In this IRB-approved retrospective study, we included consecutive patients with pathology proven primary liver cancer that underwent pre-treatment MRI including single shot echo-planar (SS-EPI) DWI (b 50, 400, 800), from 12/2013 to 5/2016. Diffusion restriction pattern of index lesions was qualitatively assessed on high b-value DWI. Lesion volume of interest measurements (VOI) were placed on DWI images excluding areas of necrosis to extract the following ADC histogram parameters: ADC mean, median, min, max, skewness, kurtosis, and 5th, 10th, 25th, 75th, 90th and 95th percentiles. Tumor grade was categorized pathologically as well (G1), moderately (G2), or poorly differentiated (G3). ADC histogram metrics were compared between different tumor types and tumor grades using the Mann-Whitney U test and Kruskal-Wallis test.

Results from 63 patients are reported. 65 lesions were assessed (mean size 46 ± 26 mm): HCC [n=36; G1 (n=11), G2 (n=16), G3 (n=9)], ICC [n=17; G2 (n=9), G3 (n=8)] and combined [n=12; G1 (n=4), G2 (n=3), G3 (n=5)]. On high b-value DWI, 35/36 (97%) HCCs, 17/17 (100%) ICCs and 11/12 (92%) combined tumors were hyperintense **(Figure 1).** ADC histogram values are shown in **Table 1**. ADC 5th, 10th and 95th percentiles were significant for discrimination between tumor types (p values <0.04)**.** ADC max, 75th, 90th, and 95th percentile were significant for discrimination between ICC and combined tumor (p values <0.04)**.** ADC mean, median, 5th, 10th, 25th, and 95th were significant for discrimination between HCC and combined tumor (p values <0.05)**.** ADC min and 5th percentiles were significant for discrimination between HCC and ICC**.** There was no difference in ADC histogram metrics for G3 vs. G1+2 for any tumor type (all p-values >0.11).

Conclusion

Our results demonstrate that primary liver cancers may potentially be distinguishable based on the advanced ADC metrics. ADC metrics did not distinguish between tumor grades for any of the primary liver cancers.

Clinical Relevance

DWI is a reasonable non-contrast technique for aiding in lesion characterization. ADC histogram quantification may potentially be useful for histopathologic diagnosis. Accurate histological tumor identification can help direct optimal treatment strategy.

Figures and tables

Table 1. Average ADC histogram values for malignant primary liver cancers.

Tumor	Mean*	Median*	Max*	Min*	Skewness	Kurtosis	5th	10th	25th	75th	90th	95th
HCC	1.29	1.25	2.12	0.67	0.23	3.18	1.00	1.06	1.16	1.49	1.66	1.78
ICC	1.30	1.27	2.30	0.34	0.04	3.60	0.80	1.03	1.19	1.49	1.68	1.79
Combined	1.13	1.12	1.81	0.40	0.08	3.09	0.82	0.88	1.01	1.27	1.40	1.47

*ADC values $x10^{-3}mm^2/s$

Figure 1. Primary liver cancers on high b800 DWI and ADC map in 3 separate patients (solid arrows). HCC in the right lobe with diffuse hyperintensity (A, B), ICC in the left lobe with hyperintense "target appearance" (C, D) and combined tumor in the right lobe with hyperintense "target appearance" (E, F). The combined tumor also contained fat (not shown) with a satellite nodule (dashed arrow) and portal vein branch invasion (red arrow).

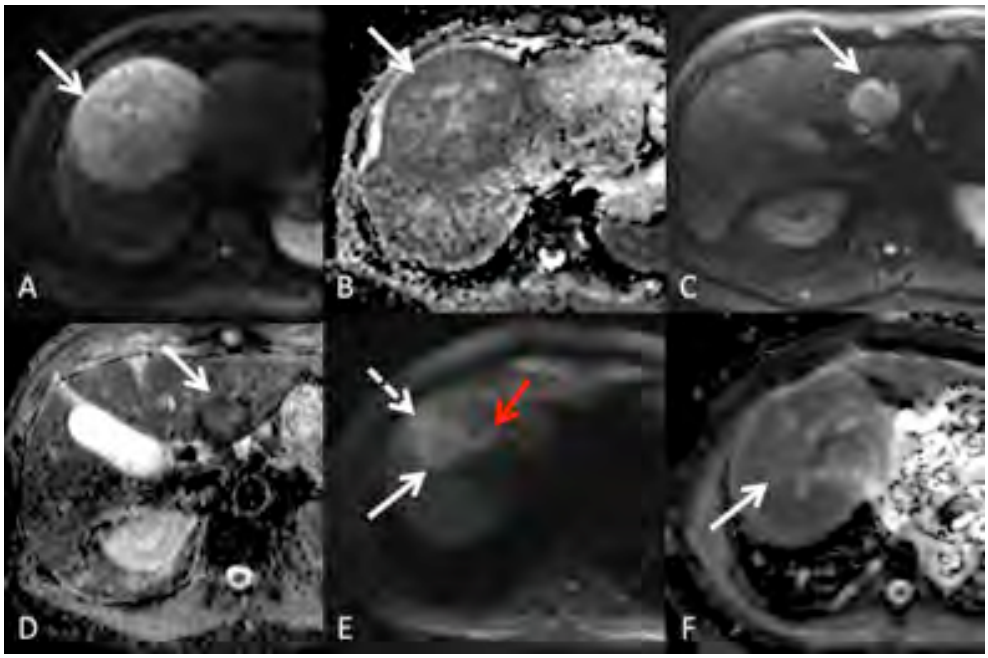

Comparison of sequential PET/CT and PET/MR in previously treated multiple myeloma patients.

Authors & Affiliations
A.M. Tuli*,[1] J. M. Bou Ayache,[1] S. Parekh,[2] K. Thamnirat,[3] S. Jagannath,[2]A. Chari,[2] L. Kostakoglu[1]

[1]Division of Nuclear Medicine, Department of Radiology, Mount Sinai Hospital, New York, NY, [2]Division of Hematology and Oncology, Department of Medicine, Mount Sinai Hospital, New York, NY, [3]Division of Nuclear Medicine, Department of Radiology, Mahidol University, Bangkok, Thailand

Introduction

FDG PET/CT (PET/CT) plays an important role in multiple myeloma (MM) management; specifically for staging, detecting extramedullary disease, evaluating therapeutic efficacy and assessing for relapse. MRI also provides detailed diagnostic and prognostic information with excellent soft tissue differentiation and high spatial resolution. FDG PET/MRI (PET/MR) is a promising hybrid imaging modality with several potential clinical applications in MM patients, including the assessment of osseous lesions. The primary aim of this study was to compare the diagnostic performance of PET/CT and PET/MR in detecting MM lesions in a post-therapy setting and the secondary aim was to determine their predictive value in both progression free survival (PFS) and therapy response.

Methods & Results

This is an IRB approved retrospective study that recruited previously treated MM patients from January 2013 to December 2016 using both PET/CT and PET/MR studies performed on the same day. PET/CT and PET/MR studies were assessed by semi-automated MIM software selecting all lesions above liver SUVmax except for those with osteosclerotic changes and hardware. The PET parameters included SUVmax, total lesion glycolysis (TLG) and metabolic tumor volume (MTV). T1, STIR and diffusion weighted imaging (DWI) of MRI were utilized to determine MM lesions. All imaging parameters were correlated with clinical laboratory data, International Myeloma Working Group (IMWG) response groups after induction chemotherapy (IT), after autologous stem cell transplant (ASCT), as well as with PFS.

The results are displayed in Table1. A total of 63 PET/CT and PET/MRI studies were analyzed after treatment (n=49 ASCT, n=14 IT only). There was significant correlation between PET/CT and PET/MR results ($p<0.00001$). Statistically significant correlation was also noted between PET/CT and post-IT and post-ASCT IMWG response dichotomized as response and no response with responders consisting of complete (CR), very good partial (VGPR) and partial (PR) response groups, and non-responders stable disease (SD) and progressive disease (PD) groups ($p=0.033$). Similarly, statistically significant correlation was noted between PET/MR and post-IT and post-ASCT IMWG response ($p=0.017$). MTV, TLG and SUVmax were neither predictive of PFS nor IMWG response. PET/MR provided incremental value in differentiating benign from malignant compression fractures (n=4/63, 6.3%), and diffuse spinal involvement with cord compression (n=1/63, 1.6%).

Conclusion

PET/CT results are strongly correlated with those of PET/MR in the detection of MM lesions, with some instances where PET/MR provides crucial incremental information regarding the extent of disease, such as in the confirmation of spinal cord involvement of MM lesions. Furthermore, PET/CT and PET/MR are both correlated to IMWG response as categorized on the same day of imaging. PET/MR alone has the potential of being a tool for evaluation of MM patients in the post-therapy setting.

Clinical Relevance

MM is the second most common age-related hematologic malignancy in the United States, which is incurable in most patients. Given the aging US population, the incidence of MM is expected to rise, along with associated costs. For instance, the total healthcare costs in the first year after diagnosis of MM is approximately $120,000. Imaging provides critical information such as evaluation of treatment response at various stages of disease, assessing/predicting high risk fracture sites, visualizing nonsecretory and oligosecretory MM tumors, which crucial for overall patient management.

Figures and tables

Table 1

Correlation of PET/CT and PET/MR results

	PET/MR(N=63)		P-value
PET/CT (N=63)	Positive	Negative	
Positive	23	4	<0.00001
Negative	1	35	

Development of a Rat Model for Medication-related Osteonecrosis of the Jaw (MRONJ)

[1]Edward Yurkow, [1]Derek Adler, [2]Michael Goedken, [3]David Reimer, [4]Samuel Y. P. Quek, & [4]Gayathri Subramanian
[1]Rutgers University Molecular Imaging Center & [2]Research Pathology Services, 41 Gordon Road Piscataway NJ,
[3]Nelson Biological Laboratories, 604 Allison Road Piscataway, NJ & [4]Rutgers School of Dental Medicine, 110 Bergen Street, Newark, NJ

Introduction

Medication-related osteonecrosis of the jaw (MRONJ) involves the progressive destruction of bone in the maxillofacial region of a subpopulation of patients treated with antiresorptive (i.e., bisphosphonates or RANKL inhibitor) and antiangiogenic drugs. In many cases dental procedures, such as tooth extraction, trigger the condition in susceptible individuals. To investigate the mechanisms involved in the development of this condition and devise screening tests to identify susceptible individuals, our group is developing a preclinical rat model of MRONJ.

Methods & Results

In preliminary studies, all three molars on one side of the upper jaw of anesthetized female Sprague Dawley rats were carefully extracted according to an animal use protocol approved by Rutgers University IACUC. Three-dimensional Computed Tomography (3D-CT) images were captured prior to extraction and periodically throughout a 56-day post-extraction period to profile changes in jaw structure and tooth socket features. Changes in radio-density of the jaw, vis-a vis bone mineral density, was also characterized. Image voxel intensity of the jaw bone, which reflects bone mineral density, was segmented into three (3) arbitrary ranges and a false color was assigned to each range to help visualize the dynamics of bone resorption, restructuring and mineralization. Frequency distributions of voxel intensity within a Region Of Interest (ROI) encompassing the affected jaw indicate that following tooth extraction, the jawbone progresses through an extended period of demineralization (~20 days) where the jaw and tooth sockets undergo marked restructuring. This period is followed by a hyper-mineralization of jaw surfaces and substructures.

Conclusion

The results of these preliminary studies provided our group with information relating to the dynamics of bone resorption in an extracted jaw and enabled our group to select sensitive endpoints required to measure and track jaw restructuring in on-going studies.

Clinical Relevance

Our research group is currently conducting this model using rats pretreated with the antiresorptive drug (Zoledronate) and dexamethasone (a combination of chemotherapy taken often by cancer patients exposed to antiresorptive medication) and we expect that this preclinical model will provide insight into the processes involved in the development of MRONJ to improved clinical management of this condition.

Figures and tables

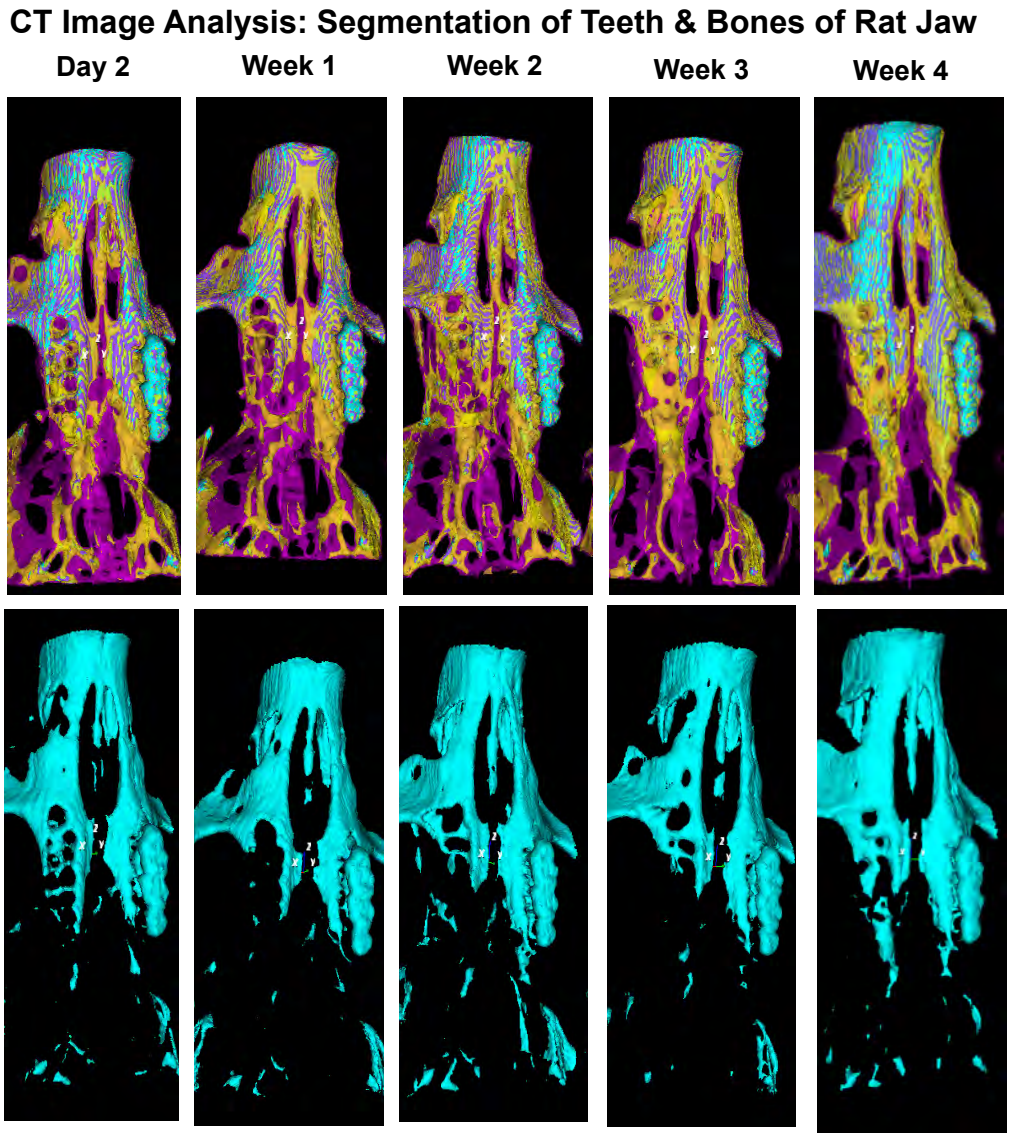

Image voxel intensity of the teeth and jaw structure, which reflects radiodensity / mineral density was segmented into three (3) arbitrary ranges and a false color was assigned to each range to help visualize the dynamics of bone resorption, restructuring and mineralization throughout a four (4) week post-extraction period. Magenta was used to colorizes bone with the lowest mineral density, while yellow and cyan colorizes mid- and high-density bone, respectively.

Cardiovascular Imaging

USEFULNESS OF 18F-SODIUM FLUORIDE PET/MR IMAGING FOR THE ASSESSMENT OF CARDIAC AMYLOIDOSIS.

Ronan Abgral[1-2], Maria G. Trivieri[1], Marc R. Dweck[1-3], Philip M. Robson[1], Nicolas Karakatsanis[1], Anaruhda Lala[4], Johanna Contreras[4], Radha Gopalan[4], Peter Gorevic[5], Valentin Fuster[4], Jagat Narula[4], Zahi A. Fayad[1].

1- Translational and Molecular Imaging Institute, Icahn School of Medicine at Mount Sinai, New York, NY, United States.
2- Department of Nuclear Medicine, European University of Brittany, EA3878 GETBO, IFR 148, Brest, France.
3- British Heart Foundation, University Centre for Cardiovascular Science, University of Edinburgh, Edinburgh EH16 4SB, United Kingdom.
4- Department of Medicine-Rheumatology, Mount Sinai Medical School, New York, NY 10029
5- Cardiovascular Institute, Icahn School of Medicine at Mount Sinai, New York, NY, United States.

Introduction

Cardiac amyloidosis exists in two predominant forms called acquired monoclonal immunoglobulin light-chain (AL) and transthyretin-related (ATTR). Their differentiation is a real diagnostic challenge for treatment management and prognosis of patient. Magnetic resonance (MR) imaging is increasingly used to aid in the diagnosis of amyloid alongside histology on the basis of characteristic appearances on late Gadolinium enhancement (LGE) but cannot distinguish ATTR and Al forms. Several series have showed that single-photon emission computed tomography using bone 99mTc-bisphosphonate tracers preferentially bind ATTR versus AL deposit in the myocardium.

Our aim was to use 18F-Sodium Fluroide (18F-NaF) positron emission tomography (PET) bone tracer in hybrid PET/MR imaging to aid in both the diagnosis of cardiac amyloidosis and differentiation of ATTR and AL forms within a single low radiation scan.

Methods & Results

Consecutive patients with biopsy-proven ATTR or AL cardiac amyloidosis and as many control subjects without clinical suspicion of amyloid disease were included in this study. All patients underwent simultaneous PET/MR (Biograph mMR, Siemens©) after IV injection of 370MBq of 18F-NaF. The selected data were reconstructed using a 3D breath-hold Dixon MR attenuation correction map. The MR protocol included LGE sequences, pre- and post-contrast T1 mapping. Maximal target-to-background ratio (TBRmax) was recorded, defined as maximal myocardial FDG uptake (SUVmax) corrected for blood pool activity (SUVmean) from right atrium. Mean TBRmax in ATTR, AL and control subjects were compared using a Student t-test.

Eighteen patients (61.3 ± 10.5 yo, 12M/6F) were prospectively recruited, comprising 6 ATTR, 3 AL and 9 control subjects. All amyloid patients had characteristic LGE appearances. Mean TBRmax were respectively 1.29 ± 0.31, 0.77 ± 0.06 and 0.68 ± 0.03 in ATTR, AL and control subjects. Mean TBRmax was significantly higher in ATTR than in AL patients (p=0.028) and in control subjects (p=0.0001). Mean TBRmax was significantly higher in AL patients than in control subjects (p=0.046). A TBRmax threshold of 0.85 appeared to differentiate all patients as having ATTR amyloidosis. There was no significant difference in terms of pre-contrast (p=0.48) and post-contrast T1 mapping (p=0.57) between ATTR and AL patients.

Conclusion

These results showed the potential of NaF-PET/MR to diagnose cardiac amyloidosis and to differentiate ATTR and AL forms, confirming our preliminary published results (Trivieri et al. J Am Coll Cardiol 2016).

Clinical Relevance

Differentiation of AL and ATTR cardiac amyloidosis is a real challenge. Combined FDG PET/MR imaging is a non-invasive method that holds major clinical potential in improving the diagnosis and guiding the treatment of patients.

Figures and tables

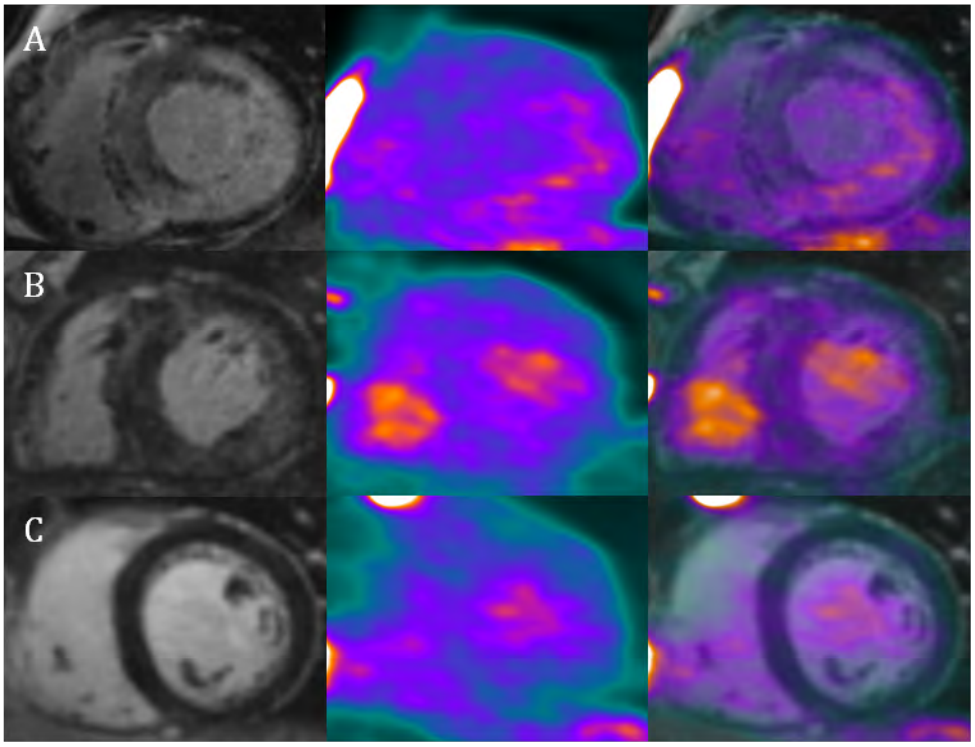

Healthy control patient **(row A)**. No late gadolinium enhancement (LGE) on CMR and low myocardial 18F-fluoride uptake (SUVmax = 0.8 lower than blood pool level, TBRmax = 0.68)**.**

Patient with AL Amyloid **(row B)**. Characteristic cardiac amyloid appearances on LGE, but again with low myocardial ^{18}F-fluoride uptake (SUVmax = 1.12 lower than blood pool level, TBRmax = 0.73).

Patient with TTR Amyloid **(row C)**. Characteristic appearances on LGE with diffuse low-level uptake of ^{18}F-fluoride throughout the myocardium (SUVmax = 1.73 upper than blood pool level, TBRmax = 1.40).

Increased Vascular Inflammation Relates to Increased Prevalence of High Risk Coronary Plaque in Psoriasis Patients.

Amit K. Dey[1], Joshua P. Rivers[1], Jonathan H. Chung[1], Joseph B. Lerman[1], Aditya A. Joshi[1], Abhishek Chaturvedi[1], Mohammad Tarek Kabbany[1], Anshuma Rana[1], Justin A. Rodante[1], Heather L. Teague[1], Charlotte L. Harrington[1], Martin P. Playford[1], Marcus Y. Chen[1], Veit Sandfort[1], David A. Bluemke[1], Nehal N. Mehta[1].

[1]National Heart, Lung, and Blood Institute, National Institutes of Health.

Introduction

Psoriasis (PSO), a chronic inflammatory disease associated with an accelerated risk of MI and vascular inflammation (VI) by 18-FDG PET/CT, provides a reliable human model to study inflammatory atherogenesis. Recently, PSO patients were shown to have increased high risk plaque (HRP) prevalence as well as VI when compared to healthy volunteers, however the inter-relationship between vascular inflammation and prevalence of high risk plaque morphology in PSO patients has yet to be described. We hypothesize that increased VI by FDG PET/CT would associate with increased prevalence of HRP by CCTA.

Methods & Results

Consecutive PSO patients (N=105) underwent FDG PET/CT scans (60 minutes post-FDG injection) to directly quantify VI represented as target-to-background ratio (TBR). Presence or absence of high risk plaque was determined by plaque characterization via CCTA (Toshiba 30 slice) using QAngio CT software (Medis, The Netherlands). HRP identification was defined as either positive remodeling (index ≥ 1.1), low attenuation (< 30 HU), and/or spotty calcification. The cohort was stratified by median TBR values and subsequently statistically analyzed via multivariable logistic regression by TBR group and prevalence of HRP (STATA 12).

Patients with high TBR were older, predominantly male, had increased cardiovascular disease risk by Framingham risk score, and increased prevalence of HRP compared to patients with low TBR (**Table 1**). Unadjusted logistic regression illustrated significant increase in odds of HRP prevalence for patients with higher TBR (Odds ratio [Confidence Interval]: 2.59 [1.13-5.96]) which remained significant independent of cardiovascular risk factors, statin use, and systemic/biologic PSO therapy (3.61 [1.06-12.28]) **(Table 2).**

Conclusion

Directly quantified VI is associated with increased prevalence of HRP in PSO beyond adjustment for cardiovascular risk factors. However larger studies are needed to confirm these findings.

Clinical Relevance

These findings suggest that VI, as a relevant biomarker for CV disease risk, may provide a valid reliable surrogate marker for early rupture prone, coronary plaques in PSO

Table 1: Comparison of baseline characteristics of the study groups based on median TBR (1.69) in psoriasis patients.

Variable	TBR<1.69 (n=52)	TBR>1.69 (n=53)	p-value
Demographic and Clinical History			
Age, years	47.7±1.8	52.6±1.6	**0.02**
Male, n (%)	24 (46)	41 (77)	**0.001**
Hypertension, n (%)	13 (25)	19 (36)	0.23
Dyslipidemia, n (%)	18 (35)	34 (64)	**0.002**
Diabetes mellitus, n (%)	5 (10)	7 (13)	0.56
Current smoking, n (%)	2 (4)	6 (11)	0.15
Clinical parameters:			
Body mass index, kg/m^2	27.1±0.5	32.6±0.9	**<0.001**
Framingham risk score	2 (1-4)	4 (3-7)	**<0.001**
Statin use	10 (19)	25 (47)	**0.002**
Lipid profile:			
Total cholesterol, mg/dL	185.1±5.9	177.8±4.8	0.17
Low-density lipoprotein cholesterol, mg/dL	101.1±5.1	100.4±3.9	0.46
High-density lipoprotein cholesterol, mg/dL	62.4±2.8	49.1±1.9	**<0.001**
Triglycerides, mg/dL	99.9±5.6	148.4±14.1	**0.001**
High-sensitivity C-reactive protein, mg/L	1.9 (0.6-3.8)	1.8 (0.8-4.2)	0.38
Psoriasis Characteristics			
Psoriasis area severity index score	4.5 (2.7-8.3)	6.2 (3.0-10.1)	0.32
Systemic/biologic treatment, n (%)	19 (37)	19 (36)	0.94
Vascular inflammation (FDG PET/CT)			
Target-to-background ratio	1.55±0.01	1.92±0.03	**<0.001**
Coronary Plaque Characterization (CCTA)			
Presence of high-risk plaque, n (%)	13 (25)	23 (43)	**0.04**

All values in table are represented as mean ± SEM or median (IQR) for continuous variables and as n (%) for categorical variables. P-values were calculated by Student's t-test or Mann-Whitney U test for continuous variables and by Pearson's chi-square test for categorical variables. TBR – target-to-background ratio.

Table 2: Logistic multivariable regression analysis of prevalence of High risk plaque with TBR group (TBR group based on median TBR of 1.69).

Model (n=105)	OR (CI)	p-value
Unadjusted.	**2.59 (1.13-5.96)**	**0.02**
Adjusted for Framingham risk score, body mass index, hyperlipidemia, type-2 diabetes, low-density lipoprotein, psoriasis severity, statin use and systemic/biologic therapy.	**3.61 (1.06-12.28)**	**0.04**

All data in the tables represented as odds ratio (confidence interval); p-value.

MRI Quantification of Ischemic Cardiomyopathy Progression in the Ovine Model: Size Does Matter

Fargnoli AS, Katz MG, Bridges CR, Gillespie V, Gordon H

Introduction

Tracking changes in myocardial function post ischemic infarction is paramount in translational models of cardiomyopathy. Too often, the degree of infarction size and left ventricular functional parameters as well as conformational histology are not reported systematically. Without a comprehensive quantification of model data, it is difficult if not impossible to justify translational therapeutic findings. Here, we utilize a robust MRI protocol to track changes in the ovine model in mild and severe cases of cardiomyopathy.

Methods & Results

Following baseline MRI, (n=10) sheep were equally divided between two groups and subsequently induced with myocardial infarction via surgical left thoracotomy mediated ligation of either CM1 artery (Mild group) or both CM1 and CM2 (Severe group). Left ventricular cardiac mechanics, infarction scar size calculated with delayed enhancement imaging **Fig1A**, and volume geometric parameters were tracked with MRI over time. Histology was performed on infarction and remote healthy specimens to confirm pathological expansion of border zone. The mild group had 10±1% LV scar size at 3 and 12 weeks post infarction, while the Severe group demonstrated higher at 3 weeks 14±1% and worsening to 17±2% at 12 weeks **Fig1B**, all $p<0.05$. Modest changes in End Diastolic volume over time [Baseline ; 3 weeks ; 12 weeks] was noted for the Mild group [94±4 ; 111±11 ; 104±4 mL], however much more accentuated in the Severe group group [94±6 ; 109±5 ; 127±7 mL], $p<0.05$. End systolic volumes followed a similar trend: Mild group [35±2 ; 48±5 ; 51±3 mL] vs. Severe group [36±3 ; 56±4 ; 75±5 mL]. A typical enlarged severe MI ventricle is shown in **Fig1C**, which demonstrates much less functional ejection fraction over time between the groups **Fig 1D**. Both groups had 62±2% at baseline, however separated at 3 weeks Mild 57±1% vs. Severe 48±5% and at 12 weeks Mild 51±1% vs. Severe 41±2%, both $p<.05$. Post mortem left ventricles demonstrating infarct and remote regions are shown for Mild **Fig1E** and Severe **Fig1F** cases. Pathological sectioning confirms healthy remote **Fig1G** and typical infarcted myocardium which was found much more extensive **Fig1H** in the severe MI cases.

Conclusion

Delayed enhancement quantification of infarct size is a robust means to classify between mild vs. severe levels of infarction. Left ventricular mechanics, dilatation, and expansion of transition border zone are functions of the MI's size and extent. MRI tracks changes precisely in the myocardium which can be leveraged to improve therapeutics dosing and evaluation in these critical large animal models.

Clinical Relevance

MRI is a gold standard tool that should be utilized for increasing the accuracy of reported results in therapeutics aiming to reverse and or attenuate left ventricular remodeling at the pre clinical level. Clinically, MRI offers unparalleled means to evaluate post myocardial infarction and can be used to accurately assess and classify patient status over time.

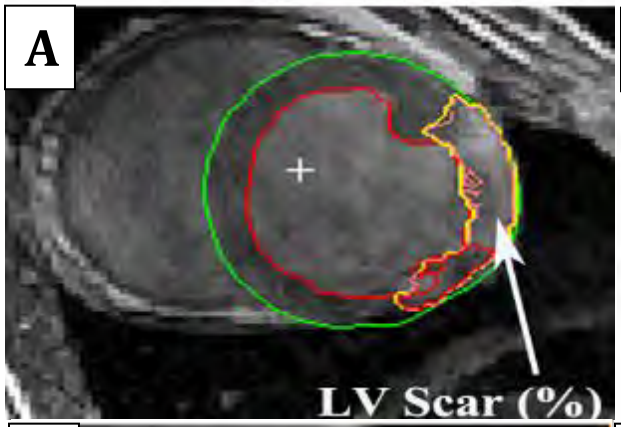
A
LV Scar (%)

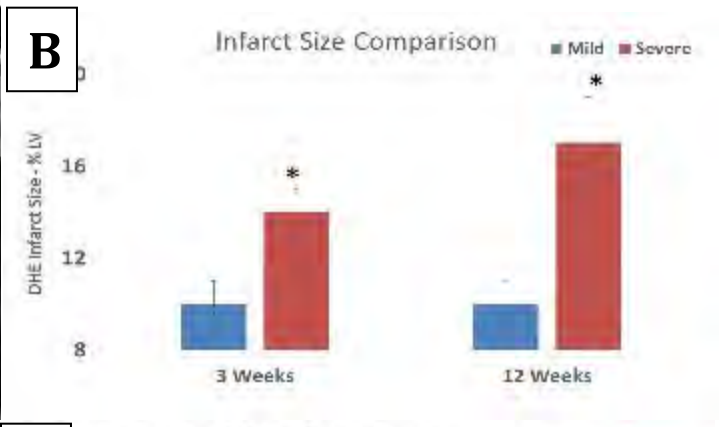
B
Infarct Size Comparison
Mild
Severe
DHE Infarct Size - % LV
16
12
8
*
*
3 Weeks
12 Weeks

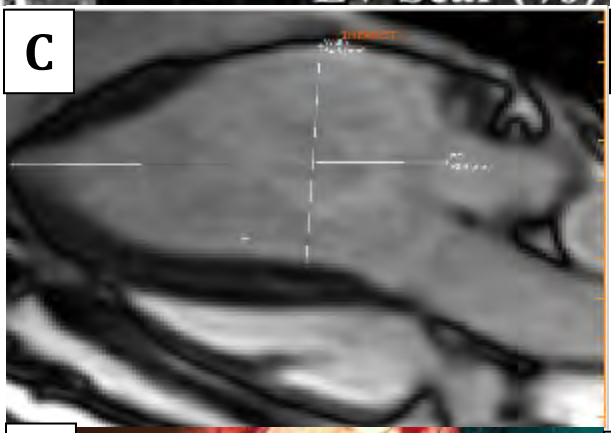
C

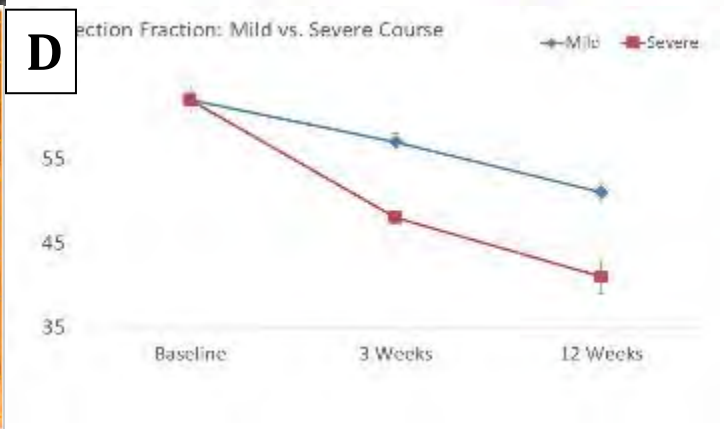
D
ection Fraction: Mild vs. Severe Course
Mild
Severe
55
45
35
Baseline
3 Weeks
12 Weeks

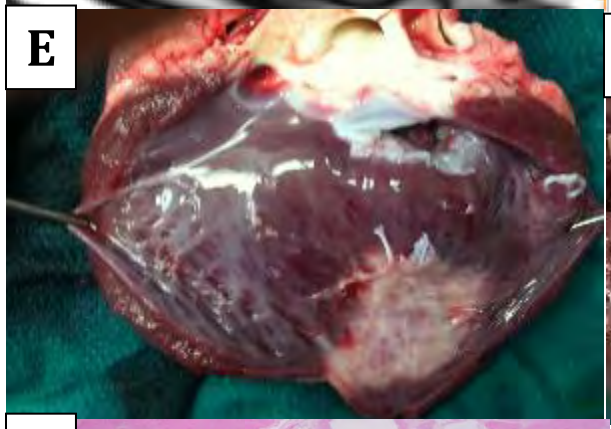
E

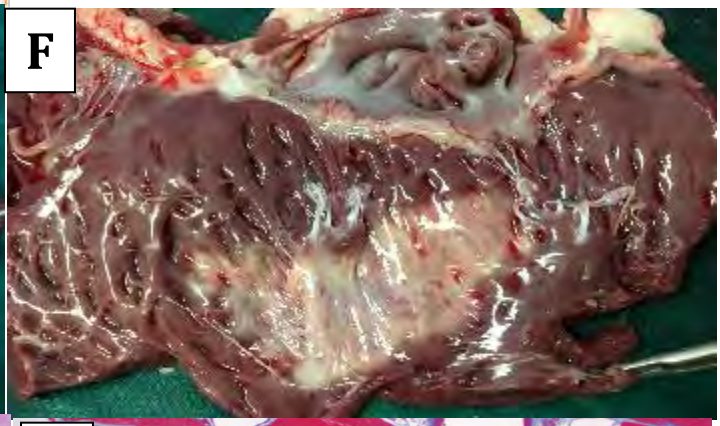
F

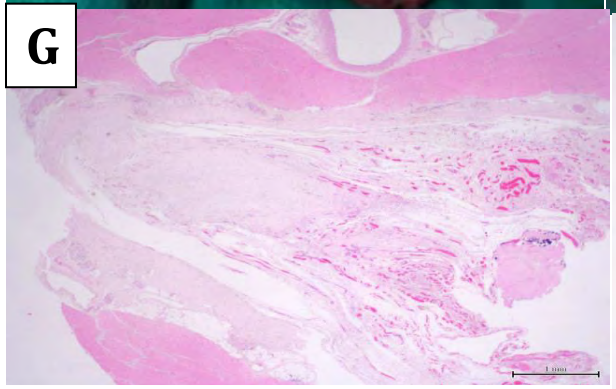
G

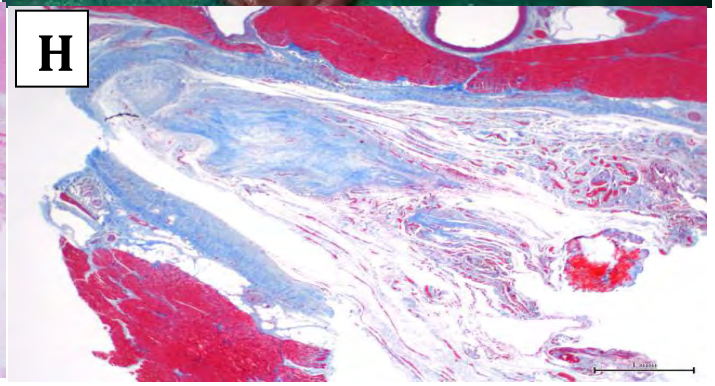
H

Comparison of Inter-observer bias between Low Resolution and High Resolution Scans using 3T and 7T Scanners

Christopher M Faries, Martin J Willemink, Bram Coolen, Zahi A Fayad, Willem J Mulder, and Claudia Calcagno. Icahn School of Medicine at Mount Sinai.

Introduction: Atherosclerosis is the main cause of heart disease and stroke, and leads to 50% of all deaths in westernized society[1]. MRI can be used to assess atherosclerotic disease severity, and to identify plaque components noninvasively[2]. Vessel wall thickening can be measured with MRI and is commonly associated with atherosclerosis[3]. However, there are observer biases when measuring the vessel wall with MRI[4]. In this study, we investigate whether there is a difference in inter-observer bias between low resolution and high resolution imaging in both 3T and 7T field strengths.

Methods & Results: Atherosclerosis was induced in 5 male New Zealand White (NZW) rabbits using a previously validated method. All rabbits were imaged after 4 months of high-fat diet. Animals were each imaged twice, once on a 7T clinical scanner (Magnetom, Siemens Healthineers, Erlangen, Germany), and once on a 3T clinical scanner (mMR, Siemens Healtineers, Erlangen, Germany). The 7T scanner utilized a custom made rabbit coil consisting of a transmit-only quadrature-driven high-pass birdcage and 12-channel receive-only loop elements. The 3T scanner used a product Tx/Rx15-channel knee coil. On both scanners we used localizer scans and time-of-flight (TOF) angiography to clearly identify the rabbit aorta. A 3D T2 weighted SPACE(23,24) (Sampling Perfection with Application optimized Contrasts using different flip angle Evolution) sequence was acquired using 0.6 mm^3 (Low Resolution) and 0.4mm^3 (High Resolution). The sequence was acquired in the sagittal plane, covering the whole rabbit abdominal aorta, from above the renal arteries down to the iliac bifurcation. Imaging data was analyzed with Osirix software. All images were reformatted in the axial plane, and all axial slices from the left renal artery to the aortic bifurcation were analyzed. Vessel wall area was measured by tracing and subtracting the inner and outer vessel wall contours. Two independent observers traced each data set. Inter-observer reliability was evaluated using Bland-Altman analysis.

For the 3T low resolution scans, the percent bias was 37.41, the percent limit of agreement were from -5.868 to 80.69, the absolute bias was 0.05566, and the absolute limit of agreement was from -0.01227 to 0.1236 (Figure 1,2). For the 3T high resolution scans, the percent bias was 34.31, the percent limit of agreement was from -5.987 to 74.62, the absolute bias was 0.03818, and the absolute limit of agreement was from -0.01884 to 0.0952 (Figure 3,4). For the 7T low resolution scans, the percent bias was 42.85, the percent limit of agreement was from -1.001 to 86.70, the absolute bias was 0.06657, and the absolute limit of agreement was from -0.002535 to 0.1375 (Figure 5,6). For the 7T high resolution scans, the percent bias was 41.35, the percent limit of agreement was from -6.707 to 89.4, the absolute bias was 0.04268, and the absolute limit of agreement was from -0.01173 to 0.09709 (Figures 7,8).

Conclusion: Bland-Altman analysis revealed a bias for all imaging sequences analyzed between the two observers. For both 3T and 7T field strengths, both percent and absolute bias were smaller for the high resolution compared to the low resolution scans. Furthermore, both the absolute and percent biases were lower for images acquired at 3T compared to images acquired at 7T. Overall, these data indicate that when tracing vessel wall contours, a significant percent and absolute bias in vessel wall area measurements can be observed among different analysts.. These biases decrease when using higher resolution imaging.

Clinical Relevance: These findings underscore the importance of analysis standardization among observers when calculating absolute measures of plaque burden in animal studies or clinical trials. Furthermore, this study is clinically relevant also because it indicates that increasing imaging spatial resolution may help to reduce bias among observers and allow for more robust quantitative analysis. By more accurately measuring vessel wall thickness, we may be able to more accurately identify atherosclerotic disease and measure its progression.

References:

1. Lusis AJ. Atherosclerosis. Nature. 2000;407:233–241. **2.** Corti R, Fuster V, Badimon JJ, Hutter R, Fayad ZA. New understanding of atherosclerosis (clinically and experimentally) with evolving MRI technology in vivo. Ann N Y Acad Sci. 2001;947:181-195 **3.** Porsche C, Walker L, Mendelow AD, Birchall D.

Assessment of vessel wall thickness in carotid atherosclerosis using spiral CT angiography. Eur J Vasc Endovasc Surg. 2002 May;23(5):437-40. **4.** Kerwin WS, Canton G. Advanced techniques for MRI of atherosclerotic plaque. Topics in magnetic resonance imaging: TMRI. 2009;20:217–25.

Figures and tables

Figure 1: Red dashed lines indicate the limits of agreement, Black dashed nonzero line indicates the bias.

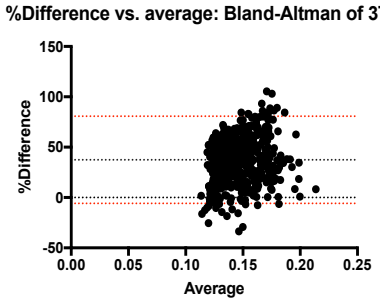

Figure 2: See figure 1 legend

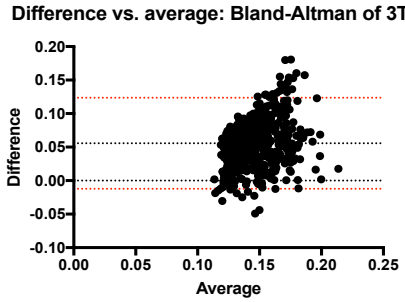

Figure 3: See figure 1 legend

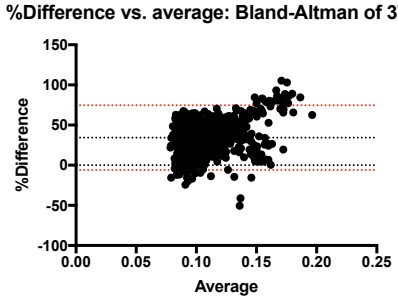

Figure 4: See figure 1 legend

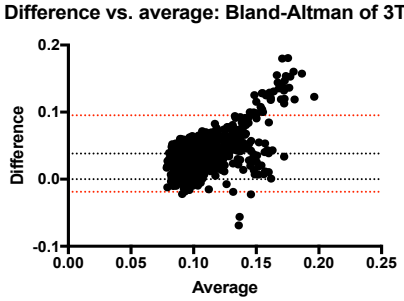

Figure 5: See figure 1 legend

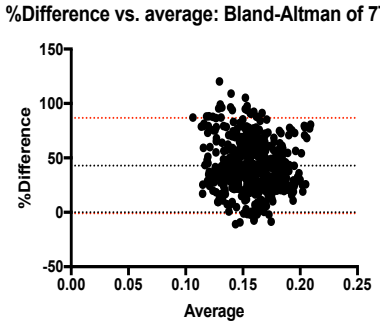

Figure 6: See figure 1 legend

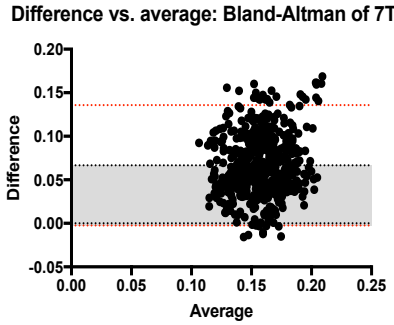

Figure 7: See figure 1 legend

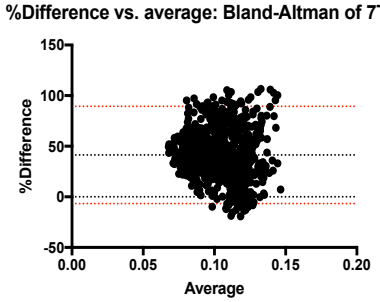

Figure 8: See figure 1 legend

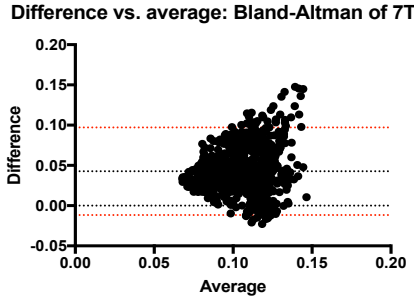

Simultaneous assessment of carotid plaque inflammation and micro-calcification with dual-tracer 18F-FDG:18F-NaF PET/MR multi-parametric imaging

N. A. Karakatsanis[1], M. G. Trivieri[1], M. R. Dweck[1,2], P. M. Robson[1], R. Abgral[1,3], R. J. Soler[1,4], C. Calcagno[1], V. Mani[1], C. Tsoumpas[1,5], Z. A. Fayad[1]

[1]Translational and Molecular Imaging Institute, Icahn School of Medicine at Mount Sinai, New York, NY,
[2]British Heart Foundation, University Centre for Cardiovascular Science, University of Edinburgh, Edinburgh, UK
[3]Department of Nuclear Medicine, European University of Brittany, Brest, France,
[4]La Timone Hospital, Vascular & Endovascular Surgery, CRMBM-CEMEREM, UMR 7339, Aix-Marseille University, Marseille, France,
[5]Division of Biomedical Imaging, University of Leeds, Leeds, United Kingdom

Introduction

Simultaneous PET/MR has recently been introduced as a multi-parametric cardiovascular imaging framework of potentially high clinical value, thanks to its unique capability of combining i) the superior vessel wall anatomical features characterization of MRI, together with ii) the PET in-vivo progress quantification of critical molecular mechanisms in atherosclerosis. In the meantime, a range of PET tracers have been independently employed to investigate the association of atherosclerosis disease progress with specific molecular processes in vessel plaques, such as inflammation with 18F-Fluorodeoxyglucose (18F-FDG) or micro-calcification with 18F-sodium fluoride (18F-NaF). In this study we introduce the concept of a novel dual-tracer cardiovascular PET-MR imaging uniquely combining 18F-FDG and 18F-NaF plaque imaging in a single clinically feasible dynamic PET-MR scan protocol of a standard of care (SOC) total dosage. Moreover, we exploit the relatively high bone uptake rate of the 18F-NaF dose component to correct for the dual-tracer PET signal attenuation in bones. Our aim is to offer co-registered in-vivo quantitative imaging of inflammation and micro-calcification molecular processes in carotid plaques within a single PET/MR exam session thereby enabling in future parallel assessments of both processes activity at multiple stages of the atherosclerosis disease.

Methods & Results

A 90min dynamic human carotid dual-tracer PET/MR scan is proposed involving: a) the initial administration of half of the SOC amount of weight-regulated 18F-FDG dosage, b) the start of a PET-MR scan at ~80min post 18F-FDG injection, c) the administration of 18F-NaF of the same dosage amount at 90min post 18F-FDG injection and, d) the completion of PET/MR acquisition at 170min post 18F-FDG injection. The dynamic PET 90min acquisition is conducted without interruption on list-mode to allow reconstruction of any time segments. The MR protocol run in parallel beginning with a 2-point Dixon MR sequence, from which 4 tissue classes (air, lungs, fat and water) were manually segmented for MR-based PET attenuation correction (MRAC). Furthermore, Patlak Ki images are estimated from the dynamic PET data to segment the bones as the 5th tissue class for enhanced MRAC. Furthermore, we applied 3D time-of-flight non-contrast enhanced carotid MR angiography and a series of diagnostic black blood T1, T2 and proton density sequences over the same set of 2D transaxial slices covering the right and left carotids bifurcation sections. The net 18F-FDG PET images for the first 10min of scan are independently reconstructed and, assuming sufficient 18F-FDG kinetics stability, the decay-corrected net 18F-FDG SUV image is linearly extrapolated to the last 10min scan period. Finally, the extrapolated FDG image is subtracted from the cocktail 18F-FDG:18F-NaF PET SUV image, after the latter is normalized according to the combined dosage and decay, to quantitatively estimate the net 18F-NaF SUV uptake for the last 10min.

Region-of-interest (ROI) based quantitative analysis in left and right carotid wall bifurcation points and proximal common carotids lumen was conducted on clinical 18F-FDG:18F-NaF PET/MR images. The results demonstrated a relatively high and kinetically stable net 18F-FDG PET signal in both carotids after 80min of 18F-FDG circulation, therefore permitting the extrapolation of the decay-corrected net 18F-FDG signal distribution for

later times. In addition, at 70min after 18F-NaF injection, i.e. for the last 10min of the scan, the total PET signal was observed to be stable thereby suggesting that a total scan time of 90min can be sufficient for simultaneous imaging of both 18F-FDG and 18F-NaF carotid plaque uptake.

Conclusion

Simultaneous imaging of inflammation and micro-calcification activity in carotid plaques within the same scan session can be clinically feasible by employing a 90min 18F-FDG:18F-NaF PET/MR carotid scan protocol and administering a standard-of-care total dosage at FDG:NaF 1:1 ratio. The introduction of a 90min delay between 18F-FDG and 18F-NaF injections allows for sufficient kinetic-based separation of the two tracer components signal as well as NaF-driven bone segmentation for enhanced PET attenuation correction in PET/MR imaging.

Clinical Relevance

18F-FDG:18F-NaF PET/MR imaging enables the co-registered in-vivo evaluation of both inflammation and micro-calcification activity in carotid plaques, in parallel to MR anatomical assessments, thereby permitting the systematic study of their correlated progress during the course of atherosclerosis and in response to therapy.

Figures and tables

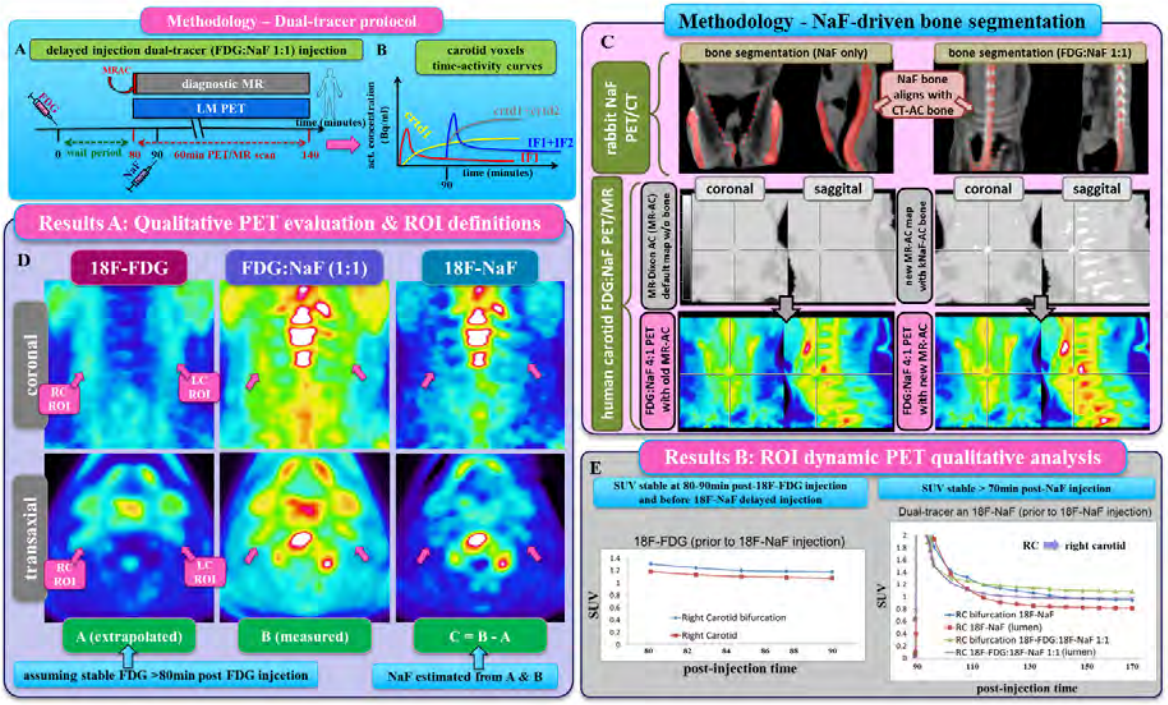

Figure (a): Proposed dual-tracer PET/MR acquisition protocol , **(b)**: Graphical illustration of ROI carotid time activity curve data, **(c)**: PET-driven bone segmentation from 18F-NaF kinetics, validation in rabbits against CT-segmented bone and application in clinical carotid PET/MR **(d)**: coronal and transaxial views of early net 18F-FDG, late cocktail 18F-FDG:18F-NaF and estimated late net 18F-NaF PET images and locations of bifurcation carotid ROIs, **(e)**: Quantitative SUV evaluations as a function of post 18F-FDG injection time for the early (upper row) and the late (bottom row) phase for the right carotid (RC) ROI.

Multi-Vessel Assessment of Atherosclerotic Activity in Patients with Sleep Apnea Using a Hybrid Positron Emission Tomography/Magnetic Resonance Imaging (PET/MRI)

Vaishnavi Kundel MD[1]; Maria Giovanna Trivieri MD[1], Phil R. Robson PhD[1], Nicolas Karakatsanis PhD[1,] Jorge Kizer MD, MSc[2], Robert Kaplan PhD[2], Zahi Fayad PhD[1], Neomi Shah MD, MPH[1,2]

[1]Division of Pulmonary, Critical Care, and Sleep Medicine, Icahn School of Medicine at Mount Sinai, New York, NY; [2]Department of Epidemiology and Population Health, Albert Einstein College of Medicine, Bronx, NY.

Introduction:
Atherosclerosis, a systemic disease process, has been linked with sleep apnea. However, much of the research has focused on individual anatomic plaque assessment rather than multi-vessel assessment of atherosclerotic disease activity. Our study is the first to provide a multi-vessel assessment of atherosclerotic activity in patients with sleep apnea (SA) using a hybrid PET/MRI with 18F-FDG (glucose analogue) as the PET tracer. 18F-FDG uptake correlates with macrophage burden in metabolically active atherosclerotic plaques. The study was conducted to assess the feasibility of measuring atherosclerotic plaque activity pre and post sleep apnea treatment using this modality.

Methods & Results:
We recruited 5 patients referred to the sleep center who met the following criteria: age >21, moderate to severe SA as defined by an apnea-hypopnea index (AHI) ≥15, and stable cardiovascular risk factors who were CPAP and statin naïve. Exclusion criteria included presence of ferromagnetic implants, glomerular filtration rate <60 mL/min/1.73m2, and insulin-dependent diabetes. Image acquisition and analysis was conducted at the Translational and Molecular Imaging Institute at Mount Sinai. The imaging procedure involved injection of 18F-FDG 80 minutes prior to PET scanning. PET data was subsequently acquired for 50 minutes during which MRI (with gadolinium contrast) was performed to assess vessel morphology, and cardiac function using standard 2D cine-images, 3D coronary MR-angiography and post-gadolinium short-axis sequences. A qualitative and quantitative analysis of tracer-uptake was performed using target-to-background ratios (TBR) computed by measuring the standardized uptake value (SUV) in the region of interest (ROI) and arterial lumen blood (background).
Eighty percent of our sample was male. Mean age was 52, mean BMI was 33.7kg/m^2. Severe SA (AHI ≥30) was present in 60% of our sample. In the pre-SA treatment phase, qualitative image analysis revealed that all patients with sleep apnea had focal elevation of FDG signal in the aorta, 60% had elevation in the carotid arteries, and no focal FDG signal was visualized in the coronary arteries. Results from post-CPAP imaging performed in one patient adherent to treatment for 12 weeks (Table 1) showed an overall reduction of FDG signal (as measured by FDG TBR_{mean}) in the aorta and both carotid arteries by 6.2%, 4.5%, and 3.5%, respectively. The remaining patients are awaiting completion of therapeutic period of 12 weeks.

Conclusion:
This is the first study to measure multi-vessel atherosclerotic disease activity in patients with SA using a hybrid PET/MRI system. Preliminary data from this study revealed metabolically active carotid and aortic plaques in a majority of patients with moderate to severe SA, and a reduction in plaque metabolic activity post-CPAP therapy.

Clinical Relevance:
We would anticipate that patients with metabolically active plaques would have a higher incidence of cardiovascular events over time, when compared to patients with stable plaques. Use of the PET/MRI platform in this study allows us to better understand individual risk prediction for future cardiovascular events as it relates to sleep apnea.

Figures and tables:

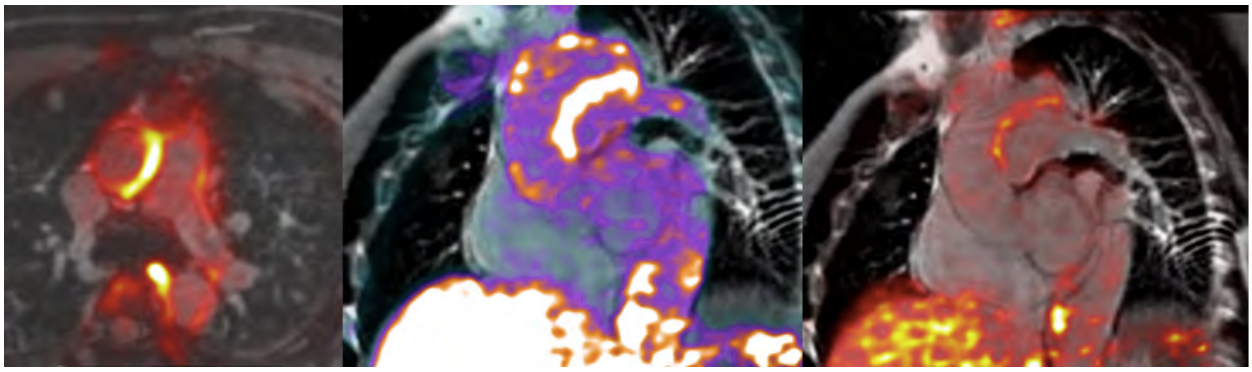

Table 1: Pre and Post SA Treatment Response of FDG uptake in the Aorta and Carotid Arteries (n=1)

Region of Interest	Pre-CPAP Therapy TBR_{mean}	Post-CPAP Therapy TBR_{mean}	Percent TBR_{mean} Reduction Post-CPAP
Aorta	1.409	1.347	6.2%
Left Carotid	1.202	1.157	4.5%
Right Carotid	1.093	1.058	3.5%

Material Decomposition in an Arbitrary Number of Dimensions using Noise Compensating Projection

Thomas O'Donnell[1] Ahmed Halaweish[1] David P. Cormode[2] Rabee Cheheltani[2] Zahi A. Fayad[3] Venkatesh Mani[3]

[1]Siemens Healthineers
[2]Dept of Radiology, University of Pennsylvania
[3]Translational and Molecular Imaging Institute, Icahn School of Medicine at Mount Sinai

Introduction

Multi-energy CT (e.g., dual energy or photon counting) facilitates the identification of certain compounds via data decomposition. However, the standard approach to decomposition (i.e., solving a system of linear equations) yields negative values for material concentrations if – due to noise - a voxel's vector of CT values falls outside the boundary of values describing possible pure or mixed basis materials. This may be addressed by projecting these points onto the closest point on this boundary.

However, when acquiring four (or more) energy volumes, the space bounded by three (or more) materials that may be found in the human body (either naturally or through injection) can be quite small. Noise may significantly limit the number of those voxels to be included within. Therefore, projection onto the boundary becomes an important option. But, projection in higher than 3 dimensional space is not possible with standard vector algebra: the cross-product is not defined.

Methods & Results

We describe a technique which employs Clifford algebra to perform projection in an arbitrary number of dimensions. Clifford algebra describes a manipulation of vectors that incorporates the concepts of addition, subtraction, multiplication, and division. Thereby, vectors may be operated on like scalars forming a true algebra.

We tested our approach on a phantom containing inserts of calcium, gadolinium, iodine, gold nanoparticles and mixtures of pairs thereof. Images were acquired on a prototype photon counting CT scanner under a range of threshold combinations. Comparisons of the accuracy of different threshold combinations versus ground truth are presented.

Conclusion

Material decomposition is possible with three or more materials and four or more energy thresholds using Clifford algebra projection to mitigate noise. In particular, projection is useful for the visualization of individual voxels in material maps since it is unclear how one might render negative contributions of a material.

Clinical Relevance

Dual Energy CT is finally starting to become accepted as clinical routine. If PCCT is to make this leap someday, the techniques described in our paper will be necessary.

Figures and tables

Figure 1: Two energy/ two material decomposition. The composite "brown" material is computed to be a combination of the "green" material and "red" materials. b) Due to noise, them arterial under study falls *outside* the boundary of possible material combinations. It may then be projected onto the closest point on the boundary.

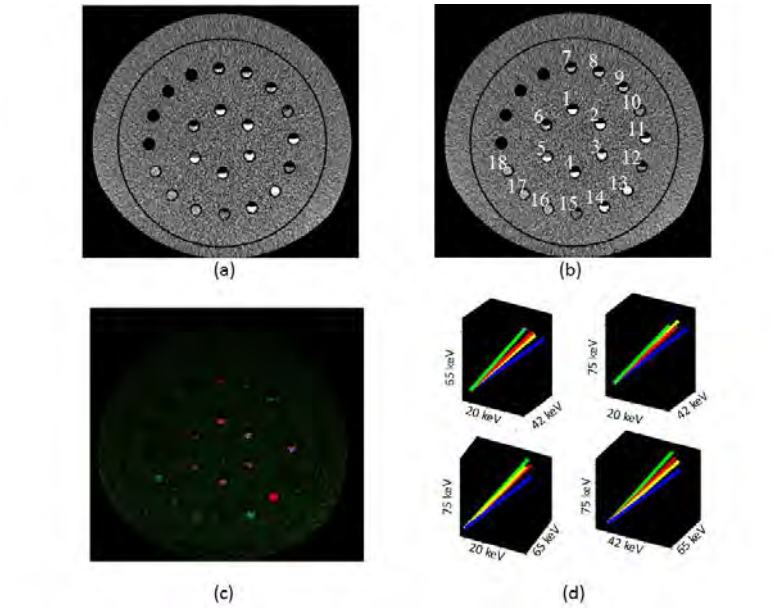

Figure 6: Phantom experiments for threshold combination (20,42,65,75) keV. a) CT image of the phantom acquired using a 75 keV threshold. b) Map of agents and their mixtures with respect to insert positions listed in Table 1. c) Material decomposition results rendered as: iodine (red), gold (green), calcium (blue), and gadolinium (yellow). d) Normalized 4D scatter plot of archetypical materials shown as four 3D projections of length 1.

	Calcium	Iodine	Gadolinium	Gold	Solvent (PBS)
1	50%	50%			
2	50%			50%	
3		50%		50%	
4	50%		50%		
5	50%				50%
6		50%			50%
7		50%	50%		
8			50%	50%	
9				50%	50%
10			50%		50%
11	100%				
12			100%		
13		100%			
14				100%	
15					100%
16				40%	
17				40%	
18				40%	

Table1: Concentrations of the basis materials in the 18 phantom inserts.

Self-gated dynamic contrast enhanced (DCE) MRI with compressed sensing acceleration to quantify permeability in the aortic root of atherosclerotic mice

Alison Pruzan[1], Arthi Sridhar[1], Chris Faries[1], Raphael J Soler [1, 5], Gustav J Strijkers[1,2,3], Claudia Calcagno[1,2]
[1] Translational and Molecular Imaging Institute, Icahn School of Medicine at Mount Sinai, New York, NY, United States, [2]Department of Radiology, Icahn School of Medicine at Mount Sinai, New York, NY, United States, [3]Department of Biomedical Engineering and Physics, Academic Medical Center, Amsterdam, The Netherlands, Netherlands, [5]Department of Vascular and Endovascular Surgery, Hôpital de la Timone, APHM, Marseille

Introduction: Atherosclerosis, a chronic inflammatory disease, is the cause of myocardial infarction and stroke.[1] Atherosclerotic plaques, which are prone to rupture, are characterized by inflammation, accompanied by endothelial permeability and endothelial dysfunction. Various studies have sought to investigate the relationship between endothelial permeability and specific cellular, genetic, and molecular pathways, yet many aspects of the atherosclerotic cascade must be further explored. For example, delayed enhancement (DE) and dynamic contrast enhanced (DCE) magnetic resonance imaging (MRI) have previously been applied in atherosclerotic patients[2] and rabbits[3-4] to quantify plaque permeability. The mouse is an ideal model to study the inflamed atherosclerotic plaque in the aortic root, since molecular and cellular assays are well established in mice. Furthermore, the root is the ideal area to focus on because atherosclerotic plaques form regularly and consistently in this location due to high blood flow velocity as well as increased turbulence compared to other blood vessels. But, because of small size, high blood flow speeds, and the fast heart rate of the mouse, imaging of the mouse aortic root is challenging. The goal of this study is to investigate the in vivo quantification of atherosclerotic plaque permeability by developing a DE and DCE-MRI protocol suitable to image the small mouse aortic root.

Methods:
Study Design: 38 8 weeks old ApoE -/- female mice were used for this study and kept on a high fat diet for increasing amount of time. At each time point (every 28 days), we imaged and sacrificed a group of six mice (groups 1 to 5) and imaged repeatedly a longitudinal group of eight mice (group 6). The longitudinal group (G6) was the only group that will be scanned during every time point. See Figure 1 for an overview of the study design.

Imaging Protocol and Analysis: A novel self-gated fast low angle shot (FLASH) sequence was applied to overcome the described challenges in DE and DCE-MRI of the mouse aortic root[5-7]. Using this acquisition, ApoE -/- atherosclerotic mice were imaged on a 7T pre-clinical MR scanner using a 35 mm volume coil for signal reception. Before imaging, we inserted a tail vein catheter into the mouse. Mice were then anesthetized with isoflurane and moved to the MRI scanner. We then acquired scout images to locate the aortic root. Afterwards, self-gated DCE-MRI was acquired continuously for 32 minutes. After the first 8 minutes, 0.3 mmol/Kg of Gd-DTPA was injected manually through the tail vein. Pre and post-contrast self-gated images were also acquired to calculate enhancement ratio in the mouse aortic root using delayed enhancement imaging. For each pre and post-contrast acquisition, a region of interest (ROI) encompassing the aortic root was selected in any cardiac frame where the inner and outer vessel wall contours were clearly visible. An ROI was also drawn in the noise for each traced cardiac frame, taking care to select artifacts void areas. Signal-to-noise ratio (SNR) before and after contrast agent injection were calculated. Enhancement was evaluated by dividing the post-contrast SNR by the pre-contrast SNR. Difference in enhancement between mice of different ages was evaluated using either paired or unpaired parametric tests, when appropriate.

Results: Here we present preliminary result of the analysis of DE MRI in mice scanned at baseline and end of study. This includes mice in groups 1 and 5 (Figure 1), and mice in the longitudinal group (group 6, Figure 1). All mice in groups 1 and 5 were included, while 1 mouse from the longitudinal group was excluded from analysis, for a total of 19 mice analyzed, and 26 imaging sessions. The longitudinal group showed a significant increase in signal to noise ratio from 0 weeks to 16 week old atherosclerotic mice. There is also a significant increase in SNR among all mice as they age from 0 to 16 weeks.

Conclusion: Our preliminary results demonstrate that self-gated DE imaging of the mouse aortic root allows quantifying an increase in endothelial permeability during atherosclerosis progression. Analysis of DCE-MRI data is under-way, and may warrant a more accurate quantification of endothelial permeability in the mouse root.

Clinical Relevance: We are currently implementing DE and DCE-MRI of the mouse aortic root to facilitate the extraction of quantitative permeability indices in the vasculature of this animal model. These measures will be correlated with genetic, molecular and cellular assays in the root, and will serve as read-outs of plaque progression or regression after anti-atherosclerotic therapy.

References: 1. Virmani et al, J Am Coll Cardiol 2006; 2. Kerwin WS et al Circulation 2003; 3. Chen H Magn Reson Med 2012; 4. Calcagno C et al ATVB 2008; 5. Coolen BF et al Magn Reson Med 2013; 6. Den Adel B et al PLoS One 2013; 7. Motaal AG et al NMR in biomedicine 2012; 8. Lustig M et al Magn Reson Med 2007.

Figures and tables:

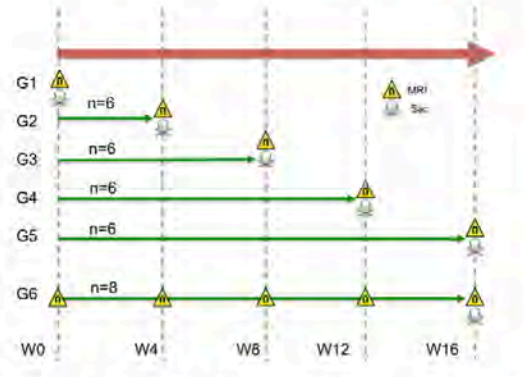

Figure 1: The dotted lines indicate the different time points from baseline (W0) until the last time point after 16 weeks of high fat diet (W16). The triangle and skull symbols show when a group is to be scanned or sacrificed respectively. The longitudinal group (G6) is the only group that will be scanned during every time point.

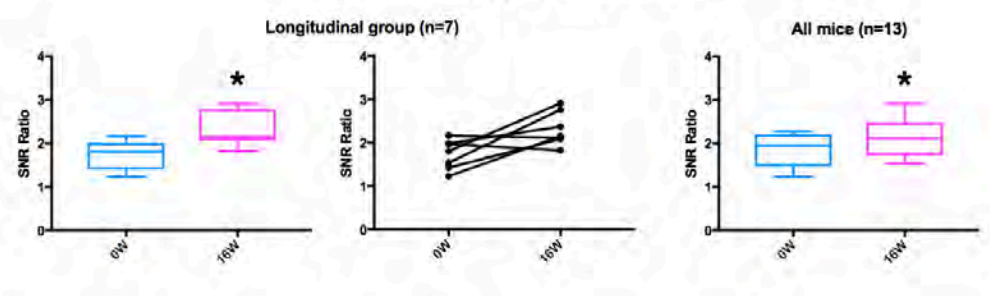

Figure 2: Figure 2 shows a significant increase in signal to noise ratio from 0 week to 16 week old atherosclerotic mice in the longitudinal group (n=7) as well as across the non-longitudinal group (n=13).

Scan-Rescan Repeatability of ^{18}F-FDG PET/MR Imaging of Vascular Inflammation

Philip M Robson[1], Patrick Brunner[2], Audrey Kauffman[1], Alison Pruzan[1], Marc R Dweck[3], Maria-Giovanna Trivieri[1,4], Ronan Abgral[5], Nicolas A. Karakatsanis[1], Venkatesh Mani[1], Emma Guttman[2], Zahi A Fayad[1,4]

[1]Translational and Molecular Imaging Institute, Icahn School of Medicine at Mount Sinai, New York, NY, United States.
[2]Department of Dermatology, Icahn School of Medicine at Mount Sinai, New York, NY, United States.
[3]British Heart Foundation/University Centre for Cardiovascular Science, University of Edinburgh, Edinburgh EH16 4SB, UK.
[4]Cardiovascular Institute, Icahn School of Medicine at Mount Sinai, New York, NY, United States.
[5]Department of Nuclear Medicine, European University of Brittany, EA3878 GETBO, IFR 148, CHRU Brest, Brest, France

Introduction

Non-invasive positron emission tomography (PET) of vascular inflammation and atherosclerotic plaque by identifying increased uptake of ^{18}F-fluordeoxuglucose (^{18}F-FDG) is a powerful tool for monitoring disease activity, progression, and its response to therapy. ^{18}F-FDG PET/computed tomography (PET/CT) of the aorta and carotid arteries has become widely used to assess changes in inflammation in clinical trials. However, the recent advent of hybrid PET/magnetic resonance (PET/MR) scanners has advantages for vascular imaging due to the reduction in radiation exposure and improved soft tissue contrast of MR compared to CT. Important for power analysis of clinical trials is an understanding of the scan-rescan repeatability of the PET measurement. While this has been studied for PET/CT [1], no data is currently available for vascular PET/MR imaging. In this study, we determine the scan-rescan repeatability of ^{18}F-FDG PET/MR in the aorta and carotid arteries.

Methods & Results

Methods: Ten patients were scanned twice within 14 days. Patients were administered 7 mCi of ^{18}F-FDG and were scanned 90 minutes later using a hybrid PET/MR (Biograph mMR, Siemens). ^{18}F-FDG activity was measured in the aorta and carotid arteries by drawing ROIs on fused time-of-flight MR angiograpahy in the carotids and axial single shot fast spin echo images in the aorta. Meaured standard uptake value (SUV) in the artery of interest was normlaized by SUV in either the jugular or superior vena cava to form target-to-background ratio (TBR). Repeatability was determined by Bland-Altman analysis of differences in TBR values between scan 1 and scan 2.

Results: Measurement repeatability was high, with a Bland-Altman repeatability of 10% when data were pooled over all arteries.

Conclusion

We have demonstrated the high degree of measurement repeatability for ^{18}F-FDG PET/MR imaging of vascular inflammation. This degree of repeatability is comparable to that found in a asimilar study for ^{18}F-FDG PET/CT indicating that the choice of PET/CT or PET/MR system does not impact the relaibility of vascular inflammation measurements.

Clinical Relevance

The ability to use PET/MR in clinical trials will reduce radiation exposure to patients compared to PET/CT, or conversely permit additional imaging exams in longitudinal clinical follow up or research studies without exceeding radiation limits, and permit the acquisition of complementary anatomical and functional information making use of the superior soft tissue contrast of MR compared to CT.

References: [1] Rudd JHF., Myers KS., Bansilal S., et al. (18)Fluorodeoxyglucose positron emission tomography imaging of atherosclerotic plaque inflammation is highly reproducible: implications for atherosclerosis therapy trials. J Am Coll Cardiol 2007;50(9):892–6.

Figures and tables

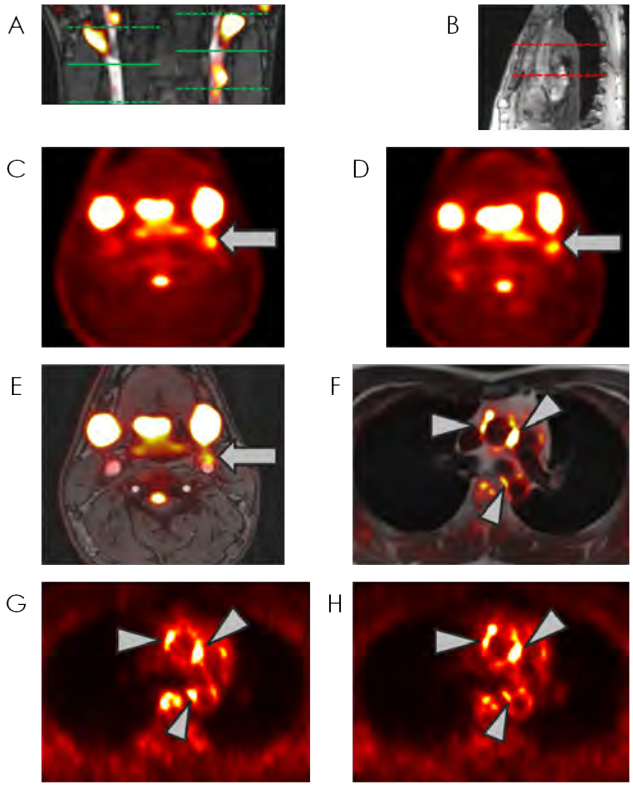

FIGURE 1: PET/MR images of the carotid arteries and aorta. TBR values were measured separately on left and right carotid arteries in a span 1 cm above and below the carotid bifurcation (green lines) as illustrated on fused PET and coronal time-of-flight MR (A); and between the aortic valve and aortic arch (red lines) shown on sagittal MR (B). ^{18}F-FDG activity was consistent between scan 1 (C) and scan 2 (D) in a vascular hotspot in the left carotid artery in this patient (arrow) identified by fusion of PET and axial time-of-flight MR images (E). ^{18}F-FDG activity was elevated in numerous hotspots in the ascending and descending aorta (arrowheads) identified on fused PET and axial MR (F) and show repeatable uptake pattern on scan 1 (G) and scan 2 (H).

Table 1: TBR values in each vessel segment for scan 1

	TBRmean	TBRmax	TBR-MDS
Aorta	1.36 (0.19)	2.22 (0.55)	2.44 (0.77)
LCC	1.45 (0.19)	1.79 (0.29)	1.97 (0.32)
RCC	1.47 (0.26)	1.79 (0.36)	1.94 (0.36)
Pooled	1.43 (0.21)	1.93 (0.45)	2.12 (0.56)

Mean (standard deviation) TBR values. There were no significant differences in any of the TBR values between any pair of vessel types. LCC = Left common carotid, RCC = Right common carotid artery. TBRmean and TBRmax calculated for the mean and max SUV in the vessel segment; TBR-MDS is the TBRmax in the most diseased segment (3 slices around the highest TBR max in the whole vessel segment).

Table 2: Bland-Altman Coefficient of Repeatability

	TBRmean		TBRmax		TBR-MDS	
	Bias	Coefficient of Repeatability	Bias	Coefficient of Repeatability	Bias	Coefficient of Repeatability
Aorta	0.020 (0.091)	0.18 (6%)	0.036 (0.379)	0.76 (16%)	-0.045 (0.429)	0.86 (14%)
LCC	-0.006 (0.159)	0.32 (10%)	0.002 (0.190)	0.38 (9%)	-0.094 (0.265)	0.53 (11%)
RCC	-0.029 (0.081)	0.16 (5%)	-0.027 (0.099)	0.20 (5%)	-0.134 (0.193)	0.39 (10%)
Pooled	-0.005 (0.114)	0.23 (7%)	0.003 (0.244)	0.49 (10%)	-0.091 (0.303)	0.61 (12%)

TBR bias is given as mean (standard deviation), while coefficient of repeatability is given as a 95% confidence interval of TBR values, and as a fractional change determined from log-transformed analysis in parentheses. LCC = Left common carotid, RCC = Right common carotid artery.

MR-Based Respiratory and Cardiac Motion Corrected ^{18}F-FDG PET/MR

Philip M. Robson, PhD[1], Nicolas A. Karakatsanis, PhD[1], Maria Giovanna Trivieri, MD, PhD[1,2], Ronan Abgral, MD, PhD[3], Marc R. Dweck, MD, PhD[4], Jason C. Kovacic, MD, PhD[2], Zahi A. Fayad, PhD[1,2]
[1]Translational and Molecular Imaging Institute, Icahn School of Medicine at Mount Sinai, New York, NY
[2]Department of Cardiology, Icahn School of Medicine at Mount Sinai, New York, NY
[3]Department of Nuclear Medicine, European University of Brittany, EA3878 GETBO, IFR 148, CHRU Brest, Brest, France
[4]British Heart Foundation/University Centre for Cardiovascular Science, University of Edinburgh, Edinburgh EH16 4SB, UK

Introduction

Hybrid PET/MR has significant potential in cardiac applications such as cardiac sarcoidpsos [1] where both functional changes and the pattern of injury can be determined by cine- and late gadolinium enhancement (LGE)-MRI and the activity of disease can be measured by ^{18}F-FDG PET. Substantial respiratory and cardiac motion during PET data acquisition can cause both image blurring and diminution of target-to-background ratios, potentially reducing sensitivity for detection of disease. In this work we utilize 3D temporally resolved MRI to estimate respiratory and cardiac motion and apply this to correct for motion in double-gated PET data.

Methods & Results

A patient with proven extra-cardiac sarcoidosis and suspected cardiac involvement underwent hybrid PET/MR (Biograph mMR, Siemens) to test the feasibility of MR-based motion correction of the PET data. ^{18}F-FDG (10 mCi) was administered. List-mode PET data acquisition began after 30 minutes and lasted for 60 minutes.

***Motion Estimation**:* Respiratory motion was estimated using a free-breathing 3D golden-angle radial VIBE sequence (based Siemens WIP-793, [2]) with 3x3x3mm-resolution acquired over 6-7min. Spokes were divided into 4 respiratory frames and reconstructed in Matlab using NUFFT algorithms [3]. Motion vector fields (MVFs) between respiratory frames were then estimated using freely-available non-rigid registration algorithms [4]. Cardiac motion was estimated separately using a similar acquisition but with higher resolution of 1.4x1.4x1.4mm and a coronal slab just covering the heart. Imaging proceeded during infusion of 0.2mmol/kg gadolinium-based contrast agent (Multihance, Bracco) to improve contrast. k-Space data for each respiratory phase were phase-shifted to correct for the head-to-foot displacement. Corrected k-space data were then sorted into 3 cardiac frames based on recorded ECG trigger timing (0-300, 300-600, 600-inf ms after trigger) before offline reconstruction. MVFs between cardiac frames were then estimated.

***Motion Corrected PET Reconstruction**:* Motion correction of PET data employed the reconstruct-transform-average (RTA) approach. Double-gated list-mode PET data were reconstructed offline (e7tools, Siemens) using attenuation maps shifted according to measured MVFs. All cardiac frames were transformed to the end expiration position using corresponding MVFs. Then each respiratory-motion-corrected cardiac frame was transformed to the diastolic position using the cardiac MVFs before averaging all frames. A flow diagram of the steps involved is given in **Fig. 1**.

Results: Focal hotspots of ^{18}F-FDG uptake were observed in the myocardium indicating active cardiac sarcoidosis. Application of the proposed MR-based motion correction scheme showed qualitative improvement in image quality by reducing blurring of the myocardium, particularly in the lateral wall, and by increasing contrast between the hotspots and the diffuse uptake in the rest of the myocardium (**Fig. 2**). TBR values of the strongest hotspot increased from 5.6 to 5.9.

Conclusion

We have demonstrated the feasibility of MR-based correction of respiratory and cardiac motion for improved imaging of myocardial PET hotspots in ^{18}F-FDG-PET imaging of patients with cardiac sarcoidosis.

Clinical Relevance

Correction of respiratory and cardiac motion will enable PET/MR of the heart and coronary arteries to become increasingly robust and accurate, improving the detectability of disease activity, risk stratification based on quantitative thresholds, and allowing robust longitudinal analysis in both clinical follow up and research studies.

References: [1] Abgral R et al. JACC Cardiovasc Imaging. 2016 Jun 29. pii: S1936-878X. [2] Grimm R et al. Med Image Comput Comput Assist Interv 2013;16:17-24. [3] Fessler J et al. Image reconstruction toolbox, University of Michigan (https://web.eecs.umich.edu/~fessler/code/index.html). [4] Buerger C et al. Medical Image Analysis, 15:551-564, 2011. [5] Robson PM et al. Proc ISMRM 2016 p2545

Figures and tables

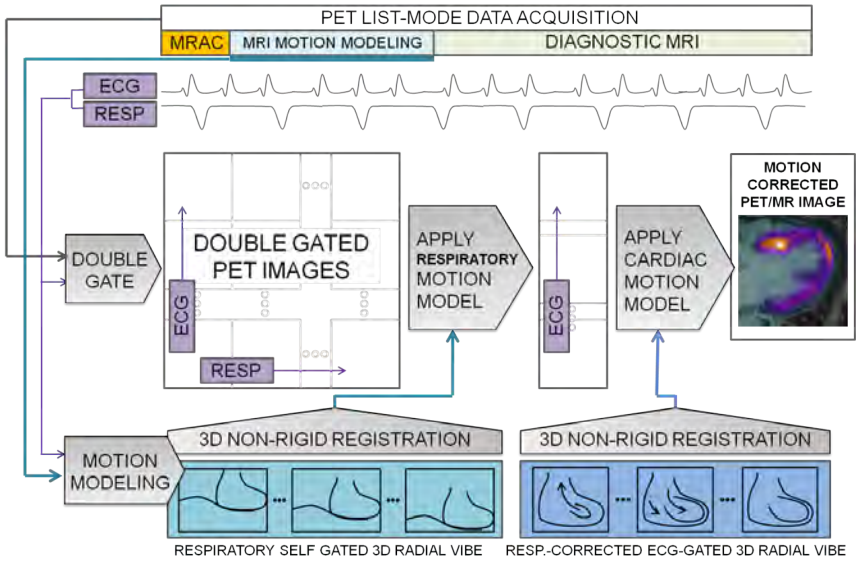

Figure 1: Flow diagram of MR-based motion correction. Temporal variation in PET data counts and ECG triggers are used to double-sort list-mode PET data into respiratory and cardiac frames respectively. Free-breathing 3D golden angle radial-VIBE MRI is used to find motion models for respiratory and cardiac motion. A reconstruct-transform-average (RTA) approach is then used to combine double-gated PET images into a single motion corrected PET/MR image.

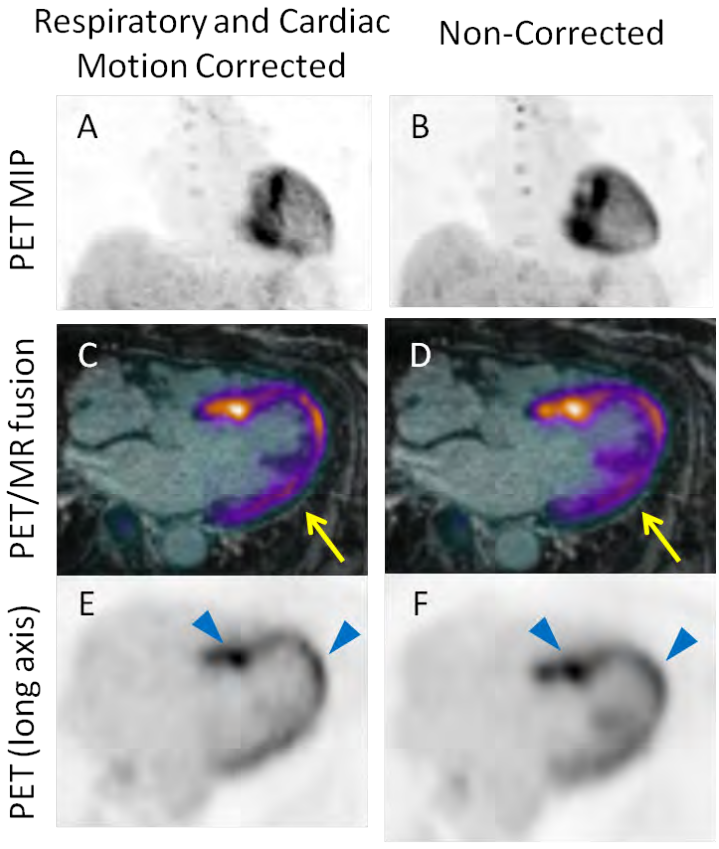

Figure 2: 18F-FDG PET images in a patient with cardiac sarcoidosis. Maximum intensity projections (A-B), long-axis PET fusion with contrast-enhanced MR (C-D), and long-axis PET in the same plane (E-F). Application of the proposed MR-based respiratory and cardiac motion correction to the PET data (left) reduces blurring of the myocardium compared to PET images without correction (right), particularly in the lateral wall (arrow), and increases the contrast of hotspots compared to diffuse uptake in the myocardium (arrowheads).

Endothelial permeability in the aortic root of atherosclerotic mice: quantification using 3-dimensional, black blood, self-gated T1 mapping

Raphael J. Soler[1,2], Alison Pruzan[1], Christopher Faries[1], Arthi Sridhar[1], Gustav Strijkers[1,3], Zahi A. Fayad[1], Claudia Calcagno[1]
[1]*Translational and Molecular Imaging Institute, Icahn School of Medicine at Mount Sinai, New York, NY, United States*
[2]*Department of Vascular and Endovascular Surgery, Hopital de la Timone, APHM, Marseille, France*
[3]*Academic Medical Center, Amsterdam, Netherlands*

Introduction. Atherosclerotic plaques prone to rupture are characterized by endothelial dysfunction and increased permeability (1–4). The aortic root is a vascular territory where permeable plaques form consistently and reliably. However, morphological and quantitative parametric imaging of the mouse aortic root is very challenging, due to the small dimensions, rapid blood flow through the valves, and high heart rate. Conventional prospectively ECG triggered and respiratory-gated acquisitions are lengthy, and therefore not well suited to capture the rapid dynamics of contrast agent extravasation in the vessel wall. Here we present a method to reliably quantify contrast agent uptake and endothelial permeability in the mouse aortic root based on a 3 dimensional, self-gated low angle shot (FLASH) sequence with black blood imaging for improved vessel wall delineation (5–7).

Methods. *Animals*: Two groups of mice were used for this study. A group of 8 weeks old ApoE$^{-/-}$ female mice (n=3) was fed a high-fat diet for 28 weeks (HFD group). A group of wild type mice (n=3) was used as control (WT group). *Image acquisition*: Mice were imaged using a pre-clinical 7T MRI scanner (BioSpec, Bruker, Billerica, MA, USA). After self-gated localizer scans to identify the mouse aortic root, a pre-contrast T1 map was acquired using a variable flip angle 3D self-gated FLASH sequence. Acquired flip angles were 2, 5, 8, 11 and 14 degrees. Following acquisition of the last flip angle, 0.3 mmol/kg of Gd-DTPA – a contrast agent commonly used in the clinics – was injected through a catheter placed in the mouse tail vein at the rate of 0.5 ml/s using a programmable syringe pump. Immediately afterwards, 5 data points after injection were acquired using the same 3D self-gated FLASH sequence, using the same imaging parameters used for pre-contrast T1 mapping, and a flip angle of 14 degrees for all time points. *Image analysis*: For each mouse, inner and outer vessel wall contours were drawn for the slice corresponding to the aortic root, and two consecutive slide above (on each cardiac frame). Contours were drawn separately on all 3D self-gated FLASH acquisitions (5 pre-contrast and 5 post-contrast), and average vessel wall region of interest (ROI) signal was calculated. One muscle ROI was also drawn on all pre-contrast and post-contrast acquisitions. Pre-contrast T1 was calculated from the 5 pre-contrast acquisitions using the DESPOT1 analysis, previously described (8). Post-contrast T1 values were then derived and converted to contrast agent concentration. Concentration curves in the vessel wall and muscle were analyzed by calculating the area under the concentration curve (AUC). *Ex vivo analysis*: Transmission electron microscopy was used after mice euthanasia to analyze endothelial junction and measure gaps between endothelial cells, as an *ex vivo* measure of endothelial permeability.

Results. Three mice were included each group. Average corrected pre-contrast T1 values for atherosclerotic mice were 604 +/- 20 ms, while they were 1027 +/- 329 ms for wild type mice (p=0.007). Ratios of area under the concentration curve for atherosclerotic mice were 11.1 +/- 2.223, while they were 2.652 +/- 0.1443 for wild type mice (p=0.008) indicating higher accumulation of contrast agent in the root of atherosclerotic mice. Transmission electron microscopy showed a disjunction of endothelial barrier with an increase of the gap junction between endothelial cells while junctions were normal in the WT group.

Conclusion. Our results indicate that 3D, self-gated, black blood T1 mapping with a FLASH sequence may be suitable for quantification of endothelial permeability in the mouse aortic root. We are currently conducting studies to further validate this technique and assess the capabilities of this technique to track plaque progression over time, and regression after therapy.

Clinical Relevance

Quantification of vascular wall permeability may be a viable marker of endothelial dysfunction and inflammation in atherosclerotic patient and is a potential surrogate marker of cardiovascular risk, or plaque regression upon intervention.

References. 1. Phinikaridou A et al, Circulation. 2012; 2. Phinikaridou A et al, J Am Heart Assoc. 2013; 3. Lavin Bet al, Circ Cardiovasc Imaging. 2015; 4. Bar A et al, NMR Biomed. 2016; 5. Coolen BFet al, J Cardiovasc Magn Reson Off J Soc Cardiovasc Magn Reson. 2011; 6. Coolen BF et al, NMR Biomed. 2011; 7. Vandoorne K et al, NMR Biomed. 2016; 8. Deoni SCL et al, Magn Reson Med. 2003

Figures and tables

Figure 1. Imaging protocol

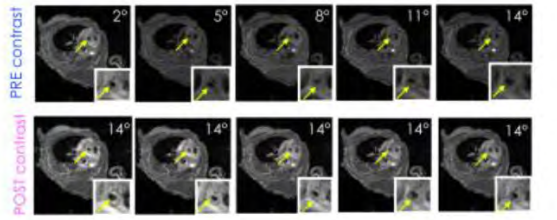

Figure 2. Pre and post contrast 3D, black blood, self-gated images used for T1 mapping. Yellow arrow indicates magnified aortic root

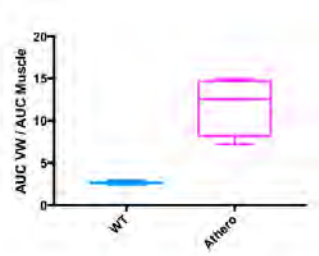

Figure 3. AUC ratio between vessel wall and muscle permeability

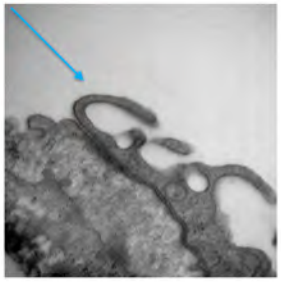

Figure 4. Transmission electron microscopy: endothelial barrier disjunction in atherosclerotic mice

Taking it to heart: Examining relations between chronic psychological stress, amygdalar activity, and cardiovascular inflammation using PET/MR imaging

Chloe J. E. Solomon[1,2], Cheuk Y. Tang[2], Claudia Calcagno[2], Venkatesh Mani[2], Abigail Collins[3], James W. Murrough[3], Ahmed A. Tawakol[4], Zahi A. Fayad[2]
[1]Graduate School of Biomedical Sciences, Icahn School of Medicine at Mount Sinai
[2]Translational and Molecular Imaging Institute, Mount Sinai Hospital
[3]Psychiatry, Icahn School of Medicine at Mount Sinai
[4]Cardiology, Massachusetts General Hospital

Introduction
Chronic psychological stress is associated with increased risk of cardiovascular disease. Innovative PET/MR imaging technology offers the opportunity to examine physiological manifestations of stress in the brain and its effects on arterial inflammation in humans.

Methods & Results
In a cross-sectional pilot study, individuals diagnosed with chronic posttraumatic stress disorder were recruited and underwent ^{18}F-fluorodeoxyglucose PET/MRI at Mount Sinai Hospital. We analyzed relationships between perceived stress (Perceived Stress Scale), amygdalar activity, and arterial inflammation.

Data analyzed from 13 subjects (median age 49 years [IQR 45.7-56.7]) diagnosed with chronic PTSD showed amygdalar activity significantly associated with arterial inflammation ($r=0.70$; $p=0.0083$). Perceived stress was also associated with amygdalar activity ($r=0.56$; $p=0.0485$), arterial inflammation ($r=0.59$; $p=0.0345$), and C-reactive protein ($r=0.83$; $p=0.0210$).

Conclusion
This pilot study is among the first to link regional brain activity to cardiovascular inflammation. These findings provide novel insights into the mechanism through which chronic psychological stress can lead to cardiovascular disease in humans.

Clinical Relevance
PET/MRI could be used to screen for atherosclerosis in severely and chronically stressed individuals, and may help measure treatment response to stress-reduction therapies.

Figures and tables

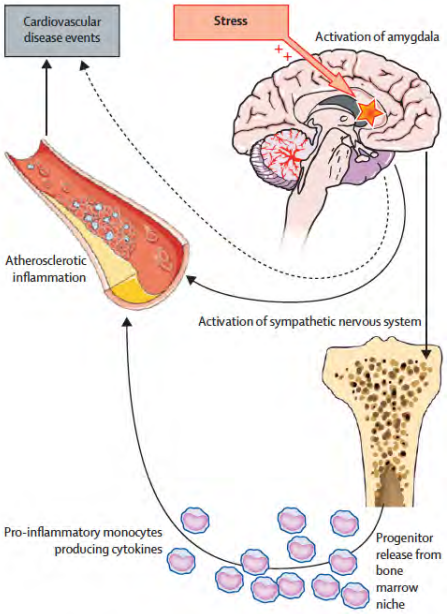

Figure: Based on gross epidemiological and emerging preclinical research, our research team believes we can use PET/MR fusion imaging to visualize and validate physiological connections between chronic psychological stress and atherosclerosis. Amygdalar activity (responsible for immediate emotional reactions, particularly to stressful stimuli) and hematopoetic tissue activity (immune response) are likely mediators in this physiological mechanism.

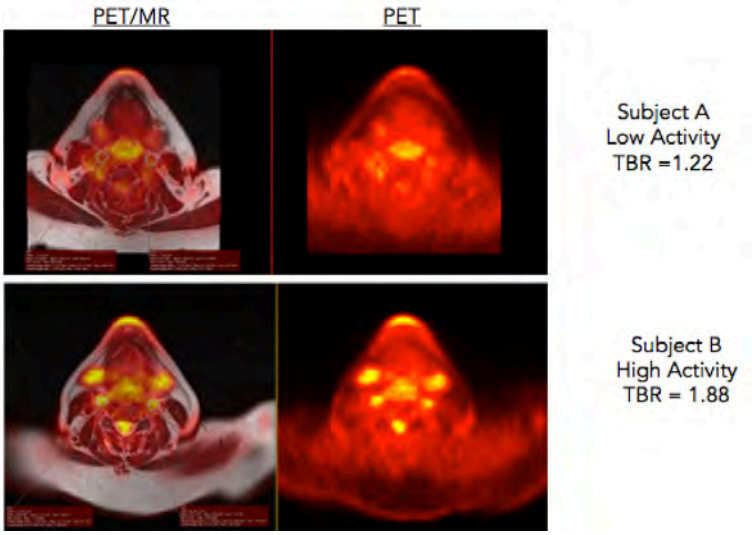

Figure: Hybrid PET/MR pictures of axial slices of the neck from two posttraumatic stress disorder (PTSD) subjects (Subjects A and B). Right side: ^{18}F-FDG PET scans showing metabolic activity and inflammation in carotid arteries. Left side: ^{18}F-FDG PET scans registered onto MRI scan acquired simultaneously to PET. MRI provides anatomical and resolution. Subject B visibly and quantitatively has more inflammation in carotid arteries.

The systematic evaluation of endothelial permeability in the aortic root of atherosclerotic mice (review)

Arthi Sridhar[1], Alison Pruzan[1], Chris Faries[1], Raphael J Soler[1,5], Zahi A. Fayad[1],Gustav J Strijkers[1,2,3], Claudia Calcagno[1,2]

[1]Translational and Molecular Imaging Institute, Icahn School of Medicine at Mount Sinai, New York, NY, United States, [2]Department of Radiology, Icahn School of Medicine at Mount Sinai, New York, NY, United States, [3]Department of Biomedical Engineering and Physics, Academic Medical Center, Amsterdam, The Netherlands, Netherlands, [5]Department of Vascular and Endovascular Surgery, Hôpital de la Timone, APHM, Marseille

Introduction

Atherosclerosis is a chronic disease of vascular endothelial dysfunction and remains as one of the leading causes of death in the Western civilization. [1] In this abstract we present a method to accurately localize the aortic root in atherosclerotic mice, and to investigate endothelial permeability in this mouse model. Our method is based on a self-gated, fast low angle shot (FLASH) MRI sequence with injection of a gadolinium based contrast agent.

Methods & Results

Imaging Protocol: The position of the heart is first localized. An apparent short axis view is planned approximately perpendicular to the septum, mid left ventricle, using a coronal view. A two chamber view is then planned from the short axis, by positioning a slice parallel to the septum, in the left ventricle. The positioning was confirmed on the coronal view of the first localize scan. To obtain a four chamber view of the heart, the two chamber view is used as a reference and a slice passing through the mitral valve and the aortic root is planned. See Figure 1 for an overview of the planning of these scans. Positioning is also checked on the apparent short-axis image used as reference. The last two localizer scans are used to specifically localise the aortic root. The four chamber view is loaded as reference and a slice passing through the apex of the heart and the aortic root is planned and cross checked on the apparent short axis. In the last localizer scan, a slice passing through the aortic root and parallel to it is positioned on the last scan. See Figure 2 for images of these scans. A pre-contrast, self-gated FLASH scan with 256 repetitions (duration ~10 minutes) is planned in the same orientation. Immediately after, this acquisition was repeated using 800 repetitions to perform dynamic contrast enhanced MRI (duration ~32 minutes) for quantification of endothelial permeability. 8 minutes into the imaging, the 0.3 mmol/kg of Gd-DTPA were manually injected. After completion of the DCE-MRI sequence, the pre-contrast scan was repeated, to allow for calculation of delayed enhancement.

Results: Using this method we are able to successfully reconstruct cardiac phases and dynamic frames from all acquisitions. Signal enhancement can be clearly seen after contrast injection and can be visualised in comparison to the pre contrast acquisitions. This pattern of temporal enhancement is consistent across mice. See Figure 3 for a sample of the results obtained.

Conclusion

Our results demonstrate how to efficiently image the mouse aortic root with a gadolinium based MR contrast agent to study endothelial permeability using DCE-MRI and delayed enhancement imaging.

Clinical Relevance

Genetically engineered atherosclerotic mice are an important animal model for cardiovascular research. A quantitative, non-invasive method to quantify endothelial permeability will help us gain a better understanding of plaque physiology, and, by being able to track disease regression after therapeutic intervention, it may aid in the development of new therapeutics for atherosclerosis.

Figures and tables

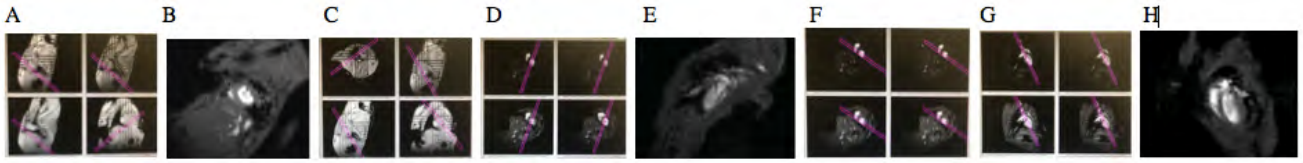

Figure 1: Represents examples of various localizer scans. **A-** Planning of the apparent short axis on the multislice scan. **B-** Apparent short axis of the heart. **C-** Planning of the two chamber view of the heart on the multslice scan. **D-** Planning of the two chamber view of the heart on the apparent short axis scan. **E-** two chamber view of the heart. **F-** Planning of the four chamber view on the apparent short axis scan. **G-** Planning of the four chamber vie w on the two chamber view scan. **H-** Four chamber view of the heart

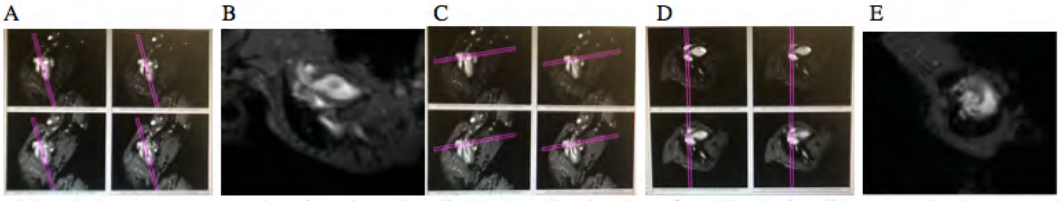

Figure 2: Represents examples of the last 2 localizer scans. **A-** Planning of the scan to localise the aortic root. **B-** Localizer scan visualising the aortic root of the heart. **C-** Planning the aortic root in the four chamber view. **D-** Planning the aortic root on the localizer scan. **E-** Aortic root of the hear

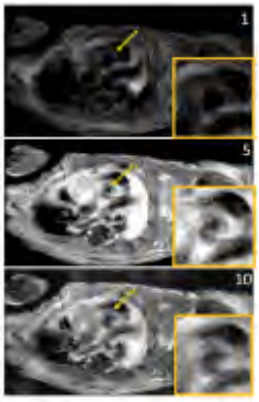

Figure 3: Represents the results. Compressed sensing reconstructionof self-gatedDCE-MRI of the aortic root. Orangearrow and zoomed-in inserts, aortic root.Numbers indicate temporal frames. The same cardiac phase was depicted

References

1. Phinikaridou A[1], Andia ME, Protti A, Indermuehle A, Shah A, Smith A, Warley A, Botnar RM.
Noninvasive Magnetic Resonance Imaging Evaluation of Endothelial Permeability in Murine Atherosclerosis Using an Albumin-Binding Contrast Agent Circulation. 2012 Aug 7;126(6):707-19.
2. Davignon J, Ganz P. Role of endothelial dysfunction in atherosclerosis. Circulation. 2004; 109:III27–III32.
3. Makowski MR[1], Wiethoff AJ, Blume U, Cuello F, Warley A, Jansen CH, Nagel E, Razavi R, Onthank DC, Cesati RR, Marber MS, Schaeffter T, Smith A, Robinson SP, Botnar RM.
Assessment of atherosclerotic plaque burden with an elastin-specific magnetic resonance contrast agent. Nat Med. 2011 Mar;17(3):383-8
4. Lauffer RB, Parmelee DJ, Ouellet HS, Dolan RP, Sajiki H, Scott DM, Bernard PJ, Buchanan EM, Ong KY, Tyeklar Z, Midelfort KS, McMurry TJ, Walovitch RC. MS-325: a small-molecule vascular imaging agent for magnetic resonance imaging. Acad Radiol. 1996;3(suppl 2):S356–S358.
5. Caravan P, Cloutier NJ, Greenfield MT, McDermid SA, Dunham SU, Bulte JW, Amedio JC Jr, Looby RJ, Supkowski RM, Horrocks WD Jr, McMurry TJ, Lauffer RB. The interaction of MS-325 with human serum albumin and its effect on proton relaxation rates. J Am Chem Soc. 2002;124:3152–

Mice Aortic Arch Information from Micro MRI and Ultrasound Imaging System

Yu Zhou[1], Johnny Ng[1], Victoria Wang[1], Lazar Fleysher[1],Chen Yang[1],Claudia Calcagno[1], Cheuk Ying Tang[1]
Ajit Magadum[2], Lior Zangi[2]
Translational and Molecular Imaging Institute[1] at Mount Sinai Medical Center
Cardiovascular Research Center[2] at Mount Sinai Medical Center

Introduction

Aortic arch syndromes are most often associated with trauma, blood clots, or malformations that develop before birth. The arteries' defects result in abnormal blood flow to the head, neck, or arms. The aortic arch structural and hemodynamic information can be detected by the combination of MRI and Ultrasound imaging.

Methods & Results

MR imaging: 7T Bruker Biospec 7/30 Micro MRI System (NCRR S10RRR02541-01).
Coil: Rapid-V-35 mm. **Protocols:** 1) TriPilot_Mulit_ig. 2) IG_FLASH_ CINE (Bright blood and self-gated).
Four chambers view and aortic arch image shows on **Figure 1**. It gives us a general cardiac and aortic arch structural imaging information.
Aortic valves closed image shows on **Figure 2**. It displays the aortic root information and structure of aortic arch when the aortic valves closed.
Aortic valves opened image shows on **Figure 3**. It displays the aortic root information and structure of aortic arch when the aortic valves opened.
Ultrasound imaging: Vevo 2100 Micro Ultrasound Instrument and scanning system (NCRR S10-RR027678-01).
A transducer, with 30M Hz and 24Hz, was used for scanning mice.
Figure 4 displays the aortic root and arch when the aortic valves closed.
Figure 5 displays the aortic root and arch when the aortic valves opened.
Figure 6 shows the mouse's aortic arch Color Doppler Blood Flow image for detecting hemodynamic information.
Figure 7 is the M mode image for detecting **systolic and diastolic aortic arch diameters.** The cross-sectional area (CSA) of the respective site is from $CSA = D2 \times \pi/4 = D2 \times 0.785$. D is the aortic diameter.
The ascending and descending aortic blood flow velocity information show on the Figure 8 and Figure 9. The measurements display: Velocity-time integral (VTI) - Integral of the velocity over time.
Mean Velocity – The mean (average) of measured spectral shifts over a specific period within a given sample site. Mean Gradient, Peak Gradient and Peak Velocity. So, we can also get the
Ascending or Descending Stroke Volume (ASV or DSV):
A**SV = CSA × VTI or DSV = CSA × VTI**

Conclusion

The combination of MRI and Ultrasound imaging will provide more aortic arch information for medical research.

Clinical Relevance

These will be helpful for clinical diagnosis, surgery plan and treatment.

Figures and tables

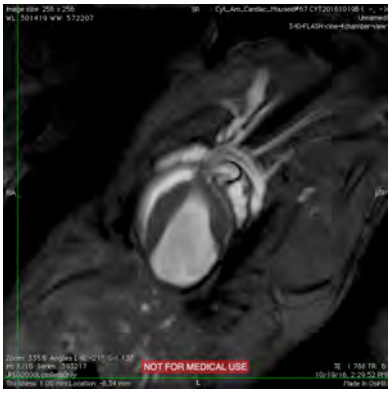

Figure 1

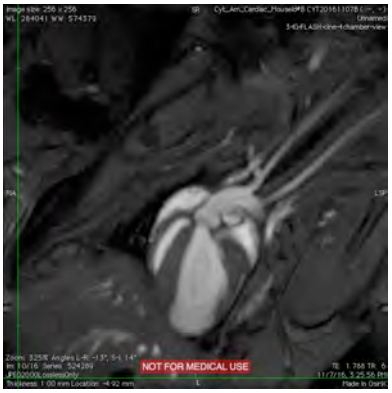

Figure 2

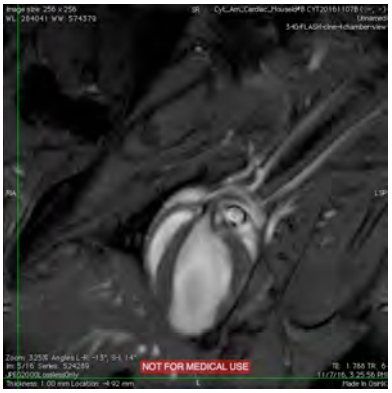

Figure 3

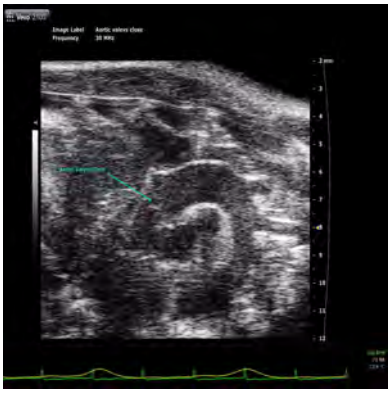

Figure 4

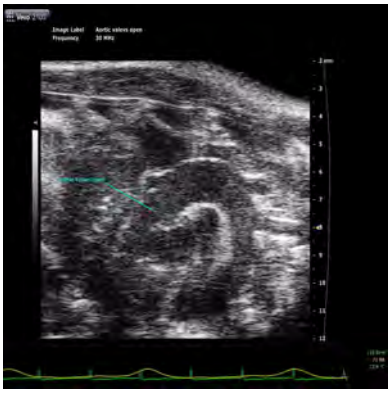

Figure 5

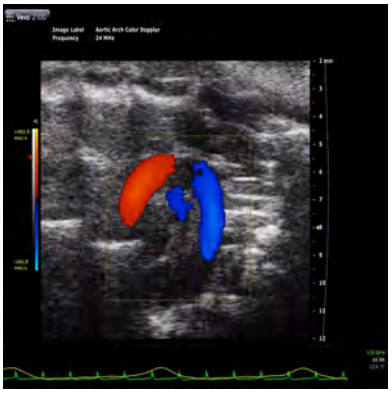

Figure 6

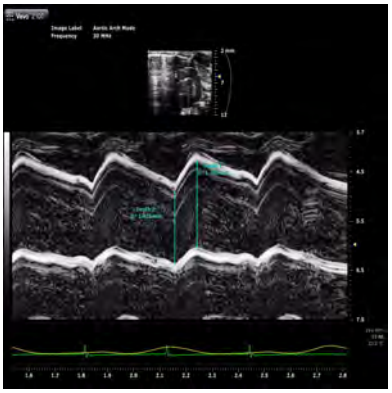

Figure 7

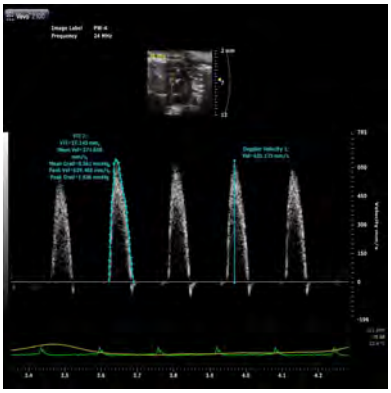

Figure 8

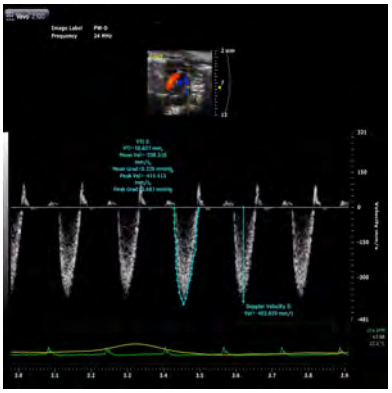

Figure 9

Nanomedicine

A systematic comparison of clinically viable nanomedicines targeting HMG-CoA reductase to resolve inflammatory atherosclerosis

Amr Alaarg[a,b,c], Max L. Senders[b,d], Aida Varela-Moreira[c,e], Carlos Pérez-Medina[b], Yiming Zhao[b], Jun Tang[f], Francois Fay[b], Thomas Reiner[f,g], Zahi A. Fayad[b], Wim E. Hennink[c], Josbert M. Metselaar[a,h], Willem J.M. Mulder[b,d*], Gert Storm[a,c*]

[a] Department of Biomaterials Science and Technology, MIRA Institute for Biomedical Technology and Technical Medicine, University of Twente, Enschede 7500 AE, The Netherlands
[b] Translational and Molecular Imaging Institute, Icahn School of Medicine at Mount Sinai, New York, New York 10029, USA
[c] Department of Pharmaceutics, Utrecht Institute for Pharmaceutical Sciences, Utrecht University, Utrecht 3584 CG, The Netherlands
[d] Department of Medical Biochemistry, Academic Medical Center, 1105 AZ Amsterdam, The Netherlands
[e] Department of Clinical Chemistry and Haematology, University Medical Centre Utrecht, Utrecht, 3584 CX, The Netherlands
[f] Department of Radiology, Memorial Sloan Kettering Cancer Center, New York, New York 10065, USA
[g] Department of Radiology, Weill Cornell Medical College, New York, NY 10065, USA
[h] Department of Experimental Molecular Imaging, University Clinic and Helmholtz Institute for Biomedical Engineering, RWTH Aachen University, Aachen 52074, Germany

Introduction

Atherosclerosis is a leading cause of worldwide morbidity and mortality whose management could benefit from novel targeted therapeutics. Nanoparticles are emerging as targeted drug delivery systems in chronic inflammatory disorders. To optimally exploit nanomedicines, understanding their biological behavior is critical for further development of clinically relevant, efficacious nanotherapeutics intended to reduce plaque inflammation

Methods & Results

Three clinically relevant nanomedicines, i.e., high-density lipoprotein ([S]-HDL), polymeric micelles ([S]-PM), and liposomes ([S]-LIP), that are loaded with the HMG-CoA reductase inhibitor simvastatin [S], were evaluated in the apolipoprotein E-deficient (Apoe−/−) mouse model of atherosclerosis. We systematically employed quantitative techniques, including in vivo positron emission tomography imaging, gamma counting, and flow cytometry to evaluate the biodistribution, nanomedicines' uptake by plaque-associated macrophages/monocytes, and their efficacy to reduce macrophage burden in atherosclerotic plaques.

The three formulations demonstrated distinct biological behavior in Apoe−/− mice. While [S]-PM and [S]-LIP possessed longer circulation half-lives, [S]-PM and [S]-HDL showed preferential uptake by plaque macrophages. Moreover, [S]-PM displayed the highest efficacy in reducing macrophage burden in advanced atherosclerotic plaques.

Conclusion

Our results emphasize the importance of a thorough understanding of nanomedicines' biological performance, ranging from the whole body to the target cells, as well their physicochemical stability. This allows a rational nanomaterials' repurposing to different disease contexts, facilitating expanding the nanomedicine horizon.

Clinical Relevance

Designing and developing novel targeted therapeutics can circumvent the side effects of small molecule drugs while maximizing their therapeutic activities. We hereby develop novel simvastatin platforms with paying careful attention to the drug-nanocarrier. Comparing the different platforms will provide insights about which platform can be taken for further pharmaceutical development under Good Manufacturing Practice (GMP) conditions, for validation in atherosclerotic patients with advanced inflammatory plaques.

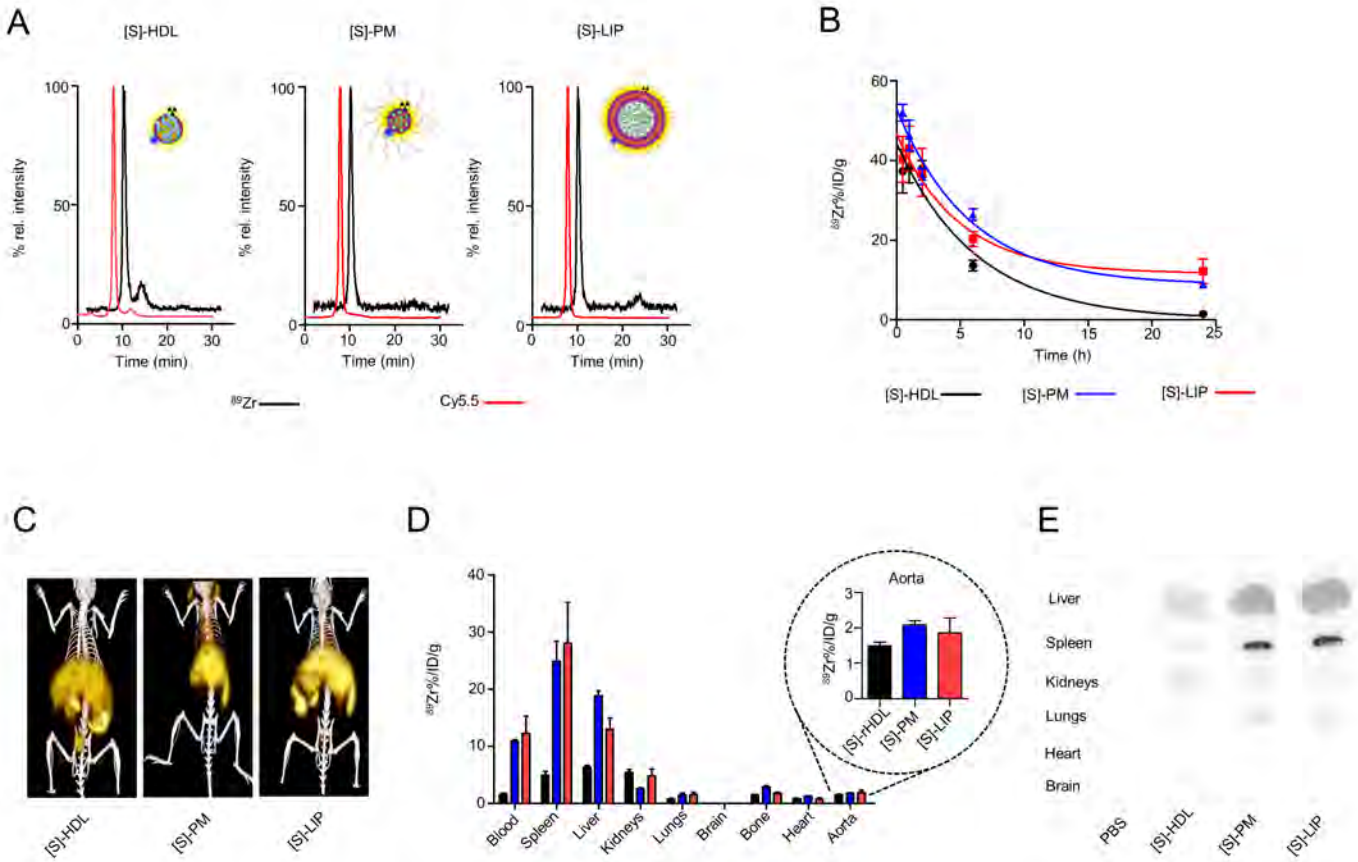

Figure 1. Dual labeling of [S]-nanomedicines, and their pharmacokinetics and biodistribution evaluation in *Apoe*$^{-/-}$ mice with advanced atherosclerosis. (A) Size exclusion chromatograms (B) Blood time-activity curves for the different ^{89}Zr-labeled [S]-nanomedicines (C) Three-dimensional rendering of PET/CT fusion images at 24 h after injection (D) Quantitative assessment of radioactivity distribution in selected tissues (E) Autoradiography images of selected tissues 24 h after injection. %ID/g, percentage injected dose per gram of tissue.

Real-time monitoring of nanoparticle formation via FRET imaging

Brenda L Sanchez-Gaytan,[1] François Fay,[1] Sjoerd Hak,[2] Amr Alaarg,[1] Zahi A Fayad,[1] Carlos Pérez-Medina,[1] Willem JM Mulder,[1] and Yiming Zhao[1]
1. Translational and Molecular Imaging Institute, Icahn School of Medicine at Mount Sinai, New York, NY, USA.
2. Department of Circulation and Medical Imaging, Norwegian University of Science and Technology, Trondheim, Norway.

Introduction
Understanding the formation process of nanoparticles is of the utmost importance to improve their design and production. This especially holds true for self-assembled nanoparticles whose formation processes have been largely overlooked. Herein, we present a new technology that integrates a microfluidic-based nanoparticle synthesis method and Förster resonance energy transfer (FRET) microscopy imaging to visualize nanoparticle self-assembly in real time.[1]

Methods & Results
NP synthesis was carried out in a staggered herringbone micromixer (SHM) and imaged using laser scanning confocal microscopy. For the first application, the nanoemulsion was self-assembled while mixing in the SHM PBS and a solution in ethanol containing medium chain triglycerides (MCT), phospholipids, and a pair of lipophilic dyes (DiO and DiI). When the nanoemulsion was formed, both dyes were confined in the emulsion and FRET was generated. The visualization of the chip showed that the nanoemulsion forms instantaneously mainly at the organic/water interphases and quickly diffuses into the aqueous phase. By increasing the flow rate, more FRET signal from nanoemulsion formation was observed and less signal from organic phase remained, indicating a better mixing of two phases.
For the second application, drug loading on polymeric NPs was investigated [2]. For this, a solution in acetonitrile containing an amphiphilic block-copolymer labeled with Cy3.5 and model drugs labeled with Cy5 was mixed with PBS. FRET was observed when the model drugs were loaded in the NP, which occurs only when the drugs are hydrophobic. Thus, no FRET signal was detected with hydrophilic model drugs, indicating a poor loading inside the NP. For the third application, we visualized the formation of nanocrystal-core high-density lipoprotein [3]. In this case, lipid coated quantum dots (QDs) were mixed with Cy5-labeled apolipoprotein-A1. At the moment of the NP formation, the emission spectra dramatically changed indicating a protein wrapping around the QD core.

Conclusion
Through combining microfluidic-based synthesis techniques and FRET imaging we were able to achieve real-time imaging of the SANPs formation. We envision this technique would facilitate the research on NP synthesis, mechanism and functionalization studies.

1. Zhao Y. et al, Angewandte Chemie, **2017**, 129, 1521-3757.
2. Zhao Y. et al, Nat. Commun. **2016**, 7, 11221
3. Skajaa T. et al, Nano Lett. **2010**, 10, 5131.

Figures and tables

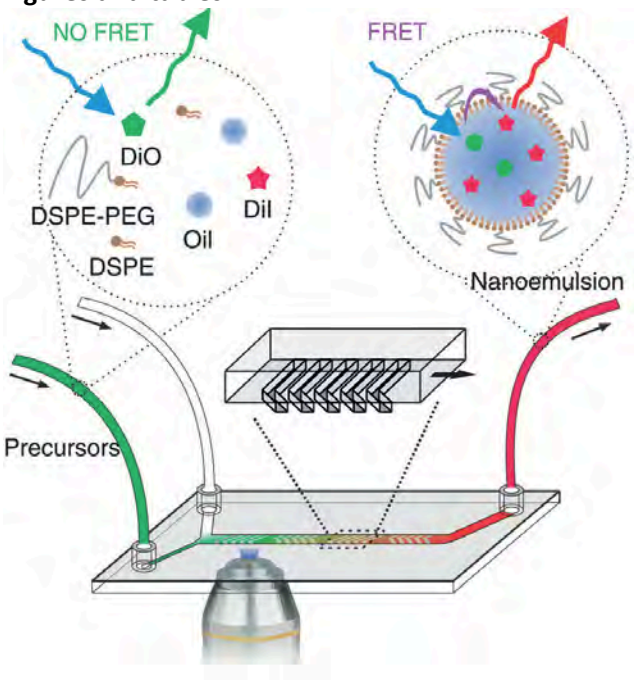

Real-time nanoemulsion formation monitoring using a fluorescence microscope on a microfluidics device.

A "natural" antibody fragment targeting malondialdehyde-acetaldehyde epitopes detects clinically-relevant atherothrombotic lesions and allows non-invasive PET/MR imaging in experimental models

Max L. Senders[1,2], MD; Xuchu Que[3], PhD; Young Seok Cho[4,5], MD, PhD; Calvin Yeang[5], MD, PhD; Hannah Groenen, BS[1]; Francois Fay[1], PhD; Claudia Calcagno[1], MD, PhD; Simone Green[5], BS, Phuong Miu[5], BS, Mark E. Lobatto[6], MD, PhD; Thomas Reiner[7,8], PhD; Zahi A. Fayad[1], PhD; Joseph L. Witztum[3], MD; Willem J.M. Mulder[1,2], PhD; Carlos Pérez-Medina[1*], PhD; and Sotirios Tsimikas[5*], MD

[1]Translational and Molecular Imaging Institute, Icahn School of Medicine at Mount Sinai, New York, NY, USA
[2]Department of Medical Biochemistry, Academic Medical Center, Amsterdam, The Netherlands
[3]Division of Endocrinology and Metabolism, Department of Medicine, University of California, La Jolla, San Diego, CA, USA.
[4]Seoul National University College of Medicine, Seoul National University Bundang Hospital
[5]Division of Cardiovascular Diseases, Sulpizio Cardiovascular Center, Department of Medicine, University of California, La Jolla, San Diego, CA, USA.
[6]Department of Radiology, Academic Medical Center, Amsterdam, The Netherlands
[7]Department of Radiology, Memorial Sloan Kettering Cancer Center, New York, NY, USA
[8]Department of Radiology, Weill Cornell Medical College, New York, NY, USA

Background. Current non-invasive imaging techniques do not adequately characterize the atherosclerotic plaque and lack sensitivity for predicting future cardiovascular events.

Methods and Results. A "natural" Fab antibody fragment, LA25, was generated from human fetal cord blood. Pharmacokinetics, biodistribution and plaque specificity studies were performed with Zirconium-89 (^{89}Zr) labeled LA25 in atherosclerotic mice. In rabbits, ^{89}Zr-LA25 was used as an imaging probe in combination with an integrated clinical positron emission tomography coupled with magnetic resonance system (PET/MR) and compared with the non-specific ^{89}Zr-LA24. ^{18}F-FDG-PET, T2-weighted MRI (T2W-MRI) and dynamic contrast enhanced MRI (DCE-MRI) were used to evaluate vessel wall inflammation, lesion area and plaque neovascularization, respectively. *Ex vivo* evaluation of biodistribution was performed with gamma counting, while macrophage content and plaque specificity were assessed by near infrared fluorescence (NIRF) and autoradiography, respectively. Dynamic PET imaging data revealed an increase in renal signal over time (**figure 1A, B**) indicative of renal clearance. The weighted half-life in atherosclerotic rabbits was 2.2 h for ^{89}Zr-LA25, 1.2 h for ^{89}Zr-LA24 (**figure 1C**). After 28 hours post injection, rabbits were sacrificed and radioactivity counting revealed a significantly higher aortic uptake for ^{89}Zr-LA25 compared to ^{89}Zr-LA24 in rabbits with atherosclerosis, 0.022 ± 0.003 vs. 0.006 ± 0.001 %ID/g, *P<0.0001* (**Figure 1D**). Autoradiography revealed a heterogeneous radioactivity distribution pattern in the ^{89}Zr-LA25 group in contrast with a homogenous distribution for ^{89}Zr-LA24 (**Figure 1E**). PET/MR imaging 24 hours after injection of ^{89}Zr-LA25 showed significantly higher uptake in the abdominal aorta of atherosclerotic rabbits compared to non-atherosclerotic controls (**figure 2A**, *P=0.0003*), confirmed by *ex vivo* gamma counting (*P<0.0001*) and autoradiography (**figure 2B)**. T2-weighted MRI, ^{18}F-FDG-PET, DCE-MRI, and NIRF signals were also significantly higher in atherosclerotic rabbit aortas compared to controls (**figure 2C-F**).

Conclusion. ^{89}Zr-LA25 is a novel PET/MRI radiotracer that non-invasively images inflamed and neovascularized atherosclerotic lesions, and may allow phenotyping of human atherosclerotic plaques at risk of rupture. Moreover, this radiotracer could further help characterize the process of atherosclerosis and ultimately serve as a biomarker in a clinical setting to evaluate therapeutic interventions

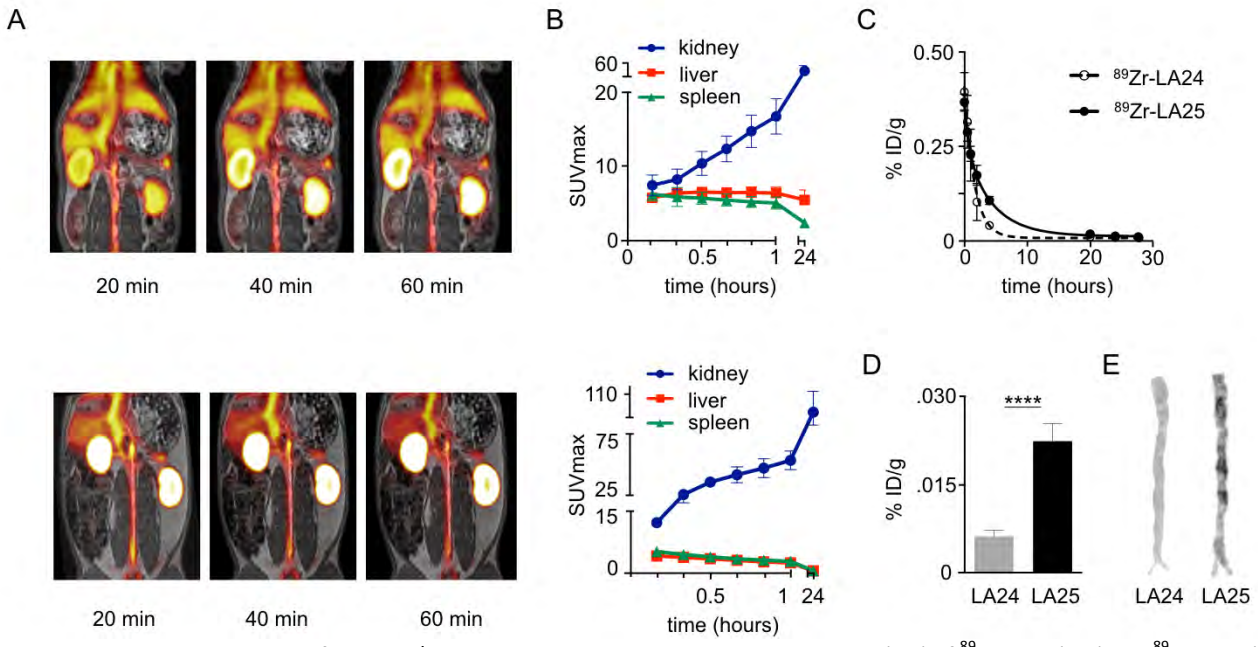

Figure 1. Representative coronal fused PET/MR images at 20, 40 and 60 min post injection (p.i.) of ^{89}Zr-LA25 (top) and ^{89}Zr-LA24 (bottom) (A). Radioactivity quantification in major organs in atherosclerotic rabbits based on PET/MR imaging (10-60 min), and 24 hours p.i. (B). SUV = Standardized uptake values. Pharmacokinetics in atherosclerotic rabbits for ^{89}Zr-LA24 and ^{89}Zr-LA25, with half-lives of 1.1 and 2.2 hours, respectively (C). *Ex vivo* radioactivity concentration (D) and autoradiography (E) for ^{89}Zr-LA24 and ^{89}Zr-LA25 in aortas from rabbits with atherosclerosis 28 hours post injection. ****$P<0.0001$.

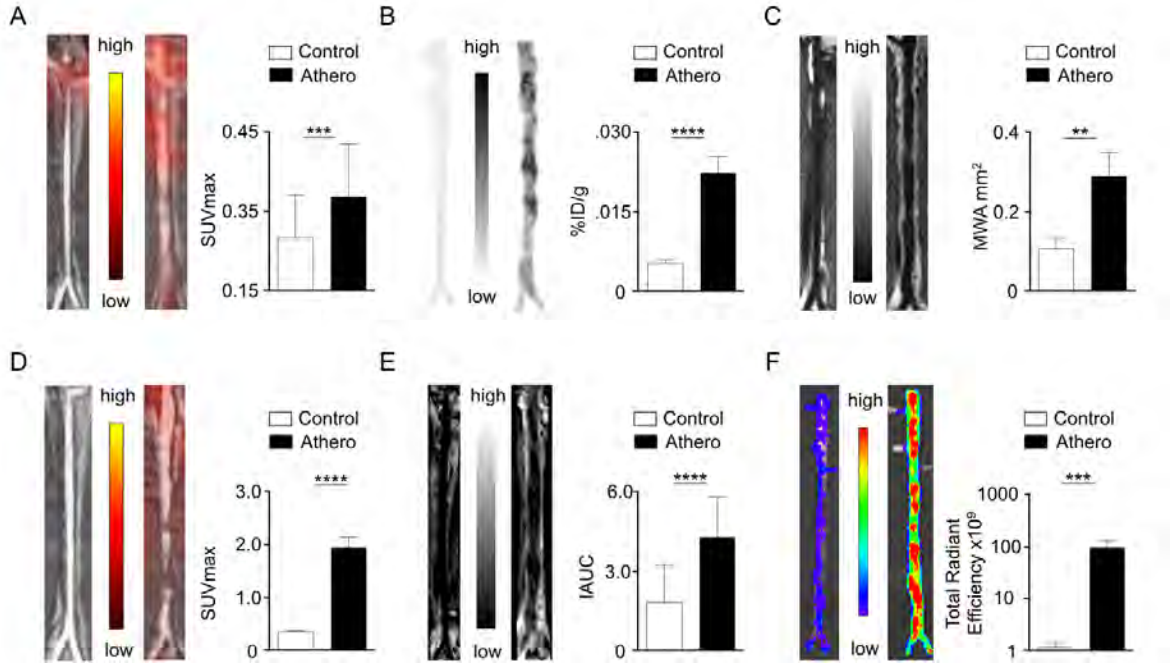

Figure 2. Representative coronal aortic fused PET/MR imaging 24 hours post injection. (A), autoradiography and gamma counting (whole aortas) 28 hours p.i. of ^{89}Zr-LA25 (B). MR T2-weighted imaging (C), ^{18}F-FDG PET/MRI (D), DCE-MRI (E) and Cy5-rHDL near infrared fluorescence imaging (F) in healthy control (white) and atherosclerotic (black) rabbit abdominal aortas. ****$P<0.0001$.

Nanobody-facilitated multiparametric PET/MRI phenotyping of experimental atherosclerosis

Max L. Senders[1,2], MD, Sophie Hernot[3], PhD, Giuseppe Carlucci[4], PhD, Jan van de Voort[1], Francois Fay[1,5], PhD, Claudia Calcagno[1], MD, PhD, Amr Alaarg[1], Yiming Zhao[1], PhD, Seigo Ishino[1], PhD, Anna Palmisano[1], MD, Jun Tang[6], PhD, Gilles Boeykens[1], Samantha Baxter[1], Laura Zendman[1], Mark Lobatto[7], MD, PhD, Nicolas A. Karakatsanis[1], PhD, Philip M. Robson[1], PhD, Thomas Reiner[6,8], PhD, Jason S. Lewis[6,8], PhD, Zahi A. Fayad[1], PhD, Nick Devoogdt[3], PhD, Willem J. Mulder[1,2,*], PhD, Carlos Pérez-Medina[1,*], PhD

[1] Translational and Molecular Imaging Institute, Icahn School of Medicine at Mount Sinai, New York, NY 10029, USA
[2] Department of Medical Biochemistry, Academic Medical Center, 1105 AZ Amsterdam, The Netherlands
[3] In vivo Cellular and Molecular Imaging laboratory, Vrije Universiteit Brussel, 1090, Brussels, Belgium
[4] Bernard and Irene Schwarz Center for Biomedical Imaging, New York University, New York, NY 10016, USA
[5] Department of Chemistry, York College of The City University of New York, New York, NY 11451, USA
[6] Department of Radiology, Memorial Sloan-Kettering Cancer Center, New York, NY 10065, USA
[7] Department of Radiology, Academic Medical Center, Amsterdam, The Netherlands
[8] Department of Radiology, Weill Cornell Medical College, New York, NY 10065, USA

Rationale – Atherosclerosis is the main underlying cause of cardiovascular disease. Although imaging has aided significantly to the non-invasive detection of disease burden, its usefulness is still hampered by limited specificity.

Objective – To develop an integrative PET/MR imaging protocol for accurate atherosclerotic plaque phenotyping, simultaneously probing different key processes that drive atherosclerosis progression.

Methods and Results – We screened a minilibrary of nanobody radiotracers targeted to different markers of atherosclerosis progression, including vascular cell adhesion molecule-1 (VCAM), lectin-like oxidized low-density lipoprotein receptor 1 (LOX-1), and macrophage mannose receptor (MMR). In *Apoe*$^{-/-}$ mice, PET/CT imaging revealed the radiotracers ^{64}Cu-VCAM and ^{64}Cu-MMR to be taken up in aortic roots and arches, sites typically rich in atherosclerotic lesions (**figure 1A**). In parallel, extensive biodistribution studies in *Apoe*$^{-/-}$ mice disclosed high kidney uptake for all nanobodies, indicative of fast renal elimination, but with varying organ/tissue distribution patterns (**figure 1B**). Autoradiography revealed intense depositions at sites of atherosclerosis in *Apoe*$^{-/-}$ mice while a control, non-targeted nanobody, showed a low and homogeneous distribution pattern (**figure 1C**). Whole-aorta radioactivity quantification showed the highest value for ^{64}Cu-MMR, so did the aorta-to-blood ratio (**figure 1D**). Radiotracer cellular specificity in the plaque was assessed in sections taken from the aortic root of mice injected with the radiolabeled Nbs (**figure 1E**). The MMR nanobody radiotracer was rationally selected for an ensuing translational study using Gallium-68 (^{68}Ga). Several processes relevant to atherosclerosis progression, including inflammation (^{18}F-FDG), macrophage burden (^{68}Ga-MMR), microcalcifications (^{18}F sodium fluoride; ^{18}F-NaF) (**figure 2A**), vessel wall area (T2W-MRI) and neovascularization (DCE-MRI) (**figure 2B**) were probed by integrative clinical PET/MRI in rabbits. A significant increase in aortic radioactivity was discovered by PET/MRI for the three radiotracers, as well as for plaque burden and permeability in rabbits with atherosclerotic lesions induced by balloon angioplasties in combination with an 8-months high-fat diet (8HFD) compared to healthy controls fed a chow diet (CD). Moreover, cardiac PET indicated a significantly higher aorta-to-heart ratio for ^{18}F-NaF compared to ^{18}F-FDG (**figure 2C**).

Conclusions – We have developed a PET/MR imaging procedure that allows simultaneous non-invasive evaluation of different key processes that drive atherosclerosis progression. This may ultimately aid in the development and evaluation of novel (nano)therapeutics.

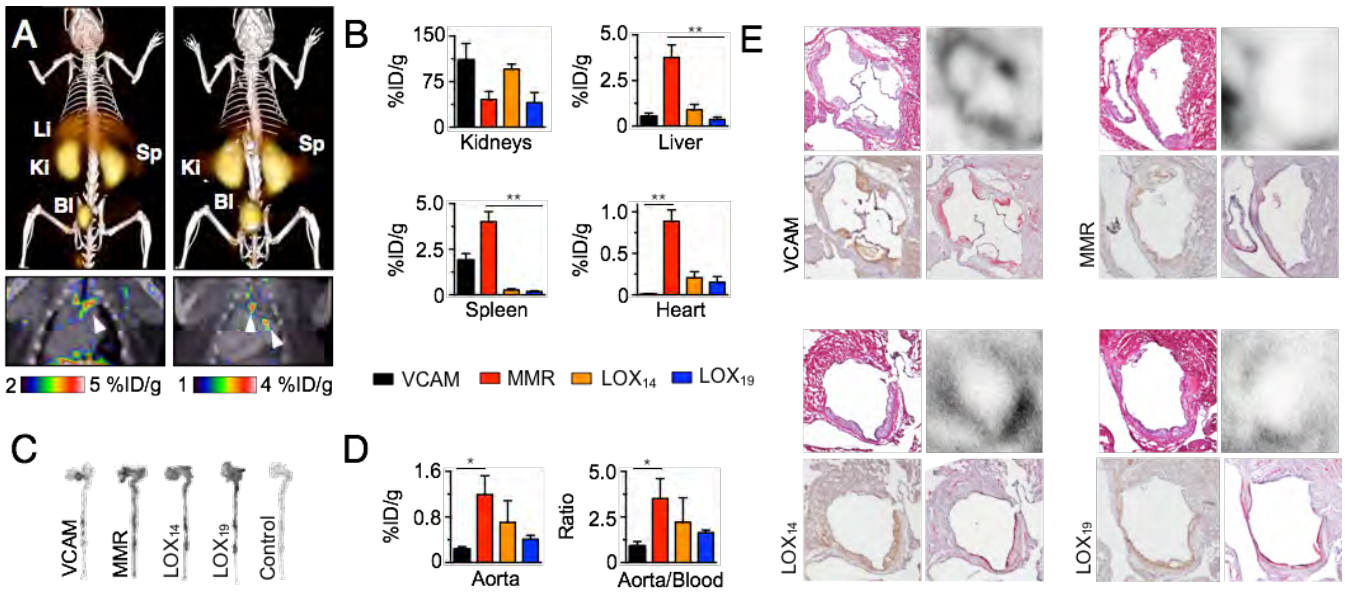

Figure 1. Representative fused PET/CT images 1 h post-injection ^{64}Cu-VCAM (*left*) and ^{64}Cu-MMR (*right*), arrows indicate enhanced uptake at the aortic arch and root, typical sites of atherosclerotic lesions in *Apoe*$^{-/-}$ *mice* (a). Biodistribtuon in *Apoe*$^{-/-}$ *mice* 3 h p.i. (b). Autoradiography and gamma counting of *Apoe*$^{-/-}$ mouse aortas (c, d).). Luminal autoradiography of aortic roots in *Apoe*$^{-/-}$ *mice* with adjacent sections stained with H&E, CD31 (endothelial cells) and CD68 (macrophages) (e). ** P < 0.05, ** P < 0.01.*

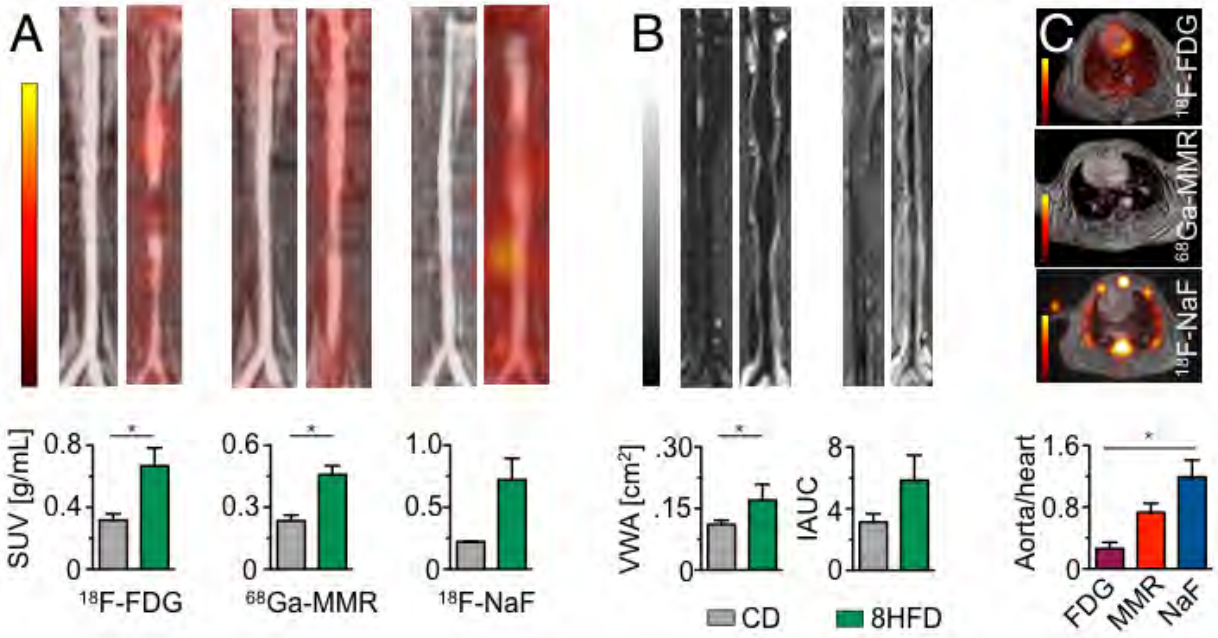

Figure 2. Representative coronal aortic fused PET/MR imaging 3 h post injection of ^{18}F-FDG (*left*), 2 h p.i. ^{68}Ga-MMR (*middle*) and 1.5 h after ^{18}F-NaF injection (*right*) in healthy control (grey) and atherosclerotic (green) rabbit abdominal aortas (a), and MR T2-weighted imaging (*left*) and DCE-MRI (*right*) (b). Cardiac PET/MR images of respective tracers (c). ** P < 0.05*.

Neuroimaging

First Application of 7T Structural, Vascular, and Diffusion Imaging to Trigeminal Neuralgia: Preliminary Results in Patients

Judy Alper[1,2], Rafael O'Halloran[3], Bradley Delman[3], Raj Shrivastava[4], Priti Balchandani[1,3]
1. Translational and Molecular Imaging Institute, Icahn School of Medicine at Mount Sinai; 2. Department of Biomedical Engineering, City College of New York; 3. Department of Radiology, ISMMS; 4. Department of Neurosurgery, Mount Sinai Medical Center

Introduction: Trigeminal neuralgia (TN) is a chronic condition characterized by severe, shock-like or burning facial pain (NINDS). The physiological mechanisms leading to pain symptoms in TN are not fully understood and may result from a range of possible conditions.[1-4] Among suspected causes for TN is neurovascular compression (NVC)[5], in which a vessel compresses the nerve. Conventional clinical imaging often fails to identify an abnormality (such as NVC) due to the lack of resolution to detect small vessels or quantify nerve integrity. 7T-MRI is capable of visualizing the anatomy in high detail, but to date has not been used for diagnostic imaging of TN.[6] In this study, we report first results of imaging TN with high-resolution 7T structural-MRI, vascular-MRI, and diffusion-weighted-MRI (dMRI). Here we evaluated a multi-modal 7T-MRI protocol for visualization of the nerve and surrounding vessels in three TN patients and three controls.

Methods: Subjects: Three TN patients ages 31(M), 45(M), and 66(F) and three controls ages 22(F), 54(F), and 55(M) under an approved IRB protocol. **MRI:** Subjects underwent the 7T-MRI protocol listed in **Table 1**. They also underwent high-angular-resolved, simultaneous multi-slice dMRI (1.05mm isotropic resolution, 68 directions). We reduced artifacts in the brainstem region by performing localized B_0 shimming. dMRI images were corrected for distortions and registered to T1-weighted images. **Processing:** Fiber orientation distributions for tractography were obtained from the corrected diffusion-weighted images by spherical deconvolution. Tractography for visualization of the TN was performed using the iFOD2 algorithm implemented in MRTRIX3 using a seed placed in the TN. **Structural Measurements:** The cross sectional area (CSA) of the nerve was measured by drawing regions of interest (ROIs) in Osirix (Pixmeo, Switzerland), using high-resolution T1-weighted coronal images. CSA was measured for both left and right trigeminal nerves, with two ROIs drawn for each nerve: the first at the most posterior point where the nerve emerges from the brainstem pons and the second at the most anterior point as the nerve enters Meckel's cave. A schematic of the nerve is shown in **Figure 1**. The two ROI CSA values were averaged to obtain the mean CSA of the nerve. An asymmetry index (AI) was calculated by subtracting right from left and dividing by the average CSA. A group comparison of AI values was performed.

Results: The 7T images enabled high-resolution visualization of the nerve source and NVC by surrounding vessels, as shown in **Figure 2**. Structural abnormalities in the nerve were found in all three patients. 7T-MRI data was used with clinical standard of care imaging for treatment planning. Patients 1 and 2 had 1.5T MRI scans. Patient 3 had a 3T MRI scan. Clinical findings are described below:

Patient 1: The images indicated a vessel in close proximity to the left trigeminal nerve root entry zone (REZ), between the lateral body of pons and trigeminal nerve before coursing over the superior aspect of the nerve. 7T-MRI images are shown in **Figure 3**. **Patient 2:** The images showed a basilar proximity to the left trigeminal nerve. This is consistent with the patient's known history of left-sided TN. 7T-MRI altered the surgical course for this patient. **Patient 3:** The images indicated a suspected vascular encroachment on right trigeminal nerve. This patient received surgical treatment, specifically microvascular decompression, with relief of symptoms.

The structural imaging quantitative metrics performed are shown in **Table 2**. Qualitatively, asymmetry was observed in the trigeminal nerves of patients. We found initial quantitative differences, with an average AI of 0.403 for patients compared to 0.144 for controls. A t-test was performed, indicating a trend towards significance ($p\sim0.1$) and an effect size of approximately 2.

Discussion: We present the first application of 7T-MRI to visualize and elucidate TN pathophysiology for guidance of treatment. This study demonstrates the feasibility of utilizing 7T-MRI to reveal nerve anatomy and surrounding structures. 7T-MRI provided increased visualization of NVC at the REZ of the trigeminal nerve, which served to further corroborate preliminary low-field imaging in all three patients. In general, greater asymmetry in patients compared to controls was found in this preliminary sample with a high effect size. Asymmetry in TN patients may arise from nerve damage or edema,

resulting in opposing effects on the CSA of the nerve on the symptomatic side. Ongoing work is focused on validating these findings in a larger sample. Future work will focus on sequence development to distinguish arteries from veins, which is useful in pre-op planning and prognosis. Ultimately, multi-modal 7T-MRI could provide a powerful tool to enhance our understanding of TN pathophysiology and provide improved diagnosis and targeted treatments for TN.

Acknowledgements: This work was supported by National Institutes of Health under NCI R01 CA202911, and the Icahn School of Medicine Capital Campaign, Translational and Molecular Imaging Institute and Department of Radiology, Icahn School of Medicine at Mount Sinai.

References:

1. Lummel, N., et al., Diffusion tensor imaging of the trigeminal nerve in patients with trigeminal neuralgia due to multiple sclerosis. Neuroradiology, 2015. 57(3): p. 259-67.
2. Samadian, M., et al., Trigeminal Neuralgia Caused by Venous Angioma: A Case Report and Review of the Literature. World Neurosurg, 2015. 84(3): p. 860-4.
3. Isik, S., et al., Trigeminal Neuralgia Caused by Cerebellopontine Angle Arteriovenous Malformation Treated With Gamma Knife Radiosurgery. J Craniofac Surg, 2016. 27(1): p. e55-7.
4. Agrawal, S.M. and D.H. Kambalimath, Trigeminal neuralgia involving supraorbital and infraorbital nerves. Natl J Maxillofac Surg, 2010. 1(2): p. 179-82.
5. Pamir, M.N., et al., *Microvascular decompression in the surgical management of trigeminal neuralgia.* Neurosurg Rev, 1995. **18**(3): p. 163-7.
6. Alper, J., R.K. Shrivastava, and P. Balchandani, *Is There an MRI-Discernible Etiology for Trigeminal Neuralgia? A Structured Review.* World Neurosurgery, 2016.

Sequence	TE (ms)	TR (ms)	Resolution (mm)
T1-W MPRAGE	3.62	6000	0.70*0.70*0.70
T2 TSE	74	7500	0.40*0.40*1.20
TOF Angiography	5.58	18	0.35*0.26*0.40

Table 1. Research protocol for structural imaging scans performed at 7T.

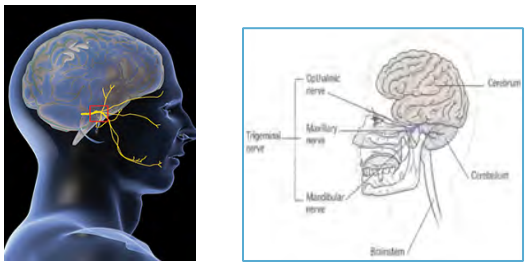

Figure 1. The trigeminal nerve is a paired nerve, in which each one of the pair supplies one side of the face. The trigeminal nerve emerges from the brainstem, enters Meckel's cave, and then splits into three main branches across the face. (Neurosurgery Notes, The Carolina Neurosurgery & Spine Associates website and David Darling Encyclopedia)

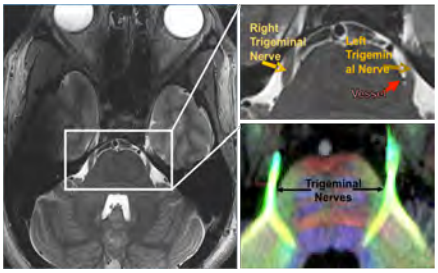

Figure 2. 7T TN patient scan showing tiny vessel pressing on trigeminal nerve and nerve tractography.

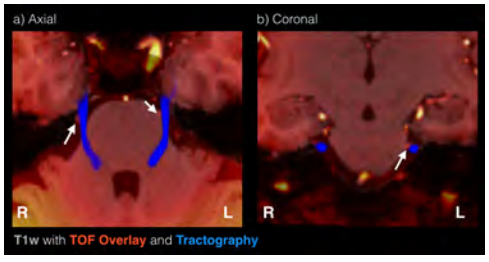

Figure 3. 7T fused T1-weighted images with tractography showing trigeminal nerve (blue) and TOF showing adjacent vessels (red, with white arrows pointing to them) on Patient 1.

Subject	ROI1 CSA (mm^2)	ROI2 CSA (mm^2)	Mean CSA (mm^2)	Asymmetry	Average Asymmetry
Patient 1 L	9.164	9.638	9.401	0.385	0.403
Patient 1 R	5.066	7.666	6.366		
Patient 2 L	4.465	8.670	6.568	0.216	
Patient 2 R	3.974	6.600	5.287		
Patient 3 L	3.472	6.368	4.920	0.607	
Patient 3 R	1.859	3.401	2.630		
Control 1 L	7.040	7.661	7.351	0.052	0.144
Control 1 R	7.804	7.683	7.744		
Control 2 L	7.115	7.391	7.253	0.142	
Control 2 R	8.943	7.773	8.358		
Control 3 L	6.748	5.444	6.096	0.238	
Control 3 R	8.073	7.406	7.740		

Table 2. Quantitative measurement of trigeminal nerve CSA and asymmetry. R0I1 is the CSA of the nerve as it emerges from the pons and ROI2 is the CSA of the nerve as it enters Meckel's cave. The blue shaded rows show patient results and green shaded rows show control results.

Behavioral and neural mentalization deficits in cocaine use disorder

Keren Bachi[1], Sivan Kinreich[1], Prantik Kundu[2], Pias Malaker[1], Thomas Maloney[1], Muhammad Parvaz[1], Nelly Alia-Klein[1], Rita Z. Goldstein[1], Scott J. Moeller[1].

Affiliations: [1]Psychiatry & Neuroscience; [2]Radiology & Psychiatry; Icahn School of Medicine at Mount Sinai

Introduction

Impairments in mentalizing (the successful attribution of mental-states to others) characterize multiple psychopathologies and may culminate in profound interpersonal disruptions. Individuals with cocaine use disorder (iCUD) show multiple social cognition deficits and thereby may exhibit alterations in mentalizing behavior and underlying circuitry (prefrontal cortex, superior temporal sulcus, temporoparietal junction, temporal poles; regions similarly implicated in the pathophysiology of drug addiction). In the current research, we therefore examine the behavioral and neural correlates of mentalizing in iCUD.

Methods & Results

16 iCUD and 10 matched healthy controls underwent a 3T multiecho multiband excitation sequence fMRI while performing the Why/How Localizer task, which presents pretested photographs of naturalistic human behaviors and asks How versus Why these behaviors are being performed; the task robustly activates the mentalizing network as previously shown in a community sample. Group differences between How and Why are examined for behavior (below) and neural activation (ongoing). Data in iCUD are compared against both the current controls and the mean values of a community sample.

The current sample of iCUD and controls did not differ in their mentalizing behavior. Nevertheless, compared to the mean of a community sample of controls, iCUD (but not our sample of controls) were less accurate [one-sample $t(15)=2.255$, p=.04] and slower [$t(15)=2.607$, $p=.02$] in responding to Why questions, consistent with hypotheses.

Conclusion

These preliminary behavioral findings suggest mentalizing deficits in iCUD, with neuroimaging analyses soon to follow.

Clinical Relevance

Enhancement of social cognition and functioning (including therapeutic relationships) can prevent relapse and, thus, augment treatment success in cocaine addiction. Future efforts can intervene in such deficits and enhance social functioning via mentalization-based treatments (which notably have been deployed for enhancing cognition in other psychiatric patients) that emphasize addiction-related facets.

Funding

NIDA: T32-DA007135-31 (KB), F32DA033088 (MAP), R01DA041528 and U01DA041174 (RZG), K01DA037452 and R21DA040046 (SJM); Department of Preventive Medicine, Icahn School of Medicine at Mount Sinai (KB).

Sequential Apparent Diffusion Coefficient for Assessment of Tumor Progression in Patients with Low Grade Glioma

Iris Chen, BS[1], Nathaniel Swinburne, MD[1], Marco Hefti, MD[2], Nadejda Tsankova, MD[2], Amit Aggarwal, MD[1], Amish Doshi, MD[1], Bradley Delman, MD[1], Kambiz Nael, MD[1],
Icahn School of Medicine at Mount Sinai, Department of Radiology[1] and Pathology[2]

Introduction:
Low grade gliomas (LGGs) are slow-growing tumors that carry the potential of high grade transformation. Conventional non-invasive methods to evaluate LGGs infer progression from an increase in tumor size or enhancement on magnetic resonance (MR) imaging, which can be challenging as LGGs often change slowly over time. Apparent diffusion coefficient (ADC) in the pretreatment evaluation of glioma grade has been shown to inversely correlate with tumor cellular density. The purpose of this study was to assess the role of ADC in sequential follow-up of patients with LGGs as a marker of tumor stability vs. progression.

Methods & Results:
Patients with a diagnosis of LGG and at least 6 months of clinical and imaging follow-up were retrospectively reviewed. Image analysis was performed independently by two board-certified neuroradiologists. Tumor progression was defined as size increase on fluid attenuation inversion recovery (FLAIR) or enhancement development on T1 post-contrast. All available MR exams were co-registered and ADC histograms determined for each patient using the volume of interest from the FLAIR hyperintense tumor volume. Normalized mean and 10^{th}-percentile ADC values were evaluated. Tumor progression was defined as 20% or greater interval decrease in ADC; any other ADC trend was considered stable disease. Out of 69 patients reviewed, 28 patients (14 male and 14 female, mean age 50.4 years) met our inclusion criteria. The mean follow-up time was 39.7 months and a total of 241 MRI (mean 8.6 scans per patient) were reviewed. A total of 15 patients were classified as stable vs. 13 patients as progression based on consensus reads of MRI scans. The 10^{th}-percentile ADC values were significantly (P=0.03) lower in patients with tumor progression compared to those with stable tumor. Interval change in 10^{th}-percentile ADC matched the expected pattern in 12/13 patients with tumor progression and 12/15 patients with stable disease with an overall diagnostic accuracy of 86% (P<0.001). The 10^{th}-percentile ADC interval change correctly predicted progression on average 14.1 months before progression was evident on conventional MRI.

Conclusion:
ADC is helpful in detection of progression that would be otherwise undetected on conventional imaging. Specifically, 10^{th} percentile ADC is superior to mean ADC in predicting tumor progression in LGGs. Sequential change in ADC value (interval change) rather than the absolute value at each time point identifies progression.

Clinical Relevance:
The results of this study provide additional insight into how interval change in 10^{th}-percentile ADC values, as an early indicator of increased cellular density and proliferation, can complement conventional imaging in earlier and more accurate detection of tumor progression in patients with low grade glioma.

Figures and tables

Table 1. Baseline and clinical data in patients with and without progression - Univariate analysis

Patient characteristics	**Total (n=28)**	**Progressed (n=13)**	**Stable (n=15)**	***P*-value**
Age in years, mean (SD)	50.4 (16.6)	49.1 (19.0)	51.6 (14.8)	0.70
Sex, M/F	14/14	7/6	7/8	0.56
Initial tumor size, mean (SD)	30.7 (33.8)	32.3 (26.3)	29.4 (40.1)	0.82
Tumor type, O/A	19/9	9/4	10/5	0.80

Table 2. Diagnostic accuracy of ADC ratios - Univariate analysis.

ADC ratios	**Stable tumors (n=15)**	**Progressed tumors (n=13)**	**Threshold value**	***P*-value**	**Overall diagnostic accuracy**
Mean	2.04 ± 0.79	1.68 ± 0.23	<1.8	0.14	62%
10^{th}-percentile	1.50 ± 0.37	1.22 ± 0.24	<1.1	0.03	70%

Table 3. Diagnostic accuracy of ADC interval change - Fisher's exact test.

ADC	**Interval change**	**Stable tumors (n=15)**	**Progressed (n=13)**	***P*-value**	**Overall diagnostic accuracy**
Mean	Decrease	7/15	6/13	0.8	50%
	Plateau/Increase	8/15	7/13		
10^{th}-percentile	Decrease	3/15	12/13	<0.001	86%
	Plateau/Increase	12/15	1/13		

Prenatal Manganese Exposure and Intrinsic Functional Connectivity of Emotional Brain Areas in Children

Erik de Water, PhD[1], Erika Proal, PhD[3], Victoria Wang, BS[2], Sandra Martínez Medina[3], Lourdes Schnaas, PhD[3], Martha María Téllez-Rojo, PhD[4], Robert O. Wright, MD[1], Cheuk Y. Tang[2], PhD, & Megan K. Horton, PhD[1]

[1] Department of Environmental Medicine and Public Health, Icahn School of Medicine at Mount Sinai, New York, NY
[2] Departments of Radiology and Psychiatry, Icahn School of Medicine at Mount Sinai, New York, NY
[3] National Institute of Perinatology (INPer), Mexico City, Mexico
[4] National Institute of Public Health (INSP), Mexico City, Mexico

Introduction

Manganese (Mn) is an essential trace metal that is neurotoxic at high levels of exposure. Disruption of brain maturation processes during the prenatal period may have lasting consequences. During this critical period, the developing human brain is uniquely vulnerable to exposure to environmental toxicants such as Mn, and prenatal Mn exposure has been associated with changes in brain areas involved in emotion processing and regulation. The goal of the present study was to examine whether prenatal Mn exposure is associated with changes in the intrinsic functional connectivity (iFC) of the brain in childhood, focusing on changes in emotional brain areas.

Methods & Results

In this pilot study, 15 subjects (aged 6-7 years) were selected from an ongoing longitudinal birth cohort study to participate in a resting state functional magnetic resonance imaging (fMRI) study. Prenatal Mn exposure was determined from maternal blood collected during the 2nd and 3rd trimesters of pregnancy. We performed seed-based correlation analyses and independent component analyses to examine whether prenatal Mn exposure was associated with the iFC of the brain in children. We found that the bilateral anterior cingulate cortex and right globus pallidus showed reduced iFC with medial and lateral prefrontal areas in children who were exposed to higher prenatal Mn levels, and these children further showed reduced iFC between the bilateral insula and occipito-temporal areas.

Conclusion

These findings indicate that prenatal Mn exposure is associated with reduced iFC of brain areas involved in emotion processing and regulation in children. Future studies should investigate whether this reduced iFC mediates the association between prenatal Mn exposure and emotional dysfunction in childhood.

Clinical Relevance

The reduced iFC we observed between emotional brain areas has also been observed in children with internalizing disorders (i.e., anxiety and depression), and prenatal Mn exposure has been linked to these disorders. The reduced iFC in emotional brain areas may therefore mediate the association between prenatal Mn exposure and internalizing disorders in children.

Figures and tables

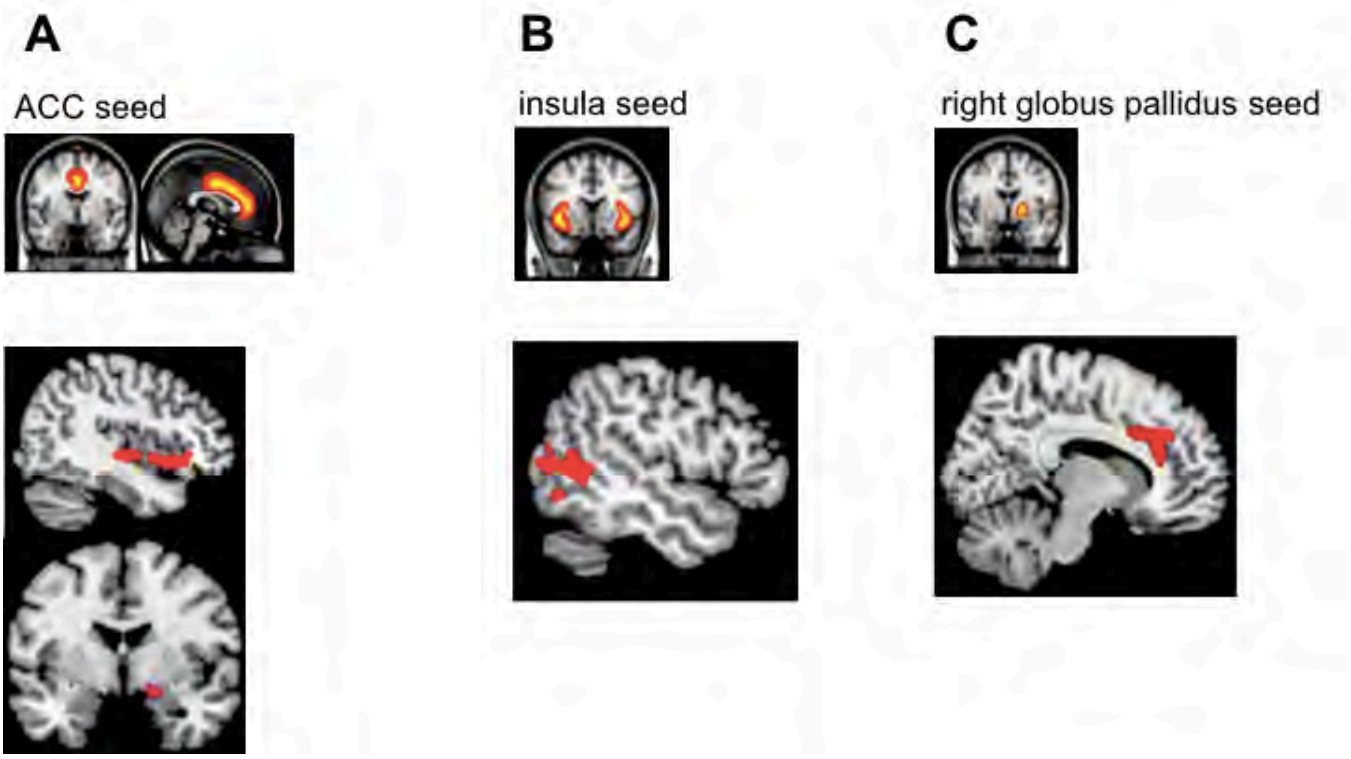

Figure 1. Negative correlations between maternal blood Mn (log) and functional connectivity with the (A) bilateral ACC; (B) bilateral insula; (C) right globus pallidus of 6-7-year-old children.

Note. Seed-based correlation analyses were performed. Seed regions are displayed at the top, while brain areas that showed reduced functional connectivity with these seed regions (depicted in red) are displayed at the bottom.

Identification of brain functional connectivity predictors of treatment response in psychosis

Gaelle Doucet, Hannah Krinsky, Alejandro Paulino, Alexander Rasgon, Sophia Frangou

Icahn School of Medicine at Mount Sinai

Introduction

A substantial proportion of patients with first-time episode psychosis show a poor treatment response, which contributes to psychosocial dysfunction. This study investigates new functional neuroimaging markers to predict symptomatic outcomes in patients with first-episode psychosis.

Methods & Results

We collected resting-state functional MRI (rs-fMRI) data on 72 patients with schizophrenia (n=56) or bipolar I disorder (n=16) (mean age=26.5, 16 females) presenting their first psychosis onset within 5 years. For each individual, the brief psychiatric rating scale (BPRS) was collected at the time of the scan and 234 days (sd: 184 days) later. Rs-fMRI data were preprocessed in SPM12. They were then parcellated based on an anatomical 638-region atlas. Functional connectivity matrices were computed for each individual. The relation between treatment response and the functional connectivity was investigated using the network-based statistics toolbox ($t>3.5$; 5,000 permutations). The total BPRS at time 1, the time between the two assessments and the head motion parameters were added as covariates of no-interest.

Improvement at time 2 (evaluated by the total BPRS) was mostly associated with increased connectivity between primary and associative cortices (sensorimotor cortex and middle frontal gyrus; visual cortex and superior temporal gyrus) at Time 1. In contrast, improved (reduced) positive symptoms at time 2 was related to reduced connectivity involving the ventral anterior cingulate and middle temporal gyri at Time 1.

Conclusion

Our results show evidence that rs-fMRI measures can predict clinical status of patients with psychosis.

Clinical Relevance

Early identification of patients that may fail to achieve remission could assist in the development of new treatment plans.

Multi-region Semi-Adiabatic Spectral-Spatial Spectroscopic Imaging (SASSI) sequence for accelerated 7T MRSI

Rebecca Feldman[1,2] and Priti Balchandani[1,2]
[1]TMII, Icahn School of Medicine at Mount Sinai, USA; [2]Radiology, Icahn School of Medicine at Mount Sinai, USA

Introduction: Magnetic resonance spectroscopic imaging (MRSI) may be used to non-invasively measure spatially varying metabolite concentrations *in vivo*. High fields such as 7 Tesla (7T) permit us to leverage increased signal-to-noise ratio (SNR) and spectral separation between metabolite peaks for more sensitive metabolite detection at higher spatial resolutions. However, the acquisition of high-resolution spectral grids can be prohibitively time intensive. The recent development of techniques aimed at accelerating MRSI acquisitions [1][2] remain challenged by the limitations at 7T, namely chemical shift (CS) artifacts, power (SAR) limits, and B_1 inhomogeneity. The semi-adiabatic spectral spatial spectroscopic imaging (SASSI) sequence [3] uses a spectral-spatial (SPSP) excitation pulse and two adiabatic SPSP refocusing pulses to overcome B_1 inhomogeneity, CS artifacts, and SAR limits to excite a volume of interest (VOI) for 7T MRSI. In this work, we develop a multi-region SPSP excitation pulse and use it to create a novel multi-region SASSI sequence to enable accelerated MRSI.

Methods & Results: We used the adiabatic SLR algorithm [4] to create a SASSI refocusing pulse and designed a non-adiabatic excitation pulse of matching bandwidth (BW). The excitation pulse had BW= 1.20 kHz and t=4.2 ms. The refocusing pulse had BW=1.12 kHz and a t=7 ms. Figure 1 shows the RF and gradient waveforms for the multi-region SASSI pulse sequence. A multi-band excitation pulse was created by combining individual pulses with phased complex addition. Figure 3 is a simulation of the signal with the modified excitation pulse is shown in along with a simulation of the sensitivity of the spatial profile to a range of B_1 values to determine sensitivity to B_1 inhomogeneity. To acquire the spectral grids and metabolite maps, the pulse sequence parameters were: spectral shift=-2.82 ppm, TE=42 ms, TR=1000 ms, time=20 minutes. For SAR comparison, spectra were acquired in a phantom using multi-region SASSI and a standard single-VOI Semi-LASER (sLASER) [6]. SAR in the phantom was recorded for each acquisition relative to sLASER for a long TR, low-resolution scan which reached the upper limit of SAR in the sLASER sequence. The pulse sequence parameters for both sLASER and SASSI for the SAR comparison were: spectral shift=-2.82 ppm, TE=42 ms, TR=2530 ms, time=30 minutes. Metabolite fitting and integration under peaks was performed using LCMODEL [7] to obtain concentrations of, Myo-Inositol (MI), N-acetyl aspartate (NAA), Choline (Cho), and Creatine (Cr).

The simulation of the SPSP profile of the multi-region SASSI excitation (Figure 3) shows two clear excitation planes. While a conventional, dual spin echo pulse would see a 50% loss in signal over a 24% change in B_1; the loss in signal for multi-region SASSI for that same B_1 change is 8%. SAR relative to the sLASER sequence (at 100%) was 36% for the multi-region SASSI. On the right region, the ratio of NAA/Cr was 1.42. On the left, the ratio of NAA/Cr was 1.45. The metabolite maps of NAA, Cho, and Cr, acquired in cross-section to highlight the two regions, are shown in Figure 5. Creating an excitation pulse capable of exciting two slices simultaneously resulted in a SPSP excitation pulse with higher peak power and higher overall SAR than a single region excitation pulse. However, in the SASSI sequence, the non-adiabatic excitation contributes significantly less power than either of the adiabatic refocusing pulses, and therefore has some room for amplification. A similar modification of the spatial sub-lobes could be applied to either of the adiabatic pulses. However, the resulting sequence would deposit higher SAR without an increase in B_1 insensitivity. The proposed multi-region SASSI is significantly less SAR intensive than other adiabatic MRSI sequences such as sLASER, making it a suitable candidate for augmentation into a simultaneous multi-region acquisition.

Conclusion: We designed and implemented a low-SAR semi-adiabatic MRSI sequence capable of exciting multiple regions. The sequence retains the B_1-insensitive volume selection and low chemical shift of SASSI while creating two spatially separated volumes of interest that could be acquired at the same time.

References: [1] Strasser B et al MRM 2016 Aug 22. [2] Chatnuntawech I et al MRM 2014 Jul 30. [3] Feldman RE et al MRM 2016 Oct [4] Balchandani P et al MRM 2010 Sep [5] Scheenen TW et al MRM 2008 Jan [6] Provencher SW MRM 1993. [7] Wijtenburg SA et al Neurosci Biobehav Rev 2015;51

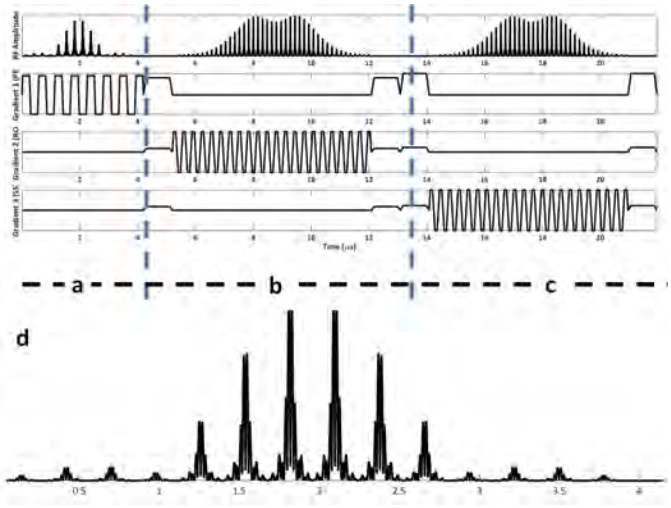

Figure 1: Pulse sequence diagram for the multi-region SASSI excitation: a and d) A multi-region spectral spatial excitation pulse with spatial sub-lobes phased to create two excitation bands in the phase encode direction. b) An adiabatic spectral spatial pulse refocusing a band in the read out direction and depositing phase in the spectral domain. c) An adiabatic spectral spatial pulse refocusing a band in the slice select direction and refocusing phase in the spectral domain.

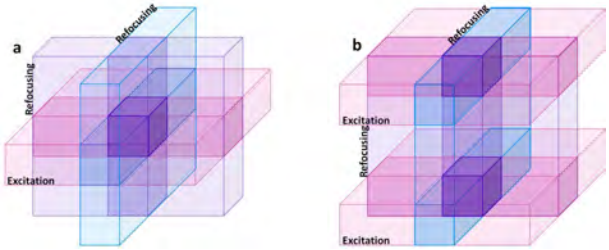

Figure 2: a) Volume of interest (VOI) selection for a single VOI. b) VOI selection for two regions.

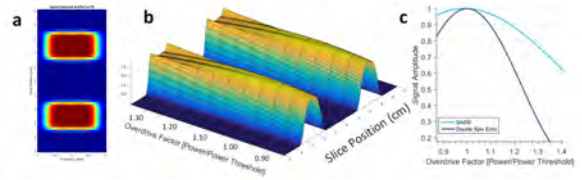

Figure 3: Pulse sequence simulations. a) Spectral spatial profile of excitation pulse for multi-region SASSI. Spectral extent is sufficient to cover the range from MI to NAA. b) Response of multi-region SASSI to a range of B_1 values. c) Projection of a single slice SASSI response (light blue) for range of B_1 values above adiabatic threshold (nominal operating B_1), compared with the response of a traditional spin echo (dark blue).

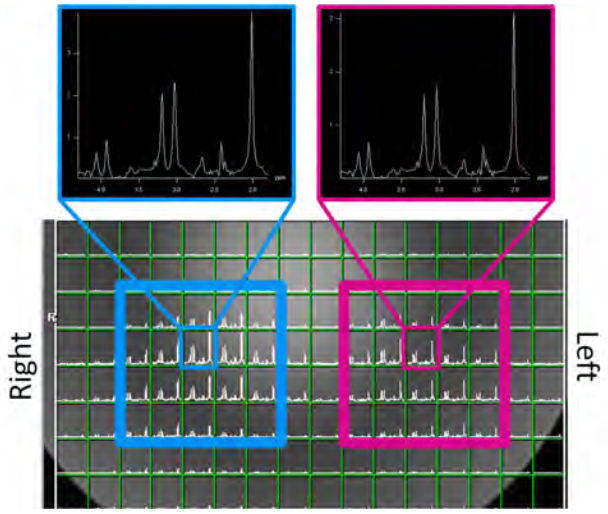

Figure 4: Spectrum obtained in 2 volumes of interest with a null region between the right and left regions.

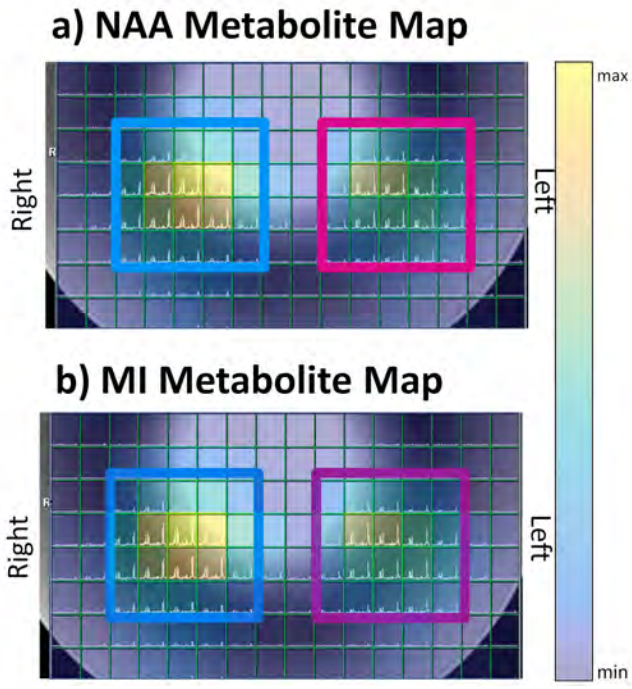

Figure 5: Metabolite maps showing minimal chemical shift a) NAA metabolite map b) MI metabolite map. Although NAA and MI are separated by a large frequency range, both remain within the selected regions due to low chemical shift of multi-region SASSI.

Characterization Of Registration Errors Prior To Voxel-Wise Whole Brain Analysis

Roman Fleysher , Namhee Kim , Asif Suri , Michael L Lipton , and Craig A Branch
Gruss Magnetic Resonance Research Center, Department of Radiology,
Albert Einstein College of Medicine, Bronx, NY

Introduction. Voxel-wise analyses of DTI, fMRI or any other MRI-derived metric, comparing groups or one patient to a control group, require quality registration of images to a template. One or several poorly registered images may skew the distributions of the metric in several voxels leading to incorrect inferences. We propose an approach to screen poorly registered images prior to voxel-wise analysis. We apply this algorithm to demonstrate morph accuracy characterization using two age extreme (16 and 86 year old) templates.

Methods & Results. This study was approved by institutional review board of Albert Einstein College of Medicine. The analysis includes 108 and 234 T1W images obtained as part of ongoing Einstein Aging (EAS) and Einstein Soccer (ESS) Studies respectively. All images were reviewed by an experienced neuroradiologist and determined to be grossly normal brains without visible structural abnormalities.

The T1-weighted 3D imaging was performed using a 3.0T Philips Achieva TX scanner (Philips Medical Systems, Best, The Netherlands) utilizing its 32-channel head coil with TR/TE/TI = 9.9/4.6/900 msec, flip angle 8deg, 1mm^3 isotropic resolution, 240x188x220 matrix. Each T1W image was registered to both young (18 years old) and elderly (86 years old) template brains (Figure 1) using nonlinear registration module of ART[1,2]. Following registrations, each brain was segmented using the ASEG of FreeSurfer[3]. Each atlas was compared to the template's atlas by assigning each voxel a displacement needed to move the voxel to its homologous region, producing the map of lower bound of the morph error (Figure 2). In most voxels, the homologous regions overlap and although morph error may be still present it cannot be detected leading to zero lower bound. Each morphed brain was then ascribed a single number: *the mean lower bound displacement*.

Registration to the elderly template (Figure 3) exhibits large displacements and scatter of the elderly brains and rather compact displacements of the young. This suggests that morph algorithm is not able to deal with variation due to brain atrophy as efficiently as with inherent morphological variation. Only 20 of the brains (3 elderly) show mean lower bound of less than 0.35 mm and represent a well morphed cohort. On contrary, 204 of the brains (1 elderly) register well to the young template (Figure 4) with brains of the elderly demonstrating larger displacements and dispersion.

Conclusion. Voxel-wise analyses rely on registration to ensure that homologous brain regions are being compared. However, registration processes are limited in the degree to which the anatomy of one brain can be mapped on to another [1,2,4]. Previously, errors in landmark alignment were used to select an overall superior morphing algorithm[1,2,4]. We propose error as a metric to assess, screen and filter poorly registered images in single subject or group analyses. Because brain atrophy due to normal aging is known to cause difficulty in registration, we tested this approach by morphing 342 brains across a wide age-span (18-91years) to both young and elderly healthy brain templates and demonstrate a quantifiable metric of morph error associated with age-related atrophy.

Clinical Relevance. Voxel-wise evaluation of brain images of patients with neurologic and psychiatric conditions such as mTBI, autism, schizophrenia etc using DTI or fMRI requires comparisons to a control group by a faithful registration of all images to a template. Because quality of registration is sensitive to the similarity of a brain to the template, one method to mitigate this known issue is to use a study-specific "central" template. Another more clinically relevant method in patient-versus-group analyses is to use patient's T1-weighted image as the template because morph errors of the controls average out and are completely eliminated for the patient's data[5]. However, full error cancellation for controls is still not guaranteed, shifting and widening the distributions.[5] Here we describe an approach to filter out poorly registered images prior to voxel-wise analysis.

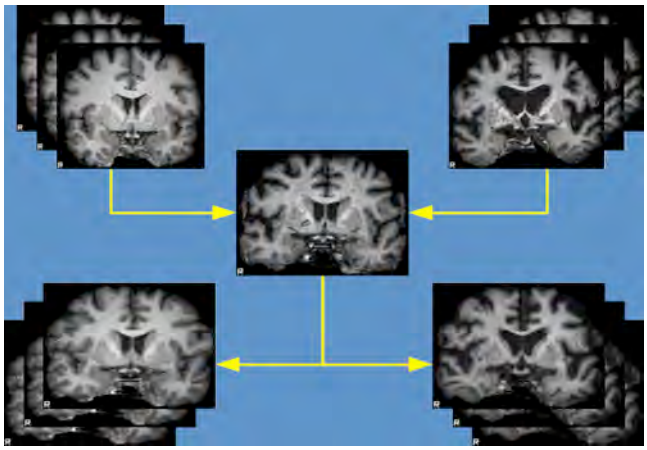

Figure 1. Representative young (top left) and elderly (top right) brains are not perfectly morphed (bottom) to a template (middle).

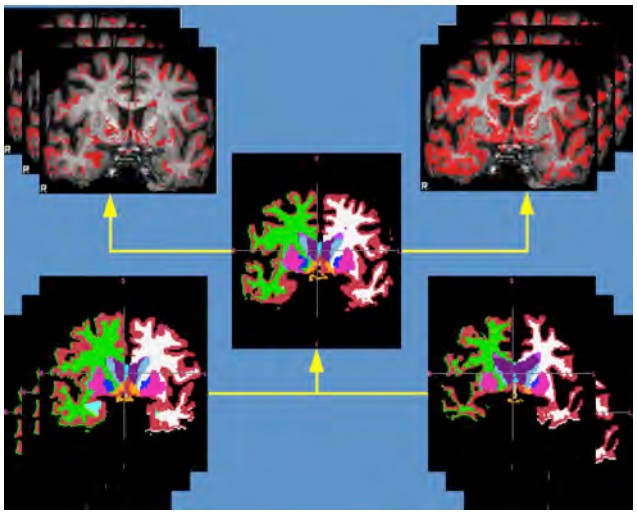

Figure 2. Map of registration errors (top) is computed based on atlases over the morphed brain (bottom) and over the template (middle). Elderly brain (top right) shows larger errors.

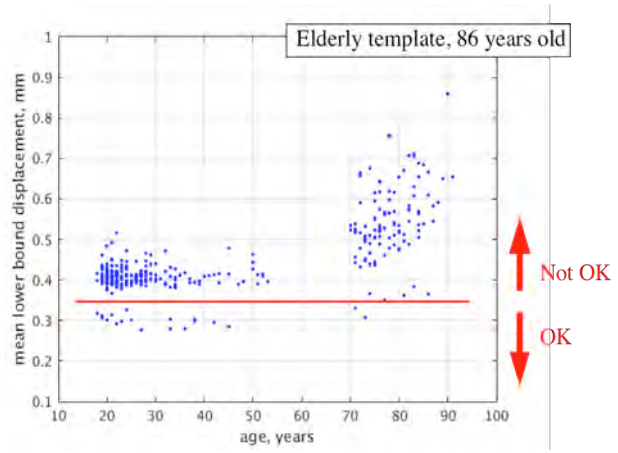

Figure 3. Mean lower bound displacement for all of the 342 brains studied as function of age when morphed to an 86-year-old brain.

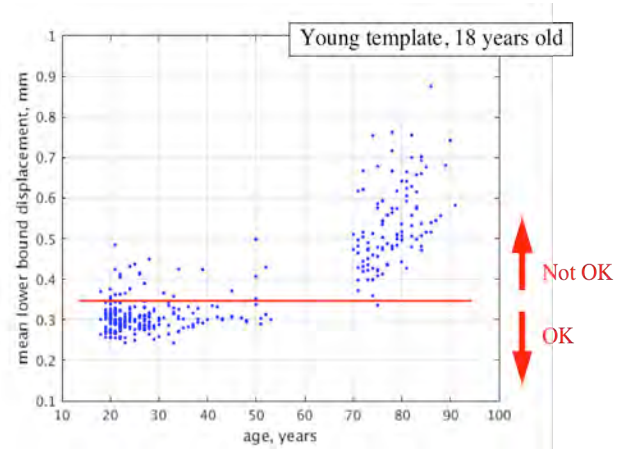

Figure 4. Same as Figure 3 but morphed to the young template.

References:

1. Ardekani B. A., Guckemus S., Bachman A., et al. Quantitative Comparison of Algorithms for Inter-Subject Registration of 3D Volumetric Brain MRI Scans. J. Neurosci. Methods 2005; 142: 67

2. Klein A., Andersson J., Ardekani B. A., et al. Evaluation of 14 Nonlinear Deformation Algorithms Applied to Human Brain MRI Registration. NeuroImage 2009; 46: 786

3. Fischl B., Salat D. H., Busa E., et al. Whole Brain Segmentation: Automated Labeling of Neuroanatomical Structures in the Human Brain. Neuron 2002; 33: 341

4. Grachev I. D., Berdichevsky D., Rauch S. L., et al. A method for assessing the accuracy of intersubject registration of the human brain using anatomic landmarks. Neuroimage 1999; 9: 250.

5. Suri A. K., Fleysher R, Lipton M. L. Subject Based Registration for Individualized
Analysis of Diffusion Tensor MRI. PLoS ONE 10(11): e0142288. doi:10.1371/journal.pone.0142288

Relationship between pre-lesion connectivity and dynamic plasticity in non-human primates

Sean Froudist-Walsh[1], Philip G.F. Browning[1,2], James J Young[1], Kathy L Murphy[3], Rogier B Mars[4,5], Lazar Fleysher[1], Paula L Croxson[1]

[1]Departments of Neuroscience, Neurology, Radiology and Psychiatry, Translational and Molecular Imaging Institute and Friedman Brain Institute, Icahn School of Medicine at Mount Sinai, New York, NY, 10029, USA
[2]Laboratory of Neuropsychology, National Institute of Mental Health, Bethesda, MD, 20892, USA
[3]Comparative Biology Centre, Medical School, Newcastle University, NE2 4HH, UK
[4]Centre for Functional MRI of the Brain, Nuffield Department of Clinical Neurosciences, John Radcliffe Hospital, University of Oxford, OX3 9DU, UK
[5]Donders Institute for Brain, Cognition and Behaviour, Radboud University, Nijmegen, 6525 EN, The Netherlands

Introduction

The brain displays a remarkable ability to adapt following injury in order to recover function. However, the principles that govern which areas undergo plasticity, and when, are not well known. This is partly due the difficulty in obtaining pre-lesion MRI scans in otherwise healthy human subjects.

Methods & Results

Here, we investigated the time-course of plasticity in monkeys after a focal neurotoxic lesion to the hippocampus using multi-modal MRI. We used a hierarchical connectivity analysis approach to analyze plastic functional connectivity changes across a range of spatial (global, cognitive and local networks) and temporal (acute and chronic) scales. We additionally acquired high-resolution structural MRI scans in order to analyse structural plasticity.

We found that widespread functional connectivity alterations occurred throughout the brain, and that timing of connectivity changes was critically dependent on connectivity with the hippocampus before the lesion. Acutely following the lesion the greatest changes occured in areas that were least functionally connected with the hippocampus, but over time this pattern reversed, indicating dynamic reorganisation. This happened despite structural damage being stable, and limited to structures directly connected with the hippocampus.

Conclusion

The brain responds to injury by widely increasing the connectivity between the majority of spared areas during the acute phase, before some normalisation of global connectivity during the chronic phase post injury, perhaps due a need to develop an energy-efficient brain network. The timing of connectivity changes in particular brain regions however is heavily dependent on pre-lesion connectivity with the injured brain area. This is likely to reflect the differing timescales of plastic responses occurring in areas with and without direct connections to the lesioned area, ranging from the release from synaptic inhibition (seconds to hours after lesion) to axon regeneration and sprouting (weeks to months later).

Clinical Relevance

Our findings shed light on the time-course of functional connectivity changes following damage in the otherwise healthy brain, and may guide studies of adaptive, and maladaptive, plasticity in human patients.

Figures and tables

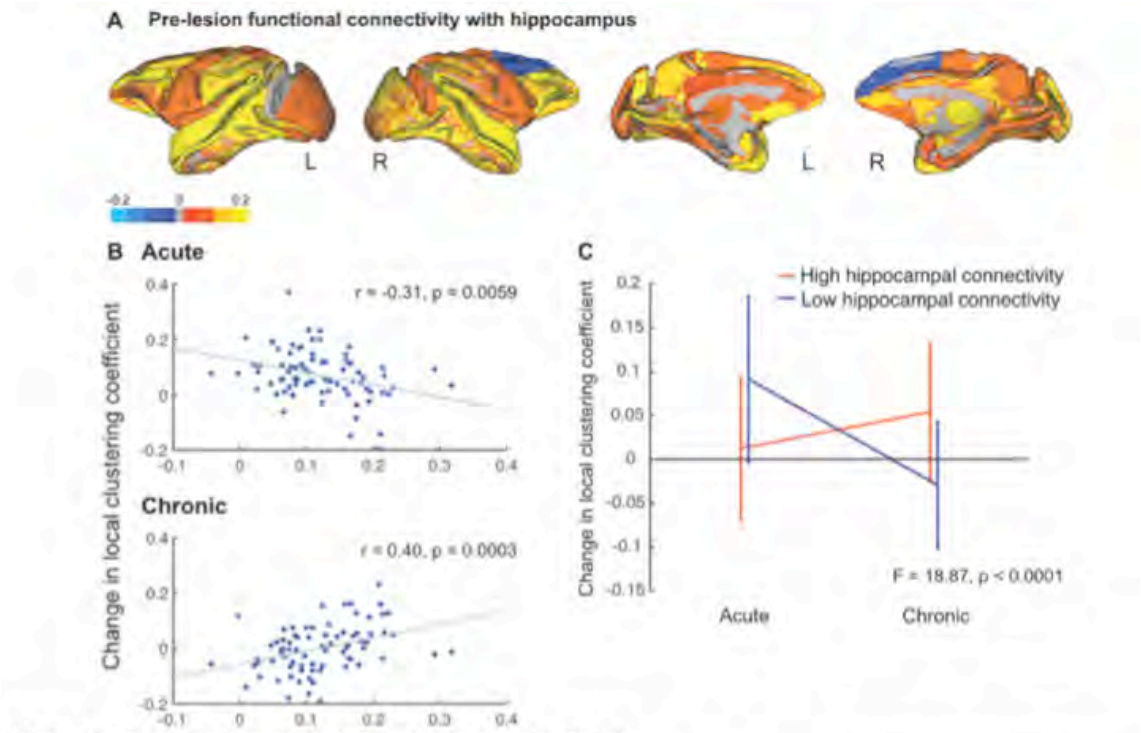

Relationship between local connectivity changes and hippocampal connectivity
(A) Hippocampal functional connectivity pre-lesion. Hot colors = positive correlation, cold colors = negative correlation. (B) Correlations between hippocampal connectivity pre-lesion and changes in the local clustering coefficient (plasticity measure) across brain regions during the acute (top) and chronic (bottom) periods. (C) A strong interaction was observed between hippocampal connectivity and time since lesion when using the plastic changes in local connectivity (as measured by the local clustering coefficient) as the dependent variable.

Clip-mounted resonator mutually coupled to a whole body birdcage for effective in utero micro-MR Imaging of the Embryonic Mouse Central Nervous System

Dung M. Hoang [1,2], Orlando Aristizabal2'[3], Choong H Lee[1], Jiangyang Zhang[1], Daniel Turnbull[2,3] and Youssef Z Wadghiri[1,2]
1. Radiology, Center for Advanced Imaging Innovation & Research & Bernard and Irene Schwartz Center for Biomedical Imaging
2. Division of Advanced Research Technologies - Preclinical Imaging
3. Skirball Institute of Biomolecular Medicine & Pathology,

Introduction

In utero mouse imaging of living embryo can be very useful for the noninvasive characterization of various background strains during embryogenesis, for phenotyping transgenic models, or for studying developmental diseases. In this case, imaging embryos is inherently prone to global periodic abdominal movements of the mother associated with respiratory breathing, cardiac contractions and bowel movement. In addition to the injection of preterm labor drug to minimize uterine contractions, the predictable direction of displacement of the abdomen can be minimized by orienting the phase encoding orthogonal to the direction of motion.

In this study, we introduce a newly designed and 3D printed clip-based setup to be used noninvasively in utero. To this effect, a set of clips of varying size were tailored to snuggle around individual embryos at various stages of the development in order to help stabilize their spontaneous movements. We demonstrate that this simple strategy can be effective in imaging individual embryo when combined with respiratory gating acquisition that were both tested successfully using whole body and surface coils. Importantly, we also used this clip as a support to further integrate a self-resonant loop that is effectively circumventing the secured embryo. This clip-mounted self-resonant coil is then inductively coupled to a much larger volume resonator that can accommodate large pregnant mice. This latter strategy helps increase the signal to noise ratio (SNR) by 3 folds compared to the volume coil alone and almost match the sensitivity of a commercial 4 channel receive-only surface coil coupled to transmit-only coil closely fitting the bore of the magnet.

Methods

A set of clips were designed using Solidworks software (Dassault Systemes, www.solidworks.com) as and 3D printed with Acrylonitrile Butadiene Styrene (ABS). The size and thickness of the clips were scaled appropriately for each stage of the embryos. In addition, a self-resonant coil was integrated as part of the clip using copper tape looped to a non-magnetic variable capacitor (Voltronics) and tuned to a frequency slightly lower but within re-adjustable range (in this case 296Mhz) to the Larmor frequency (300MHz in the current 7-Tesla scanner).

Animals: Mice were maintained according to IACUC approved protocols at the NYU School of Medicine.

To illustrate the effectiveness of our clip-based strategy in reducing spontaneous motion of individual embryos, pregnant mice were administered intra-peritoneally (i.p.) with 30mM MnCl2 in isotonic saline (0.9% NaCl in water) using dose of 0.16 mmol/kg (33 mg/kg) per body weight. Manganese-enhanced MRI was used to generate highly detailed embryonic CNS structures as previously shown. The embryos were clipped and imaged 4h after the injection of MnCl2.

Results

The high resolution 3D MEMRI scan (figure 1d) showed that the clip helps to secure the imaged embryos in position during the whole scanning time. The sharpness of the images was obtained without any post data processing and the enhancement enabled recognition of the neuronal architecture of the embryo. In order to increase the throughput, the clipping setup was tested in the homemade whole body Litzcage coil. Due to the large size of the coil, hence the lack of filling factor, a drop of more 3.6 folds in SNR was observed. This drop in signal can be compensated by introducing an inductive coupling loop wrap closely to the region of interest (the imaged embryo). This inductive coupling loop helped to focus the magnetic energy to a more confined volume (increasing the filling factor) (figure 2d, SNR of 608) that lead to a SNR ~3.2 fold higher compare to the whole body coil alone (figure 2c, SNR of 190) and only 12% less than the commercial surface coil (figure 2e, SNR of 688).

Conclusions

- The design can be integrated into any MRI system using existing commercial hardware.
- Compared with a commercial 25-mm-diameter birdcage, the signal-to-noise ratio was increased by a factor of 3.8, corresponding to an approximate 15-fold reduction in the data acquisition time. An example is shown of ex vivo samples from patients with Alzheimer's disease,

Figure 1

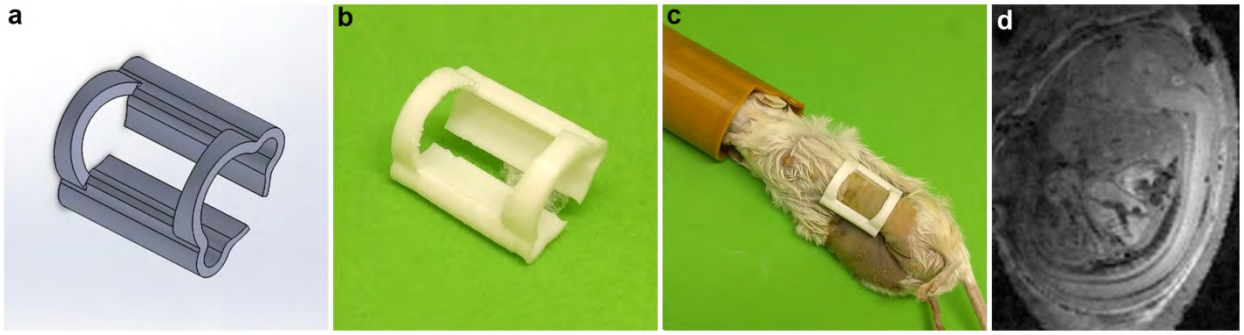

a) 3D CAD model of the embryo clip. **b)** 3D printed clip with ABS. **c)** example of the use of the clip on a pregnant adult mouse. **d)** example of in-utero embryonic MEMRI

Figure 2

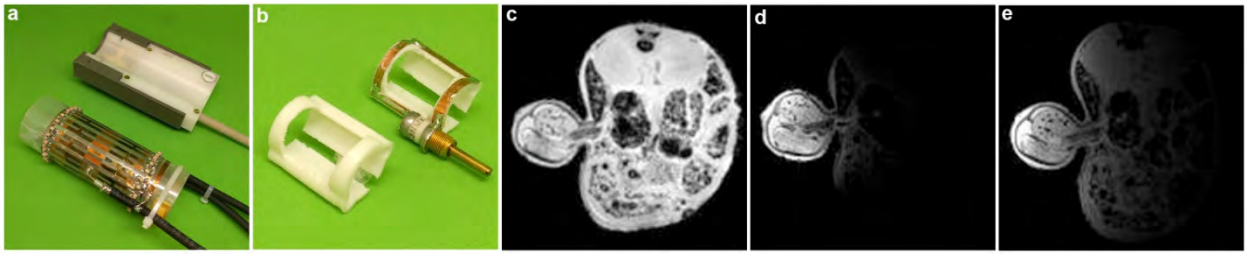

a) Bruker 4 channel received only surface coil (top) and homemade dual Litz cage body coil (bottom). **b)** Embryo clip and clip with integrated inductive coupling loop. **c)** MRI of mouse body using the clip and whole mouse body coil. **d)** MRI of mouse body using inductive coupling loop clip and whole mouse body coil. **e)** MRI of mouse body using Bruker 4 channel received only surface coil

Meta-Analytic Connectivity Modeling Reveals Thalamus Connectivity Dysfunction in Drug Addiction.

Huang, A.S. & Goldstein, R.

Introduction

Drug addiction is a complex disorder, characterized by excessive drug use despite adverse consequences. Current models highlight the importance of the midbrain reward system and the prefrontal cortex cognitive control network. The thalamus is thought to link these two networks, however, its involvement in drug addiction is not well understood.

Methods & Results

Here we examine the network of regions that co-activate with the thalamus in drug addiction using the activation likelihood estimation (ALE) with meta-analytic connectivity modelling (MACM). We identified 17 drug addiction-related papers that showed activation within the thalamus in the BrainMap database. Of these, 6 papers had a Drug Abuse > Healthy Control contrast, resulting in 189 subjects across 10 experiments; 5 papers had a Healthy Control > Drug Abuse contrast resulting in 155 subjects across 9 experiments. We find that in the Drug Abuse > Healthy Control contrast, the thalamus co-activates with a network of frontal, parietal and limbic regions including the dlPFC, ACC, anterior insula, PCC, IPS, and hippocampus. In the Healthy Control > Drug Abuse contrast the thalamus co-activates with temporal and striatal regions.

Conclusion

Our results indicate that in drug addiction, the thalamus co-activates with regions of the default, salience and cognitive control networks. In contrast healthy controls show thalamus coactivation with temporal and striatal regions. These differential coactivation patterns indicate the potential dysregulation of the thalamus dysregulated in drug addiction, particularly in its connectivity patterns with other cortical and subcortical networks. Our findings represent the importance of further investigation of the thalamus in drug addiction.

Clinically Feasible Optic Nerve Diffusion Basis Spectrum Imaging at 3T

Joo-won Kim[1], Peng Sun[2], Sheng-Kwei Song[2], Samantha Lancia[2], Courtney Dula[2], Robert T. Naismith[2], Junqian Xu[1]
[1]Icahn School of Medicine at Mount Sinai, [2]Washing University at Saint Louis

Introduction

Optic nerve MRI is susceptible to eyeball movement. The relatively long acquisition time of advanced diffusion MRI (dMRI) methods exacerbates the motion sensitivity in optic nerve dMRI and limits the clinical implementation of these methods. In this work, we evaluate a short (less than 2.5 min per eye) single slice coronal optic nerve dMRI acquisition protocol at 3T and propose a 2D optic nerve center searching algorithm customized for such dMRI data.

Methods & Results

Methods: MRI: Optic nerve dMRI data were acquired in five healthy adult subjects on a 3T scanner (Trio, Siemens) with a 32-ch head coil (12 anterior receive elements only). An inner-volume-imaging spin echo EPI diffusion sequence was used to acquire reduced field-of-view (FOV) optic nerve images at 1.3 mm × 1.3 mm in-plane resolution, single 3 mm thick slice (coronal slice positioned perpendicular to and at the center of the intraorbital optic nerve, **Fig. 1**), TR/TE=2500/56 ms, monopolar diffusion encoding, optimized 25 multi-b_{val} (linearly spaced) multi-b_{vec} diffusion scheme with b_{max}=1000 s/mm^2 and two b0, two effective averages with alternating diffusion gradient polarity, T_{acq}=2 min 20 sec per eye. Optic nerve center alignment: A manual mask for all dMRI frames was drawn including the optic nerve but excluding extraocular muscles for image alignment (**Fig. 2**, cyan color). On each frame, the optic nerve center was defined on 0.1 voxel unit space (spline interpolation) within the mask region by finding a square 5×5 (voxel) kernel whose sum of image intensities was maximal (**Fig. 2**, red color). The resulting 5×5 kernel from each dMRI frame were concatenated for diffusion signal modeling. Diffusion analysis: DBSI maps and DTI maps were generated using an in-house MATLAB program. The region-of-interest (ROI) of the optic nerve was the center voxel of the 5×5 kernel.
Results: Sufficient optic nerve contrast to the surrounding suppressed fat signal allows definition of the optic nerve (including CSF and dura) for every dMRI frame (**Fig. 2**). The DBSI maps also showed the expected contrast of optic nerve center (e.g., **Fig. 2**, fiber ratio). The DBSI results at the optic nerve center were comparable to our previous studies and demonstrated the expected robustness to partial volume effects as compared to DTI results (**Table 1**).

Conclusion

High resolution optic nerve DBSI with sufficient data quality can be achieved with a short (<2.5 min) single slice coronal optic nerve dMRI protocol at 3T for clinical neuroradiology integration.

Figures and tables

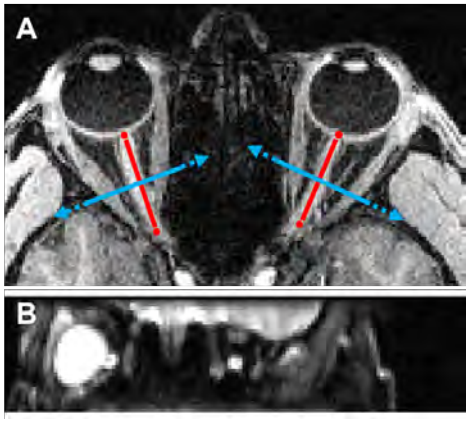

Figure 1. Axial structural MRI localizer for dMRI slice positioning (A) and single slice optic nerve dMRI b0 image from one of the eyes (B). Red lines (A) indicate the optic nerves and blue lines (A) indicate the dMRI slice location.

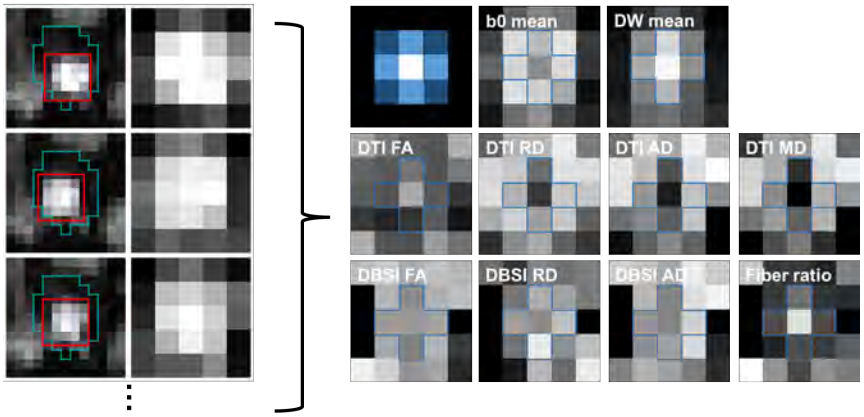

Figure 2. Illustration of the customized 2D optic nerve center registration (left panel) and the results after image registration (right panel). Three representative dMRI frames (first column) and the 5x5 optic nerve region (second column, same as the red squares in the first column). Cyan-colored region (first column) is the manual mask over all frames. The top-left plot in the right panel illustrates the optic nerve center (center voxel, white), partial-volumed optic nerve with more (dark blue) or less (light blue) CSF, and saturated fat (black). The nerve regions were outlined (blue) in the DBSI and DTI maps.

	Mean ± SD		Mean ± SD		Mean ± SD
DTI FA	0.49 ± 0.10	DBSI FA	0.79 ± 0.06	Fiber ratio	0.61 ± 0.15
DTI RD	0.76 ± 0.21	DBSI RD	0.37 ± 0.09	Hindered ratio	0.25 ± 0.16
DTI AD	1.75 ± 0.24	DBSI AD	2.09 ± 0.26	Restricted ratio	0.02 ± 0.03
DTI MD	1.09 ± 0.20			Water ratio	0.11 ± 0.06

Table 1. Optic nerve diffusion basis spectrum imaging (DBSI) and diffusion tensor imaging (DTI) measurements of five healthy subjects. For each subject, measurements from the left and right eyes were averaged. FA: fractional anisotropy, RD: radial diffusivity, AD: axial diffusivity, MD: mean diffusivity.

Sex differences in the brain's gray matter in cocaine addiction

Sivan Kinreich, ENIGMA Consortium, Rebecca Preston-Campbell, Keren Bachi, Thomas Maloney, Muhammad Parvaz, Rita Z. Goldstein

Introduction

Imaging studies published to date in individuals with cocaine use disorder (iCUD) *have* overlooked sex differences in neuroanatomy. Here we used voxel-based morphometry (VBM) to study the differences in reduction of gray matter (GM) volume between female and male iCUD.

Methods & Results

Brain structure (T1-weighted MRI) was pooled from 6 laboratories including 184 individuals (92 iCUD). The data is part of the multi-site Enigma Consortium, preprocessed similarly at each site by the FreeSurfer pipeline and analyzed using the VBM toolbox. General linear model was applied with contrasts between female control vs. iCUD and male control vs. iCUD. Total intracranial volume, age and laboratories were included in the model as covariates.

Preliminary results revealed significant sex differences in the reduction of GM in two brain regions. Left orbitofrontal cortex GM reduction was found for the male iCUD compared to the male control group while right anterior insula GM reduction was found in the female iCUD compared to the female control group ($P<0.001$, uncorrected).

Conclusion

Findings suggest sex differences in GM reduction in iCUD such that male iCUD showed Left orbitofrontal cortex GM reduction and female iCUD showed right anterior insula GM reduction.

Clinical Relevance

Given that differential brain regions are affected may help to guide different treatment approaches, for example treatment for females may emphasize self-awareness and regulation of salience, while male treatment may emphasize emotion regulation and decision making related to reward.

Patterns of n-back related Activation, Connectivity and Behavior in the Human Connectome Project

Dominik A. Moser*1, Gaelle Doucet*1, Alex Ing2, Jakob Heinze3, Klaas Enno Stephan3, Sophia Frangou1
1 Icahn Scholl of Medicine at Mount Sinai Hospital, New York, NY, USA, 2 Kings College, London, United Kingdom. 3 Translational Neuromodeling Unit (TNU), UZH & ETH Zurich, Zürich, Switzerland

Introduction

It has previously been shown that patterns of resting state functional connectivity overall correlate to behavioral patterns (Smith et al 2015). In this study we mined the working memory task of the Human Connectome Project (HCP) to test whether similar correlations hold when activity and connectivity is specifically related to a task. The n-back task for working memory is one of the most classically used tasks used in neuroimaging, giving robust results.

Methods & Results

We investigated 106 non-imaging variables (consisting in demographic characteristics (e.g., age, sex), physical health, lifestyle (e.g., smoking, drug use) and personality and neurocognitive measures) available in the HCP database. We then extracted i) effective connectivity measures from a dynamic causal model from 823 participants of the HCP as well as ii) activities from overall peaks (contrast: 2back – 0back) and iii) resting state functional connectivity from those same peaks. We then performed a sparse canonical correlation between the behavioral pattern and each of the 3 patterns of neuroimaging measures. Significance was tested via permutation testing ($p<0.05$, 5,000 permutations). Results indicated significant canonical correlations between behavior and neuroimaging, with a pattern of significant behavioral variables looking very similar to that Smith et al found for resting state. In detail, the task activity was more correlated than the effective and functional connectivity measures, although all were significantly correlated to the behavior variables. Sparse canonical correlation explained 30% of behavioral variability. The behavioral variables of importance in these analyses, were related to visual tasks (Line orientation, picture vocabulary), reading comprehension, and fluid intelligence.

Conclusion

Our results indicate that different task-related neuroimaging measures have predictive variance toward human behavioral patterns on a very general level, and allows to better focus working memory related imaging research.

Is Iron Concentration Linked to Structural Connectivity in the Subthalamic Nucleus? Implications for Planning of Deep Brain Stimulation

Wahaj Patel[1,4], Alexey Dimov[5], Yi Wang[5], Brian Kopell[2,3], Rafael O'Halloran[1,2]

Departments of Radiology[1], Psychiatry[2], and Neurosurgery[3], Icahn School of Medicine at Mount Sinai, The City College of the City University of New York[4], Weill Cornell Medical College[5]

Introduction

Deep brain stimulation (DBS) is used to treat a variety of neurological and psychiatric conditions. Previously, the potential impact of white matter tractography on pre-surgical planning in DBS has been demonstrated, but not widely adopted in clinical practice. Current clinical planning of DBS is done using structural images, including quantitative susceptibility mapping (QSM), which is sensitive to iron content. Given success in targeting iron-rich structures such as the subthalamic nucleus (STN) and previous results indicating that white matter localization using tractography is useful in DBS planning[2] and possibly predicting side-effects[3], we hypothesize that there is a relationship between QSM intensities and white matter connectivity. To test this we compared connectivity profiles from fiber tractography and QSM intensities in several manually drawn ROIs in the STN in three subjects that were candidates for DBS.

Methods & Results

Subjects: Five patients with Parkinson's Disease who were candidates for bilateral DBS of the STN were used for this study. Preoperative MRI: MRI performed prior to surgery included a T1-weighted anatomical scan, diffusion-weighted imaging (DWI) (2mm x 2mm x 2mm resolution, 60 directions and 5 b0 scans) and QSM. CT was performed preoperatively (0.5 x 0.5 x 1 mm resolution). Data Processing: Cortical and sub-cortical segmentation was performed from the T1-weighted image with Freesurfer (http://freesurfer.net/). Geometric distortions were removed from DWI images by estimating and correcting for susceptibility-induced magnetic fields. Fibre-tracking was performed using the MRtrix package[4] (https://github.com/MRtrix3/mrtrix3). QSM and T1-weighted anatomical scans were be registered to post- operative CT. Connectivity matrices were computed for each voxel from tractography seeded from that voxel and the Freesurfer parcellation. ROI: ROIs were drawn manually on the STN of each subject. The connectivity profiles and the total number of tracks connected to each ROI were computed by summing the columns of the connectivity matrices for each ROI. The connectivity profiles were compared to the QSM intensity in each ROI.

Conclusion

Strong negative correlations of connectivity to the QSM value were observed in several anatomical regions relevant to DBS. A simple map of connectivity of 3 priori regions - the superior frontal, pre- and post-central gyri - that captures regional variations in connectivity was presented. Such a mapping may be useful in surgical planning. If these patterns are consistent over many patients, they could be used to avoid/prevent cognitive/psychiatric side effects associated with DBS. Future will work will extend this to a larger sample as well as other DBS targets such as the globus pallidus and caudal zona incerta.

Clinical Relevance

Connectivity information can be used to improve efficacy and reduce side effects resulting from DBS surgery.

Improved signal uniformity for balanced Steady-State Free Precession (bSSFP) by employing Direct Signal Control parallel transmission

Francesco Padormo and Priti Balchandani
Translational and Molecular Imaging Institute, Icahn School of Medicine at Mount Sinai, New York, NY, United States

Introduction

bSSFP offers ultra-high resolution structural imaging at ultra-high field (UHF), but is impaired by B_0 and transmit field (B_1+) inhomogeneity resulting in images with uneven signal/contrast. Here we propose a novel approach to mitigate B_0 and B_1+ inhomogeneity for bSSFP in a single unified manner. We apply Direct Signal Control to bSSFP for the first time, harnessing PTx to improve image uniformity in spite of field inhomogeneities.

Methods

The bSSFP steady-state magnetization at TE=TR/2 with flip angle α and 0-180° phase cycling with relaxation times T_1 and T_2 and off-resonance dω is given below ($\mathbf{R}_\beta$ = rotation matrix of angle β, $\mathbf{P}_t$=precession/T_2 decay matrix for duration t, **b** = T_1 recovery vector).

$$\mathbf{M}(TR,\alpha,d\omega,T_1,T_2)=\mathbf{P}_{TR/2}[\mathbf{I}-\mathbf{R}_\alpha\mathbf{P}_{TR}\mathbf{R}_{-\alpha}\mathbf{P}_{TR}]^{-1}[\mathbf{R}_\alpha\mathbf{P}_{TR}\mathbf{R}_{-\alpha}\mathbf{b}+\mathbf{R}_\alpha\mathbf{b}]$$

B_0/B_1+ inhomogeneity results in spatially variable fields (i.e. α = α_j, dω = $d\omega_j$; j = voxel index), causing spatially variable signal f(TR, α_j, $d\omega_j$, T_1, T_2)=√(M_x^2+M_y^2). We propose exploiting additional freedom offered by multiple (N_{tx}) transmitters to achieve signal uniformity by solving the optimization problem below (Φ = cost function to be minimized, **w** = N_{tx}x1 complex vector of RF shims, α_j^k = flip angle profile of transmitter k, i = 1, …, N_{tiss} is an index of included tissues, d_i=desired signal, P_{lim} = RF power limit used as a surrogate for SAR).

$$\underset{\mathbf{w}}{\text{minimize}}\ \Phi=\sum_{i=1}^{N_{tiss}}\sum_{j=1}^{N_{vox}}\left|d_i-f\quad TR,\sum_{k=1}^{N_{tx}}\alpha_j^k w^k,d\omega_j,T_1^i,T_2^i\right)\right|^2\quad\text{subject to}\ \ \mathbf{w}^*\mathbf{w}\le P_{lim}$$

This approach was tested experimentally. Measurements were performed on a Siemens Magnetom 7T with an eight-channel transmit/receive head coil (Rapid Biomedical). A phantom was constructed containing Magnevist-doped saline (T_1 = 1236ms, T_2 = 611ms) with two chambers of 0%-fat milk (T_1=1949ms, T_2=91ms) and a spherical air cavity (diameter = 40mm) to induce B_0 inhomogeneity. Images were acquired in a single transverse slice with FOV=200x112.5mm, located 30mm superior to the cavity. Flip angle profiles were obtained by B_1+ mapping. B_0 shimming utilized a manufacturer-provided protocol (WIP-452G). The center frequency was set to minimize the maximum $|d\omega_j|$. B_0 mapping was performed with a multi-echo SPGR (TEs=2,4,…,10ms).

Two RF shims were used for bSSFP acquisitions (vox=2x2x1mm, TR=6.7ms, BW=685Hz/pix). The first, $\mathbf{w}_{COV}$, producing flip angle map α_{COV}, was obtained from a Coefficient-of-Variation (COV) optimisation, and scaled to achieved an average α = 20. The second, $\mathbf{w}_{OPT}$, producing flip angle map α_{OPT}, was obtained from the proposed method. Target signals d_i were set as the signals obtained on-resonance with α = 20° (i.e. f(TR, 20°, 0, T_1^i,T_2^i)), and P_{lim} = $\mathbf{w}_{COV}$*$\mathbf{w}_{COV}$. $\mathbf{w}_{COV}$ was found using the Matlab routine fmincon. The bSSFP acquisitions were corrected for receiver bias to produce I_{COV}^{meas} and I_{OPT}^{meas}, which were compared to the predicted images for each substance and method, $I_{COV,i}^{pred}$ and $I_{OPT,i}^{pred}$.

Results

The B_0 map (Fig.1b) shows a central perturbation (+55Hz) due to the air cavity. α_{COV} is more uniform than α_{OPT} (Figs.1c/d). Whilst in conventional sequences α_{COV} would produce a more uniform image than α_{OPT}, Fig.2

demonstrates that the converse is true for bSSFP in this scenario. I_{COV}^{pred} (Fig.2b) has signal hyper/hypo-intensities (black/red arrows) in regions of large B_0 inhomogeneities. These also appear in I_{COV}^{meas} (Fig.2d, blue arrows). I_{OPT}^{pred} shows reduced signal inhomogeneity (Fig.2c, white arrows), which is confirmed by experiment (I_{OPT}^{meas}, Fig.2e, green arrows).

Conclusion

Joint B_0/B_1+ inhomogeneity correction for bSSFP using PTx has been demonstrated for the first time at 7T. We anticipate incorporating B_0 shim calculation into the optimization will yield further benefits. Future work will test the method in-vivo and incorporate global/local SAR limits.

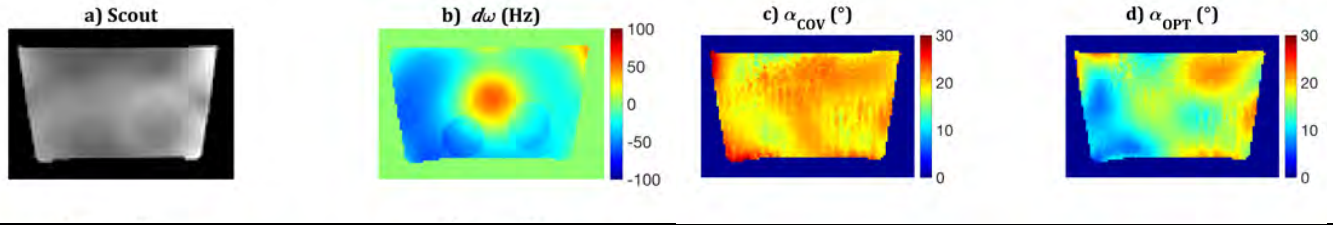

Figure 1 – a) Scout image, b) B_0 map, c) COV-optimized flip angle map, d) flip angle map from proposed technique. Although the optimized flip angle map is less uniform, Fig.2 demonstrates that the measured signals are more uniform.

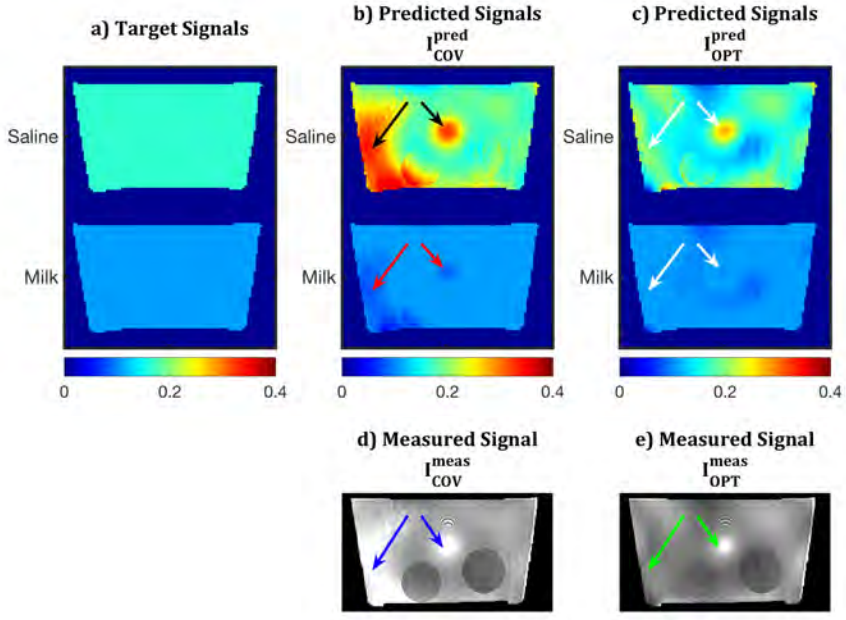

Figure 2 – a) Target signals for saline (top) and milk (bottom), b) Predicted saline/milk signals using COV - optimisation, c) Predicted signals - proposed method, d) Measured image - COV RF shim, e) Measured image - proposed method. Black/red/blue arrows indicate where signals are non-uniform when using $\mathbf{w}_{COV}$ due to B_0 inhomogeneity. White/green arrows indicate areas of improved uniformity with proposed method.

Hyper-connectivity of the Seizure Onset Zone: A Potential Epilepsy Biomarker at 7T

Jack Rutland[1,2], Rebecca Feldman[1], Lara Marcuse[3], Madeline Fields[3], Bradley Delman[1], Priti Balchandani[1], Rafael O'Halloran[1]
[1] *Radiology, Icahn School of Medicine at Mount Sinai, New York, New York, United States,* [2] *Wake forest University,* [3] *Department of Neurology, Mount Sinai Hospital, New York, New York, United States*

Introduction

Locating the seizure onset zone (SOZ) in non-lesional epilepsy patients can be challenging with current clinical approaches. Epileptic seizures result from hyper-excited and overly-synchronous neuronal firing in the cerebral cortex [1]. This hyper-activity originates in the SOZ, and propagates to adjacent regions via white matter fibers [1] . Previous investigations of epileptic seizures have found both hyper and hypo-connectivity between various brain regions, however conclusive evidence of altered connectivity of the suspected SOZ in MRI-negative patients has not yet been identified [2]. Given recent findings of aberrant white matter structure in non-lesional epilepsy we hypothesize that differences in structural connectivity [3,4]. Here, we compare structural connectivity of eight non-lesional epilepsy patients and 8 healthy controls using 7T MRI.

Methods & Results

8 healthy control subjects and 8 epilepsy patients without lesions on clinical MRI scans were scanned using a 7T whole body scanner (Siemens Magnetom) under an approved IRB protocol. The MRI protocol consisting of a T1-weighted MP2RAGE sequence (0.7 mm isotropic resolution) and high-angular-resolved diffusion-weighted dMRI (1.05 mm isotropic resolution, 68 directions). Diffusion-weighted images were corrected for distortions and registered to T1-weighted images.Cortical and subcortical segmentations were obtained using FreeSurfer software (http://freesurfer.net/). Whole brain tractography (Figure 1a) was performed using spherical deconvolution and the iFOD2 [5] algorithm and SIFT in MRTRIX3 to obtain 10,000,000 fibers. Structural connectivity matrices were calculated by counting tracks connecting each region in the FreeSurfer segmentation (Figure 1b). Because suspected SOZ are identified on a very coarse scale (often by lobe) the structural connectivity matrix (Figure 1d) was resampled onto a coarser segmentation (Figure 1c) consisting of the following 18 regions (9 per hemisphere): Superior Frontal, Mid-Frontal, Inferior Frontal, Pre-central, Post-central, Superior Parietal, Temporal Parietal, Temporal, and Occipital.A normative connectivity map was computed by averaging the connectivity maps of the 8 healthy controls. As an initial assessment of aberrant connectivity, for each epilepsy subject, regions 2 or more standard deviations (SD) from the normative connectivity matrix (edgewise) were identified (Figure 1). For subjects with epilepsy, suspected SOZ was determined by experienced neurologists. In order to compare connections in the suspected SOZ for each subject, regions in the SOZ were grouped together and compared to all other regions. Connectivity values were normalized to the normative distribution by z-score to remove region variations in connectivity. The mean connectivity of all the SOZ regions and non-SOZ regions were computed for each epilepsy subject and compared using a paired t-test.

Conclusion

Table 1 quantifies the location and number of hyper-connected nodes (greater than 2 SD above the mean) for the eight epilepsy subjects. Connectivity diagrams, example in Figure 2, show the same data as Table 1 but in graphical form for one exemplary subject. Note the left parietal-temporal region (L-PT, Figure 2) in the seizure onset zone with 4 hyper-connections (Table 1, row 2, 3rd to last column). Overall, there were regions of increased connectivity in all eight epilepsy subjects as shown by the prevalence of hyper-connections. Notably, there were no nodes with connectivity densities that differed from the average controls by two or more SD for any of the control subjects. This is consistent with previous studies that have linked seizure activity to increases in white matter fiber volume in the brain.[2] The mean number of hyper-connected nodes in the suspected seizure onset zone for the eight epilepsy subjects (M= 1.604, SD= 1.156), was significantly greater than the mean number of hyper-connections to the regions not associated with the suspected SOZ (M=0.978, SD=0.626), p= 0.047.

Clinical Relevance

In non-lesional epilepsy patients, nodes in the suspected SOZ were found to be hyper-connected compared non-SOZ regions. The findings in this study may have implications for diagnosing and treating patients with MRI-negative epilepsy, especially those that are also refractory to pharmacological intervention. Future work will increase the total number of subjects analyzed in this experiment.

Figures and tables

		Number of white matter fiber connections (left/right)									
Epilepsy Patient	SOZ	Suspected SOZ [Left /Right]	Superior Frontal	Middle Frontal	Inferior Frontal	Pre-Central	Post-Central	Superior Parietal	Parietal Temporal	Temporal	Occipital
1	Left Frontal Temporal	Left	2/1	0/0	3/0	2/1	2/1	0/0	4/1	0/0	0/3
2	Left Temporal	Left	2/1	0/0	3/0	2/1	1/0	0/0	4/2	0/0	0/2
3	Left Frontal	Left	0/2	3/2	5/2	3/1	1/0	6/0	0/2	1/0	5/1
4	Left Temporal	Left	0/0	2/1	2/1	2/2	0/1	3/1	0/1	0/0	0/0
5	Bilateral Frontal	Bilateral	1/0	1/0	0/0	1/0	1/0	0/0	0/1	0/0	1/0
6	Bilateral Frontal	Bilateral	0/0	0/0	2/2	2/1	0/0	1/0	0/0	1/0	0/1
7	Bilateral Temporal	Bilateral	0/1	6/1	3/1	4/3	1/2	1/3	8/3	0/0	5/1
8	Bilateral Temporal	Bilateral	1/1	3/0	2/0	2/3	1/0	0/1	6/1	4/1	1/1

Table 1. This table provides the suspected SOZ and the number of white matter fiber connections to the left/right sides of each of the 9 brain regions that were at least two SD above the average of the healthy controls, in each of the eight epilepsy subjects.

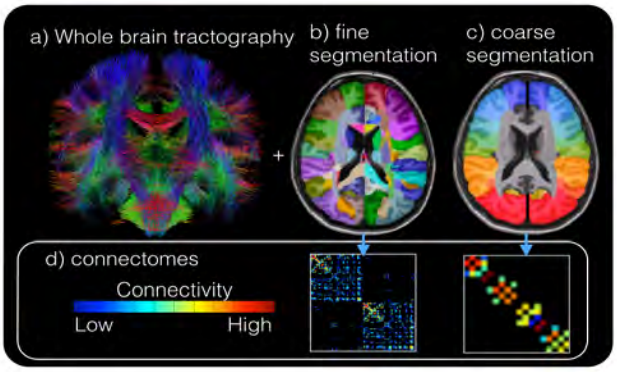

Figure 1. Connectome construction: Whole brain tractography (a) is combined with a fine segmentation(b) and a coarse segmentation (c) to produce connectomes(d) consisting of track counts between the brain regions of their respective segmentation (b,c).

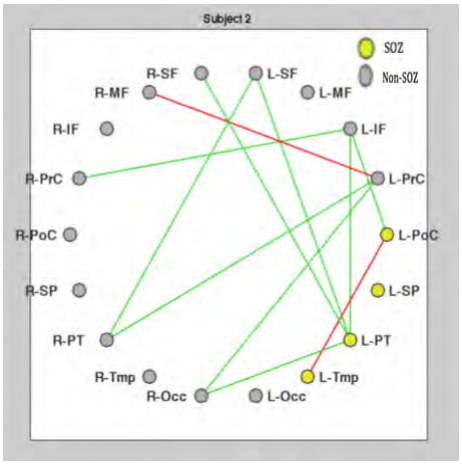

Figure 2. A connectivity diagram illustrating the white matter fibers in epilepsy subject 2, with left temporal seizure onset. Green lines represent hyper-connections (fibers at least 2 SD above the control mean), red lines represent hypo-connections (fibers at least 2 SD below the control mean), and the yellow circles indicate SOZ

Estimation of Infarction Volume Using CT Perfusion: Comparison Between Bayesian and Singular-Value Deconvolution Postprocessing

Yu Sakai, Joseph Marchione, Nathaniel Swinburne, Josep Puig, Javin Schefflein, Bradley Delman, Kambiz Nael
Mount Sinai Medical Center, New York, NY, United States, Department of Radiology, Mount Sinai Medical Center, New York, NY, United States

Introduction

CT perfusion (CTP) based infarction estimation has been challenging mainly due to noise associated with CTP data. The Bayesian method is a robust probabilistic method that minimizes effects of oscillation, tracer delay and noise during residue function estimation compared with other deconvolution methods. In this study we compared the CTP-estimated infarction volume between Bayesian method and commonly used block-circulant singular value deconvolution technique (cSVD).

Methods & Results

METHODS: Patients were included if they had 1) Anterior circulation ischemic stroke; 2) Baseline CTP; 3) Successful recanalization defined by TICI ≥ IIb; 4) Minimum infarction-volume of > 5mL on the follow-up MRI. CTP data were processed with cSVD and Bayesian methods. Two established CTP threshold criteria for estimation of infarction volume were applied: Method-1 (rCBF < 30% within the region of delay more than 2 sec) and Method-2 (CBV < 2 within the region of rMTT > 145%). Statistical analysis was performed using repeated measure ANOVA, regression and Bland-Altman analysis.

RESULTS: So far, twenty patients have met inclusion criteria. Infarct volume (Mean±SD, mL) was 23.7±28.6 on MRI; 30.4±28.4 (Bayesian) and 16.3±23.14 (cSVD) using Method-1; 20.6±24.3 (Bayesian) and 8.8±4.8 (cSVD) using method-2. With MRI as the standard, there was no statistically significant ($p>0.05$) difference between CTP-estimated infarction volumes, except for cSVD-CBV ($p=0.006$). Bayesian-estimated infarction volume showed smaller mean differences when compared to MRI infarction volume. Mean-difference and correlation coefficient between MRI and CTP-estimated infarction are summarized in Table-1.

Conclusion

While cSVD provides acceptable estimation of infarction volume using rCBF<30%, volumetric accuracy for estimation of infarction from CTP is superior using Bayesian postprocessing regardless of the threshold methodology utilized.

Clinical Relevance

From stroke onset, the window of opportunity for effective thrombolysis is only 3-4.5 hours. The central premise of the procedure is to rescue the ischemic penumbra. Therefore, fast and accurate estimation of infarction volume in acute stroke patients is critical. CT perfusion (CTP) is readily available in emergency settings, but CTP based infarction estimation has been challenging mainly due to noise associated with CTP data. So far our results suggest that incorporation of the Bayesian method will enable a more accurate estimation, in comparison to the conventional cSVD approach.

Figures and tables

Table 1

CTP-estimated infarction volume compared to MRI				
		Mean difference volume with MRI	ANOVA, p	Correlation coefficient, p
Method-1 (rCBF<30% within the region of delay > 2sec)	Bayesian	6.7 mL	0.81	r^2 = 0.64, p<0.001
	cSVD	-9.0 mL	0.69	r^2 = 0.54, p<0.001
Method-2 (CBV<2 within the region of rMTT> 145%)	Bayesian	-3.1 mL	0.90	r^2 = 0.50, p=0.01
	cSVD	-22.6 mL	**0.006**	r^2 = 0.1, p=0.2

Anthropomorphic Spinal Cord Phantom with Induced Field Inhomogeneity

Alan C. Seifert[1,2,3], Vaishali Patel[1], Merin Grace[1], Robin Li[1], Mohammad Molla[4], Joseph Borrello[1,2,3], and Junqian Xu[1,2,3,5]

[1]Translational and Molecular Imaging Institute, Icahn School of Medicine at Mount Sinai, New York, NY USA
[2]Department of Radiology, Icahn School of Medicine at Mount Sinai, New York, NY USA
[3]Graduate School of Biomedical Sciences, Icahn School of Medicine at Mount Sinai, New York, NY USA
[4]Department of Mechanical Engineering, The City College of New York, New York, NY USA
[5]Department of Neuroscience, Icahn School of Medicine at Mount Sinai, New York, NY USA

Introduction

The human spinal cord contains important neural tracts and circuits that can be assessed by MRI[1], but exists in a particularly unfavorable magnetic field environment. The adjacent vertebral bodies and intervertebral discs, having different magnetic susceptibilities, create spatially periodic field distortions in the spinal canal. The lungs, which fill and empty of paramagnetic air, also create temporally-varying field disturbances[2]. The echo-planar imaging (EPI) sequences most commonly used in functional and diffusion studies are especially sensitive to field disturbances[3]. Development of advanced shimming techniques, pulse sequences, and reconstruction techniques robust to these field disturbances has been actively pursued by the spinal cord MRI research community. To facilitate these technical developments, we have designed and constructed a phantom of the human spinal cord and canal capable of simulating these specific field disturbances.

Methods & Results

Phantom: The spinal cord and canal between the C1 and L1 vertebral levels were modelled in SolidWorks CAD software (Dassault Systèmes, Waltham, MA) based on in vivo measurements[4,5,6]. The canal was machined from optically clear acrylic sheets, and a solution of 16% w/w polyvinyl alcohol (PVA)[7,8,9] in distilled water was injected and allowed to solidify in a 3D printed mold of the spinal cord. The denticular ligaments were attached to the walls of the canal with silicone epoxy adhesive, and the two halves of the acrylic canal were sealed together using acrylic adhesive (Weld-On 4, SciGrip, Durham, NC). The phantom was filled with distilled water.

CT and MRI: Axial anatomical images were acquired using Force CT and Skyra 3T MRI scanners (Siemens, Erlangen, Germany). Echo-planar imaging and field mapping were performed with the phantom immersed in a tub of water with and without three 50-mL vials of air tethered to the phantom to create field distortions.

Results: The phantom is shown in Figure 1. In Figure 2, distortion and signal drop-out caused by magnetic field inhomogeneities (Figure 1b,c) are demonstrated. Air-filled vials create spatially-periodic frequency shifts of -100 Hz within the spinal canal (Figure 3). T_1 of the PVA spinal cord was 839 ms, T_2 was 107 ms, and the apparent diffusion coefficient (ADC) was 1.480 $\mu m^2/ms$.

Conclusion

Both T_1 and T_2 relaxation times and ADC are determined by the concentration of PVA, and are all within reasonable ranges in our current phantom prototype. Future phantom development will make use of inhomogeneities that are periodic in both space and time to simultaneously simulate the effects of vertebrae and respiratory motion on the magnetic field in the spinal canal.

Clinical Relevance

This phantom was designed to accurately reproduce normal adult human anatomy and mimic MR properties in healthy human spinal cord[10,11], and will facilitate and accelerate technical improvements to imaging methods in the spinal cord.

Figures and tables

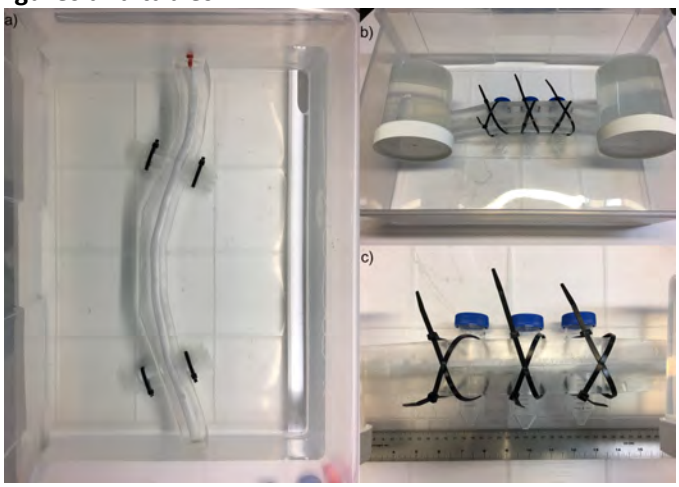

Figure 1: Photographs of the anthropomorphic spinal cord phantom. The phantom was scanned in a head-first left lateral orientation (a) for CT and anatomical MR scans, and in a head-first prone orientation immersed in water (b,c) for echo-planar and field mapping MR scans. Three 50 mL vials of air were secured to the anterior of the phantom to simulate the susceptibility-induced field inhomogeneities caused by vertebrae and intervertebral discs. Jars of water were placed on the ends of the phantom to counter the buoyancy of the vials. These vials were removed without moving the phantom or table for comparison scans.

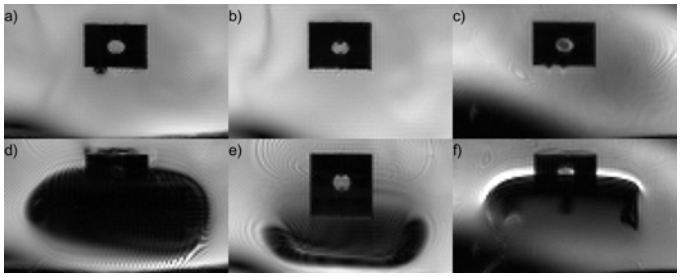

Figure 2: Illustrative axial BOLD fMRI (a,b,d,e, GRE-EPI, TR = 1200 ms, TE = 50 ms, 90° flip angle) and diffusion MRI (c,f, SE-EPI, TR = 2000 ms, TE = 200 ms, 90° flip angle) images. In the top row (a-c), no induced field inhomogeneities were present, while in the bottom row (d-f), field inhomogeneities caused by air-filled vials caused signal drop-out and image distortion. Frames (d) and (f) were acquired through the center of a vial. Frame (e) was acquired in the gap between two vials.

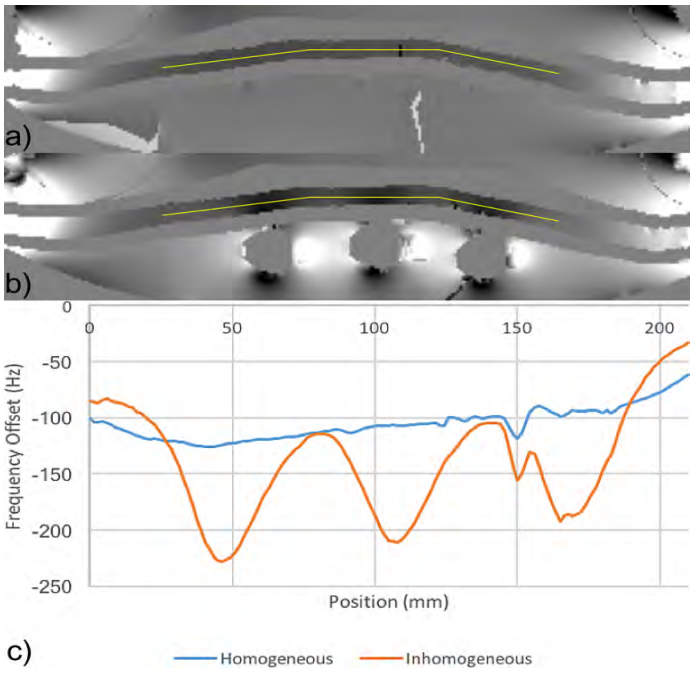

Figure 3: Field maps (range: ± 275 Hz) of the spinal cord phantom without (a) and with (b) field inhomogeneities. Dipole-like fields, positive along B0 and negative orthogonal to B0, were created by paramagnetic air within air-filled vials. These induced fields offset the field within the spinal canal adjacent to the vials by approximately -100 Hz, while the field is relatively unaffected within the canal in the gaps between vials, where the canal is at approximately the magic angle (± 54.7°) relative to the two adjacent vials. B0 profiles along the yellow lines in (a,b) are plotted in (c).

Assessment of frontal-cortex glutathione, GABA, and glutamate in individuals with relapsing-remitting and progressive multiple sclerosis using proton magnetic resonance spectroscopy at 7 Tesla

Kelley M. Swanberg*[1,2], Hetty Prinsen*[1], Katherine Destefano[3], Mary Bailey[3], David Pitt[3], Robert K. Fulbright[1], and Christoph Juchem[1-4]

[1] Radiology and Biomedical Imaging, Yale University School of Medicine, New Haven, CT, United States
[2] Biomedical Engineering, Columbia University School of Engineering and Applied Science, New York, NY, United States
[3] Neurology, Yale University School of Medicine, New Haven, CT, United States
[4] Radiology, Columbia University School of Engineering and Applied Science, New York, NY, United States

- These authors contributed equally to this work.

Note: Portions of this work have been accepted as a presentation to the 2017 Annual Meeting of the International Society for Magnetic Resonance in Medicine in Honolulu, Hawaii from April 22 through April 27.

Introduction

Multiple sclerosis (MS) is an autoimmune illness that targets central nervous white and grey matter. Though MS affects over 2 million people worldwide, treatment options, especially for progressive cases, continue to fall short of full efficacy. Proton magnetic resonance spectroscopy (^{1}H MRS) enables the noninvasive measurement of metabolites in tissues affected by MS, particularly the brain. A number of considerations have, however, complicated the precise spectroscopic quantification of several compounds potentially implicated in the pathophysiology of the disease, including endogenous antioxidant glutathione (GSH), inhibitory neurotransmitter γ-amino-butyric acid (GABA), and excitatory neurotransmitter glutamate. A dearth of spectroscopic data thus exists on the effects of disease state, especially in progressive (P-MS) relative to relapsing-remitting (R-MS) multiple sclerosis, on in vivo concentrations of these compounds within the central nervous system.

Methods & Results

We have previously published a scanning methodology that reproducibly measures GSH, GABA, glutamate, and a number of other biochemicals in a single 70-minute ^{1}H MRS scan. We executed this procedure in a mixed-tissue frontal cortex voxel in twenty-six relapsing-remitting MS patients (18 female; mean ± S.E.M. 44 ± 2.5 y.o.), twenty-one progressive MS patients (12 female; 55 ± 1.7 y.o.), and twenty-five non-MS controls (12 female; 43 ± 3.0 y.o.). Among these groups, disease state exhibited a significant effect on concentrations of N-acetyl aspartate (NAA), a putative biomarker of neuronal membrane integrity, and glutamate, the primary neurotransmitter of excitatory central nervous circuitry, relative to reference compound total creatine. In both cases, P-MS patients exhibited a significant reduction in metabolite concentrations relative to both control and RR-MS patients. Significant frontal cortex reductions in NAA for P-MS relative to both control and RR-MS patient participants were recapitulated across two different scan types (GSH-JDE sLASER and GABA-JDE sLASER) as well as in a similar analysis independently applied to age- and sex-matched groups (P-MS N=21, 12 female, 55 ± 1.7 y.o.; RR-MS N = 19, 13 female, 50 ± 2.4 y.o.; control N = 16, 9 female, 52 ± 2.6 y.o.). No significant effect of disease state on ratios of GSH or GABA to total creatine was observed. Quantification of water-referenced absolute cortical metabolite concentrations is ongoing.

Conclusion

Our results suggest that the frontal cortex metabolic signature of progressive multiple sclerosis may exhibit some features distinct from those of relapsing-remitting MS or non-MS control. Small effect sizes for groupwise differences in relative metabolite concentrations may demand higher statistical power in future ^{1}H MRS investigations of this disease.

Clinical Relevance

In vivo measurement of cortical metabolites by ^{1}H spectroscopy continues to demonstrate some promise as a potential means of characterizing heterogeneous variants of MS. Further work is needed to justify the sensitivity of this method to prodromal biomarkers of eventual MS progression.

T_2 quantification by echo-time-variant signal refocusing for accurate measurement of glutathione and other metabolites in the human brain at 7 Tesla

Kelley M. Swanberg[1,2], Hetty Prinsen[2], Daniel Coman[2], Robin A. de Graaf[2,3], and Christoph Juchem[1,2,4,5]
[1]Department of Biomedical Engineering, Columbia University Fu Foundation School of Engineering and Applied Science, 1210 Amsterdam Ave., New York, NY 10027, United States
[2]Department of Radiology and Biomedical Imaging, Yale University School of Medicine, 330 Cedar Street, New Haven, CT 06520, United States
[3]Department of Biomedical Engineering, Yale University School of Engineering and Applied Science, 10 Hillhouse Avenue, New Haven, CT 06511, United States
[4]Department of Radiology, Columbia University School of Medicine, 622 W 168 Street, New York, NY 10032, United States
5Department of Neurology, Yale University School of Medicine, 330 Cedar Street, New Haven, CT 06520, United States

Note: Portions of this work have been accepted as a presentation to the 2017 Annual Meeting of the International Society for Magnetic Resonance in Medicine in Honolulu, Hawaii from April 22 through April 27.

Introduction

Glutathione (GSH) is an endogenously synthesized antioxidant involved in a range of neurological illnesses, including multiple sclerosis, Parkinson's disease, dementia, epilepsy, and others. Proton magnetic resonance spectroscopy (^{1}H MRS) remains a promising means to noninvasively measure GSH and other disease-related compounds in vivo. The accuracy of this method may be limited by uncharacterized disparities in transverse signal decay time T_2 across different compounds, which affects metabolite signal magnitude and therefore apparent concentration at a given time of measurement. The quantification error resulting from such T_2-based differences in signal magnitude becomes especially pronounced at the high echo times demanded by some experiments.

Methods & Results

To date, the quantification of GSH T_2 has been complicated by the complex behavior of a spin system that yields signals overlapping with those of other metabolites. We addressed these issues by extending a previously published method for quantifying the T_2 of GABA to measure that of the glutathione cysteinyl CH_2 in the occipital cortex of nine human adults (five female; mean age 41±S.E.M. 4 years) at 7 Tesla while simultaneously quantifying the T_2 of additional metabolites glutamate, myoinositol, total choline, total creatine, and total N-acetyl aspartate (NAA). We isolated signals from the 2.95-ppm cysteinyl moiety of glutathione from surrounding resonances using *J*-difference editing (JDE) at eight different echo times (72, 109, 117, 127, 192, 222, 282, and 322 ms) and additional refocusing pulse pairs of variable selectivity, frequency offset, and echo time symmetry to maximize the signal at each time point. Application of a monoexponential model to signal across eight echo times yielded smooth fits for GSH, glutamate, myoinositol, and total choline, creatine, and NAA. GSH exhibited a lower T_2 than that of commonly used reference compound total creatine. T_2 of the other metabolites measured, particularly total NAA and creatine, accorded with previously published values quantified without *J*-difference editing.

Conclusion

We successfully applied a protocol using *J*-difference editing and refocusing pulse pairs of variable selectivity, offset, and symmetry to quantify the in vivo T_2 of glutathione and several other metabolites in the human brain at 7 Tesla. Variable T_2 across measured compounds, particularly between GSH and the commonly applied reference creatine, underlines the importance of considering this property in the translation from spectroscopic signal to putative metabolite concentration.

Clinical Relevance

Cortical metabolites measured by ^{1}H spectroscopy constitute potential biomarkers of neurological illness. The practical application of these signals in the clinic depends, however, on their precise quantification. We developed a method that supports this quantification at 7 Tesla, a field strength of growing clinical applicability, by measuring the T_2 of several metabolites, including the historically difficult-to-quantify glutathione.

Semi-Automated Assessment for Distinguishing Glioblastoma and Solitary Brain Metastasis: A Machine Learning Approach

Nathaniel Swinburne[1] , Javin Schefflein[1] , Yu Sakai[2], Iris Chen[2] , Ehsan Tadayon[2] , and Kambiz Nael[1]
[1]Department of Radiology, Mount Sinai Medical Center, New York, NY, United States, [2]Icahn School of Medicine at Mount Sinai, New York, NY, United States

Introduction

Differentiating glioblastoma and solitary brain metastasis in patients with an undiagnosed primary malignancy can be challenging using conventional MR imaging, however accuracy may be improved with the addition of MR diffusion and perfusion parameters [1,2]. Recent advances in machine learning (ML) have demonstrated promise in enabling interpretation of multimodal imaging data to differentiate neoplastic processes within the brain [3,4]. We investigate whether ML evaluation of multimodal MR can reliably differentiate glioblastoma from brain metastasis.

Methods & Results

Methods:

Preoperative MR imaging including fluid attenuated inversion recovery (FLAIR), diffusion-weighted images (DWI), dynamic contrast enhanced (DCE), dynamic susceptibility contrast (DSC) perfusion and post-contrast T1 (T1C+) in patients with solitary enhancing lesions were retrospectively reviewed.

MR perfusion studies were first processed using commercially available FDA-approved software (Olea Sphere, Olea Medical SAS, La Ciotat, France). The arterial input function was selected automatically and multiparametric perfusion maps were calculated using an extended Toft model[5] for DCE and Bayesian probabilistic method for DSC[6]. The relative cerebral blood volume (rCBV) and relative cerebral blood flow (rCBF) from DSC, volume transfer constant from plasma to extravascular extracellular space (EES) (K^{trans}), rate constant between EES to plasma (K^{ep}), plasma volume per unit tissue volume (V^{p}) and EES-volume per unit tissue volume (V^{e}) from DCE in addition to apparent diffusion coefficient (ADC) maps from DWI were calculated and exported from the software for subsequent analysis.

Conventional (T1C+, FLAIR) and above processed maps were then analyzed using the fMRI Software Library (Analysis Group, Oxford, UK) Version 5.0.[7] Preprocessing steps included brain extraction, histogram normalization and coregistration. Adequacy of sequence coregistration was ensured using visual inspection for all cases. Two separate volumes of interest (VOIs) were drawn manually on enhancing tumor and non-enhancing T2 hyperintense (NET2) region using coregistered T1C+ and FLAIR images respectively.

The preprocessed imaging data were utilized for supervised training of a ML classifier using the Pattern Recognition for Neuroimaging Toolbox (PRoNTo; University College London, London, UK) Version 2.0.[8] Training entailed evaluation of labeled (i.e., glioblastoma vs. metastasis) MR imaging data for creation of a support vector machine kernel, which was validated on unlabeled cases using the leave-one-subject-out method. Quantitative analysis from VOIs (including ADC 10th percentile, rCBV 90th percentile, rCBF 90th percentile, k^{trans} 90th percentile, K^{ep} 90th percentile, V^{P} 90th percentile and V^{e} 90th percentile), ML balanced and class-specific accuracies, and receiver operating statistical data were collected. Balanced accuracy is a weighted composite of the individual accuracies obtained for each test case and is sensitive to any imbalance in the number of subjects in each classification group. Individual class accuracies are adjunctive measures that may reveal whether a trained model favors one class over another.

Results:

Surgical pathology revealed glioblastoma in 7 patients and metastasis in 5 patients (lung carcinoma=2, esophageal carcinoma=1, melanoma=1, neuroendocrine carcinoma=1). Patient demographics included 7 male and 5 female with average age 52 ± 11 years. The trained ML kernel discriminated with 72.6% balanced accuracy (p=0.0001; 10,000 permutations) between glioblastoma [k1] (class accuracy 64.3%; p=0.28; 10,000 permutations) and metastasis (class accuracy 81.0%; p=0.004; 10,000 permutations), with the highest accuracy achieved from combined evaluation of ADC, rCBV, k^{trans} and V^{P} using enhancement-based VOIs. Discrimination accuracy was decreased using NET2 VOIs, yielding 67.6% balanced accuracy (p=0.02; 1000 permutations) for glioblastoma (class accuracy 61.9%; p=0.35; 1000 permutations) and metastasis (class accuracy 73.3%; p=0.08; 1000 permutations).

Conclusion

Given a set of VOIs defined by lesional contrast enhancement, a trained support vector machine kernel can accurately differentiate between glioblastoma and brain metastasis utilizing ADC, rCBV, k^{trans} and V^{P}. VOIs defined by perilesional NET2 yielded a support vector machine kernel with reduced accuracy. A larger prospective study is needed to validate our results.

Clinical Relevance

Although machine learning applications for non-medical imaging are well-established, its use in radiologic imaging interpretation remains nascent. We trained a support vector machine using advanced MR imaging to differentiate glioblastoma and brain metastasis with 72.6% balanced accuracy. The ability for machine learning to aid radiologists in differentiating pathologies with similar appearance on conventional imaging appears promising.

References

1. Calli, Cem, et al. "Perfusion and diffusion MR imaging in enhancing malignant cerebral tumors." European journal of radiology 58.3 (2006): 394-403.
2. Svolos, Patricia, et al. "The role of diffusion and perfusion weighted imaging in the differential diagnosis of cerebral tumors: a review and future perspectives." Cancer Imaging 14.1 (2014): 1.
3. Goetz, Michael, et al. "Learning from small amounts of labeled data in a brain tumor classification task." Second Workshop on Transfer and Multi-Task Learning: Theory meets Practice, Montreal, Canada. 2014.
4. Zacharaki, Evangelia I., et al. "Classification of brain tumor type and grade using MRI texture and shape in a machine learning scheme." Magnetic Resonance in Medicine 62.6 (2009): 1609-1618.
5. Patlak, Clifford S., and Ronald G. Blasberg. "Graphical evaluation of blood-to-brain transfer constants from multiple-time uptake data. Generalizations." Journal of Cerebral Blood Flow & Metabolism 5.4 (1985): 584-590.
6. Boutelier, Timothé, et al. "Bayesian hemodynamic parameter estimation by bolus tracking perfusion weighted imaging." IEEE transactions on medical imaging 31.7 (2012): 1381-1395.
7. M.W. Woolrich, S. Jbabdi, B. Patenaude, M. Chappell, S. Makni, T. Behrens, C. Beckmann, M. Jenkinson, S.M. Smith. Bayesian analysis of neuroimaging data in FSL. NeuroImage, 45:S173-86, 200
8. J. Schrou, M. J. Rosa, J. M. Rodina, A. F. Marquand, C. Chu, J. Ashburner, C. Phillips, J. Richiardi, and J. Mourao-Miranda. PRoNTo: Pattern Recognition for Neuroimaging Toolbox. Neuroinformatics, 11(3):319{337, 2013.

Figures and tables

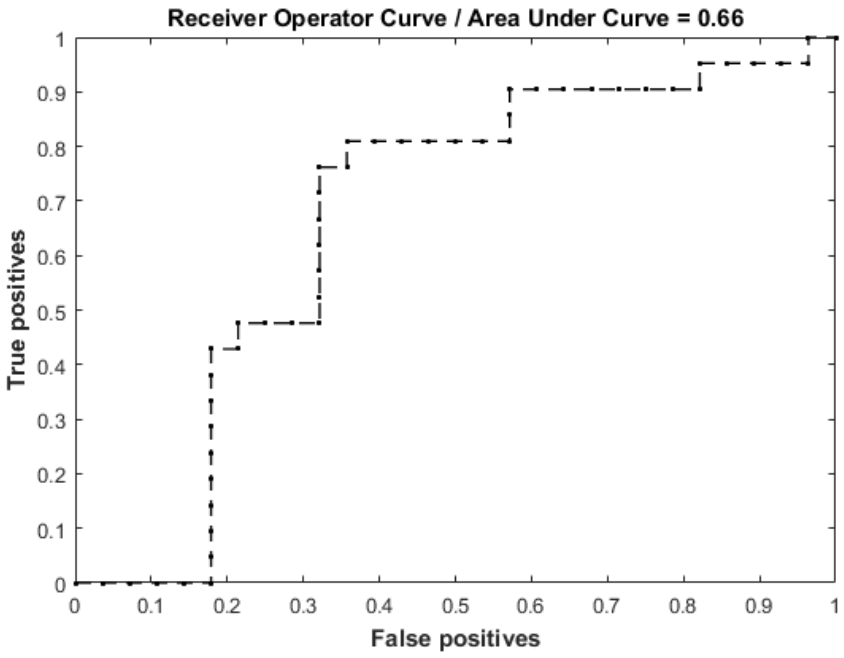

Fig 1 - Receiver Operator Curve for a trained SVM kernel for classification of glioblastoma and brain metastasis using conventional and advanced MR imaging and enhancement-based VOIs.

Spectroscopic Imaging-based detection of 2-hydroxyglutarate (2HG) in IDH1 mutant human gliomas on 3T Clinical MRI

Gaurav Verma[1], Sanjeev Chawla[2], Harish Poptani[3], MacLean Nasrallah[2], Michael Albert Thomas[4], Arati Desai[2], Steven Brem[2], Suyash Mohan[2] Priti Balchandani[1]
[1]Mount Sinai School of Medicine, [2]University of Pennsylvania, [3]University of Liverpook (UK), [4]University of California Los Angeles,

Introduction Mutations in isocitrate dehydrogenase (IDH) have received greater clinical interest with the restructuring of the 2016 WHO Classification of central nervous system (CNS) tumors. These mutations may disrupt the usual catalysis of isocitrate into α-ketoglutarate, instead producing the "oncometabolite" 2-hydroxyglutarate (2HG) (3), present in majorities of WHO Grade II/III gliomas (1,2) and are associated with better prognosis, including longer survival and greater sensitivity to chemo-radiation therapy. Magnetic resonance spectroscopy (MRS) has emerged as a technique for reliably and non-invasively detecting this putative biomarker (4,5)(6)(7)(8) This study aims to assess the performance MRS as part of a routine clinical magnetic resonance imaging (MRI) protocol in detecting 2HG in patients harboring mutant-IDH gliomas.

Methods Fifteen patients harboring gliomas (10 male, 5 female, mean age 57 ± 16.3 years) were scanned using on 3T clinical MRI. CSI scan parameters included TE = 97 ms, TR = 2 s, NEX = 1, 2048 points with BW = 2000 Hz, 16x16 array of 3 cm^3 voxels with 6:53 min scan time. IDH-mutant determination was performed using LCModel fitting where: presence of 2HG in multiple neighboring voxels, with correlation to T_1 contrast or T_2 FLAIR, and CRLB ≤40%. Following biopsy, immunohistochemical (IHC) staining was used to verify IDH mutation status.

Results Figures 1 and 2 show quantified 2HG/Cr maps in patients with gliomas harboring IDH mutation. Both patients showed 2HG in the area of the tumor. Figure 3 shows LCModel-fitted spectra from the same tumor shown in Figure 2 with the 4.02 ppm resonance of 2HG present in the spectra (identified by a red box). Figure 4 shows spectra localized within a wild-type IDH glioma identified as absent of 2HG showing high CRLBs and no resonance visible in the 4.02 ppm range identified by the red boxes. Table 1 shows the performance of LCModel-based quantification of 3T CSI in prospectively detecting presence of 2HG. Four of five gliomas showing presence of 2HG were subsequently identified by immunohistochemistry as mutant-IDH (80% specificity). Five of eight gliomas where presence of 2HG not identified were determined to be wild-type IDH (63% sensitivity). Determination of 2HG presence was not possible for two of the fifteen patients due to poor signal quality.

Discussion & Conclusion

LCModel quantification of 3T CSI data successfully detected 2HG, confirming previous research and suggesting the potential to non-invasively identify IDH mutation in a routine clinical MRI scanning protocol. Prospectively restricting the criteria for determining presence of 2HG to require multiple positive voxels and CRLBs ≤40% resulted in relatively high sensitivity and positive predictive values, but sensitivity lagged behind. This lower sensitivity may be a result of the lower signal quality afforded by routine clinical hardware and scan parameters. Improving signal quality may require larger voxel size, more averages or a more sensitive receiver coil, though these may result in more restrictive inclusion criteria, longer scan times or greater facility costs, respectively.

Clinical Relevance

Non-invasive detection of 2HG could improve and accelerate treatment decisions for mutant-IDH gliomas including initiation of chemo-radiation or other targeted therapies.

Figures and tables

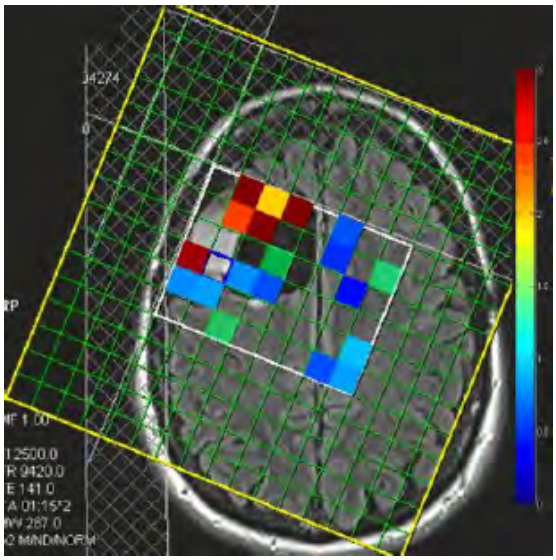

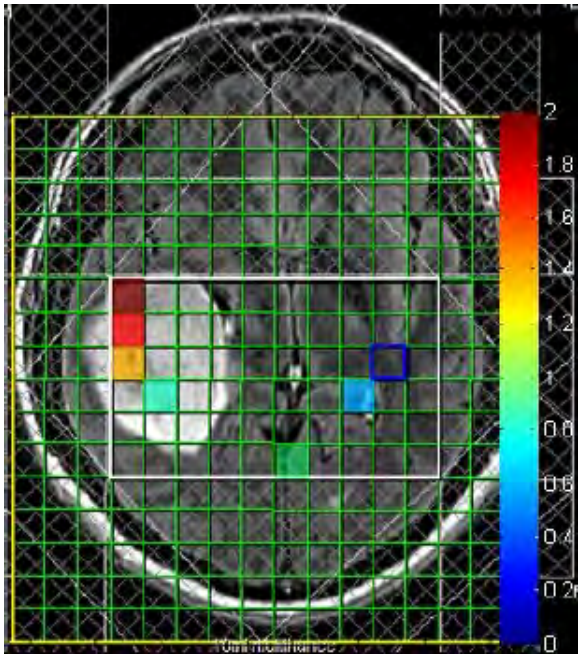

Figure 1 (left): 2HG/Cr map from a mutant-IDH WHO Grade II/III oligodendroglioma patient showing presence of 2HG within the tumor.
Figure 2 (right): 2HG/Cr map from a mutant-IDH WHO Grade III anaplastic astrocytoma patient showing presence of 2HG within the tumor.

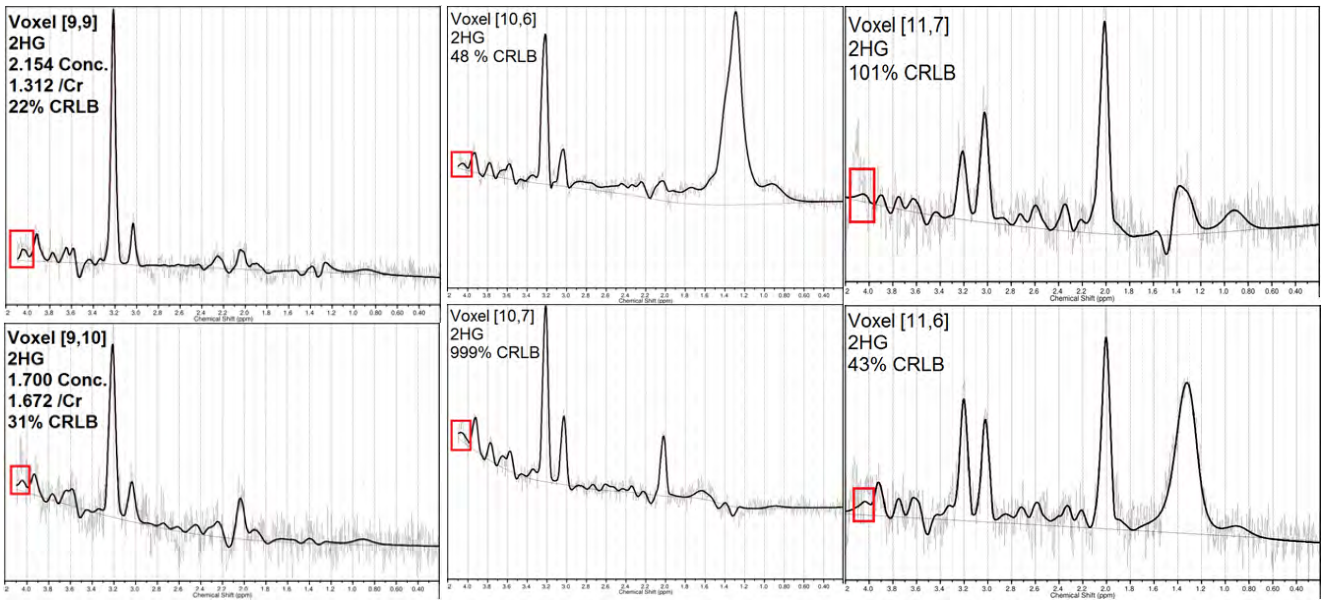

Figure 3 (left): LCModel □tted spectra from enhancing region of a the WHO Grade III mutant-IDH anaplastic astrocytoma as Figure 2. LCModel detected presence of 2HG and 4.02 ppm resonance due to 2HG is identi□ed in the red box.

Figure 4 (right): LCModel □tted spectra from enhancing region of a wild-type IDH glioma. High CRLB values indicate no meaningful detection of 2HG and absence of 2HG resonance at 4.02 ppm is highlighted in red square.

Efficiency in global brain network organization decreases with recency of use in cocaine addicted individuals

A Zilverstand[1], S Kalayci[2,3], P Kundu[4], MA Parvaz[1], T Maloney[1], N Alia-Klein[1,5], ZH Gümüş[2,3], RZ Goldstein[1,5]

[1]Department of Psychiatry; [2]Department of Genetics and Genomic Sciences; [3]Icahn Institute for Genomics and Multiscale Biology;
[4]Department of Radiology, [5]Department of Neuroscience;
All at Icahn School of Medicine at Mount Sinai

Introduction

Previous studies in individuals with cocaine use disorder have focused on describing localized changes in resting-state functional connectivity. Here we used complex network analysis from graph theory to study how the whole-brain network organization is modulated by recency of use. The goal is to investigate if measurements of whole-brain network organization can provide a novel whole-brain tool for monitoring disease status and identifying potential targets for interventions.

Methods & Results

High-resolution resting-state fMRI scans (10 min) were acquired in individuals with recent use (urine positive, N=26, age 47±8 yrs), in abstinent users (urine negative, N=17, age 47±8 yrs) and in race- and gender-matched controls (N=32; age 40±8 yrs; co-varying for age). Imaging data were preprocessed following standard procedures and analyzed with CONN (MIT, Cambridge). For each group, its average connectivity matrix was derived using a 638-region anatomical template, and network structure was visualized using spring-embedded layout with our 3D complex network visualization tool, iCAVE (doi: https://doi.org/10.1101/061374). Global efficiency per brain region was computed to evaluate the functional integration of brain networks.

The resting-state analysis demonstrated linearly decreased global functional integration of frontal and subcortical brain regions as a function of recency of use (recent users < abstinent users < controls). Frontal and subcortical brain networks were less efficiently connected with the rest of the brain, as evidenced both by a lower number of global connections (lower efficiency) and altered position in the network topography (see Figure). Frontal brain regions particularly showed visible disintegration from the global network with more recent use.

Conclusion

Beyond localized changes, these results demonstrate whole-brain changes in functional integration in cocaine addiction. Specifically, we observed reduced global integration of frontal and subcortical regions involved in executive functioning, reward processing and memory, aggravated by recency of use. The altered positioning of these brain regions in the overall network topography suggests changes in neurophysiological mechanisms involving subcortical and frontal brain regions.

Clinical Relevance

Development of novel brain-based interventions may require targeting entire brain networks, rather than focusing on region-specific parameters of brain function. Our results demonstrate that whole-brain resting-state connectivity could be used for identifying targets for interventions and to develop a tool for monitoring disease status.

Figures

Healthy Control Participants

Abstinent Cocaine Users

Recent Users of Cocaine

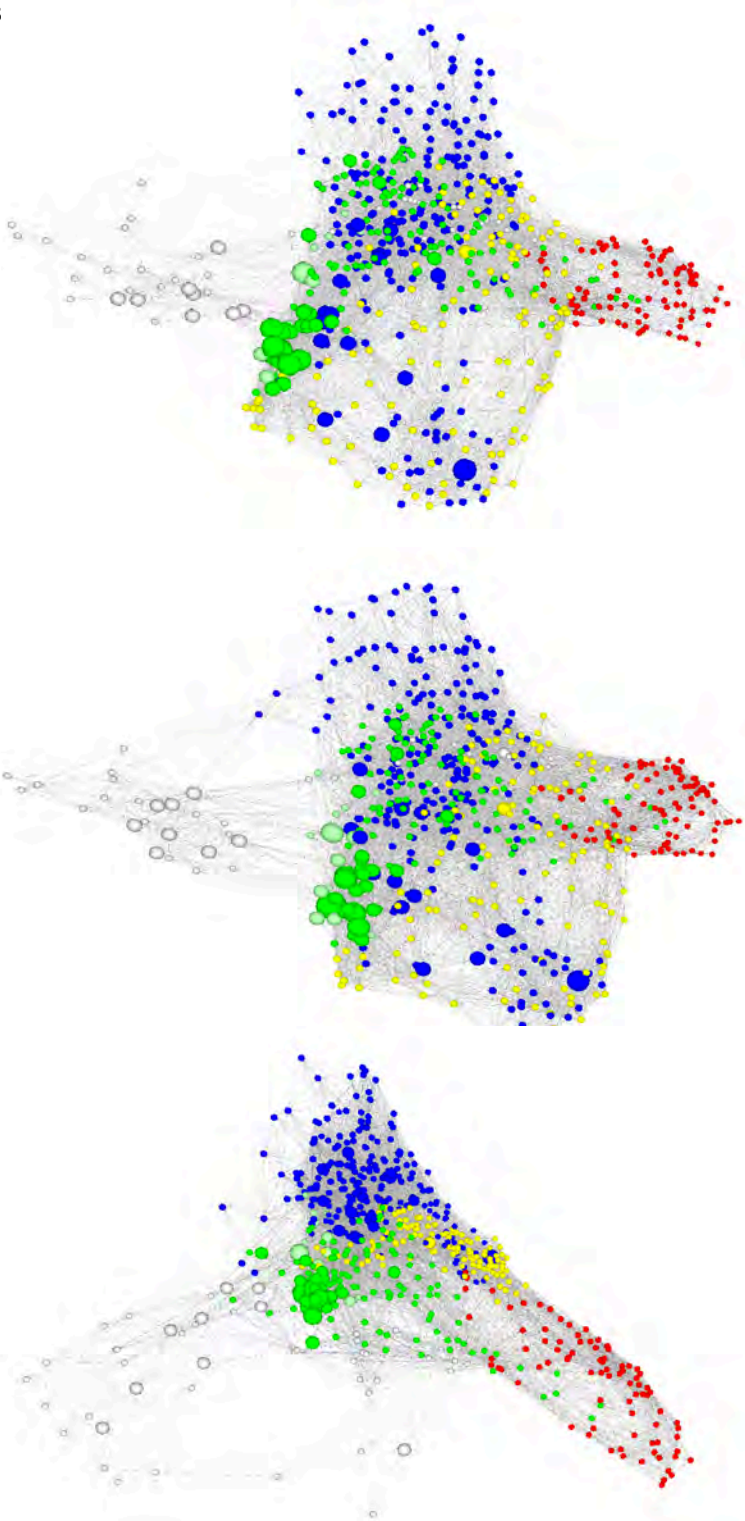

Color

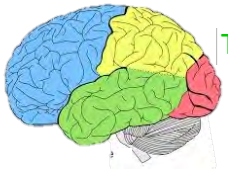

Frontal
Parietal
Temporal
Insula
Occipital
Subcortical

Global efficiency in frontal brain regions with group differences

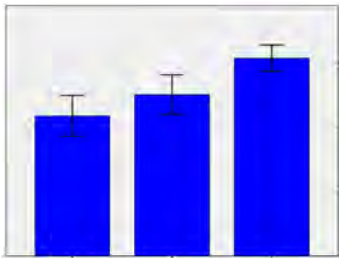

Recent | Abstinent users | Healthy

Global efficiency in subcortical regions with group differences

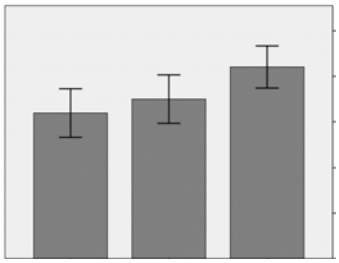

Recent | Abstinent users | Healthy

On the left:
The network structure during resting-state is depicted as a spring-embedded network layout derived from the average group functional connectivity matrix[1]. The nodes are color coded according to the different lobes of the brain. Nodes showing a linear modulation across groups (decreased global efficiency with more recent use) are enlarged.

[1]**Spring embedded networks:** The classical force-directed algorithm treats the network as a physical system with edges analogous to springs and nodes to electrically charged particles that repel each other. The final layout is established at the state at which the repulsive and attractive forces balance each other.

Sponsors & Contributors

Sponsors

GOLD

Bristol-Myers Squibb

Sponsors

Silver

Advanced Accelerator Applications
BRIDGING SCIENCE WITH LIFE

MedisoUSA

SA Instruments, Inc.
Stony Brook, New York

Contributors

FUJIFILM
Value from Innovation

VISUALSONICS

\

TMII Highlights 2016/2017

Icahn School of Medicine a Mount Sinai

Translational & Molecular Imaging Institute

Spring 2016
Issue 10
tmii.mssm.edu

Message from the Director

This has been a very exciting couple of months. We just concluded our 6th Annual TMII Symposium with again excellent invited external and internal speakers that featured and captured the best science from our imaging and nanomedicine research community. Don't miss reading about our selected abstract and poster winners. We have already started planning the TMII 2017 meeting. Please feel free to email me any feedback and suggestions.

That excitement continued with the TMII external advisory board strategic planning (SP) meeting where we received very strong feedback. Thanks for the wonderful input and suggestions as we continue to put together our TMII SP to submit to the Dean's office. I can't thank enough TMII, the Department of Radiology faculty and all other committee members and stakeholders for their hard work and suggestions.

More excitement is apparent by the several stories in this issue celebrating the success of our TMII members such as Dr. Priti Balchandani who secured her first NIH R01 and was bestowed this year with the Harold and Golden Lamppost Research Award. We are also featuring Dr. Claudia Calcagno-Mani for her Scientist Development Grant from the American Heart Association. Just to mention one more, I am proud of my Master's student Chloe Solomon for her Community Service that was Recognized by Mount Sinai Graduate School. Finally, remember to participate in the October 19, 2016 3rd Annual Brain Imaging Center Symposium where Dr. Rita Goldstein (whom we will feature in the upcoming issue) and this year annual meeting committee have organized a very exciting meeting on brain imaging research.

I wish you all a great read of the TMII Newsletter and a great start of the Summer!

Zahi Fayad, PhD
Director, Translational & Molecular Imaging Institute
Professor of Radiology and Medicine
zahi.fayad@mssm.edu

WHAT'S NEW?

TMII News & Updates

The 6th Annual TMII Symposium was again a resounding success. The invited speakers gave visionary talks and the quality (and number) of the abstracts submitted were outstanding. See the special feature inside for more information.

TMII would like to welcome a few new members to the team. Paul Kennedy has joined us from the University of Edinburgh where he completed his PhD on the topic of Magnetic Resonance Elastography (MRE) in skeletal muscle. He will continue his work on MRE with Dr. Taouli's group with particular focus on improving MRE markers of liver, kidney and spleen diseases.

Additionally, the Imaging Core has hired a new full time and part time technologist, Emily Wu and Bill Fazio (respectively) allowing the Core to better address the increase in usage of our systems.

Some of you may have attended the Brainhack Americas event TMII & BIC jointly co-hosted with NYU & The Child Mind Institute. The organizers of this and other Brainhack events have published a great new article in GigaScience, check it out: http://www.gigasciencejournal.com/content/5/1/16/email?from=email

UPCOMING EVENTS

TMII Frontiers of Imaging Seminar Series

> May 26, 2016 1pm - 2pm: James Rudd, PhD - Senior Lecturer, University of Cambridge *TBD* Hess Center - Seminar Room B

> June 23, 2016 1pm - 2pm: Hersh Chandarana, MD - Associate Professor, NYU School of Medicine *TBD* Hess Center - Seminar Room B

> July 27, 2016 1pm - 2pm: Thomas Hope, MD - Assistant Professor, University of California, San Francisco *"Current and future applications of PET/MRI in abdominopelvic malignancies"* Hess Center - Seminar Room B

> July 28, 2016 1pm - 2pm: Michael Hope, MD - Associate Professor, University of California, San Francisco *"Advanced Cardiovascular Imaging Techniques"* Hess Center - Seminar Room B

> August 25, 2016 1pm - 2pm: Aytekin Oto, MD - Professor, University of Chicago *TBD* Hess Center - Seminar Room B

TMII Seminar Series

> May 23, 2016 3pm - 4pm: Sonia Nielles-Vallespin, PhD - Staff Scientist, National Heart, Lung and Blood Institute *"The micro-structural dynamics of myocardial wall thickening. An in vivo cardiac diffusion tensor magnetic resonance imaging study"* Hess Center - TMII Large Conference Room s1-117

For more information on these and other events go to: http://tmii.mssm.edu/events

FACULTY SPOTLIGHT

Ultra High Field 7 Tesla MRI used for Cutting Edge Surgical Treatment

Priti Balchandani, PhD

As the Director of the High Field MRI program at TMII, Dr. Balchandani focuses on developing novel techniques to exploit the power of high-field MR magnets to visualize the brain in unprecedented detail. She leads a team of 7T scientists to devise creative engineering methods to overcome some of the main limitations of operating at high magnetic fields, thereby enabling high-resolution whole-brain anatomical, spectroscopic and diffusion imaging as well as unlocking new contrast mechanisms and sources of signal. In order to achieve these goals, Dr. Balchandani's team focuses on novel radio frequency (RF) pulse and pulse sequence design as well as specialized hardware solutions such as parallel transmission. These techniques are ultimately applied to improve diagnosis, treatment and surgical planning for a wide range of neurological diseases and disorders. Some clinical areas of focus for Dr. Balchandani's team are: improved localization of epileptogenic foci; imaging to reveal the neurobiology of depression; and development of imaging methods to better guide neurosurgical resection of brain tumors.

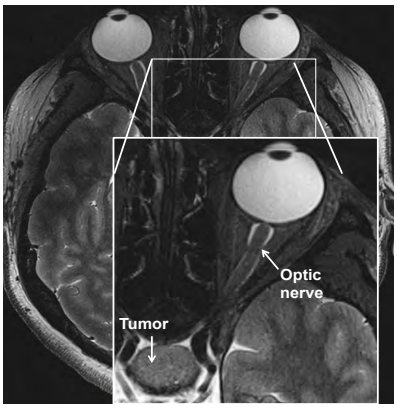

High resolution depiction of optic nerve in relation to pituitary tumor.

In 2016, Dr. Balchandani was awarded an R01 grant from the National Cancer Institute entitled "7T Neurosurgical Mapping Protocol for Endoscopic Resection of Skull Base Tumors" with her Co-Investigator, Dr. Raj Shrivastava, Associate Professor of Neurosurgery. Recently, Priti was named the recipient of The Dr. Harold and Golden Lamport Research Award given to Assistant Professors who show exceptional potential for making significant contributions over an extended period of time. She has also been awarded the NARSAD Young Investigator Grant for her work in imaging depression. Dr. Balchandani is also forging collaborative relationships with institutions such University of Pennsylvania as well as industry partners. As a result of these collaborations, she is acting as PI of the academic sub-award of an upcoming transfer of a NIH Small Business Technology Transfer grant.

Dr. Balchandani has launched the ultra-high field MRI program at TMII and has successfully translated 7T MRI to clinical use. She has already recruited and trained a strong team of scientists and engineers for her research lab and initiated collaborative relationships with clinicians and researchers in Neurosurgery, Neurology, Neuroradiology and Psychiatry. These collaborative relationships have resulted in translational work which has directly benefitted patients and already resulted in several publications and funded grants, including her recent R01.

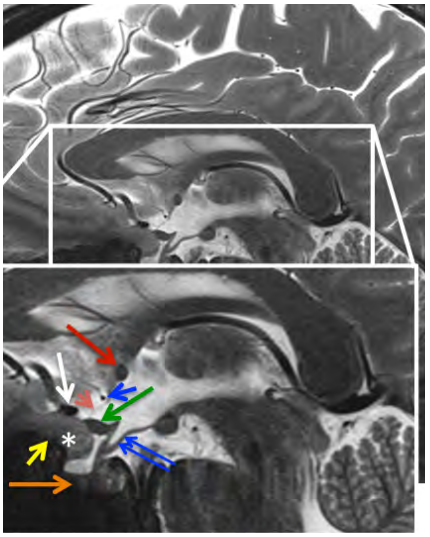

The Balchandani lab has been highly productive over the last year. All lab members, including graduate student Judy Alper, postdoctoral scholar Rebecca Feldman, and former instructor Hadrien Dyvorne, have obtained several talks and posters for the upcoming International Society for Magnetic Resonance in Medicine (ISMRM) meeting in Singapore. Recently, Rebecca Feldman was named junior fellow of ISMRM, a prestigious designation which was also awarded to Dr. Balchandani earlier in her career.

Congratulations to the Balchandani Lab!

Priti Balchandani PhD
Director, TMII High-field MRI
Assistant Professor of Radiology and Psychiatry
priti.balchanani@mssm.edu

SCIENCE SPOTLIGHT

New AHA Funding to Develop Advanced Methods in Cardiovascular Mouse MRI

Claudia Calcagno, MD, PhD

Dr. Calcagno, MD, PhD, is an Instructor of Radiology at the Icahn School of Medicine at Mount Sinai. Her research focuses on the development of non-invasive quantitative imaging to cardiovascular disease, with specific focus on the measurement of atherosclerotic plaque permeability and inflammation with MRI and PET. She has been extensively involved in applying these techniques in pre-clinical drug trials in atherosclerotic rabbits, and clinical trials in humans.

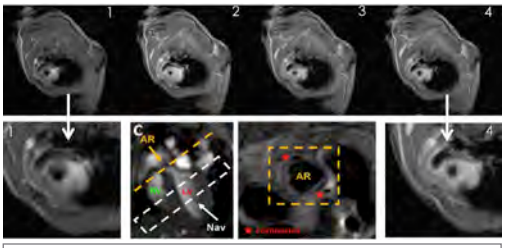

Self-gated dynamic and ECG triggered images of the mouse aortic root are shown before and after contrast agent injection.

Dr. Calcagno was recently awarded a highly competitive Scientist Development Grant from the American Heart Association entitled "Quantitative permeability imaging of the mouse atherosclerotic vessel wall by self-gated DCE-MRI with compressed sensing". This work will develop an optimized self-gated acquisition and compressed sensing reconstruction to develop high temporal and spatial resolution DCE-MRI to quantify endothelial permeability in the aortic root of atherosclerotic mice. By investigating the relationship between imaging, and genetics, cellular and molecular assays in the arterial wall, the application also aims to take the first step in integrating quantitative, non-invasive imaging with -omics in this important animal model of cardiovascular disease.

Claudia Calcagno, MD, PhD
Fayad Lab (Cardiovascular Imaging)
Instructor of Radiology
claudia.calcagno@mssm.edu

IMAGING SPOTLIGHT

Community Service Recognized by Graduate School

Chloe Solomon, BS

Chloe Solomon is first year graduate student in the Masters of Science in Biomedical Sciences (MSBS) who, under the supervision of TMII Director Dr. Zahi Fayad, is examining the relationship between chronic psychological stress and cardiovascular inflammation in patients diagnosed with post-traumatic stress disorder using PET/MR imaging. Chloe was recently recognized for her extensive work in the community when she received the graduate student award for Outstanding Community Service.

As a part of the East Harlem Health Outreach Partnership (EHHOP) http://icahn.mssm.edu/education/medical/clinical/ehhop, a student run clinic at Mount Sinai, Chloe is the Radiology Referrals Manager coordinating all radiology scans for the clinic and helps to resolve patients' outstanding radiology bills.

Chloe is also an advocate for the Sexual Assault and Violence Intervention (SAVI) Program at Mount Sinai. There she advocates and provides crisis counseling for survivors of sexual assault and interpersonal partner violence in seven emergency departments across NYC. For more information: http://www.mountsinai.org/patient-care/service-areas/community-medicine/areas-of-care/sexual-assault-and-violence-intervention-program-savi

As a teacher for MedDocs at Mount Sinai, which provides science enrichment classes to inner city high school students, Chloe in taught two semesters on the cardiovascular system the pulmonary system. For more info: http://webcommons.mssm.edu/meddocs/

Lastly, Chloe volunteered last semester with First Generation Scholars at Mount Sinai that provides one-on-one consulting for high school seniors first in their family to apply to college. She helped a student create her college list, fill out college applications and develop/revise a personal statement. For more information: http://icahn.mssm.edu/education/student-resources/student-organizations/community-outreach/first-generation-scholars

Chloe Solomon, BS
Fayad Lab (Cardiovascular Imaging)
Graduate Student - Biomedical Sciences
chloe.solomon@icahn.mssm.edu

CORE SPOTLIGHT

TMII Human Imaging Core

TMII Human Imaging Core is the backbone of the Translational and Molecular Imaging Institute and is responsible for coordinating, supporting and executing imaging research at Mount Sinai including, neuroimaging, cardiovascular imaging, cancer imaging, nanomedicine (molecular imaging and drug delivery), and image processing.

The Core is fully staffed to support all the image acquisition (1.5T, 3T, 7T, PET/MRI, PET/CT, Dual Source CT, Ultrasound), image analysis, scheduling, and performance of the proposed experiments. The Core has an extensive and expanding inventory of research imaging facilities and equipment, including ancillary support which encompasses exam rooms, imaging processing workstations, and laboratories (wet lab space, cell and chemistry preparation and a radionuclear lab). The Core's resources are fully supported by user fees drawn from research grants, instrumentation grants, industry contracts, and agreements. Our core facilities are available for use to all qualified investigators from academic, medical, government, and industry laboratories.

SPECIAL FEATURE

6th TMII Symposium

April 22, 2016

The 6th Annual TMII Symposium was held at the Icahn School of Medicine to nearly 200 attended from departments and campuses across Mount Sinai Health System, including ISMMS, St. Luke's, West and Beth Israel, as well as area institutions such as SUNY Stony Brook, NYU, Rutgers, Columbia, MSKCC, Albert Einstein College of Medicine and NHLBI.

Thank you to all those who attended and who helped organize.

World renowned in their fields, the invited speakers discussed

- Cutting edge methods in connectivity in human brain,

Bruce Fischl, PhD - Harvard/MGH - Keynote speaker

- PET imaging in Alzheimer's disease,

(right) Julie Price, PhD - University of Pittsburgh - Neuroimaging Session - moderated by Priti Balchandani, PhD - ISMMS (left)

- Quantitative imaging using MRI Fingerprinting

Mark Griswold PhD - Case Western Reserve University - Cancer/ Body Session

- Image-guided cancer therapy using nanomedicine and

(left) Anna Moore, PhD - Havard/MGH - Nanomedicine Session moderated by Willem Mulder ISMMS (right)

- The latest advance in vessel wall imaging using MR coronary angiography.

Debiao Li, PhD - Cedars Sinai Medical Center - Cardiovascular Imaging Session

Videos of the talks are available now. You can find them on the TMII YouTube playlist or follow the link: http://tmii.mssm.edu/tmii2016.

From the 50 abstracts submitted 4 were and chosen for talks

- Alan Seifert, PhD (ISMMS) "DANTE-EPI for CSF Suppression in Cervical Spinal Cord BOLD fMRI at 7T" - Neuroimaging Session
- Stefanie Hectors, PhD (ISMMS) "Assessment of tumor heterogeneity in hepatocellular carcinoma using combined DCE-MRI and BOLD measurements" - Cancer/Body Imaging Session
- Yiming Zhao, PhD (ISMMS) "Augmenting drug-carrier compatibility improves tumor nanotherapy efficacy" - Nanomedicine Session
- Joseph Lerman (NHLBI) "Lack of improvement in aortic vascular inflammation is associated with an increase in coronary plaque burden in psoriasis" - Cardiovascular Imaging Session

Additionally, one poster from each program was awarded Best Poster:

- Ronan Abgral, (ISMMS/University of Brittany) "Usefulness of Combined FDG-PET/MRI to Diagnose Active Cardiac Sarcoidosis" - Cardiovascular Imaging
- Octavia Bane, (ISMMS) "Assessment of inter platform variability of T1 quantification methods used for DCE-MRI in a multicenter QIN phantom study" - Cancer/ Body Imaging
- Lindsay Hill, (NYU) "Rapid Qualification of Gadolinium in Nanoparticles by Time-Resolved Fluorescence" - Nanomedicine
- Rafael O'Halloran, (ISMMS) "Clustered, Connectivity-Based Surgical Planning for Deep Brain Stimulation" - Neuroimaging

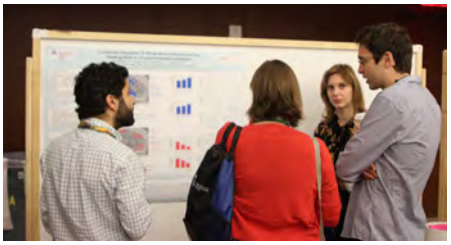

International Society for Magnetic Resonance in Medicine - 24rd Annual Meeting & Exhibition
May 7 - May 13, 2016 - Singapore

Phil Robson	Motion Averaged MR-Based Attenuation Correction for Coronary 18F-Fluoride Hybrid PET/MR	Poster	CV Novel Techniques	12-May	13:30	Fayad	Cardiovascular
Alison Pruzan	Feasibility of Vessel Wall Imaging of the Superficial Palmar Arch using 7T and 3T MRI	E-Poster	Atheroslerosis Imaging	9-May	10:45	Fayad	Cardiovascular
Claudia Calcagno	Distribution and metabolism of 89Zr-labeled HDL nanoparticles in atherosclerotic rabbits: in vivo, longitudinal imaging with PET/MRI	Oral	Whole Body PET/MRI	12-May	10:30	Fayad	Cardiovascular
Claudia Calcagno	Optimization of 3 dimensional (3D), high resolution T2 weighted SPACE for carotid vessel wall imaging on a 7T whole-body clinical scanner	Oral	Atheroslerosis Imaging	12-May	13:30	Fayad	Cardiovascular
Stefanie Hectors	MR elastography and DCE-MRI of the liver and spleen for non-invasive prediction of portal pressure	Oral	Hepatobiliary I: Liver Perfusion/ Flow & Function	9-May	14:15	Taouli	Cancer/Body
Stefanie Hectors	Intravoxel incoherent motion diffusion-weighted imaging of hepatocellular carcinoma: is there a correlation with flow and perfusion metrics obtained with dynamic contrast-enhanced MRI?	Oral	Abdominal Technique & Pulse Seq	11-May	10:00	Taouli	Cancer/Body
Stefanie Hectors	Prostate DWI: comparison of a shorter diagonal acquisition to standard 3-scan-trace acquisition	E-Poster	Prostate Cancer	9-May	11:45	Taouli	Cancer/Body
Cheuk Tang	Relationship between neuropsychological stress and inflammation: a PET and MRI study.	Oral	Pychiatric Disorders: Translational Approaches	12-May	16:00	Tang	Neuro/ Cardiovasular
Victoria Wang	Functional connectivity and neuroanatomical differences in a stress susceptible and resilient mouse model	E-Poster	Psychiatric Disorders: General	10-Dec	13:30	Tang	Neuro
Cheuk Tang	Transient Changes in White Matter Microstructure during Anesthesia	E-Poster	Microstructure in Health & Disease	10-May	13:30	Tang	Neuro
Lazar Flysher	Diffusion Method to Image Normal Human Optic Nerve	Poster	Head & Neck	9-May	10:45	Tang	Neuro
Judy Alper	Frequency Shift Imaging (FSI) for characterization of cells labeled with superparamagnetic iron-oxide nanoparticles	E-Poster	Pulse Sequences	10-May	10:00	Balchandani	Neuro
Rebecca Feldman	B1-Insensitive Simultaneous Multi-Slice DWI at 7T using SEAMS PINS	Poster	RF Pulses	10-May	16:00	Balchandani	Neuro
Rebecca Feldman	7T MRI detection of epileptogenic foci in previously non-lesional patients with focal epilepsy	Oral	Epilepsy	11-May	16:00	Balchandani	Neuro
Rebecca Feldman	Perivascular Space Analysis in Non-lesional Epilepsy: Exploring a Biomarker for Epilepsy	Oral	Epilepsy	11-May	16:00	Balchandani	Neuro
Hadrien Dyvorne	Evaluation of 7T MRI for endoscopic surgical planning and guidance for skull base tumors - preliminary experience	Poster	Brain Tumors: Pre-Clinical & Clinical Applications	9-May	10:45	Balchandani	Neuro
Rafael O'Halloran	U-fiber Quantification in Non-Lesional Epilepsy	Oral	Diffusion Tractography	9-May	14:15	O'Halloran	Neuro/BIC
Joo-won Kim	Non-linear Distortion Correction in Human Optic Nerve Diffusion Imaging	Poster	Diffusion Analysis and Tractography	11-May	10:00	Xu	Neuro
Alan Seifert	DANTE-EPI for CSF Suppression in Cervical Spinal Cord BOLD fMRI at 7T	E-Poster	Acquisition	11-May	10:00	Xu	Neuro
Joseph Borello	Towards accurate spinal cord morphometry with in situ grid phantom calibrated gradient non-linearity correction	Oral	Spine Imaging: Normal Structure/ Novel Methods	13-May	08:00	Xu	Neuro
Prantik Kundu	High-Frequency and Other Pathological Network Hemodynamics Observed in Epilepsy Patients Imaged With Multi-Band Multi-Echo BOLD Functional MRI at 7T	Oral	fMRI of Disease	9-May	16:30	Kundu	Neuro/BIC
	HONORS, AWARDS & STIPENDS						
Rebecca Feldman	Selected as Junior Fellow to ISMRM					Balchandani	Neuro
Rebecca Feldman	Travel Award					Balchandani	Neuro
Judy Alper	Educational Stipend					Balchandani	Neuro
Priti Balchandani	Distinguished Reviewer for 2015 in the journal Magnetic Resonance in Medicine					Balchandani	Neuro
Joseph Borello	Educational Stipend					Xu	Neuro
Joseph Borello	Waived Registration Cost					Xu	Neuro
Joo-won Kim	Waived Registration Cost					Xu	Neuro
	MODERATORS, EDUCATIONAL TALKS, & Study Groups						
Priti Balchandani	Moderator		Head & Neck	7-May	16:30	Balchandani	Neuro
Priti Balchandani	Moderator		Characterizing Field Environment in the MR Scanner: B0, B1 & Gradients	12-May	13:30	Balchandani	Neuro
Joo-won Kim	Non-linear Distortion Correction in Human Optic Nerve Diffusion Imaging	Poster	Diffusion Study Group	10-May	16:00	Xu	Neuro
Rafael O'Halloran	K-Space	Educational Talk	MR Physics & Techniques for Clinicians	9-May	17:50	O'Halloran	Neuro/BIC
Willem Mulder	Theranostics: Delivering Drug & Contrast Agent Simultaneously	Educational Talk	Imaging Drug Delivery & Drug Function	10-May	13:30	Mulder	Nanomedicine
Willem Mulder	Chair		Molecular Imaging Study Group	TBD	TBD	Mulder	Nanomedicine

Organization for Human Brain Mapping - 2016 Annual Meeting - June 26-30, 2016 - Geneva, Switzerland

Researcher	Title	Format	Session	Day	Time	PI	TMII Program
Benjamin Ely	Functional Region of Interest Optimization for Small Structures Like the Habenula	Poster	TBD	TBD	TBD	Xu	Neuro
Joo-won Kim	Repeatability and Reproducibility of Objective Semi-automated Human Habenula Segm	Poster	TBD	TBD	TBD	Xu	Neuro
Rafael O'Halloran	Clustered, Connectivity-Based Surgical Planning for Deep Brain Stimulation	Poster	TBD	TBD	TBD	O'Halloran	Neuro/BIC

BIC CORNER

Congratulations to Dr. Willem Mulder, who placed first among more than 40 participants in the first annual BIC 10k event in Central Park. The drizzling rain cooperated by ending just before the start and seemed to invigorate everyone. Please have a look through pictures of many of the fit and happy participants on the BIC website: https://bic.mssm.edu/about/2016-bic-10k/.

On October 19, 2016, please plan to attend the 3rd Annual BIC Symposium. Advance registration is now open and can be completed online at https://bic.mssm.edu/blog/bicday/bicdayregistration/. The organizing committee has arranged for Helen Mayberg MD to present the keynote address before the series of sessions on computational approaches to neuropsychiatric disease, novel and naturalistic fMRI methods, and brain stimulation. Poster presentations will be followed by time for wine and cheese. The symposium flyer is attached and we look forward to seeing you there!

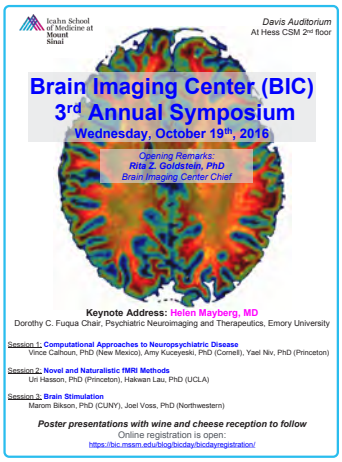

At the 7T high-field MRI, installation of the video and audio capabilities for presenting and collecting functional data is complete and finishing testing. You can contact the BIC technical group to inform us of your plans for research at 7T (as well as 3T and PET-MR/mMR) and to solicit feedback and advice. A survey to describe planned studies is available at https://www.inchoir.org/redcap/redcap/surveys/?s=yvQFxxdbJV. The BIC website now allows registration using your existing Mount Sinai account for single-sign-on with your familiar account name and password. When you logon, and as NIH submission deadlines approach, please remember the importance of including BIC in applications for funding. A document with reference language for justifications of support is available for use in grant preparations, at https://bic.mssm.edu/blog/including-bic-in-upcoming-nih-grant-submissions/.

CONTACTS

Zahi A. Fayad, PhD
Director, Translational and Molecular Imaging Institute

Director, Cardiovascular Imaging Program

Professor of Radiology and Medicine (Cardiology)
zahi.fayad@mssm.edu

Priti Balchandani, PhD
Director, High-Field MRI Program

Assistant Professor of Radiology and Neuroscience
priti.balchandani@mssm.edu

Prantik Kundu, PhD
Chief, Image Analysis Section & Advanced Functional Neuroimaging Section - BIC Faculty

Assistant Professor of Radiology and Psychiatry
prantik.kundu@mssm.edu

Venkatesh Mani, PhD
Director, Cardiovascular Imaging Clinical Trials Unit

Assistant Professor of Radiology
venkatesh.mani@mssm.edu

Willem J. M. Mulder, PhD
Director, Nanomedicine Program

Professor of Radiology
willem.mulder@mssm.edu

Rafael O'Halloran, PhD
Chief, Imaging Acquisition - BIC Faculty

Assistant Professor of Radiology and Psychiatry
rafael.ohalloran@mssm.edu

Cheuk Y. Tang, PhD
Director, Imaging Core

Associate Professor of Radiology and Psychiatry
cheuk.tang@mssm.edu

Bachir Taouli, MD
Director, Cancer and Body Imaging Program

Professor of Radiology and Medicine
bachir.taouli@mountsinai.org

Junqian Gordon Xu, PhD
Neuroimaging

Assistant Professor of Radiology and Neuroscience
junqian.xu@mssm.edu

Christopher J. Cannistraci, MS
Program Manager

Technical Operations Manager
christopher.cannistraci@mssm.edu

Ways to keep in touch

Twitter: @TMIInyc
Facebook: TMII.SINAI
Youtube: https://www.youtube.com/playlist?list=PLqLDR0CTP9_otAZpwEy3EgOStthPo7V9f
Linkedin: https://www.linkedin.com/groups/Translational-Molecular-Imaging-Institute-TMII-8358896/about

Website: http://tmii.mssm.edu

Mailing Address: One Gustave L. Levy Place, Box 1234
New York, NY 10029
Numbers: Tel: (212) 824-8466 Fax: (646) 537-9589

Icahn School of Medicine at Mount Sinai

Translational & Molecular Imaging Institute

Fall 2016
Issue 11
tmii.mssm.edu

Message from the Director

Hope you all had an exciting Summer with some time for rest and rejuvenation. My summer was great. Like all of you I love that time of the year, sun, beach, family time but also a time to reflect, learning new things and recharging. I keep learning that the "key to resilience is trying really hard, stopping, recovering and repeating" (https://hbr.org/2016/06/resilience-is-about-how-you-recharge-not-how-you-endure). It is apparent that all of us at TMII are practicing this routine with glimpses about this given in this Newsletter.

We look forward to the October 9 Brain Imaging Center Annual Symposium which promises again to be as stimulating and successful as in past years. Your hard work is also leading to top publications, patents, research grants, and new application such as the new AHA Scientific Development Grant by one of our junior faculty member Dr. Carlos Perez-Medina on PET imaging of atherosclerosis.

Other announcement such as the TMII seminar series, TMII 2nd Annual TMII Medical Imaging and Bioengineering lecture by Dr. Todd Constable from Yale and the TMII 2017 7th Annual Symposium (April 7, 2017). We also feature Dr. Venkatesh Mani and his clinical trial unit efforts and group, mentoring activities within TMII, one of your F31 fellow Benjamin Ely, and some quick updates from BIC and recent exciting developments and new services which we will feature in more details in an upcoming issue.

Again, I thank all of you for making all this possible and wish you a great TMII newsletter read. Finally, I cannot conclude this message without expressing all our best and wishes to our most resilient leader Dean Dennis Charney.

Zahi Fayad, PhD
Director, Translational & Molecular Imaging Institute
Professor of Radiology and Medicine
zahi.fayad@mssm.edu

WHAT'S NEW?

TMII News & Updates

Congratulations to Carlos Perez-Medina, PhD on his recently awarded AHA Scientist Development Grant. This 3 year grant, of over $230,000, will help Dr. Perez-Medina study "Atherosclerosis phenotyping and targeted treatment by nanoreporter PET imaging"

TMII would like you to join us and welcoming Francesco Padormo, PhD to the group. Dr. Padormo obtained his PhD in MRI Physics from Imperial College London in 2012. He then undertook a postdoc at King's College London, working on Parallel Transmission at 3T and 7T in collaboration with Oxford University. Now working under Priti Balchandani, PhD, he will be developing imaging methods for 7T.

Dr. Fayad's graduate student Mootaz Eldib, PhD successfully defended his PhD distertation and has moved on to a biotech company upstate.

Don't forget the abstract submission deadline for the ISMRM 25th Annual Meeting & Exhibition, November 9, 2016.

Lastly, TMII has reached another major milestone, @TMIInyc has surpassed 100 followers on Twitter. Follow us and stay current on the latest happenings.

UPCOMING EVENTS

TMII Frontiers of Imaging Seminar Series

> Sept 27 2017 - 1pm - 2pm: CSM Davis Seminar Room B - *Hersh Chandarana, PhD* Associate Professor, Department of Radiology, NYU School of Medicine "Motion robust continuous comprehensive abdominal MR imaging"

TMII Seminar Series

> Oct 4, 2016 - 10am - 11am: CSM Davis Seminar Room A - *Mark Does, PhD,* Professor of Biomedical Engineering, Vanderbilt University "Advances in MRI Methods of Evaluating Bone Fracture Risk"

2nd Annual TMII Medical Imaging and Bioengineering Lecture

> Dec 16, 2016 - 2pm - 3pm: CSM Davis Auditorium - *R. Todd Constable, PhD,* Professor Radiology and Biomedical Imaging, Yale University Medical School "Connectome Predictive Models: Brain/Behavior Predictions and Extension to Clinical Variables"

For more info on these and other events go to http://tmii.mssm.edu/events

FACULTY SPOTLIGHT

Leading Academic Research Organization in Cardiovascular Imaging

Venkatesh Mani, PhD

Venkatesh Mani is a Biomedical Engineer by training. His undergraduate education was completed in India and he graduated summa cum laude from the Manipal Institute of Technology; a college whose notable alumni include the current CEOs of Microsoft and Nokia. He then completed his graduate education also in Biomedical Engineering at Virginia Commonwealth University before joining Dr. Fayad's lab in Mount Sinai as a post-doctoral fellow in 2002. He is currently Assistant Professor of Radiology.

Dr. Mani's research interests include multimodality imaging of cardiovascular diseases, specifically focusing on atherosclerosis, thrombosis and their complications using PET, CT, ultrasound and MRI. Over the years, he has developed several novel imaging and analysis methodologies for cardiovascular MRI and PET/CT and has been instrumental in pioneering the widespread application of these imaging techniques all the way from pre-clinical studies to multi-center clinical drug development trials that use imaging as an endpoint. Some of the technical developments that Dr. Mani has pioneered include MRI methods for fast dark blood vessel wall imaging, methods to suppress flow signal for fast T1 species for optimized dark blood imaging, development of methods for positive contrast imaging of iron oxide particles and development of methods for dynamic contrast enhanced MRI. Additionally, he has developed methods for image analysis such as the use of spatially enhanced cluster analysis for quantifying images of atherosclerotic plaque, been involved in the development and validation of PET/MR as a modality for cardiovascular imaging.

Dr. Mani is Director of the Cardiovascular Imaging Clinical Trials Unit of TMII. It is a modern hybrid between a contract research organization (CRO) and an imaging core lab. It undertakes and manages all aspects; ranging from scientific conduct to administrative management of clinical trials with imaging endpoints led by the cardiovascular group of TMII. Typical services offered include but are not limited to trial design and consultation, imaging protocol development, site training and qualification, data repository and database management, data quality control and analysis, and publication support. In addition to Dr. Mani, the core members of this group (pictured above) are Sarayu Huang, data manager, Audrey Kaufman, radiologist/image analyst, Alison Pruzan, image analyst and Renata Pyzik, research coordinator. Drs. Fayad, Calcagno, Robson, Jacobi and Karakatsanis also currently provide scientific expertise to this unit, and Dr. Gilbert Aguinaldo and Catherine Ma provide help with budgets and contracts for the group. The group is currently overseeing 3 pharmaceutical-sponsored clinical trials examining vascular inflammation, atherosclerotic burden and pulmonary embolism with 2 more currently in the pipeline. Additionally, the group is also currently serving as the core laboratory for 3 NIH sponsored clinical trials with 2 more in the pipeline.

Venkatesh Mani, PhD
Director, Cardiovascular Imaging Clinical Trial Unit (CICTU)
Assistant Professor of Radiology
venkatesh.mani@mssm.edu

SCIENCE SPOTLIGHT

Training the Future

The Translational Molecular Imaging Institute (TMII) and the Department of Radiology have an active joint mentoring program for imaging scientists ranging from graduate students and postdoctoral fellows to junior faculty. This program, which is chaired by the TMII director, Dr. Zahi Fayad, provides mentoring resources and promotes academic progress for young scientists, and is assessed annually by the institution and department leadership. As part of TMII, trainees have access to a variety of resources for training, spanning from one-on-one interactions with a diverse body of faculty members (experts in clinical and pre-clinical cardiovascular, body, and neuroimaging, as well as nanomedicine), to more formal training opportunities such as lectures, TMII Frontiers of Imaging seminar series, and the yearly TMII symposium.

Imaging is inherently interdisciplinary. New predoctoral and postdoctoral trainees at TMII have the opportunity to apply for various NIH T32 training programs in collaborating departments of neuroscience, oncology, pharmacology, or immunology. If accepted by these competitive T32 training programs, the T32 trainee will be exposed not only to laboratory research, but also the particular T32 educational program with formal course work, seminar series, journal clubs and work in progress meetings.

Whether or not participating in any T32 program at Mount Sinai, predoctoral and postdoctoral trainees at TMII are highly encouraged to apply for NIH NRSA F31 (predoctoral) or F32 (postdoctoral) fellowship, or similar foundation fellowship, as mentored by faculty advisors. The entire fellowship application process is a great opportunity to sharpen research hypothesis, gain experiences in grantsmanship, and foster maturation towards an independent career. The outstanding body of faculty members at Mount Sinai provides ample opportunities for co-mentoring (as in the case of Benjamin Ely's F31 predoctoral fellowship, featured in this issue). At the predoctoral level, the focus is on mentoring trainees to conduct fruitful and impactful dissertation research without significant delays in PhD defense. At the postdoctoral level, besides research productivity, additional focus is put on career independence, with protected time at the end of postdoctoral training for grant writing, networking, and faculty-level job search.

Should some postdoctoral fellows decide to develop his/her independent research career at Mount Sinai, TMII has instructor level positions open for qualifying candidates.

SCIENCE SPOTLIGHT

Training the Future - continued

Selected recent achievements of trainees in Dr. Junqian Xu's Neuroimaging laboratory

Benjamin Ely (graduate student in Neuroscience, co-mentored with Drs. Vilma Gabbay and Emily Stern)

1. NIMH F31 NRSA predoctoral fellowship [see below]
2. Open Science Grid (OSG) User School 2016: full travel stipend.

Joseph Borrello (graduate student in Biomedical Science, co-mentored with Dr. Kevin Costa)

1. 24th Annual Meeting of the International Society for Magnetic Resonance in Medicine (ISMRM): Summa cum laude Award and New Entrant educational stipend for his oral presentation, titled "Towards accurate spinal cord morphometry with in situ grid phantom calibrated gradient non-linearity correction".

Dr. Alan Seifert (post-doc) TMII

1. Gordon Research Conference (GRC) 2016: In-vivo Magnetic Resonance: outstanding poster award and travel stipend for his abstract, titled "Myelin density measurement by ZTE in the D2O-exchanged spinal cord is unaffected by tissue fixation".
2. Radiological Society of North America (RSNA) 2016: travel stipend for his Introduction to Academic Radiology for Scientists (ITARSc) program acceptance and his oral presentation, titled "Structural, functional, and diffusion MRI of the cervical spinal cord at ultra-high field".

Dr. Joo-won Kim (post-doc) TMII

1. 24th Annual Meeting of the ISMRM: Trainee educational stipend and the Diffusion & Perfusion study group selection of his poster, titled "Non-linear distortion correction in human optic nerve diffusion-weighted image".
2. 32nd Congress of the European Committee for Treatment and Research in Multiple Sclerosis (ECTRIMS): travel stipend for his poster, titled "Reproducible quantitative cervical spinal cord MRI for progressive MS".

Junqian "Gordon" Xu PhD
Assistant Professor, Radiology & Neuroscience
Neuroimaging Section
junqian.xu@mssm.edu

IMAGING SPOTLIGHT

Predoctoral Fellowship Award

Benjamin Ely, BS

I am a fourth year graduate student in neuroscience. My PhD dissertation project examines the role of reward circuitry in psychiatric disorders, particularly major depression, using high-resolution fMRI and high-fidelity analysis techniques. I am particularly interested in the habenula (Hb), a pair of small nuclei near the dorsomedial thalamus that inhibits dopaminergic reward signaling in a range of animal models. Mounting evidence implicates the Hb in depression; however, in vivo imaging research has been limited by its small size.

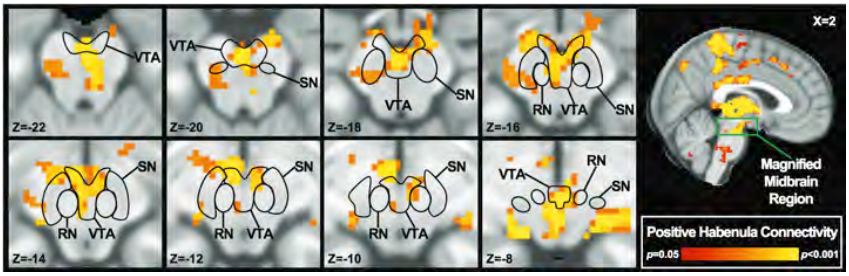

Building on the recent advances in fMRI resolution and the objective Hb segmentation methodology developed by our group (Kim J-W et al., NeuroImage, 2016), last year I conducted the first-ever whole-brain Hb resting-state functional connectivity study in a healthy adult population (25 with high and 25 with low subclinical depression scores) from the Human Connectome Project (Ely BA et al., Human Brain Mapping, 2016). My analyses revealed Hb connectivity with key reward regions, including the ventral tegmental area (VTA) and anterior cingulate. In addition, Hb connectivity with the amygdala and anterior insula differed between the subclinical depression groups.

This work served as the basis for my F31 NRSA predoctoral fellowship, which was awarded by NIH/NIMH earlier this year. Under the guidance of my mentorship team of Drs. Vilma Gabbay, Emily Stern, and Junqian (Gordon) Xu, I am now pursuing fMRI studies to examine reward processing in depressed patients, as well as refining the definition of small subcortical regions in functional image space, a key analysis step for further Hb fMRI research.

Benjamin Ely, BS
Emily Stern, Junqian (Gordon) Xu, Vilma Gabbay - Co-Mentors
Graduate Student (Neuroscience)
benjamin.ely@mssm.edu

CORE SPOTLIGHT

TMII XNAT Database

TMII XNAT serves as the central point for research data transfer, archive, and sharing. TMII XNAT is built upon a secure database, supports automated pipelines for processing managed data, and provides tools for exploring the data. Only users authorized by the study investigators can access their data. TMII XNAT is fully HIPAA compliant and team provides support for data migration between various DICOM repositories, HIPAA de-identification,

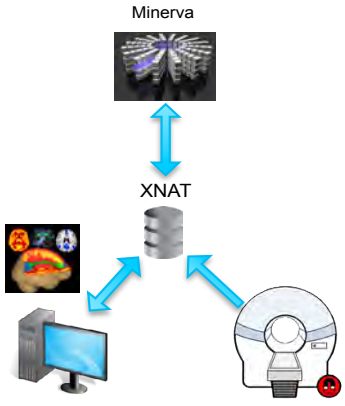

image preprocessing, image quality control, and other customized services. Currently TMII XNAT runs on two mirrored Linux servers with 60TB storage space on each. It can host more than 15,000 image sessions with backups. TMII XNAT user training, documentation, and imaging data management consultations are available by request (https://tmii.mssm.edu/xnat).

BIC CORNER

The Brain Imaging Center's (BIC) Third Annual Symposium is quickly approaching. This year's keynote address will be presented by Helen Mayberg MD, ahead of sessions on Computational Approaches to Neuropsychiatric Disease, Novel and Naturalistic fMRI Methods, and Brain Stimulation. This BIC DAY will be held on Wednesday October 19, so please be sure to register soon at https:\\bic.mssm.edu.

BIC is pleased to announce the new addition of Anna Zilverstand's baby daughter. Her expanded family is reported to be quite happily experiencing the very best neurofeedback nature provides.

BIC's Prantik Kundu and Rafael O'Halloran design and implementation of the web-based BIC. BOT service will be the topic of upcoming presentations at the Department of Psychiatry's Mood and Anxiety Program (9/7 at 2 pm) and BIC User venues this fall. The BICBOT integrates and automates user simplifications for organizing and executing study-wide pre-processing of MRI data. BIC. BOT will unify many of the presently separate operations between the XNAT study database and Minerva supercomputing platforms. Users will immediately benefit from simplification in defining and collecting datasets for processing. Streamlined and self-documenting pipeline operations will substantially increase processing efficiency while eliminating the need for users to operate the Minerva system directly. The system will better-enable BIC's vision for data analysis across multiple studies, leveraging the collection of data using the BIC standard protocol by many Mount Sinai investigators.

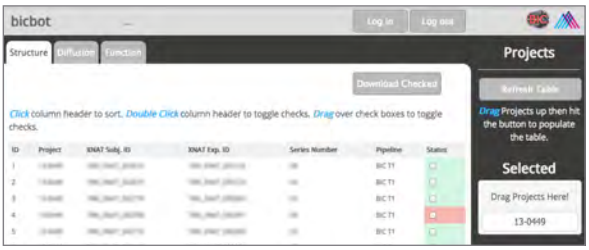

The BIC is also gearing towards supporting the NIH funded multi-site ABCD study, longitudinally tracking elementary level children for the study of brain development, to be launched at Sinai in September.

CONTACTS

Zahi A. Fayad, PhD
Director, Translational and Molecular Imaging Institute

Director, Cardiovascular Imaging Program

Professor of Radiology and Medicine (Cardiology)
zahi.fayad@mssm.edu

Priti Balchandani, PhD
Director, High-Field MRI Program

Assistant Professor of Radiology and Neuroscience
priti.balchandani@mssm.edu

Prantik Kundu, PhD
Chief, Image Analysis Section & Advanced Functional Neuroimaging Section

Assistant Professor of Radiology and Psychiatry
prantik.kundu@mssm.edu

Venkatesh Mani, PhD
Director, Cardiovascular Imaging Clinical Trials Unit

Assistant Professor of Radiology
venkatesh.mani@mssm.edu

Willem J. M. Mulder, PhD
Director, Nanomedicine Program

Professor of Radiology
willem.mulder@mssm.edu

Rafael O'Halloran, PhD
Chief, Imaging Acquisition

Assistant Professor of Radiology and Psychiatry
rafael.ohalloran@mssm.edu

Cheuk Y. Tang, PhD
Director, Imaging Core

Associate Professor of Radiology and Psychiatry
cheuk.tang@mssm.edu

Bachir Taouli, MD
Director, Cancer and Body Imaging Program

Professor of Radiology and Medicine
bachir.taouli@mountsinai.org

Junqian Gordon Xu, PhD
Neuroimaging

Assistant Professor of Radiology and Neuroscience
junqian.xu@mssm.edu

Christopher J. Cannistraci, MS
Program Manager

Technical Operations Manager
christopher.cannistraci@mssm.edu

Ways to keep in touch

Twitter: @TMIInyc
Facebook: TMII.SINAI
Youtube: https://www.youtube.com/playlist?list=PLqLDR0CTP9_otAZpwEy3EgOStthPo7V9f
Linkedin: https://www.linkedin.com/groups/Translational-Molecular-Imaging-Institute-TMII-8358896/about

Website: http://tmii.mssm.edu

Mailing Address: One Gustave L. Levy Place, Box 1234
New York, NY 10029
Numbers: Tel: (212) 824-8466 Fax: (646) 537-9589

TMII Human Imaging Core

Mount Sinai TMII Translational and Molecular Imaging Institute

Cheuk Ying Tang, Dr. Lazar Fleysher, Dr. Johnny Ng, Edmund Wong, Daniel Samber, Victoria Wang, Chen Yang, Christopher Cannistraci

Skyra

PET/MR

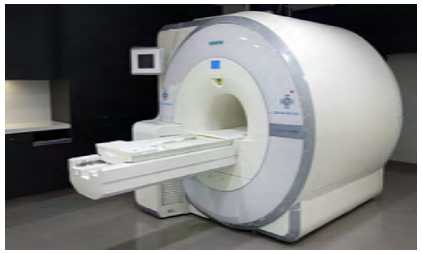

7T

Force CT

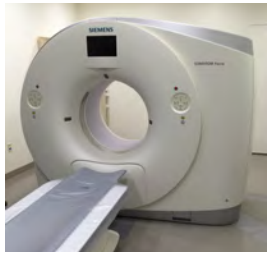

MR Simulator

Neuro-testing room

Clinical Exam room

TMII Neuro Functional Imaging Peripherals

Anesthesia Support

TMII Server & Cluster in Data Center

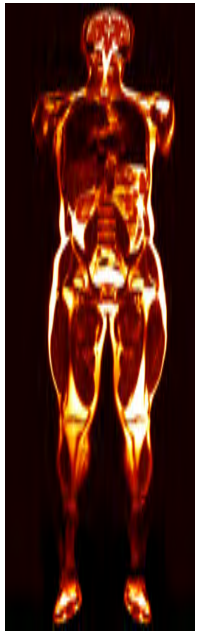

Wholebody MRI

Fusion: DTI – MRA - CT

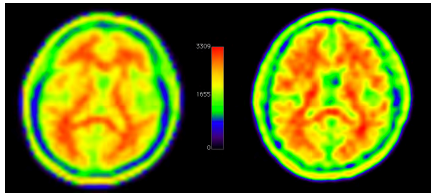

Amyloid Imaging (AV45): PET-MR vs PET-CT

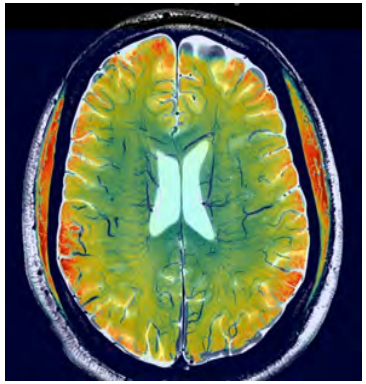

MRI SWI at 7 Tesla

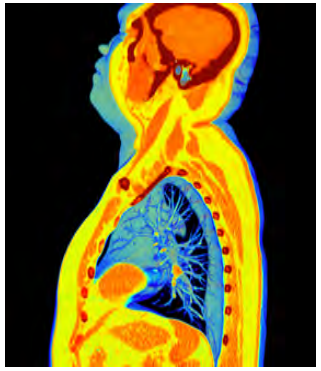

Low-dose CT

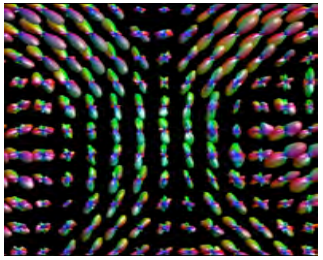

Diffusion Spectrum Imaging

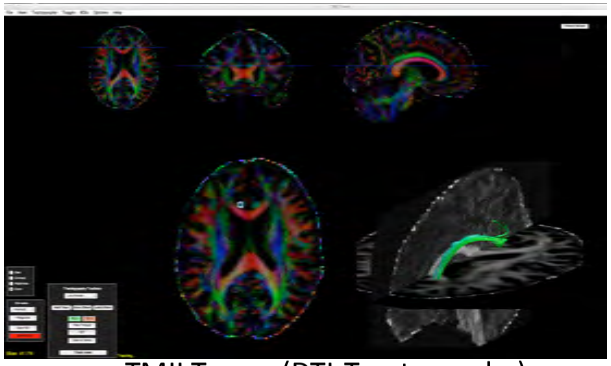

TMII Tracer (DTI-Tractography)

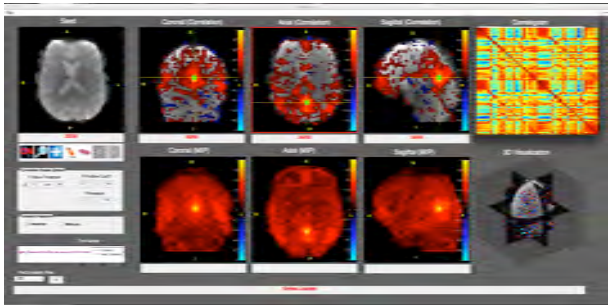

TMII Connectivity Explorer

TMII Pre-Clinical Imaging Core

Mount Sinai TMII Translational and Molecular Imaging Institute

Dr. Cheuk Ying Tang, Yu Zhou, Dr. Lazar Fleysher and Dr. Johnny Ng, Victoria Wang, , Christopher Cannistraci

Bruker Micro MRI – 7T & 9.4T

- Bruker Biospec 70/30USR with large bore B-GA 20S gradient (200mT/m, 640 T/m/s) and high performance gradient B-GA 12S (440mT/m, 3,440 T/m/s)
  - Coils: 154mm CP
  - 4Ch Mouse Brain Phased Array
  - 4Ch Mouse Cardiac Phased Array
  - CP body coil
  - CP $^{1}H/^{31}P$, $^{1}H/^{13}C$, $^{1}H/^{19}F$
- Bruker 9.4T 89mm vertical bore magnet with Micro 2.5 Gradient System (2.5G/cm/A, up to 100G at 40A) and MICWB40 In-Vivo micro imaging probe
  - 25mm & 30mm ID quadrature coils
- SA Isoflurane Anesthesia Setup
- SA Instruments Animal monitoring system

Bruker 7T

Bruker 9.4T

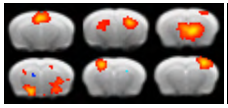

7T: Metabolic Syndromes (rsfMRI, DTI) *Drs. Pasinetti, Wang, Tang*

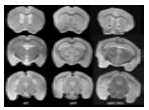

9.4T: Alzheimer's (Hi-Res , beta Amyloid) *Drs. Hof, Tang*

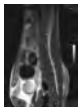

7T: Multiple Sclerosis, EAE (T2W,DTI) *Drs. Casaccia, Haines*

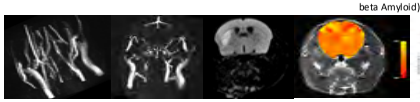

7T:Neovascularization - stroke (MRA, DWI, DCE) *Drs. Georgakopoulos, Tang*

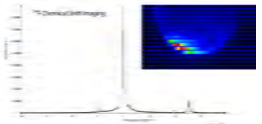

7T: ^{19}F Spectroscopy of ^{19}F, Drs. Fleysher, Martinez, Goldstein, Tang,

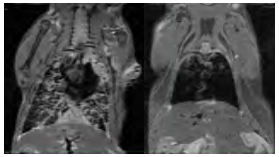

7T: Lung Tumor (T2W) *Dr. Goutham Narla*

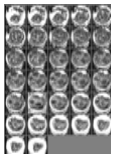

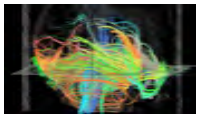

7T: Prostate Cancer (T2W,DWI) *Drs. Pisipati, Tewari , Tang, Taouli*

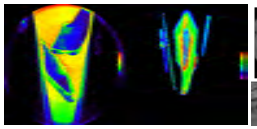

9.4T: Teeth as archives of exposure (T1W-T2W) *Drs. Arora, Mani*

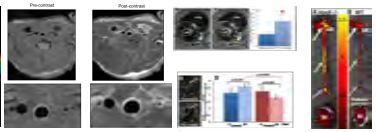

7T: permeability in ApoE-/- atherosclerotic mice , Drs. Fayad, Calcagno

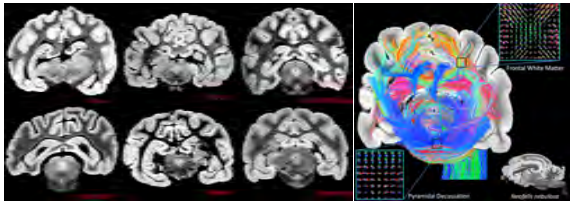

7T: Canine brains (hi-resT1, DSI) *Drs. Spocter, Tang, Hof*

IVIS-Spectrum Optical Imaging System

- The **IVIS Spectrum** in vivo imaging system uses a novel patented optical imaging technology to facilitate non-invasive longitudinal monitoring of disease progression, cell trafficking and gene expression patterns in living animals.
- The IVIS Spectrum is a versatile and advanced in vivo imaging system. An optimized set of high efficiency filters and spectral un-mixing algorithms lets you take full advantage of bioluminescent and fluorescent reporters across the blue to near infrared wavelength region.
- It also has the capability to use either trans-illumination (from the bottom) or epi-illumination (from the top) to illuminate in vivo fluorescent sources. 3D diffuse fluorescence tomography can be performed to determine source localization and concentration using the combination of structured light and trans illumination fluorescent images.
- The instrument is equipped with 10 narrow band excitation filters (30nm bandwidth) and 18 narrow band emission filters (20nm bandwidth) that assist in significantly reducing autofluorescence by the spectral scanning of filters and the use of spectral unmixing algorithms. In addition, the spectral unmixing tools allow the researcher to separate signals from multiple fluorescent reporters within the same animal.

IVIS-Spectrum System

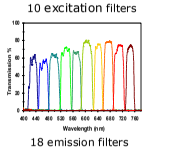

10 excitation filters

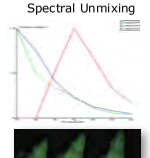

Spectral Unmixing

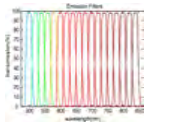

18 emission filters

Image from Perkinelmer

Breast Cancer Firefly Luciferase Images from Dr. Mihaela Skobe's Lab

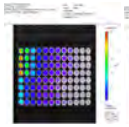

Bioluminescent image with Firefly luciferase tumor cells in 96 wells plate from Zewei Jiang (Dr. Samir Parekh's lab)

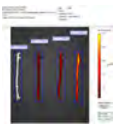

Aorta of Rabbit Cy5.5 Image from Mark Lobatto (TMII)

Optimal Transillumination for Deep Tissue Sources

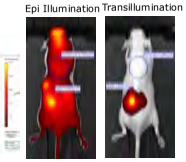

Epi Illumination Transillumination

sig/ bkg=1.43 sig/ bkg=90.51

Image from Perkinelmer

Automatic Mouse Atlas Registration in LI4.0

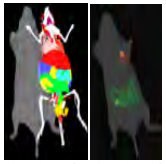

Unregistered Coregistered

Image from Perkinelmer

Vevo2100 Micro-Ultrasound System

- **B-Mode (2D)** imaging for anatomical visualization and quantification, with enhanced temporal resolution with frame rates up to 740 fps (in 2D for a 4x4 mm FOV) , and enhanced image uniformity with multiple focal zones.
- **M-Mode** for visualization and quantification of wall motion in cardiovascular research, single line acquisition allows for the very high-temporal (1000 fps) resolution necessary for analysis of LV function
- **Pulsed-Wave Doppler Mode (PW)** for quantification of blood flow
- **Color Doppler Mode** for detection of blood vessels including flow directional information and mean velocities; as well as for identification of small vessels not visible in B-Mode
- **Power Doppler Mode** for detection and quantification of blood flow in small vessels not visible in B-Mode; increased frame rates allow for significantly faster data acquisition
- **Tissue Doppler Mode** for quantification of myocardial tissue movement; for example in assessing diastolic dysfunction
- **Vevo MicroMarker® Nonlinear Contrast Agent Imaging** – for quantification of relative perfusion & molecular expression of endothelial cell surface markers; enhanced sensitivity to Vevo MicroMarker contrast agents as linear tissue signal is suppressed
- **3D-Mode** Imaging for anatomical and vascular visualization, when combined with either B-Mode, Power Doppler Mode or Nonlinear Contrast Imaging; allows for quantification of volume and vascularity within a defined anatomical structure
- **ECG and Respiration Gating** are used to suppress imaging artifacts due to respiration and cardiac movements. Both are important in cardiac and abdominal imaging for both 2D and 3D data sets.

VEVO 2100 Micro-Ultrasound System

Transducers:

*MS-200 12.5 or 21 MHz, Depth from 2mm to 36mm
*MS-250 16 or 21 MHz, Depth from 2mm to 30mm
*MS-400 24 or 30 MHz, Depth from 2mm to 20mm
*MS-550D 32 or 40 MHz, Depth from 1mm to 15mm

B-Mode and Color Doppler Mode

M-Mode

Pulsed-Wave Doppler Mode (PW)

Power Doppler Mode

Tissue Doppler Mode

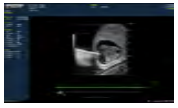

Image-Guided Needle Injection

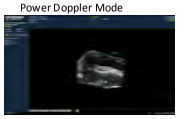

3D-Mode Imaging

Vevo MicroMarker® Nonlinear Contrast Agent Imaging

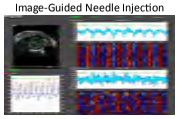

VevoStrain™ Analysis software for cardiac research

Ancillaries

Gamma Counter

Centrifuge

Shielded Fume Hood

Dose Calibrator

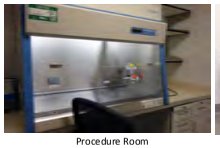

Procedure Room

Procedure Room (radioactive)

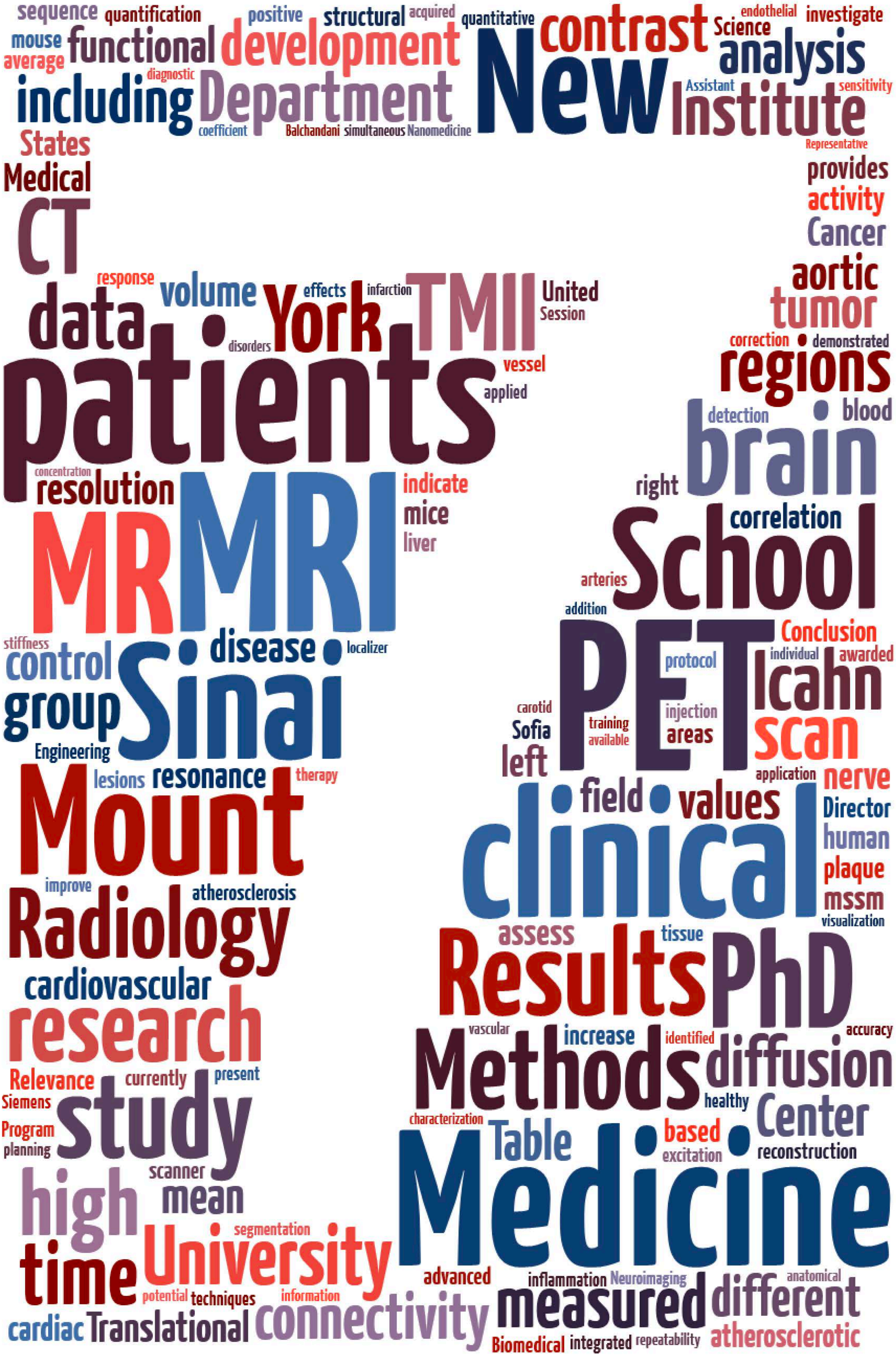
sequence
quantification
positive
structural
acquired
quantitative
endothelial
investigate
mouse
functional
development
contrast
Science
analysis
average
diagnostic
including
Department
New
Assistant
sensitivity
Institute
coefficient
Balchandani
simultaneous
Nanomedicine
States
Representative
Medical
provides
activity
CT
Cancer
aortic
response
volume
effects
infarction
TMII
United
data
tumor
Session
York
disorders
correction
demonstrated
patients
vessel
regions
applied
detection
blood
concentration
resolution
brain
right
indicate
MR
MRI
mice
correlation
liver
School
arteries
addition
PET
Conclusion
stiffness
control
disease
localizer
protocol
individual
awarded
Icahn
Sinai
group
carotid
injection
Sofia
training
scan
Engineering
available
areas
left
application
nerve
lesions
resonance
therapy
field
values
Director
Mount
clinical
human
improve
atherosclerosis
plaque
mssm
visualization
Radiology
assess
tissue
Results
PhD
cardiovascular
vascular
increase
identified
accuracy
research
Methods
diffusion
Relevance
currently
present
healthy
Siemens
study
Center
Program
planning
characterization
Table
based
Medicine
scanner
excitation
reconstruction
high
mean
segmentation
time
University
advanced
inflammation
Neuroimaging
anatomical
potential
techniques
information
measured
different
cardiac
Translational
connectivity
Biomedical
integrated
repeatability
atherosclerotic